Plasmonics at Liquid-Liquid Interfaces

Vladimir A. Turek

Submitted in partial fulfilment of the requirement for the degree of Doctor of Philosophy

Imperial College London, Department of Chemistry

January 2014

Statement of Originality

I declare that the work presented in this thesis is my own and that all other material is referenced appropriately and reprinted with permission.

Acknowledgements

I am indebted to my supervisors: Joshua Edel, Anthony Kucernak and Alexei Kornyshev for giving me an opportunity to pursue such a fascinating and multidisciplinary project. Their patient guidance, vision and extensive expertise were key in the realization of this work.

I also thank the people that I've collaborated with over the years. Jack Paget for his help with theoretical matters. Dr. Arwen Tyler and Prof. John Seddon for the XRD experiments of the high density solutions. Aeneas Weiner for the simulations. Dr. Nico Cousens for his early stage guidance. Dr. Steve Roser for XRD studies of particles at the interface. Dr. Angela Demetriadou for simulations of the high density solutions. Antoni Llopis Lorente for his help at Diamond and the reflection measurements. Dr. James Wilton-Ely, Dr. George Britovsek and Prof. Tom Welton for their discussions on the heavy metal ion detections. Laura Elliott for her help with the high density solutions. Dr. Thao Le for her help with the preliminary protein purification studies. Dr. Xavier Casadevall i Solvas for some fascinating microfluids work and for my first publication. And of course, Mark Draper for the super-hydrophobic work.

Of all the collaborations that I've had over the course of the project, none have been as fruitful as the ongoing one with Dr. Michael Cecchini. Aside from being a fantastic scientist, I consider him a true friend. His expertise in Matlab, optics and Raman spectroscopy were crucial in most aspects of the project. Though he has decided to move away from academia, I wish him the best of luck in future.

I wish to thank all the people that have made the work environment so enjoyable, for their discussions and for their time, in particular, Youngeun Choi, Maryam Qurashi, Dr. Neveen Hosny, Dr. Amol Patil, Dr. Kerry Wilson, Dr. Colin Crick, Dr. Margarita Stapountzi, Dr. Simon Dowland, Dr. Alex Ivanov, Dr. Soongwon Cho, William Pitchford, Dr. Monica Marinescu and Dr. Jonathan Dusting, as well as all the past and present members of the Edel, Kornyshev, Kucernak, Albrecht, Kuimova and Haque groups.

Additionally, I would like to thank my out-of-work friends, Salim Essemiani, Ralph Schlüssel, Natalia Yankova, Pierluigi Frison and Nickolai Vysokov for their understanding and much needed respite.

Last, but by no means least, I would like to thank my family – my wonderful wife Elena, our son Mikhail, my loving parents, my sisters, Tatiana and Yuliya, my brothers, Alex and Yura, and of course, my god-daughter Maria. Your unconditional support throughout the years has made this work possible.

Table of Contents

Chapter 1: Background

Chapter 2: Experimental Overview

Chapter 3: A Plasmon Ruler at the Liquid-Liquid Interface

Chapter 4: Ultra-concentration of nanoparticles

Chapter 5: Surface Enhanced Raman Spectroscopy (SERS) at the LLI

Chapter 6: Conclusions and Outlook

List of Figures

Chapter 1

Chapter 2

Chapter 3

Chapter 4

Chapter 5

List of Abbreviations

1,8-DAN	-	1,8-Diaminonaphthalene
AFM	-	Atomic Force Microscopy
ATP	-	Adenosine triphosphate
CTAB	-	Cetyl trimethylammonium bromide
DBDAC	-	1,10-dibenzyl-1,10-diaza-18-crown-6
DCE	-	1,2-Dichloroethane
DDA	-	Discrete Dipole Approximation
DI	-	De-ionized
DLS	-	Dynamic Light Scattering
DLVO theory	-	Derjaguin Landau Verwey Overbeek theory
FWHM	-	Full Width at Half Maximum
GI-SAXS	-	Grazing Incidence Small Angle X-Ray Scattering
HCP	-	Hexagonally Close Packed
HWHM	-	Half Width at Half Maximum
ITIES	-	Interface between Two Immiscible Electrolyte Solutions
LAI	-	Liquid-Air Interface
LLI	-	Liquid-Liquid Interface
LSPR	-	Localized Surface Plasmon Resonance
MATT	-	Methoxy-α-toluenethiol
MDDA	-	12-Mercaptododecanoic acid
MGITC	-	Malachite green isothiocyanate
MNBI	-	2-Mercapto-5-nitrobenzimidazole
MSA	-	Mercaptosuccinic acid
NPs	-	Nanoparticles
PTTBA	-	4,4′,4″,4‴-(Porphine-5,10,15,20-tetrayl)tetrakis(benzoic acid)
RB	-	Rose Bengal

RCF	-	Relative Centrifugal Force
SEM	-	Scanning Electron Microscopy
SERRS	-	Surface Enhanced Resonance Raman Scattering
SERS	-	Surface Enhanced Raman Scattering
STM	-	Scanning Tunneling Microscopy
TEM	-	Transmission Electron Microscopy
UV-Vis	-	Ultraviolet-Visible Spectroscopy
XRD	-	X-Ray Diffraction

Chapter 1: Background

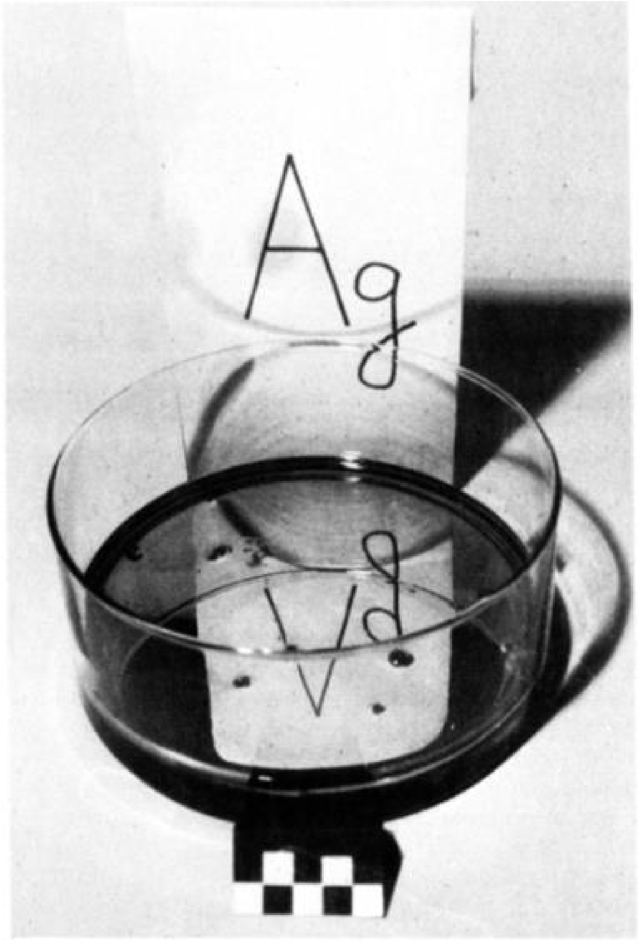

Reprinted with permission from Yogev and Efrima[1]. Copyright (1988) American Chemical Society.

1.1 Project aims: Plasmonics at the LLI

The first demonstration of plasmonic nanoparticles (NPs) at the liquid-liquid interface (LLI) was carried out in 1988 by Yogev and Efrima[1], who reported on a metallic liquid-like film formed by silver colloids at the water-dichloromethane interface. The 2D self-assembly that the LLI offers is a natural match to the unique optical properties of plasmonic NPs. With diverse applications ranging from detection[2-6], novel optical properties[1, 7, 8], electro-variable optics[9, 10] and hierarchical self-assembly[11-14], the field of plasmonics at the LLI has been growing rapidly in the last 10 years.

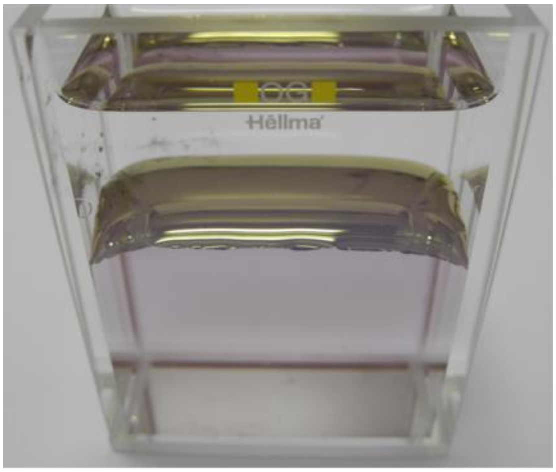

Figure 1.1 | Photograph of gold nanoparticles at the LLI demonstrating their reflective properties. Reprinted with permission from Fang *et al*[7]. Copyright (2013) American Chemical Society.

Of particular importance to the work in this thesis is a theoretical description of tuneable optical properties as a function of the inter-particle separation published by Flatte *et al*[9]. It was predicted that, a 2D array of NP at the LLI would show a red-shift and peak broadening of the localized surface plasmon resonance (LSPR) maximum as the inter-particle separation is reduced (or the NP coverage of the interface increased). This shift would be accompanied by an increase in the magnitude of the reflection coefficient that would enable the demonstration of a smart-mirror – such that when the NPs are in the bulk solution, the plasmon would be in the ultraviolet regime and hence colourless, while when assemble to the interface, the red-shift would mean that high reflectivities would be obtained across the visible spectrum (Figure 1.2). The inter-particle separation and the number of particles adsorbed to the interface were proposed to be modulated by a small applied potential across the interface between two immiscible electrolyte solutions (ITIES).

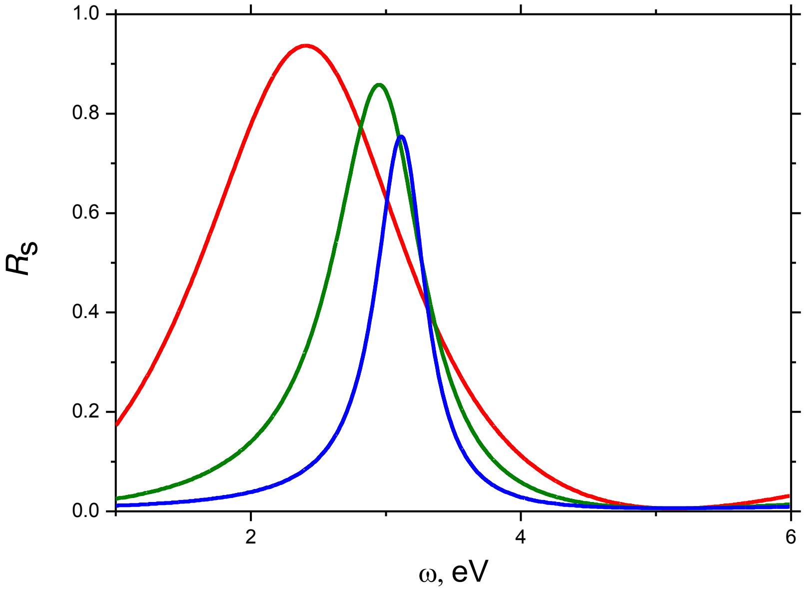

Figure 1.2 | Reflection coefficient of s-polarized light as a function of particle coverage at the water-DCE interface for silver nanoparticles of 20 nm radius at an incidence angle of 45°. Reprinted with permission from Flatté *et al*[9]. Copyright (2010) American Chemical Society.

The project aim was therefore to experimentally study the optical properties of plasmonic NP arrays adsorbed at the liquid-liquid interface. It was aimed to establish control over the inter-particle separation and to achieve reversibility of the adsorption process – though initial aims were to achieved this through electrochemical means at the ITIES, it was decided to use alternative means of assembly for preliminary studies. Following this investigation, some practical applications of these assemblies were to be investigated. In particular, it was envisaged that the plasmon coupling between the NPs at the LLI could be used for the detection of analytes through surface enhanced Raman scattering (SERS).

The central theme behind the project was therefore the use of plasmonic NPs at a LLI. Throughout most of the work, spherical gold particles were used at a water/1,2-dichloroethane (DCE) interface. The multidisciplinary nature of the work means that a comprehensive review of all the covered topics is not feasible, instead this introduction will briefly introduce the key aspects of the major fields. Firstly, NPs will be introduced – though much could be said about current research efforts using NPs, the discussion will focus more about their stability and their plasmonic properties. The latter will be introduced through a brief description of the 'plasmon', the ability of plasmons to hybridize and finally the key aspects of the vast field of surface enhanced Raman spectroscopy will touched upon. Following this, some fundamentals of the LLI and NPs adsorbed to the LLI will be discussed. No discussion can omit the surface tension which dominates the interfacial properties or the forces acting on and between NPs at the LLI. Following this a thesis overview will be given.

1.2 Nanomaterials

Nanotechnology promises to revolutionize science (and in many respects already has)[15-18]. The bridging of molecular and macroscopic materials leads to some unique properties of nanomaterials – from optical[7, 19-24], to magnetic[25-27], electrical[28-30], catalytic[31-33] and physical[34-36], the opportunities that nanomaterials offer are unprecedented. One of the main types of nanomaterials are nanoparticles (loosely defined as a particle of any shape with dimensions between 10-100 nm). Their use is now common place in many different branches of science with applications including catalysis[37-39], medicine[40, 41], anti-bacterial[42, 43], drug delivery systems[44, 45], detectors[46-49], novel materials[50, 51], optics[52-54], solar-cells[55-57], fuel-cells[58, 59] and even clothing[60].

Despite the recent surge in research activity involving NPs, as an entity, they are not new to science. For example Richard Feynman in 1959 gave his famous talk 'There's plenty of room at the bottom' – widely accredited as the conceptual birth of nanotechnology, yet 8 years earlier, John Turkevich published a manuscript on the synthesis of colloidal gold[61] – which is to this day, the mostly widely used synthesis of the most widely used nanoparticles[62]. In fact Richard Adolf Zsigmondy won the 1925 Nobel Prize in chemistry for his work on colloids. Even before this, Michael Faraday's work in 1857 is accredited as the first identification gold nanoparticles as the cause for the 'ruby fluid'[63], however reports on colloidal gold predate even this work[37]. While the earliest applications of gold NPs date to at least the 4th century in Roman glass making[64]. The renewed interest in nanoparticles is attributed to both the technological advantages they offer as well as the development of high resolution imaging techniques such as electron microscopy and scanning probe microscopies. With respect to the context of the work demonstrated in this thesis, a detailed overview of NPs is perhaps less relevant. Despite being central to every aspect of the project, there was little variation in the type of NPs used. Throughout the project, spherical gold NPs, prepared by the citrate reduction of tetrachloroaurate were used. Perhaps the most important aspect of the NPs was their stability with respect to aggregation and their plasmonic properties. These will be summarized below.

1.3 Stability of NPs in the Bulk

A key property of NPs is that they possess a large surface area-to-volume ratio. This fact leads to a large portion of the atoms in NPs being at the surface. This property is highly advantageous for a great deal of research, but does nevertheless lead to a significant challenge – aggregation[65] (please note: aggregation/agglomeration/flocculation etc. are terms that are often used interchangeably, however throughout the thesis 'aggregation' will refer to the irreversible process, while 'agglomeration' will refer to the reversible process[66]). The incomplete bonding of the surface layer of atoms in a NP means that they are energetically unstable. In fact this instability may give rise to enhanced reactivity[67] and even to catalytic properties of otherwise noble metals[37] and is a key factor of NP synthesis after the nucleation stage[68]. However this instability also leads to aggregation of particles[69]. In solution, this aggregation will be promoted by short-ranged van der Waals forces and countered by the long range repulsive electrostatic forces. This approximation, known as the DLVO (Derjaguin, Landau, Verwey, Overbeek) theory[70-72] is expressed in eq. 1.1. This theory states that the total inter-particle interaction is a sum of the repulsive electrostatic interactions and the attractive van der Waal's forces (assuming that H-bonding networks and hydrophobic effects are not applicable to the system[73]).

$$V_T = V_{elec} + V_{vdW} \qquad \text{(Eq. 1.1)}$$

For two equally sized particles, V_{elec} takes on the form,

$$\frac{V_{elec}}{k_B T} = \frac{e^2 Z^2}{4\pi\varepsilon k_B T}\left[\frac{e^{\kappa a}}{1+\kappa a}\right]^2 \frac{e^{-\kappa r}}{r} \qquad \text{(Eq. 1.2)}$$

Where r is center-center inter-particle separation; a is the radius of the NPs; Z is the number of charges on the NPs; and κ^{-1} is the Debye-Hückel screening length.

V_{vdW} is given by,

$$\frac{V_{vdW}}{k_B T} = -\frac{A_H}{6k_B T}\left[\frac{2a^2}{r^2-4a^2} + \frac{2a^2}{r^2} + \ln\left(1-\frac{4a^2}{r^2}\right)\right] \qquad \text{(Eq. 1.3)}$$

Where A_H is the Hamaker constant[74].

Despite assuming that only two forces are present between NPs, the DLVO theory is sufficient to account for the stability of a large portion of NPs[70, 75]. In short, the theory suggests that the long range electrostatic term will provide an energy barrier that prevents 2 particles coming close together. The strength of this barrier (for a fixed NP size at a fixed inter-particle separation) will depend on the charge of the NPs and the ionic strength of the solution (increasing for more charged NPs and decreasing for higher ionic strengths). If the NPs are brought closer together, then the short range, but stronger van der Waals forces will dominate leading to aggregation/agglomeration of the particles. In effect, to prevent aggregation, two strategies can be implemented – the first is to increase the charge on the NPs, for example, either through changes in the functionality or through equilibration of the Fermi energy of the particles with the surrounding medium.. The other method to increase NP stability is through a reduction of the ionic strength of the solution – this is a relatively straightforward parameter to control, therefore in general researchers tend to avoid increasing the ionic strength of colloidal solutions. To give an example of the effect of the ionic strength, for citrate stabilized NPs, the threshold KCl concentration at which aggregation occurs is approximately 20 mM[74] (Figure 1.3), while 'as made' citrate stabilized NPs tend to have an effective NaCl concentration of 2.5 mM.

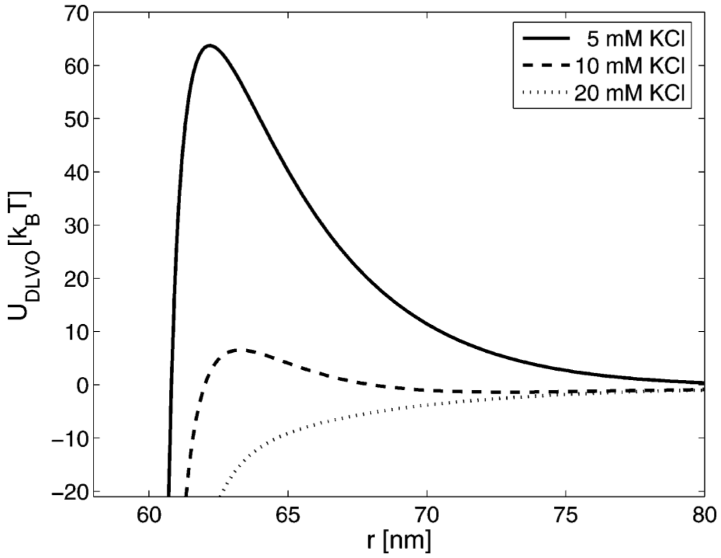

Figure 1.3 | DLVO interactions between 30 nm (radius) NPs with Z=1000 as a function of their separation at different salt concentrations. Reprinted with permission from Meyer *et al*[74]. Copyright (2006) American Chemical Society.

It should be mentioned that alternative stabilizing techniques are needed for NPs dispersed in organic solvents. For gold, this is usually achieved through steric stabilization of the NPs with long alkane thiols[37, 76]. The principle behind this is that a charge can rarely be accommodated in non-polar solvents, meaning that electrostatics cannot be relied on to provide stability. In order to counter the effect of van der Waals, the sterically bulky functionality prevents the NPs from coming into close enough proximity for these to dominate. Purely sterically stabilized particles tend to be more prone to agglomeration than those stabilized electrostatically; however simple agitation of the solution is usually sufficient to redisperse the particles.

1.4.1 Plasmonics

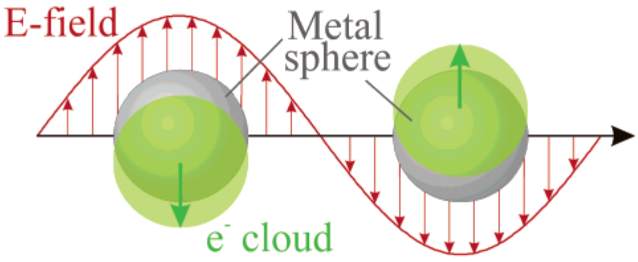

Figure 1.4 | Schematic of the plasmon. The plasmon is an oscillation of the electron in a metallic surface that is induced by the electric field of incident light. Reprinted with permission from Kelly *et al.*[24]. Copyright (2003) American Chemical Society.

Plasmonics in the study of the interaction of light with metals. The electric field of electromagnetic radiation causes oscillations of the electrons in a metallic surface, this oscillation is the ‘plasmon’. When certain criteria are met, the electrons and the electric field may resonate, this is called plasmon resonance, or more usually (as the oscillations occur at a surface) surface plasmon resonance (SPR) (Figure 1.4). The SPR is very sensitive to dielectric properties of both the surrounding medium of the surface and the surface itself[47, 77]. This property has led to the development of SPR sensors[6, 78, 79] – through either the Kretschmann or the Otto configuration[80, 81], it is possible to excite the plasmons at incident angles of total internal reflectance. The excitation leads to an apparent loss in the reflectivity (as the plasmons propagate along the metal’s surface). In other words if analytes bind onto a gold surface, the change in the dielectric property of the surrounding medium will shift the angles at which the plasmons are excited – coupled with specificity groups on the gold surface, this type of sensor has found uses in diagnostics.

Though plasmons in a bulk metal have already found practical applications, the main interest that the field has garnered has been on the interaction of light with confined metallic nanostructures[82-85]. In order to differentiate from the bulk metal, the term localized surface plasmon resonance (LSPR) is used for nanostructures. The simplest of such nanostructures is a spherical nanoparticle. For a small spherical NP, the polarizability, α, is given by

$$\alpha = 4\pi a^3 \frac{\varepsilon - \varepsilon_m}{\varepsilon + 2\varepsilon_m} \qquad \text{(Eq. 1.4)}$$

Where ε is the dielectric permittivity of the metal; ε_m is the dielectric permittivity of the surround medium and a is the radius of the particle. The polarizability can then be related to the scattering and extinction cross-sections by,

$$C_{ext} = kIm[\alpha] \qquad \text{(Eq. 1.5)}$$

and

$$C_{sca} = \frac{k^4}{6\pi}|\alpha|^2 \qquad \text{(Eq. 1.6)}$$

Where $k = \frac{2\pi}{\lambda}$; and λ is the wavelength[19].

In other words, the localized plasmon resonance depends on the size and material of the particle and the dielectric constant of the surrounding material. Practically, this leads to a visible coloration of colloidal solutions. The position and the broadness of the LSPR peak carries with it information on the particle size, polydispersity, functionality and aggregation. This enables a quick and convenient estimation of the NPs' behavior in solution through UV-Vis spectroscopy[86, 87]. For example the 16 nm citrate stabilized gold particles used in this project had a peak maximum at ≈519 nm, when functionalized with 12-mercaptododecanoic acid, this shifted to 525 nm, whilst the larger 43 nm citrate-stabilized particles used for Chapter 5 had a maximum at 532 nm. When aggregation occurred however, the peak of the 16 nm particles shifted to 630 nm – this is a result of plasmon coupling at closer inter-particle separations.

1.4.2 Plasmon coupling

An intriguing property of plasmons is their ability to couple once two metallic objects are brought into close proximity[88-90]. The coupling changes the frequency of the two interacting plasmons – for the case of spherical NPs, this has the effect of reducing the energies required to excite the plasmon, thereby red-shifting the LSPR to higher wavelengths.

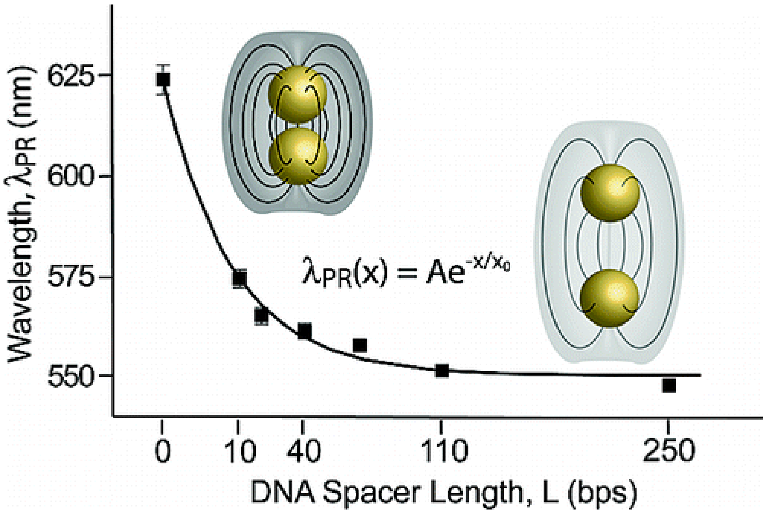

Figure 1.5 | Plasmon coupling of two attached NPs leads to an exponential dependence on the spacer length with respect to the λ_{max} of the plasmon resonance. Reprinted with permission from Reinhard *et al.*[91]. Copyright (2005) American Chemical Society.

The exponential dependence on the plasmon resonance maximum as a function of distance between the NPs has led to the development of 'molecular/plasmonic rulers'[91-96]. The principle behind these is that the shift in the LSPR of interacting NPs enables one to determine the separation between them. This can be experimentally achieved by, for example attaching two NPs together through a DNA linker (Figure 1.5). This information therefore allows precise spatial information from a very simple optical measurement. The 1D nature of the first demonstrated plasmon rulers is not limiting. They have since been demonstrated to allow spatial information to be extracted in both 2D[8, 97-99] and even in 3D[100, 101].

As a side note, it should be mentioned that when anisotropy is introduced with respect to the incident light and the nanostructure (such as the case in plasmon coupling of 2 NPs), the excitation of plasmons becomes polarization dependent. For the purposes of the work detailed in this thesis however, the polarization of the light is not important – in all the case covered in Chapters 3-5 the light was directed at normal incidence with respect to the samples.

1.5 Surface enhanced Raman scattering

Raman scattering is a result of the inelastic scattering of light upon its interaction with a molecule. The observation of this effect by C.V. Raman[102] resulted in the 1930 Physics Nobel Prize. Most of the light scattered elastically, with no change in energy of the photon being observed, this is called Rayleigh scattering. However, a very small fraction of photons (approximately 1 in 10^7) will induce a change in the polarizability of the molecular vibrations, thereby exciting them to a virtual energy level. Most often, Raman scattering gives rise to a decrease in the photon energy (Stokes shift), in which the change in energy is characteristic to specific molecular vibrations. In other words, similar to infrared spectroscopy, Raman scattering will produce a characteristic spectrum of the molecule, based on the bonding present in the molecule, however unlike infrared, a single wavelength (usually from a laser in the visible spectrum) is used for Raman. Additionally, the selection rule for Raman is that the vibration must induce a change in the polarizability rather than in the dipole moment. The ability to identify the molecular structure by Raman scattering has therefore made it a commonplace technique in analytical chemistry[103].

Nevertheless, there is a significant limitation to conventional Raman spectroscopy, which is the aforementioned low probability of inelastic scattering of the photons. This limitation was overcome in 1974 when Martin Fleischmann and coworkers observed an anomalously strong Raman scattering intensity of pyridine adsorbed on a roughened silver electrode[104], which could not be accounted for by the concentration of pyridine arising from the increased surface area of the electrode[105, 106]. This observation gave rise to the field of surface enhanced Raman scattering (SERS).

SERS is one of the most important practical outcomes of the field of plasmonics. A molecule in close proximity to a plasmonic surface will experience a dramatic increase in its effective Raman cross-section. The enhancement factor from the surface may reach 10^{10}-10^{11}[107, 108]. In effect, the plasmonic surface is therefore able to make an insensitive technique capable of single molecule detection[109-111]. Aside from its sensitivity, SERS, like Raman spectroscopy also provides a spectral fingerprint of the molecule being detected (though changes in molecular orientation at the surface may make Raman spectra and SERS spectra not directly comparable). This fact makes SERS a highly attractive detection technique – unlike alternative ultrasensitive/single molecule techniques which are able to detect analytes, SERS creates the opportunity to identify the molecule[112]. As such SERS has attracted an immense amount of research in recent years[113-119].

Despite this intense research it is surprising that the exact mechanism by which SERS operates is still debated[112]. It is generally accepted that two main enhancement mechanisms exist, the chemical enhancement[120, 121] and the electromagnetic enhancement[112, 122]. The contributions to the observed signal follow,

$$P_{SERS} \propto NI_L|A(\nu_L)|^2|A(\nu_s)|^2\sigma_{ads}^R \qquad \text{(Eq. 1.7)}$$

Where P_{SERS} is the probability of an incident photon giving rise to a SERS signal; N is the number of molecules involved in the SERS process; I_L is the intensity of incident light; $A(\nu_L)$ and $A(\nu_s)$ are the field enhancement factors of the excitation and scattered field; and $\sigma_{ads}^R$is the increased Raman cross section of the adsorbed molecules compared to conventional Raman[123].

In eq. 1.7, $A(\nu_L)$ and $A(\nu_s)$ are approximately equal, meaning that the P_{SERS} scales as approximately E^4, where E is the local optical field enhancement. In other words a relatively small increase in electric field arising from plasmon resonance at the surface of a metallic structure can lead to a large increase in the observed SERS intensity[123]. With the emergence of nanotechnology and the ability to control through either top-down or bottom-up techniques nanostructure, a lot of work has therefore focused on optimizing this field enhancement[113, 119, 124]. Some of this work will be discussed in more detail in chapter 5.

Briefly, there are mainly two broad strategies for generating an enhanced SERS signal from substrates. The first, and more widely employed strategy, is through plasmon coupling. As two metallic structures approach, the field generated between the structures is increased – if optimally positioned, the field becomes sufficiently high to allow for even single molecule detection within its volume[125]. This is typically called a 'hot-spot'. For example, such hot-spots may arise in a random fashion from a macroscopic assembly of nanoparticles (such as aggregates or 2D arrays)[11, 46, 111, 126, 127] or from a small clusters (dimers/trimers)[119, 128-130].

The second strategy is through careful engineering of a single non-interacting nanostructure. Uncoated, spherical, non-interacting NPs generally only achieve an enhancement factor of 10^3 and are therefore not ideal as substrates[112]. However, 'exotic' spherical particles such as nanoshells or core-shell particles show a substantially improved SERS signal[128, 131]. By introducing sharp features in nanostructures, it is possible to direct the plasmons to focus at a specific point, this leads to higher field strengths at that point and thereby an increased SERS intensity[132, 133].

One final strategy for generating increased signal strength should be mentioned, this is through surface enhanced resonant Raman scattering (SERRS). This strategy involves the use of analytes that have an electronic transition close to the wavelength of the incident laser. Though not strictly advantageous for detection purposes, SERRS is capable of enhancement factors exceeding 10^{14}. Its main use is for proof-of-principle studies on novel substrates or for fundamental studies to aid the signal-to-noise ratio[49, 134, 135].

1.6.1 Surface tension

The importance of interfacial science cannot be overstated. Almost all aspects of life, at its centre, involve an interface. On many occasions the interface plays a significant role on the behaviour of the system, in some cases even dominating its behaviour. Some classic examples of this include water droplets; mechanical failure of solids; and heterogeneous catalysis. In particular, the liquid-liquid interface plays a key role in emulsions[136, 137], droplet-based microfluidics[138, 139], the interface between two immiscible electrolyte solutions[140-142], organic synthesis[143], optics[144-146] and even in food (e.g. milk and salad dressing).

One of the main aspects of an interface is the incomplete bonding structure of the interfacial layer, which leads to surface tension, γ. The surface tension acts to reduce the interfacial area of the material. The effects of surface tension are most relevant for liquids. The liquid phase will aim to reduce its total surface tension. If the interaction with its surrounding medium is unfavourable, the surface tension can be high enough to lead to macroscopic rearrangements in its structure to reduce the interfacial area – this effect is especially pronounced in liquids which have strong intermolecular interactions such as water or mercury. For the most common case, the interaction of water with solids, this has important implications – the more unfavourable the interaction with the solid, the more spherical a droplet of water will be. The modulation of unfavourable solid interactions with water has led to the development of superhydrophobic surfaces which have practical applications in stainless clothing, 'self-cleaning' surfaces, ship coatings and even to aid detection[147-149].

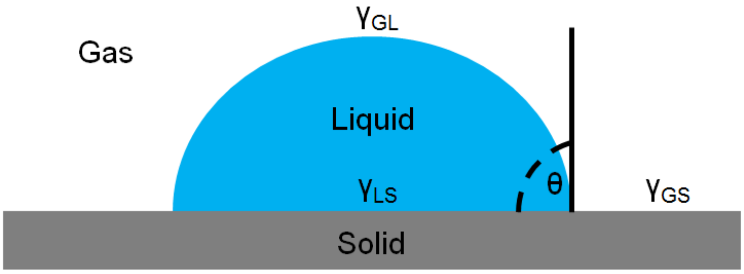

Figure 1.6 | The three phase contact angle that a droplet makes with a solid surface, carries with it information on the surface tensions of the gas-solid, gas-liquid and the liquid-solid interfaces.

If the interactions with a solid substrate are favourable however, then the liquid will aim to maximize its contact area. This will be countered by the unfavorable creation of additional interfacial area with the surrounding medium (such as air or an immiscible second liquid). The counterbalance of these forces means that the contact angle which the liquid makes with the solid carries with it the information on the surface tensions of the liquid-solid, air/second immiscible liquid-solid and the air-liquid/liquid-liquid. For a case such as shown in Figure 1.6 for a droplet wetting a solid interface surrounded by air, Young's equation states that,

$$\gamma_{GS} = \gamma_{LS} + \gamma_{GL}\cos\theta \qquad \text{(Eq. 1.8)}$$

Where γ_{GS}, γ_{LS} and γ_{GL} are the surface tensions between the gas-solid, liquid-solid and gas-liquid interfaces respectively; and θ is the three phase contact angle. Young's equation also holds for case of two immiscible liquids, with the gas term being replaced by the second liquid. In other words, from the knowledge the contact angle it is possible to extract all the related surface tensions of the relevant system.

It is worth noting also that adsorption of charged species at an interface leads to mirror opposite charges accumulating on the opposite interface. The favourable electrostatic attraction between the charges leads to an overall reduction of the surface tension of such interfaces and as a result, the contact angle. This modulation of contact angle through electrochemical means (electro-capillarity) has led to the development of electro-variable optics, such as variable focal point lenses and even colour e-paper[150-152].

1.6.2 Particles at the LLI

Another way to minimize the surface tension of an interface is through adsorption of substrates which reduce the contact area of the two phases. Undoubtedly the most commonly used substrates that lower the surface tension are chemical surfactants (such as soaps), however for the purposes of this thesis, the adsorption of NPs is the most relevant. The adsorption of particles to the LLI was first reported in 1903 by Ramsden[153] (and separately in 1907 by Pickering[137]). Their work described the stabilization of emulsions by adsorbed particles and has led to the term 'Pickering emulsions'.

Though industrial applications of particles at the LLI already exist the field has experienced a resurgence in recent years. With developments in nanotechnology, it has become increasingly desirable to achieve self-assembly through bottom-up techniques[17]. The intrinsically self-healing and almost molecularly flat properties of the LLI[1, 154], coupled with its ability to spontaneously adsorb particles to yield macroscopic 2D assemblies from nanoscopic building blocks[155-158] make it an attractive platform for template self-assembly.

1.6.3 Forces on particles at the LLI

Despite the opportunities that the LLI offers, it also comes with challenges, perhaps the main of which is the difficulty in imaging such an interface[159]. Nanometer-resolution imaging techniques are not readily available – most electron microscopies need a vacuum; STM requires a conductive substrate; and while AFM is possible, non-contact mode is required (if the AFM tip makes contact with the LLI, it will adsorb), which together with the lack of rigidity of particles at the interface means that accurate AFM imaging is challenging. The difficulty in imaging NPs at the LLI means that one of the most crucial parameters, the three phase contact angle cannot be determined with ease.

The main driving force for adsorption is the interfacial stabilization. The stabilization energy is highly dependent on NP size and the contact angle and is given by,

$$E = \pi R^2 \gamma_{ow} (1 + \cos\theta)^2 \qquad \text{(Eq. 1.9)}$$

Where R is the particle radius, $\gamma_{ow}$is the oil-water surface tension and θ is the three phase contact angle[160].

It is clear from Figure 1.7 that even for a relatively small particle (20 nm diameter) that the energy of adsorption can be >1000 k_BT for contact angles approaching 90°. The magnitude of this force means that once adsorbed, particles are generally very stable and desorption does not readily occur (in fact desorption can be challenging to achieve experimentally) – the R^2 dependence also means that this is especially true for larger particles. Additionally, the line tension can either increase or decrease the stability of particles at the interface however experimental determination of its magnitude has yielded varied results[161, 162]. For charged particles, due to the difference in the dielectric constants of the aqueous and organic phases, solvation will also result in a destabilizing force for NPs at the LLI[163].

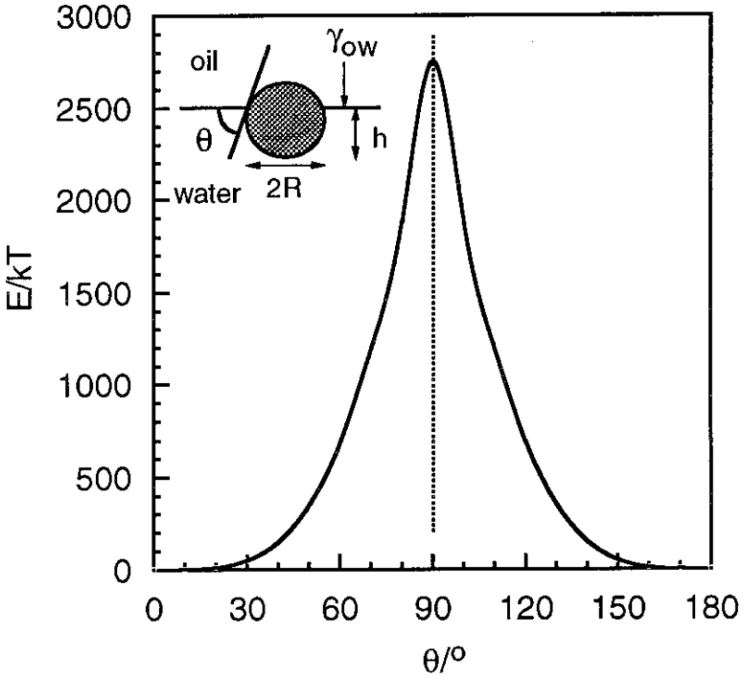

Figure 1.7 l Energy of adsorption of a spherical particle of 10 nm radius to an oil-water interface with a surface tension of 36 N m^{-1} as a function of the three phase contact angle. Reprinted with permission from Binks *et al*[160]. Copyright (2000) American Chemical Society.

Unlike in the bulk solution, the interactions between the NPs themselves, once adsorbed to the LLI are not as straightforward; additional liquid interface-specific forces are introduced and even the van der Waals and electrostatic interactions become altered[162]. The liquid-interface specific forces include capillary forces (which attract particles over a long range as a result of the interfacial deformation arising from the NPs' charge) and capillary waves (which attract particles as a result of thermal fluctuations of the interface itself)[161, 162, 164]. The van der Waals forces are expected to be stronger between particles at the LLI as compared to the bulk solution – this is due to the fact that the Hamaker constant will be altered for particles that are partially immersed in the organic phase[162]. Finally, the LLI has a very pronounced effect on the electrostatic repulsion between particles. A dipole-dipole interaction arises from the asymmetric charge build up on the NPs. For μm-sized particles this can lead to a strong repulsive force that acts over 10's of μm[165].

It is clear that both the adsorption energy and the inter-particle interactions are strongly dependent on the position of the NPs with respect to the interface and the three phase-contact angle. Unfortunately, these parameters are challenging to determine experimentally even for micron-sized particles[166-168] and only either indirect methods (which may alter these parameters) [169-171] or non-trivial measurements (such as XRD)[172] have been able to determine these for nm sized particles. One of the most common techniques for characterization of the energies involved has been through surface tension measurements with techniques such as the pendant-drop method[155, 157] (Figure 1.8). Surface tension measurements allow for the determination of the energy of adsorption, which in turn, through Eq. 1.9 allows for an estimation of the contact angles.

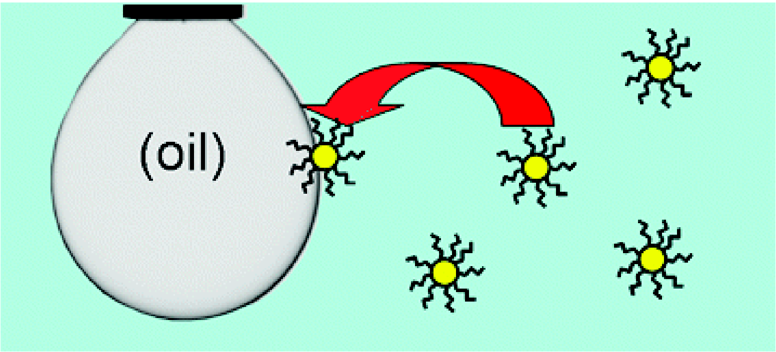

Figure 1.8 | Surface tension measurements of the oil-water interface using the droplet pendant technique allows for the determination of the energy of NP adsorption. Reprinted with permission from Du *et al*.[157]. Copyright (2010) American Chemical Society.

1.7 Thesis outline

As the title suggests, the central theme behind the project is plasmonics at liquid-liquid interfaces. As mentioned above, the initial aims were to study the optical properties of NPs at the LLI with controlled inter-particle separations. Initially it was perceived that in order to control the separation, only a controlled coverage is needed, however as chapter 2 will discuss, this was found not to be the case. The work described in chapter 2 will be a broad overview of the experimental progression. Through trial and error, it was established that centrifugation can be used as a tool to aid the adsorption of particles to the interface. The functionality of the particles was also established to be crucial to their stability at the interface – citrate and mercaptosuccinic acid were initially investigated, however both functionalities lead to 2D aggregation of the particles. By introducing an aliphatic spacer between the thiol linker and the carboxyl charge carrying group, it was established that 12-mercaptododecanoic acid (MDDA) prevented 2D aggregation. By centrifuging MDDA functionalized particles to a water-DCE interface, while tuning the ionic strength of the aqueous solution, it was established that transmission spectroscopy through aqueous droplets surrounded by DCE enabled confirmation and estimation of the inter-particle separations. This aspect of the work will be covered in detail chapter 3. In addition, the first demonstration of a plasmon ruler at the LLI as well as reversible adsorption of 16 nm gold particles will also be covered in this section. A characterization of the NP concentration dependence on the number of particles adsorbed and their LSPR lead to an anomalous result. It was established that if the particle concentration in the aqueous phase is above a critical threshold, then a high density aqueous phase is observed at the bottom of the centrifuge tubes. Chapter 4 will discuss some of the properties of this aqueous phase and its applications. In particular, it will be shown that the density of the resulting solution is dependent on the ionic strength of the initial aqueous solution and can exceed 4.5 g/cm^3 – this dependence in and of itself arises from a controlled 3D inter-particle separation. In fact under certain conditions, the NPs actually arrange themselves into crystal – like structure, giving rise to clear Bragg’s scattering peaks. Aside from the physical properties, chapter 4 will also demonstrate the applicability of these solutions to NP purification and size separation.

The plasmon coupling of the NPs at the LLI will be taken advantage of in chapter 5, in which it will be demonstrated that the assembly, directly at the LLI is a versatile sensor. Detection of hydrophilic, hydrophobic and airborne analytes will be demonstrated. In addition, the simultaneous detection of both hydrophobic and hydrophilic will also be shown to be possible. This aspect has important consequences for the latter part of the chapter, in which a hydrophobic SERS reported molecule (1,8-diaminonaphthalene) will be shown to have a remarkable affinity and good selectivity to mercury ions. Finally, NPs at the air-liquid interface in the presence of 1,8-diaminonaphthalene will also be shown to provide the first SERS-based airborne mercury detection capabilities.

1.8 References

1. Yogev, D.; Efrima, S. *The Journal of Physical Chemistry* **1988,** 92, (20), 5754-5760.
2. Yogev, D.; Efrima, S. *The Journal of Physical Chemistry* **1988,** 92, (20), 5761-5765.
3. Gordon, K. C.; McGarvey, J. J.; Taylor, K. P. *The Journal of Physical Chemistry* **1989,** 93, (18), 6814-6817.
4. Guo, S.; Dong, S.; Wang, E. *Cryst Growth Des* **2008,** 9, (1), 372-377.
5. Cohanoschi, I.; Thibert, A.; Toro, C.; Zou, S.; Hernández, F. *Plasmonics* **2007,** 2, (2), 89-94.
6. Hojeij, M.; Younan, N.; Ribeaucourt, L.; Girault, H. H. *Nanoscale* **2010,** 2, (9), 1665-1669.
7. Fang, P.-P.; Chen, S.; Deng, H.; Scanlon, M. D.; Gumy, F.; Lee, H. J.; Momotenko, D.; Amstutz, V.; Cortés-Salazar, F.; Pereira, C. M.; Yang, Z.; Girault, H. H. *ACS Nano* **2013,** 7, (10), 9241-9248.
8. Turek, V. A.; Cecchini, M. P.; Paget, J.; Kucernak, A. R.; Kornyshev, A. A.; Edel, J. B. *ACS Nano* **2012,** 6, (9), 7789-7799.
9. Flatté, M. E.; Kornyshev, A. A.; Urbakh, M. *The Journal of Physical Chemistry C* **2010,** 114, (4), 1735-1747.
10. Flatte, M. E.; Kornyshev, A. A.; Urbakh, M. *Faraday Discussions* **2009,** 143, 109-115.
11. Liu, J.-W.; Zhang, S.-Y.; Qi, H.; Wen, W.-C.; Yu, S.-H. *Small* **2012,** 8, (15), 2412-2420.
12. Balmes, O.; Bovin, J.-O.; Malm, J.-O.; Xu, H. *Vibrational Spectroscopy* **2005,** 37, (2), 189-193.
13. Rao, C. N. R.; Kalyanikutty, K. P. *Accounts of Chemical Research* **2008,** 41, (4), 489-499.
14. Zheng, L.; Li, J. *The Journal of Physical Chemistry B* **2004,** 109, (3), 1108-1112.
15. Kroto, H. W.; Heath, J. R.; O'Brien, S. C.; Curl, R. F.; Smalley, R. E. *Nature* **1985,** 318, (6042), 162-163.
16. Drexler, K. E., *Nanosystems: molecular machinery, manufacturing, and computation*. John Wiley & Sons, Inc.: 1992.
17. Whitesides, G. M.; Grzybowski, B. *Science* **2002,** 295, (5564), 2418-2421.
18. Bhushan, B., *Springer handbook of nanotechnology*. Springer: 2010.
19. Maier, S. A., *Plasmonics: Fundamentals and Applications*. 2007.
20. Maier, S. A.; Brongersma, M. L.; Kik, P. G.; Meltzer, S.; Requicha, A. A.; Atwater, H. A. *Advanced Materials* **2001,** 13, (19), 1501-1505.
21. Alivisatos, A. *Science* **1996,** 271, (5251), 933-937.
22. Kealley, C. S.; Cortie, M. B.; Maaroof, A. I.; Xu, X. *Physical Chemistry Chemical Physics* **2009,** 11, (28), 5897-5902.
23. Khlebtsov, N. G. *Quantum Electronics* **2008,** 38, (6), 504.
24. Kelly, K. L.; Coronado, E.; Zhao, L. L.; Schatz, G. C. *The Journal of Physical Chemistry B* **2002,** 107, (3), 668-677.
25. Zitoun, D.; Respaud, M.; Fromen, M.-C.; Casanove, M. J.; Lecante, P.; Amiens, C.; Chaudret, B. *Physical Review Letters* **2002,** 89, (3), 037203.
26. Pankhurst, Q. A.; Connolly, J.; Jones, S.; Dobson, J. *Journal of physics D: Applied physics* **2003,** 36, (13), R167.
27. Lewin, M.; Carlesso, N.; Tung, C.-H.; Tang, X.-W.; Cory, D.; Scadden, D. T.; Weissleder, R. *Nature biotechnology* **2000,** 18, (4), 410-414.

28. Neto, A. C.; Guinea, F.; Peres, N.; Novoselov, K. S.; Geim, A. K. *Rev Mod Phys* **2009,** 81, (1), 109.
29. Bachtold, A.; Hadley, P.; Nakanishi, T.; Dekker, C. *Science* **2001,** 294, (5545), 1317-1320.
30. Javey, A.; Guo, J.; Wang, Q.; Lundstrom, M.; Dai, H. *Nature* **2003,** 424, (6949), 654-657.
31. Zhou, Z.-Y.; Tian, N.; Li, J.-T.; Broadwell, I.; Sun, S.-G. *Chemical Society Reviews* **2011,** 40, (7), 4167-4185.
32. Turner, M.; Golovko, V. B.; Vaughan, O. P.; Abdulkin, P.; Berenguer-Murcia, A.; Tikhov, M. S.; Johnson, B. F.; Lambert, R. M. *Nature* **2008,** 454, (7207), 981-983.
33. Crooks, R. M.; Zhao, M.; Sun, L.; Chechik, V.; Yeung, L. K. *Accounts of Chemical Research* **2000,** 34, (3), 181-190.
34. Velev, O. D.; Kaler, E. W. *Advanced Materials* **2000,** 12, (7), 531-534.
35. Das, S. K.; Choi, S. U. S.; Patel, H. E. *Heat Transfer Engineering* **2006,** 27, (10), 3-19.
36. Saito, R. **1998**.
37. Daniel, M.-C.; Astruc, D. *Chemical Reviews* **2003,** 104, (1), 293-346.
38. Haruta, M.; Daté, M. *Applied Catalysis A: General* **2001,** 222, (1), 427-437.
39. Nieminen, J. J.; Hatay, I.; Ge, P.; Mendez, M. A.; Murtomaki, L.; Girault, H. H. *Chemical Communications* **2011,** 47, (19).
40. Kennedy, L. C.; Bickford, L. R.; Lewinski, N. A.; Coughlin, A. J.; Hu, Y.; Day, E. S.; West, J. L.; Drezek, R. A. *Small* **2011,** 7, (2), 169-183.
41. Zhang, L.; Gu, F.; Chan, J.; Wang, A.; Langer, R.; Farokhzad, O. *Clinical Pharmacology & Therapeutics* **2007,** 83, (5), 761-769.
42. Kim, J. S.; Kuk, E.; Yu, K. N.; Kim, J.-H.; Park, S. J.; Lee, H. J.; Kim, S. H.; Park, Y. K.; Park, Y. H.; Hwang, C.-Y. *Nanomedicine: Nanotechnology, Biology and Medicine* **2007,** 3, (1), 95-101.
43. Rai, M.; Yadav, A.; Gade, A. *Biotechnology advances* **2009,** 27, (1), 76-83.
44. Liong, M.; Lu, J.; Kovochich, M.; Xia, T.; Ruehm, S. G.; Nel, A. E.; Tamanoi, F.; Zink, J. I. *ACS Nano* **2008,** 2, (5), 889-896.
45. Kostarelos, K.; Miller, A. D. *Chemical Society Reviews* **2005,** 34, (11), 970-994.
46. Cecchini, M. P.; Turek, V. A.; Paget, J.; Kornyshev, A. A.; Edel, J. B. *Nat Mater* **2013,** 12, (2), 165-171.
47. Zijlstra, P.; Paulo, P. M.; Orrit, M. *Nat Nanotechnol* **2012,** 7, (6), 379-382.
48. Maxwell, D. J.; Taylor, J. R.; Nie, S. *Journal of the American Chemical Society* **2002,** 124, (32), 9606-9612.
49. Cecchini, M. P.; Hong, J.; Lim, C.; Choo, J.; Albrecht, T.; deMello, A. J.; Edel, J. B. *Analytical Chemistry* **2011,** 83, (8), 3076-3081.
50. Turek, V. A.; Elliott, L. N.; Tyler, A. I. I.; Demetriadou, A.; Paget, J.; Cecchini, M. P.; Kucernak, A. R.; Kornyshev, A. A.; Edel, J. B. *ACS Nano* **2013,** 7, (10), 8753-8759.
51. Holtz, J. H.; Asher, S. A. *Nature* **1997,** 389, (6653), 829-832.
52. Garnett, E. C.; Cai, W.; Cha, J. J.; Mahmood, F.; Connor, S. T.; Greyson Christoforo, M.; Cui, Y.; McGehee, M. D.; Brongersma, M. L. *Nat Mater* **2012,** 11, (3), 241-249.
53. Flatté, M. E.; Kornyshev, A. A.; Urbakh, M. *Proceedings of the National Academy of Sciences* **2008,** 105, (47), 18212-18214.
54. Hägglund, C.; Zeltzer, G.; Ruiz, R.; Thomann, I.; Lee, H.-B.-R.; Brongersma, M. L.; Bent, S. F. *Nano letters* **2013,** 13, (7), 3352-3357.
55. Brown, M. D.; Suteewong, T.; Kumar, R. S. S.; D'Innocenzo, V.; Petrozza, A.; Lee, M. M.; Wiesner, U.; Snaith, H. J. *Nano Letters* **2011,** 11, (2), 438.
56. O'regan, B.; Grfitzeli, M. *nature* **1991,** 353, 24.
57. Nakayama, K.; Tanabe, K.; Atwater, H. A. *Applied Physics Letters* **2008,** 93, (12), 121904-121904-3.
58. Liu, Z.; Ling, X. Y.; Su, X.; Lee, J. Y. *The Journal of Physical Chemistry B* **2004,** 108, (24), 8234-8240.
59. Li, L.; Xing, Y. *The Journal of Physical Chemistry C* **2007,** 111, (6), 2803-2808.

60. Benn, T. M.; Westerhoff, P. *Environmental science & technology* **2008,** 42, (11), 4133-4139.
61. Turkevich, J. *Discussions of the Faraday Society* **1951,** 11, 55.
62. Kimling, J.; Maier, M.; Okenve, B.; Kotaidis, V.; Ballot, H.; Plech, A. *The Journal of Physical Chemistry B* **2006,** 110, (32), 15700-15707.
63. Faraday, M. *Philosophical Transactions of the Royal Society of London* **1857,** 147, 145-181.
64. Freestone, I.; Meeks, N.; Sax, M.; Higgitt, C. *Gold Bulletin* **2007,** 40, (4), 270-277.
65. Zhou, J.; Ralston, J.; Sedev, R.; Beattie, D. A. *Journal of Colloid and Interface Science* **2009,** 331, (2), 251-262.
66. Slomkowski, S.; Alemán, J. V.; Gilbert, R. G.; Hess, M.; Horie, K.; Jones, R. G.; Kubisa, P.; Meisel, I.; Mormann, W.; Penczek, S. *Pure and Applied Chemistry* **2011,** 83, (12), 2229-2259.
67. Narayanan, R.; El-Sayed, M. A. *Nano Letters* **2004,** 4, (7), 1343-1348.
68. Grzelczak, M.; Perez-Juste, J.; Mulvaney, P.; Liz-Marzan, L. M. *Chemical Society Reviews* **2008,** 37, (9), 1783-1791.
69. Li, D.; Kaner, R. B. *Journal of Materials Chemistry* **2007,** 17, (22), 2279-2282.
70. Lyklema, J.; van Leeuwen, H. P.; Minor, M. *Advances in Colloid and Interface Science* **1999,** 83, (1-3), 33-69.
71. Verwey, E. J. W. *The Journal of Physical and Colloid Chemistry* **1947,** 51, (3), 631-636.
72. Derjaguin, B.; Landau, L. *Acta Physiocochim USSR* **1941,** 14, 663.
73. Grasso, D.; Subramaniam, K.; Butkus, M.; Strevett, K.; Bergendahl, J. *Reviews in Environmental Science and Biotechnology* **2002,** 1, (1), 17-38.
74. Meyer, M.; Le Ru, E. C.; Etchegoin, P. G. *The Journal of Physical Chemistry B* **2006,** 110, (12), 6040-6047.
75. Ninham, B. *Advances in colloid and interface science* **1999,** 83, (1), 1-17.
76. Brust, M. *Journal of the Chemical Society. Chemical communications* **1994**, (7), 801.
77. Pattnaik, P. *Appl Biochem Biotech* **2005,** 126, (2), 79-92.
78. Homola, J.; Yee, S. S.; Gauglitz, G. *Sensors and Actuators B: Chemical* **1999,** 54, (1-2), 3-15.
79. Homola, J. *Chemical Reviews* **2008,** 108, (2), 462-493.
80. Kretschmann, E. *Zeitschrift fÃ¼r Physik. C, Particles and fields* **1971,** 241, (4), 313.
81. Otto, A. *Zeitschrift für Physik A Hadrons and Nuclei* **1968,** 216, (4), 398-410.
82. Jain, P.; Huang, X.; El-Sayed, I.; El-Sayed, M. *Plasmonics* **2007,** 2, (3), 107-118.
83. Maier, S. A.; Kik, P. G.; Atwater, H. A.; Meltzer, S.; Harel, E.; Koel, B. E.; Requicha, A. A. *Nature materials* **2003,** 2, (4), 229-232.
84. Wu, L. Y.; Ross, B. M.; Lee, L. P. *Nano Letters* **2009,** 9, (5), 1956-1961.
85. Wang, H.; Brandl, D. W.; Le, F.; Nordlander, P.; Halas, N. J. *Nano Letters* **2006,** 6, (4), 827-832.
86. Haiss, W.; Thanh, N. T. K.; Aveyard, J.; Fernig, D. G. *Analytical Chemistry* **2007,** 79, (11), 4215-4221.
87. Amendola, V.; Meneghetti, M. *The Journal of Physical Chemistry C* **2009,** 113, (11), 4277-4285.
88. Nordlander, P.; Oubre, C.; Prodan, E.; Li, K.; Stockman, M. I. *Nano Letters* **2004,** 4, (5), 899-903.
89. Tong, L.; Miljković, V. D.; Johansson, P.; Käll, M. *Nano Letters* **2010**, null-null.
90. Prodan, E.; Radloff, C.; Halas, N. J.; Nordlander, P. *Science* **2003,** 302, (5644), 419-422.
91. Reinhard, B. M.; Siu, M.; Agarwal, H.; Alivisatos, A. P.; Liphardt, J. *Nano Letters* **2005,** 5, (11), 2246-2252.
92. Rong, G.; Wang, H.; Reinhard, B. r. M. *Nano Letters* **2009,** 10, (1), 230-238.
93. Sonnichsen, C.; Reinhard, B. M.; Liphardt, J.; Alivisatos, A. P., A molecular ruler based on plasmon coupling of single gold and silver nanoparticles. 2005.
94. Funston, A. M.; Novo, C.; Davis, T. J.; Mulvaney, P. *Nano Letters* **2009,** 9, (4), 1651-1658.
95. Jain, P. K.; Huang, W.; El-Sayed, M. A. *Nano Letters* **2007,** 7, (7), 2080-2088.
96. Tabor, C.; Murali, R.; Mahmoud, M.; El-Sayed, M. A. *The Journal of Physical Chemistry A* **2008,** 113, (10), 1946-1953.

97. Ben, X.; Park, H. S. *The Journal of Physical Chemistry C* **2011,** 115, (32), 15915-15926.
98. Kinnan, M. K.; Kachan, S.; Simmons, C. K.; Chumanov, G. *The Journal of Physical Chemistry C* **2009,** 113, (17), 7079-7084.
99. Kinnan, M. K.; Chumanov, G. *The Journal of Physical Chemistry C* **2010,** 114, (16), 7496-7501.
100. Liu, N.; Hentschel, M.; Weiss, T.; Alivisatos, A. P.; Giessen, H. *Science* **2011,** 332, (6036), 1407-1410.
101. Hentschel, M.; Schäferling, M.; Weiss, T.; Liu, N.; Giessen, H. *Nano Letters* **2012,** 12, (5), 2542-2547.
102. Raman, C.; Krishnan, K. *Nature* **1928,** 121, (3048), 501-502.
103. Ferraro, J. R., *Introductory raman spectroscopy*. Access Online via Elsevier: 2003.
104. Fleischmann, M.; Hendra, P.; McQuillan, A. *Chemical Physics Letters* **1974,** 26, (2), 163-166.
105. Jeanmaire, D. L.; Van Duyne, R. P. *Journal of Electroanalytical Chemistry and Interfacial Electrochemistry* **1977,** 84, (1), 1-20.
106. Albrecht, M. G.; Creighton, J. A. *Journal of the American Chemical Society* **1977,** 99, (15), 5215-5217.
107. Le Ru, E.; Blackie, E.; Meyer, M.; Etchegoin, P. *The Journal of Physical Chemistry C* **2007,** 111, (37), 13794-13803.
108. Rodríguez-Lorenzo, L.; Álvarez-Puebla, R. n. A.; Pastoriza-Santos, I.; Mazzucco, S.; Stéphan, O.; Kociak, M.; Liz-Marzán, L. M.; García de Abajo, F. J. *Journal of the American Chemical Society* **2009,** 131, (13), 4616-4618.
109. Xu, H.; Bjerneld, E. J.; Käll, M.; Börjesson, L. *Physical Review Letters* **1999,** 83, (21), 4357.
110. Nie, S.; Emory, S. R. *Science* **1997,** 275, (5303), 1102-1106.
111. Kneipp, K.; Wang, Y.; Kneipp, H.; Perelman, L. T.; Itzkan, I.; Dasari, R. R.; Feld, M. S. *Physical Review Letters* **1997,** 78, (9), 1667.
112. Le Ru, E.; Etchegoin, P., *Principles of Surface-Enhanced Raman Spectroscopy: and related plasmonic effects*. Access Online via Elsevier: 2008.
113. Cintra, S.; Abdelsalam, M. E.; Bartlett, P. N.; Baumberg, J. J.; Kelf, T. A.; Sugawara, Y.; Russell, A. E. *Faraday discussions* **2006,** 132, 191-199.
114. Wrzesien, J.; Graham, D. *Tetrahedron* **2012,** 68, (4), 1230-1240.
115. Ren, W.; Zhu, C.; Wang, E. *Nanoscale* **2012,** 4, (19), 5902-5909.
116. Schlücker, S. *ChemPhysChem* **2009,** 10, (9-10), 1344-1354.
117. Moskovits, M. *Journal of Raman Spectroscopy* **2005,** 36, (6-7), 485-496.
118. Stiles, P. L.; Dieringer, J. A.; Shah, N. C.; Van Duyne, R. P. *Annual Review of Analytical Chemistry* **2008,** 1, (1), 601-626.
119. Wustholz, K. L.; Henry, A.-I.; McMahon, J. M.; Freeman, R. G.; Valley, N.; Piotti, M. E.; Natan, M. J.; Schatz, G. C.; Duyne, R. P. V. *Journal of the American Chemical Society* **2010,** 132, (31), 10903-10910.
120. Persson, B. N. J.; Zhao, K.; Zhang, Z. *Physical Review Letters* **2006,** 96, (20), 207401.
121. Fromm, D. P.; Sundaramurthy, A.; Kinkhabwala, A.; Schuck, P. J.; Kino, G. S.; Moerner, W. *J Chem Phys* **2006,** 124, (6), 61101-64100.
122. Xu, H.; Aizpurua, J.; Käll, M.; Apell, P. *Physical Review E* **2000,** 62, (3), 4318-4324.
123. Kneipp, J.; Kneipp, H.; Kneipp, K. *Chemical Society Reviews* **2008,** 37, (5), 1052-1060.
124. Chen, A.; DePrince, A. E.; Demortière, A.; Joshi-Imre, A.; Shevchenko, E. V.; Gray, S. K.; Welp, U.; Vlasko-Vlasov, V. K. *Small* **2011,** 7, (16), 2365-2371.
125. Camden, J. P.; Dieringer, J. A.; Wang, Y.; Masiello, D. J.; Marks, L. D.; Schatz, G. C.; Van Duyne, R. P. *Journal of the American Chemical Society* **2008,** 130, (38), 12616-12617.
126. Jiang, L.; Zou, C.; Zhang, Z.; Sun, Y.; Jiang, Y.; Leow, W.; Liedberg, B.; Li, S.; Chen, X. *Small* **2013**, n/a-n/a.
127. Schwartzberg, A. M.; Grant, C. D.; Wolcott, A.; Talley, C. E.; Huser, T. R.; Bogomolni, R.; Zhang, J. Z. *The Journal of Physical Chemistry B* **2004,** 108, (50), 19191-19197.

128. Talley, C. E.; Jackson, J. B.; Oubre, C.; Grady, N. K.; Hollars, C. W.; Lane, S. M.; Huser, T. R.; Nordlander, P.; Halas, N. J. *Nano Letters* **2005,** 5, (8), 1569-1574.
129. Chen, G.; Wang, Y.; Yang, M.; Xu, J.; Goh, S. J.; Pan, M.; Chen, H. *Journal of the American Chemical Society* **2010,** 132, (11), 3644-3645.
130. Li, W.; Camargo, P. H. C.; Lu, X.; Xia, Y. *Nano Letters* **2008,** 9, (1), 485-490.
131. Doering, W. E.; Nie, S. *Analytical Chemistry* **2003,** 75, (22), 6171-6176.
132. Vigderman, L.; Zubarev, E. R. *Langmuir* **2012,** 28, (24), 9034.
133. Lu, Y.; Liu, G. L.; Kim, J.; Mejia, Y. X.; Lee, L. P. *Nano Letters* **2004,** 5, (1), 119-124.
134. Faulds, K.; Smith, W. E.; Graham, D. *Analytical Chemistry* **2003,** 76, (2), 412-417.
135. Constantino, C. J. L.; Lemma, T.; Antunes, P. A.; Aroca, R. *Analytical Chemistry* **2001,** 73, (15), 3674-3678.
136. Boker, A.; van Rijn, P.; Wang, H. H. *Soft Matter* **2011,** 7, (11), 5274-5280.
137. Pickering, S. U. *Journal of the Chemical Society D: Chemical Communications* **1907,** 91, (2001), 2021.
138. Teh, S.-Y.; Lin, R.; Hung, L.-H.; Lee, A. P. *Lab on a Chip* **2008,** 8, (2), 198-220.
139. i Solvas, X. C. *Chemical Communications* **2011,** 47, (7), 1936-1942.
140. Reymond, F.; Fermín, D.; Lee, H. J.; Girault, H. H. *Electrochimica Acta* **2000,** 45, (15-16), 2647-2662.
141. Younan, N.; Hojeij, M.; Ribeaucourt, L.; Girault, H. H. *Electrochemistry Communications* **2010,** 12, (7), 912-915.
142. Kornyshev, A.; Kucernak, A.; Marinescu, M.; Monroe, C.; Sleightholme, A.; Urbakh, M. *The Journal of Physical Chemistry C* **2010,** 114, (35), 14885-14890.
143. Hisamoto, H.; Saito, T.; Tokeshi, M.; Hibara, A.; Kitamori, T. *Chem. Commun.* **2001**, (24), 2662-2663.
144. Berge, B.; Peseux, J. *The European Physical Journal E: Soft Matter and Biological Physics* **2000,** 3, (2), 159-163.
145. Graham-Rowe, D. *Nature Photonics* **2008,** 2, (4), 204-205.
146. Kuiper, S.; Hendriks, B. *Applied physics letters* **2004,** 85, 1128.
147. Dorrer, C.; Rühe, J. *Soft Matter* **2009,** 5, (1), 51-61.
148. Zhang, X.; Shi, F.; Niu, J.; Jiang, Y.; Wang, Z. *Journal of Materials Chemistry* **2008,** 18, (6), 621-633.
149. De Angelis, F.; Gentile, F.; Mecarini, F.; Das, G.; Moretti, M.; Candeloro, P.; Coluccio, M.; Cojoc, G.; Accardo, A.; Liberale, C. *Nature Photonics* **2011,** 5, (11), 682-687.
150. Shamai, R.; Andelman, D.; Berge, B.; Hayes, R. *Soft Matter* **2008,** 4, (1), 38-45.
151. Graham-Rowe, D. *Nat Photon* **2008,** 2, (4), 204-205.
152. Hayes, R. A. *Nature* **2003,** 425, (6956), 383.
153. Ramsden, W. *Proceedings of the Royal Society of London* **1903,** 72, 156-164.
154. Bresme, F.; Chacón, E.; Tarazona, P.; Tay, K. *Physical Review Letters* **2008,** 101, (5), 056102.
155. Kutuzov, S.; He, J.; Tangirala, R.; Emrick, T.; Russell, T. P.; Boker, A. *Physical Chemistry Chemical Physics* **2007,** 9, (48), 6351-6358.
156. Lin, Y.; Böker, A.; Skaff, H.; Cookson, D.; Dinsmore, A. D.; Emrick, T.; Russell, T. P. *Langmuir* **2004,** 21, (1), 191-194.
157. Du, K.; Glogowski, E.; Emrick, T.; Russell, T. P.; Dinsmore, A. D. *Langmuir* **2010,** 26, (15), 12518-12522.
158. Dryfe, R. A. W.; Luo, K.; Schroeder, S. L. M. *Chemistry of Materials* **2009,** 21, (18), 4172-4183.
159. Dai, L. L.; Sharma, R.; Wu, C.-y. *Langmuir* **2005,** 21, (7), 2641-2643.
160. Binks, B. P.; Lumsdon, S. O. *Langmuir* **2000,** 16, (23), 8622-8631.
161. Lehle, H.; Oettel, M. *Journal of Physics: Condensed Matter* **2008,** 20, (40), 404224.
162. Bresme, F.; Oettel, M. *Journal of Physics: Condensed Matter* **2007,** 19, (41), 413101.
163. Flatté, M. E.; et al. *Journal of Physics: Condensed Matter* **2008,** 20, (7), 073102.
164. McGorty, R.; Fung, J.; Kaz, D.; Manoharan, V. N. *Mater Today* **2010,** 13, (6), 34-42.

165. Park, B. J.; Vermant, J.; Furst, E. M. *Soft Matter* **2010,** 6, (21), 5327-5333.

166. Reed, K. M.; Borovicka, J.; Horozov, T. S.; Paunov, V. N.; Thompson, K. L.; Walsh, A.; Armes, S. P. *Langmuir* **2012,** 28, (18), 7291-7298.

167. Horozov, T. S.; Braz, D. A.; Fletcher, P. D.; Binks, B. P.; Clint, J. H. *Langmuir* **2008,** 24, (5), 1678-1681.

168. Gillies, G.; Kappl, M.; Butt, H.-J. *Advances in Colloid and Interface Science* **2005,** 114–115, (0), 165-172.

169. Isa, L.; Lucas, F.; Wepf, R.; Reimhult, E. *Nat Commun* **2011,** 2, 438.

170. Paunov, V. N. *Langmuir* **2003,** 19, (19), 7970-7976.

171. Arnaudov, L. N.; Cayre, O. J.; Stuart, M. A. C.; Stoyanov, S. D.; Paunov, V. N. *Physical Chemistry Chemical Physics* **2010,** 12, (2), 328-331.

172. Weon, B. M.; Lee, J. S.; Kim, J. T.; Pyo, J.; Je, J. H. *Curr Opin Colloid In* **2012,** 17, (6), 388-395.

Chapter 2: Experimental Overview

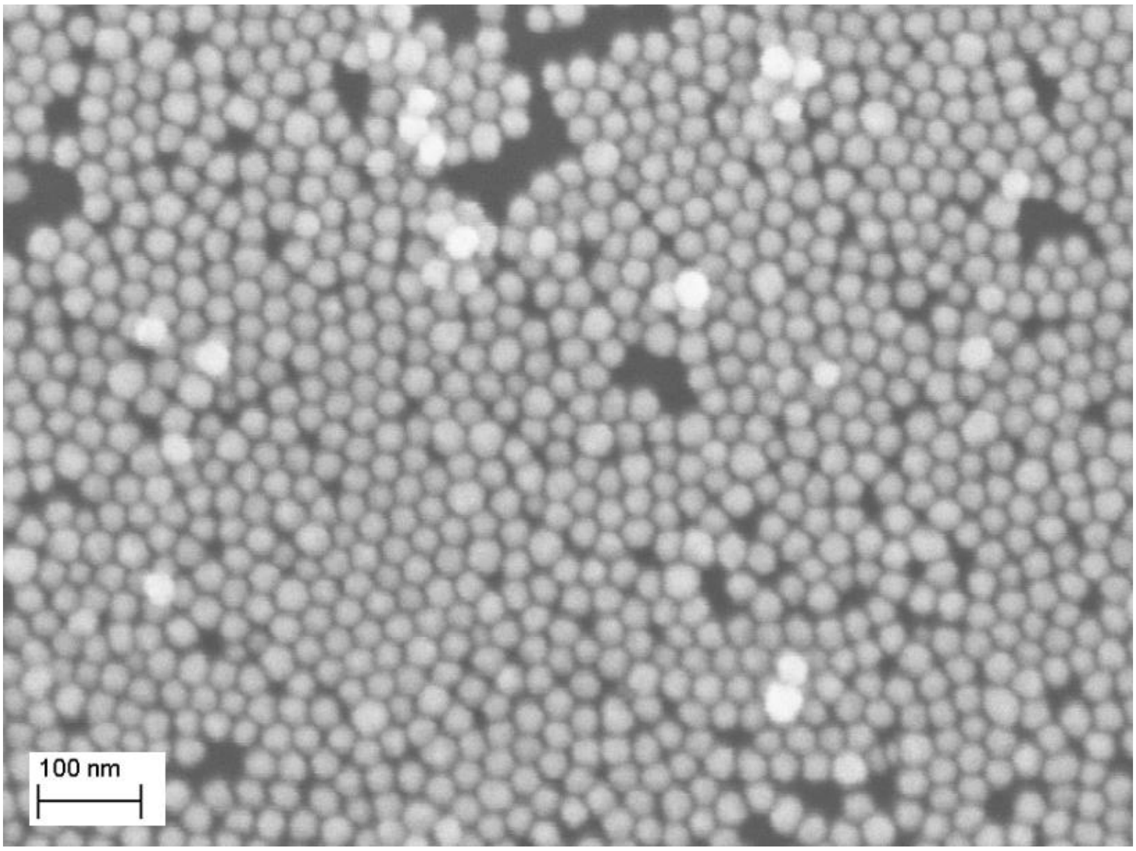

2.1 Abstract

As was discussed in Chapter 1, the initial project aims were to study the optical properties of plasmonic NPs at sub-monolayer coverage at the LLI. This chapter outlines the experimental progression as well as describes some of the initial challenges that were associated with this goal. Nevertheless, the solution of these challenges became invaluable for the subsequent work described in Chapter 3, 4, and 5. Though this chapter outlines results that are either not publishable, or were already known in the literature, the fundamental developments of this stage set the scene for most of the subsequent results for the entire PhD. This chapter establishes: gold nanoparticle synthesis; functionalization and stability of NPs with 12-mercaptododecanoic acid (MDDA); centrifugation as a tool to aid assembly; emulsification as an alternative to speed up diffusion-limited self-assembly of NPs; transmission spectroscopy of aqueous droplets as a means to extract spectral information from the assembly; SERS from aqueous droplets deposited on a glass coverslip; XRD studies of MDDA functionalized particles at the toluene-water interface.

2.2.1 Nanoparticles

The first question when choosing which type of particles to work with is: what material to use? The most widely used plasmonic particles in the literature have been gold and silver[1, 2]. Silver particles have optical properties that more suited to the realization of a smart-mirror than gold – first the LSPR maximum of spherical silver nanoparticles in the range of 20 nm (diameter) lies at approximately 400 nm, whereas similar sized gold particles have a maximum at around 520 nm. The blue shift of this peak as particle separation is reduced (i.e. when the interfacial coverage is increased) is expected to lie in the centre of the visible spectrum and due to its broadness reflect visible light well at most wavelengths. Nevertheless, silver nanoparticles are not perfectly suited to the smart mirror concept – the LSPR maximum, while close to being outside of the visible spectrum, does nevertheless absorb blue light. In other words particles that are freely dispersed in solution will not be 'invisible'; in fact spherical silver nanoparticle solutions appear yellow[3]. So despite silver being 'better' suited than gold, neither material is ideal for the system. On top of this, from a synthetic point view, monodisperse, spherical silver particles are more challenging to make than their gold counterparts. Of course, there are countless publications that outline in detail how monodisperse silver nanoparticles can be made, which could have been followed, however, nanoparticle synthesis was a small part of the project. It was therefore decided to use the standard nanoparticle synthesis – the 'Turkevich-Frens'[4-6], or citrate-reduction method for gold nanoparticles, with the intention to investigate alternative NPs at a later stage. Although alternative synthesis methods exist that can produce particles of a better monodispersity, its speed and simplicity, together with a reasonable particle monodispersity, controlled size between 10 and 150 nm and a readily displaceable functionality, make it an extremely attractive synthesis and one of the most widely used to date (despite having been first demonstrated over 60 years ago).

The typical procedure for gold nanoparticle synthesis involved – 95ml of $HAuCl_4$ solution containing 5 mg of Au being brought to 100^{o}C, after which 5 ml aqueous trisodium citrate dihydrate was added. The concentration of the citrate was varied to produce different sized nanoparticles – for the most commonly used particles in the project, 16 nm and 43 nm, 20.0 and 6.4 mg of citrate was used, respectively. The initial colour of the solution was a very faint yellow, which, after the addition of citrate started to darken to a blue/ purple colour after 1-2 minutes, this solution then turned into the wine-red that is normally observed for gold NPs.

The blue colour is associated with the formation of nanowires[7] and as these broke up the plasmon resonance of the NPs stabilized to its standard value thereby giving the red colour. Figure 2.1 shows the colour of the solution at various times during the reaction.

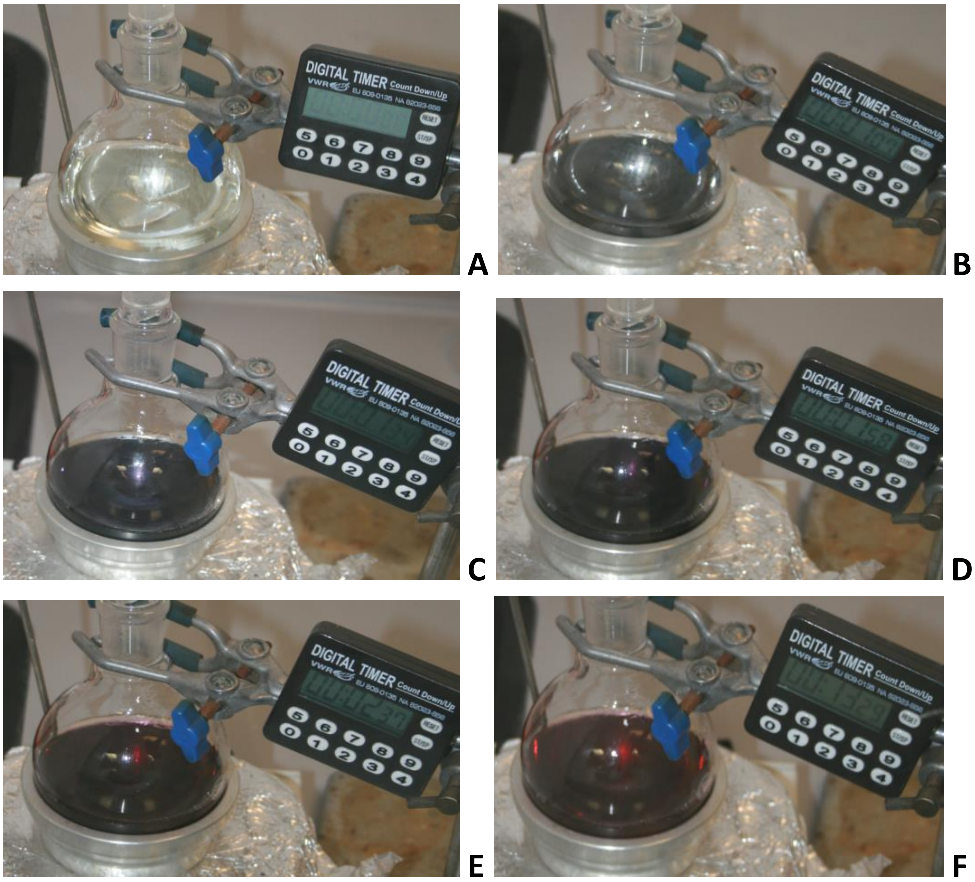

Figure 2.1 | Photographs of gold NP solutions at various points during the synthesis. Time= 0secs (A) is when the citrate solution was added; the faint yellow solution starts to darken (B). The blue/purple colour seen in C and D is due to gold nanowire intermediates, at E these nanowires break up into individual particles giving rise to the final 'wine-red' colour at F.

The resulting particles were imaged by UV-Vis and had a LSPR maximum at 519-521 and 533-535 nm for 16 and 43 nm respectively. DLS showed the particles to have a hydrodynamic diameter of 20 ± 4 and 65 ± 31 nm for '16' and '43' respectively. The particles were determined to be 16 and 43 nm from electron microscopy images, Figure 2.2. As can be clearly seen, the smaller particles have a spherical geometry, while the larger particles have an elongation along one of the axes. This elongation is the reason why the 'hydrodynamic diameter' of the larger particles is substantially larger than the actual core size – the autocorrelation function in DLS assumes the particles to be spherical which was not the case for these particles. Alternative methods of gold nanoparticle synthesis where tested, for example sodium borohydride reduced 5 nm NPs[8], CTAB-mediated nanorods[9] and sodium acrylate[10] reduced spherical. However none of these particles were used significantly for the project:

- Nanorods contain surfactants which add extra unknowns to an already difficult to characterize system – as a possible continuation of chapter 3 and 4, nanorods (or even other more exotic geometries) could be revisited and studied in more detail;
- Particles produced by sodium borohydride, while relatively simple and quick to make, are very small – it is more challenging to obtain stable arrays at the LLI with such particles;
- Sodium acrylate particles, while highly monodisperse and spherical in geometry, took 3 days to make. Additionally, there is a great deal of literature on citrate stabilized particles, while not as many researchers work with acrylate. In order to not run into some unforeseen problems later down the line, it was decided to stick to the 'safer' citrate reduction over this method.

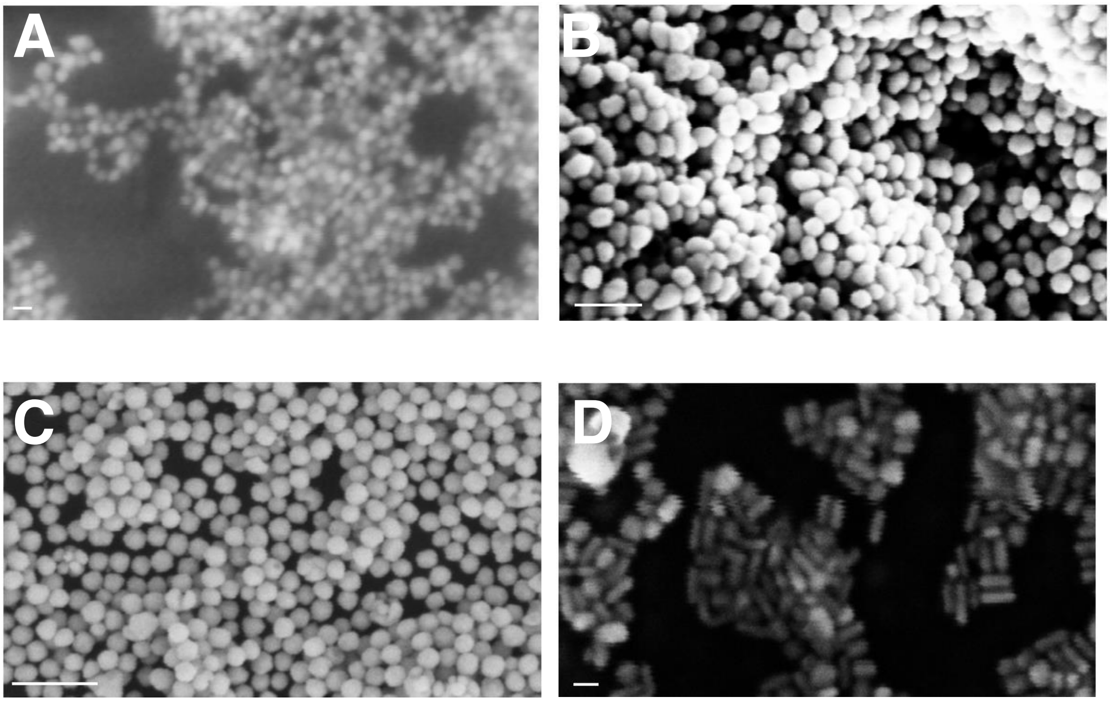

Figure 2.2 | SEMs of 16 (A) and 43 (B) nm citrate stabilized gold particles as well as acrylate (C) and nanorods (D). Scale bars represent 20 nm (A and D), 100 nm (B) and 200 nm (C).

2.2.2 Aggregation

It soon became apparent that citrate stabilized particles aggregate very rapidly after even mild changes to 'as-made' solution conditions. pH changes (in either direction, though especially a reduction), salt concentration and even excessive centrifugation caused irreversible aggregation. Nevertheless, the plasmonic NP solutions undergo a colour change upon aggregation – this was an invaluable tool in understanding and gaining experience in nanoparticle handling. Aggregated particles display a red-shift of their LSPR maximum – for 16 nm citrate particles, this peak was determined to be 630 nm. From UV-Vis spectra it is therefore possible to determine the relative state of aggregation by taking the peak ratios between 520 nm and 630 nm (Figure 2.3). As-made particles typically had a ratio of 10, while for particles that experience some aggregation this ratio falls.

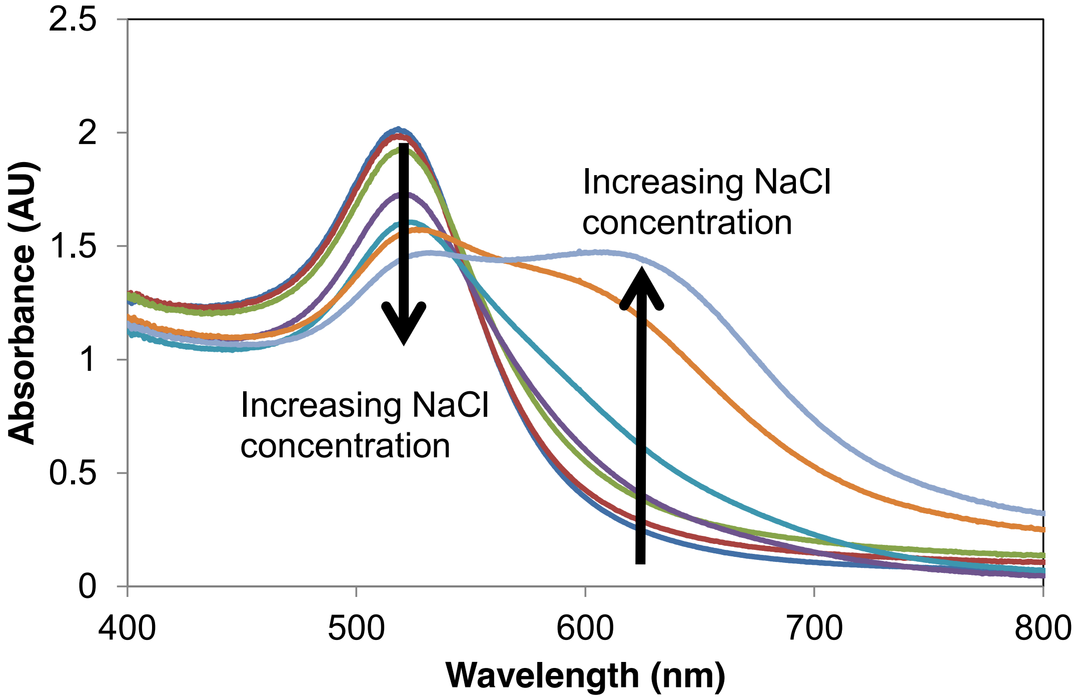

Figure 2.3 | UV-Vis of citrate stabilized 16 nm Au NPs as a function of NaCl concentration – aggregation leads to a decrease in the absorbance at 520 nm and an increase at 630 nm.

2.3 Adsorption to the liquid-liquid interface

Having synthesised 16 nm spherical gold nanoparticles, two new questions now arose: how do we adsorb them to the interface? Additionally, which interface should be used (i.e. what should the organic phase be)? Toluene was initially selected as a standard insoluble organic phase, however in conjunction 1,2-dichloroethane (DCE) was used. The main difference between these two organic phases was initially believed to be the density and therefore the organic phase was chosen only such that the interface would be better suited for optical measurements. The reason these two organic phases were chosen were because toluene is one of the most common organic phases in the literature[11, 12], while the theoretical predictions were performed at a DCE interface. As was later determined, for control over the inter-particle separations DCE was a fortunate choice, as many of the properties subsequently demonstrated at this interface are not readily observed at the toluene interface.

The question of particle adsorption however, was more difficult to answer. There are several ways that this has been achieved in the literature: electrochemistry[13, 14]; (m)ethanol addition[15, 16]; pH reduction[17]; diffusion limited[18]. Though each method has their pros and cons, most of these methods have not been reported to allow for a controlled assembly. A reduction in the pH leads to aggregation, after which the particles readily adsorb (due to a reduction in the NP's charge and larger effective diameter of the aggregated clusters); (m)ethanol was observed to work, though the reason as to why it works, was being investigated in the field[19] – in order to reduce the already significant amount of 'unknowns' it was decided to avoid in detail investigations using this adsorption mechanism; diffusion is slow, especially for bulky objects such as nanoparticles, therefore, without 'assistance', the timescales needed for this to be an effective mechanism of adsorption can be hours, if not days. Electrochemistry is perhaps one of the most attractive adsorption mechanisms as true control can be achieved through the applied potential. However integration of optical and electrochemical measurements in the same cell, as well as combining organic and inorganic electrolytes with NPs, whilst preventing aggregation as well as allowing for adsorption is experimentally highly challenging. Some of the initial experiments (results not shown) attempted electrochemical control over the self-assembly of particles to the LLI however, it proved difficult to differentiate the significance of the multitude of parameters, making these initial experiments comparable to finding a needle in a haystack.

Due to the complexity of electrochemistry and the unreasonable timescales of diffusion, it was decided that initially, the optical properties of NP arrays at the LLI would be performed by ethanol addition. The hypothesis was that by controlling the amount of ethanol added to an aqueous nanoparticle solution in the presence of an organic phase, it would be possible to control the number of particles adsorbed and hence the inter-particle separation. The experimental optical properties would then be compared to theoretical calculations, in order to confirm theory.

For some quick tests, a petri dish was chosen as the container, with reflection measurements at an angle of 45° as the optical detection. Figure 2.4, shows the films formed by gradual ethanol addition. It can be clearly seen that the film is inhomogeneous – with patches of the interface having seemingly no NPs, while others containing a bluish tint, which at sharper angles appears to be golden in colour.

Figure 2.4 | Nanoparticles adsorbed to toluene-water interface by the addition of ethanol.

However, the reflection spectra as a function of ethanol addition, Figure 2.5, did not give the expected red-shift that theory predicts. Instead, 3 distinct peaks were seen, which increased in intensity as (presumably) more particles adsorbed (Figure 2.5).

It was clear that ethanol addition did not give reliable results. The lack of shifting of the plasmon peaks suggest that the particles are in the same environment at all stages of the experiments. Because of the increased reflectivity, it is highly probable that more particles are assembled as a function of ethanol added, however even this trend wasn't concrete – there was a negligible change in reflectivity between 8 and 9 mL ethanol added, while 10 mL gave an increased reflectivity again. The importance of this result is that an early stage assumption turned out to be false – controlling particle coverage of the LLI does not necessarily lead to control of the inter-particle separation. Furthermore, due to irreproducibility and a lack of mechanistic understanding, ethanol addition was concluded to be unsuitable as a means to control the inter-particle separation at the LLI.

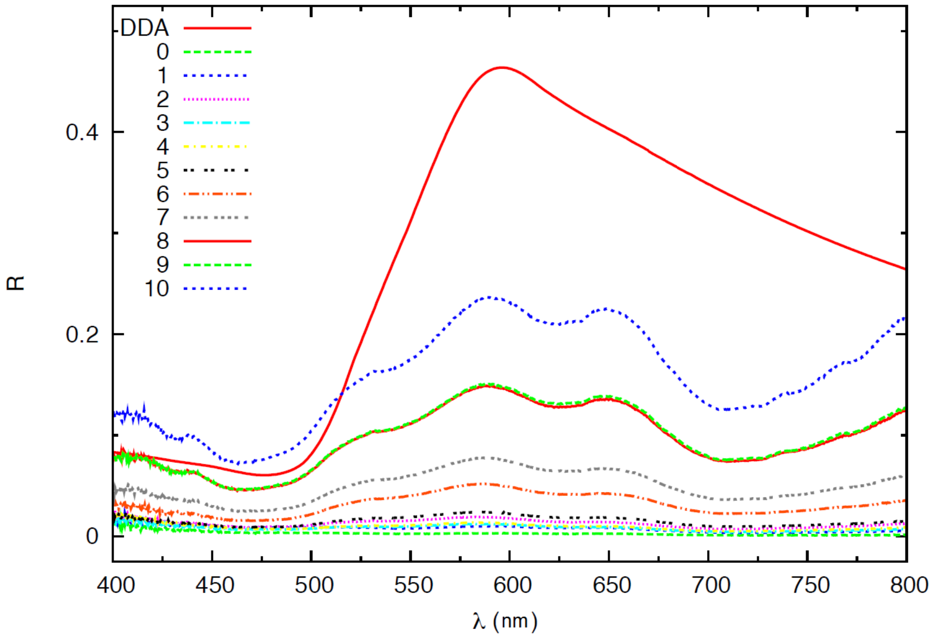

Figure 2.5 | Reflection spectra of 16 nm citrate stabilize Au NPs as a function of ethanol addition, compared to theoretical prediction of a hexagonal lattice with 5 nm surface-surface NP separation. Experimental conditions: 20 mL aq. NP solution (NP concentration 1.8 nM), with 20 mL toluene; 0-10 denotes mL of ethanol added (i.e. 5 means 5mL ethanol added); 45° incidence angle from an unpolarised halogen light source. DDA predictions courtesy of Aeneas Weiner.

2.4 Centrifugation as a means to assemble nanoparticles

One of the most important benefits of electrochemistry as a means of NP adsorption is that there is a well-defined and intuitive force that drives the particles to the interface. This makes subsequent analysis of results and patterns easy to understand. The lack of mechanistic understanding of the forces involved for ethanol addition means that studying a single parameter is no longer possible making the system highly complex to disentangle. The limitations of electrochemistry are that the experimental design for such a system is highly complex and though it allows the investigation of a single parameter (e.g. effect of particle size/ pH/ NP functionality etc.), this comes at a cost of introducing additional parameters. A custom-built 4 electrode setup with bulky leads needs to be precisely positioned with respect to the optics. An additional challenge of the studying the optical properties of NPs at the LLI by electrochemical means is electro-wetting – a change in potential across the interface leads to changes in the 3 phase contact angle between the oil, water and glass container walls, which in turn can lead to changes in interfacial position with respect to the optics. The complexity and time consuming nature of using electrochemistry to de-convolute the variables of NP adsorption was a daunting and impractical task. It was realised therefore that an alternative force could be used (and in fact was already used on a regular basis) to drive the NPs to the interface – that was the centrifugal force. Traditionally, organic phases are less dense than water, but the inter-changeability of using toluene and DCE at this point lead to an obvious test of attempting to add DCE and aqueous NPs to a centrifuge tube and centrifuge the biphasic system.

This simple, yet surprisingly powerful test was a pivotal point during the project. The novelty of centrifugation as a tool in achieving NP adsorption was unexpected – despite its ease and being universally applicable to the vast majority of particles, it was not reported in the literature. This was initially therefore treated with caution – it was believed that there had to be a reason as to why nobody has reported it before, though it is now believed that centrifugation has simply been overlooked as a means to assemble the particles. As is expected the initial tests proved successful in adsorbing citrate stabilized NPs to a water-DCE interface. Nevertheless, extracting spectral properties of the particles at the LLI in the centrifuge tubes was initially deemed unrealistic - the curvature of the interface meant that establishing a reproducible reflection spectrum would be extremely challenging (without the use of larger tubes). Furthermore, was centrifugation giving rise to actual monolayers, or were multilayers formed as a result of centrifugation-induced aggregation?

2.5 Electron microscopy of the NP arrays

As was quickly established, the liquid-liquid interface is difficult to image. Optical measurements are challenging due to the ill-defined position of the interface, while smaller interfaces are also greatly influenced by curvature, meaning that optical setups need to be constructed with some flexibility in their focal points. Nevertheless, the difficulty in extracting spectral information is dwarfed by the difficulty in obtaining structural information. Electron microscopy, AFM and STM are traditional methods to image nanostructures with nanometer resolution, however none of these methods are directly applicable to imaging the LLI – sample requirements such as vacuum, conductivity (for STM) and rigidity (for AFM) make these techniques close to impossible to implement at the LLI (with few limited exceptions[20, 21]). This of course, puts a severe limitation on the value of spectral results - measuring the optical properties of the arrays requires knowledge of the structural information.

Due to the fact that little-to-no information was available of the resulting arrays, as a first approach, it was decided to investigate the structural arrangement of nanoparticles adsorbed at the liquid-liquid interface by drying them onto a flat substrate, followed by electron microscopy. That such an estimate was dangerous and unrepresentative was known, however it was reasoned that if a monolayer could be obtained once dried, then the particles at the LLI must also be arranged in monolayer. Drying would if anything, induce further aggregation and clustering. However an additional challenge was in actually drying the arrays. Literature reports that these arrays can be ‘scooped up’ onto a TEM grid[22], however the arrays formed in the centrifuge tubes are not readily accessible for scooping.

It was noticed that by reducing the volume of the aqueous phase, the 2 distinct phases turn into an aqueous droplet suspended in DCE. The hydrophobic nature of the tube walls makes this the preferred aqueous geometry. Additionally, it was noticed that the droplet could then be pipetted out from the tubes, whilst the NPs remain adsorbed to the interface (in other words, disassembly does not occur). As long as the interface was allowed to be maintained inside the pipette tip (this was achieved by pipetting DCE along with the aqueous phase) then the adsorbed particles will migrate inside the tip. It is worth noting, that in order to transfer the particles into the pipette tip, the pipetting has to be done close to the interface, rather than in the centre of the droplet – in the latter case, the reduction of the interfacial area leads to the particles compressing in on themselves leading to '3D-intrefaces'[23].

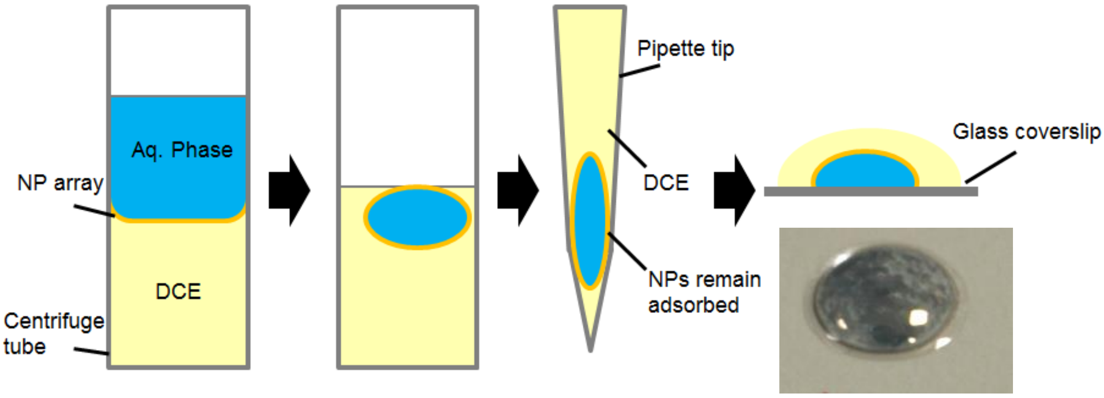

Figure 2.6 | Citrate stabilized NPs adsorbed at the LLI can be transferred from the centrifuge tubes simply by pipetting – desorption from the LLI does not occur as the interfacial area is compressed. This allows the arrays to be transferred onto a glass coverslip.

Then, by pipetting these particles onto a glass coverslip, the aqueous phase, despite being less dense than DCE, now has contact with the glass, while the DCE surrounds it on top. During this step, the particles rearrange themselves to preferentially cover the LLI, rather than the glass-water interface. Note: This extremely simple realization subsequently lead to the work outlined in Chapter 5. Inevitably, the aqueous phase will contain ions, if the droplet is allowed to dry naturally at this point, salt crystals will form, obscuring the NP array by electron microscopy. Instead, the aqueous phase is further reduced to minimize its volume – the aqueous contact area with glass remains approximately the same during the volume reduction. As the water evaporates completely, the NP array is allowed to gently settle onto the glass, leaving a circular film of NPs on the glass surface. A requirement of electron microscopy is that the sample needs to be conductive. The benefits of using a glass coverslip to deposit the arrays on was they have a very uniform and flat surface, though are of course not conductive, it was found however that if the coverslips were attached to the SEM stubs by carbon tape and silver paint was applied to the edge of the array, then the entire array could be imaged without the need to sputter an additional metallic layer on the arrays.

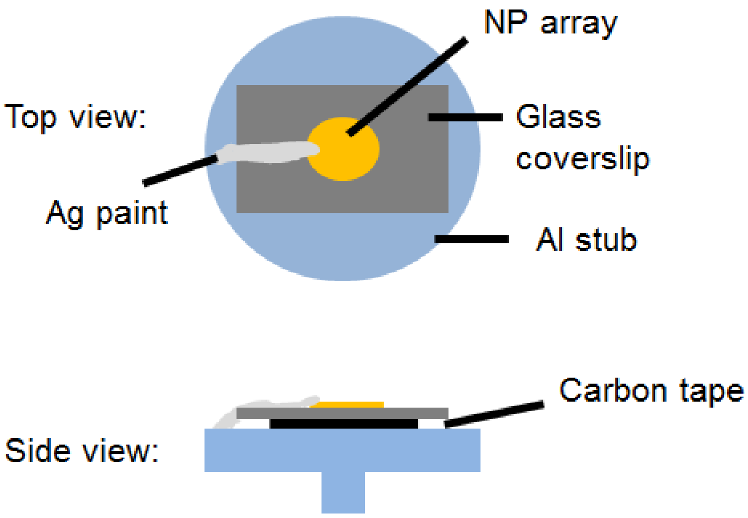

Figure 2.7 | NP array preparation for imaging by SEM. NP arrays deposited onto a glass coverslip is attached to the aluminium stub by carbon tape. Silver paint is then used to provide contact between the NP array and the aluminium. This procedure negates the need to sputter a metallic film across the entire array.

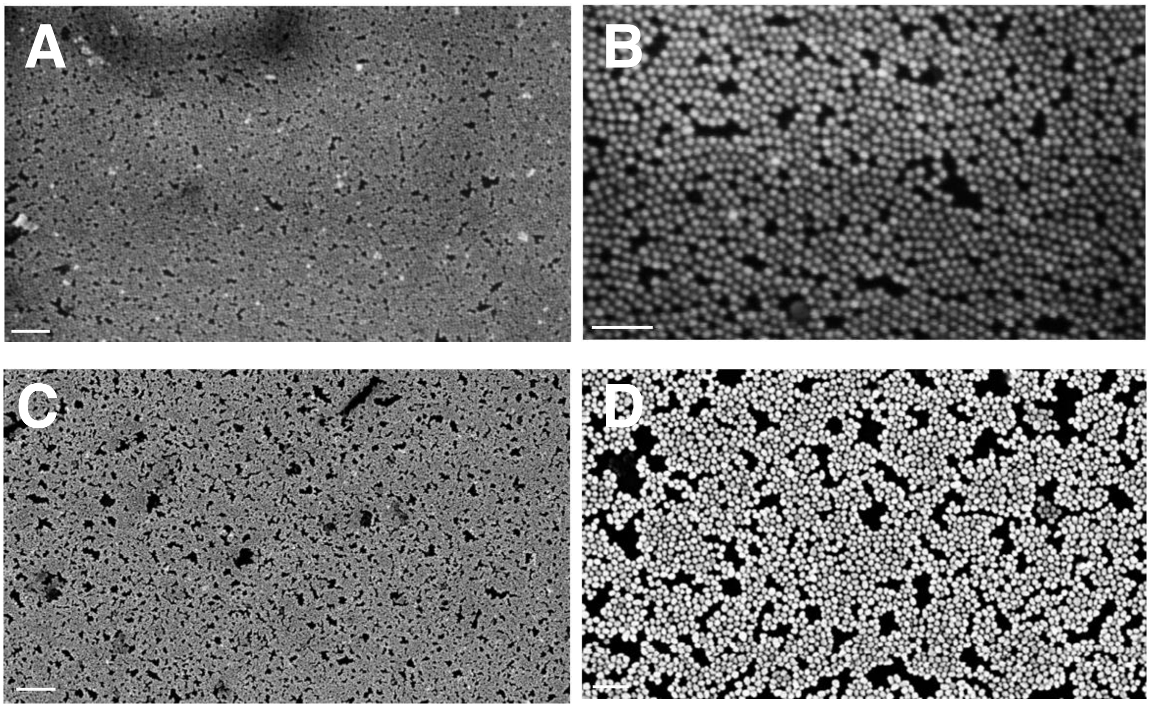

Figure 2.8 | Example SEMs of 16 (A and B) and 43 (C and D) nm citrate stabilized NP arrays on a glass coverslip, prepared as described above. Scale bars correspond to 200 nm, 100 nm, 1 μm and 200 nm for A, B, C and D respectively.

The fact that charging does not occur even when the opposite side of the array is imaged with respect to the side that the paint is applied on, suggests that the particles in these arrays are touching. Nevertheless, despite this 2D aggregation, the SEMs of these arrays clearly display monolayer characteristics, meaning that centrifugation does not induce 3D clustering (Figure 2.8).

2.6 2D Aggregation at the LLI

Despite the evidence that the arrays do indeed form a monolayer, the close packed nature of this assembly is only a limiting case of inter-particle separations. The aim was to study the optical properties of these arrays by controlling the inter-particle separation. As already mentioned, controlling the coverage of the interfacial area does not automatically lead to controlled separation. This observation is clearly highlighted in Figure 2.9 – despite regions of intense reflection at certain areas of the interface there is visibly no particles in others.

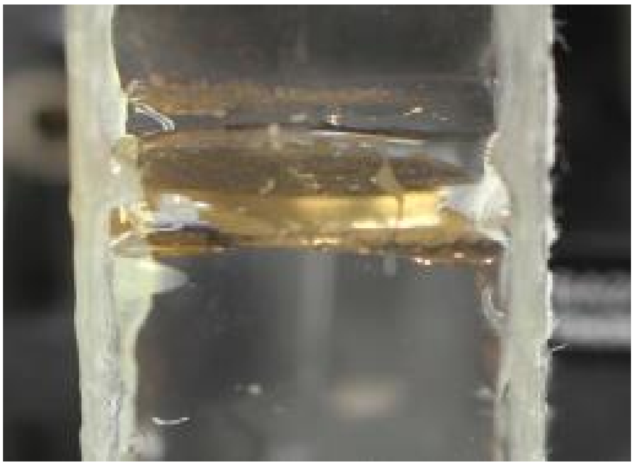

Figure 2.9 | Control over the interfacial coverage does not lead to controlled inter-particle separation.

In fact, despite the numerous studies on plasmonic nanoparticles, literature did not report methods in achieving control over the separations. It was hypothesised that the close packed nature of the NPs is a result of 2D aggregation at the interface as a consequence of the poor stability of citrate stabilized NPs. Citrate stabilized particles can easily lose their functionality, this is beneficial for subsequent functionalization, however in order to ensure that a repulsive force is maintained at the LLI it was clear that alternatives to citrate would needed. As a first choice, it was deemed that maximizing the charge carriers on the NPs would allow this to be achieved through pure electrostatic repulsion. Mercaptosuccinic acid (MSA) was therefore chosen, as it has 2 carboxyl groups per thiol – it was believed that this would aid in maximizing the surface charge density:

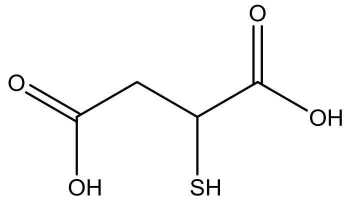

Mercaptosuccinic acid

Nevertheless, even particles functionalized with MSA lead to similar aggregation behaviour to those shown in Figure 2.9. The main problem remained in imaging the arrays. Pipetting, whilst allowing one to transfer the arrays into different containers that are more suited to imaging, reduces the interfacial area, thereby compressing the NPs. This compression may therefore lead to a substantial force that drives the particles closer together until ultimately the van der Waals force dominate over the electrostatic repulsion. It was therefore evident that pipetting these arrays should be avoided if control over the inter-particle separation was to be achieved.

2.7 Transmission Spectroscopy

The challenge of how to image these arrays was a significant one. Instead of attempting to carry out reflection measurements, it was decided to focus instead on transmission. As pipetting and transferring the arrays away from the centrifuge tubes was not desired due to the possibility that such an action would distort or aggregate the particles, reflection measurements would be hindered by curvature of the interface (due to the small interfacial area in these tubes) – transmission was therefore decided to be carried out in the actual centrifuge tubes. Due to the shape of the tubes, scattering from the walls would lead to non-quantifiable losses in the signal intensity, therefore quantitative information on the absorbance was sacrificed to be able to extract the shape of the LSPR through normalization of the spectra. Given a reduction in spacing, the position of the peak maximum should red-shift. Furthermore this shift may also be used to gain structural information by comparing to theory and simulations.

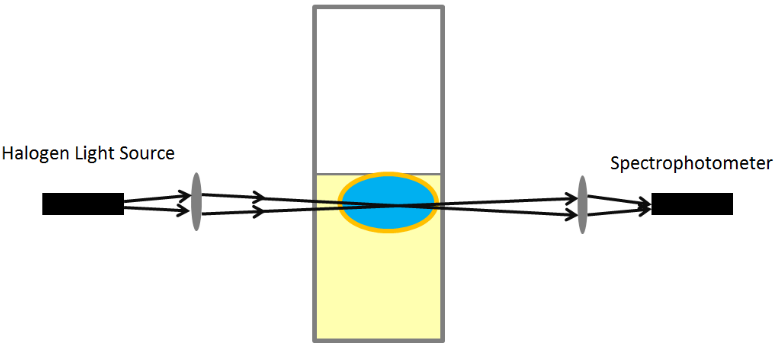

Figure 2.10 | Schematic of the transmission spectroscopy through aqueous droplets surrounded by DCE to extract spectral information of NP arrays at the LLI.

MSA particles at as made conditions (*i.e.* no modifications to the ionic strength of the aqueous solution) gave rise to a single peak with a maximum at 542 nm, however a visible red-shifted shoulder was seen in the spectrum (Figure 2.11).

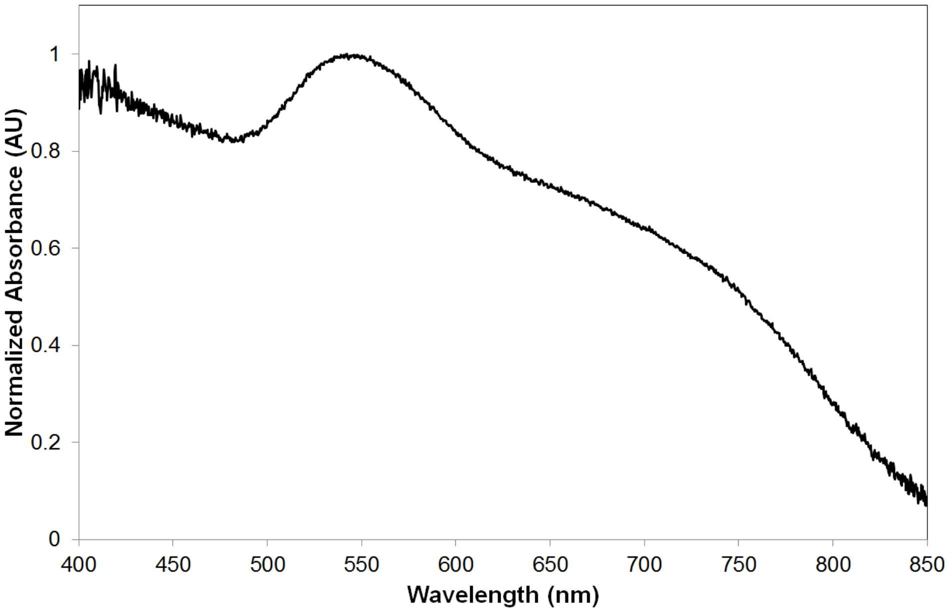

Figure 2.11 | Normalized absorbance of MSA-functionalized 16 nm gold particles at as made conditions, centrifuged for 10 minutes at 9391 *g*.

It was hypothesised that this shoulder is a result of partial aggregation – in other words that the adsorbed particles exist in two states. The important result however was that the peak maximum was well below that which would be expected of aggregates (for aggregates, the expected peak would be in the region of 650 nm). In other words, though the spectrum did not perfectly match that of theory, it was probable at least some of these particles were unaggregated and remained as discrete particles with a certain separation between them.

It was therefore decided that despite the crudeness of the transmission setup, it could be used as a means to probe the behaviour of the NPs at the LLI. More importantly, it provided a quick, easy and reliable way to image the optical properties of the NP at the LLI.

2.8 Controlling the separation

Having established a means to control the NP assembly to the LLI through centrifugation as well as having a way to extract optical spectra through normalized transmission measurements, the challenge now remained of how to actually vary the inter-particle separation.

Three options presented themselves:

1. Controlling the charge density of the NP's surface through pH: Though theoretically possible, this would require the use of a buffer to modulate the pH changes, which may in turn influence the NP's behaviour. Additionally, it is probable that instead a smooth transition from separation to aggregation, that a 'jump' would be seen at a critical pH when the van der Waals would start dominating the inter-particle forces – in other words not all inter-particle separations may be possible by controlling the pH.
2. Controlling the length of the NP's functionality and inducing aggregation: through the fact that the coating will have different thicknesses, this will effectively control the interparticle separation. Nevertheless, only very discrete inter-particle separations will be possible through this method. Additionally, changing the NP functionality leads to may follow on effects (for example, it may lead to a change in the particle position with respect to the interface, as well as change the optical dielectric constant of the NP's surrounding medium) that would mean more than one parameter will be changed at a time.
3. By controlling the ionic strength of the solution, thereby tuning the screening length and the position of the energy minimum at which the NPs will reside. This should in principle allow the inter-particle separation to be controlled without changing additional parameters. However this would require particles that are very stable with

respect to aggregation – upon the addition of salt NPs are expected to aggregate, while in order for this method to work, this has to be carried in a controlled manner. Additionally, predicting the ionic distribution around a monolayer of particles at the LLI is challenging therefore the actual screening length cannot be approximated to that of the screening length in free solution.

Of these, it was decided that controlling the inter-particle separation through the ionic strength would be the most beneficial. Though the distribution of the ions around the particles at the LLI is difficult to describe, which may lead to unpredictable behaviour, controlling the length of the functionality would lead to more than one variable changing as a function of inter-particle separation – though pH control could also have been used to control the separation.

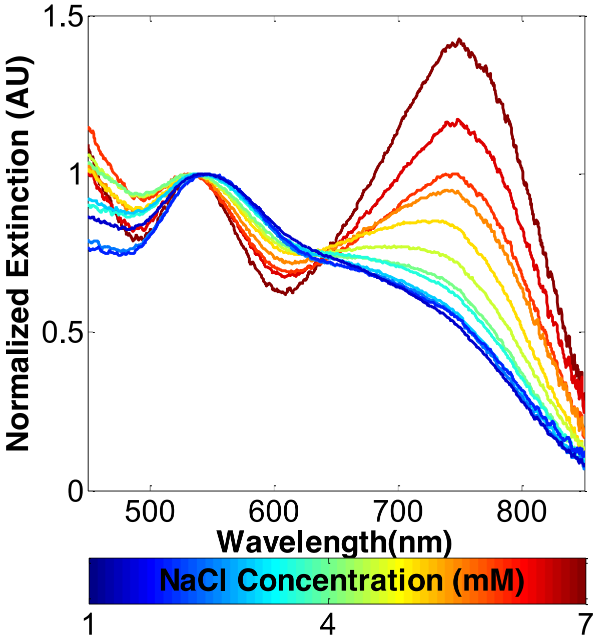

Figure 2.12 | Normalized extinction of 16 nm MSA functionalized nanoparticles as a function of NaCl concentration. Centrifugation was performed for 10 minutes at 9391 *g* with 2.75x10^{11} NPs in the aqueous phase and 0.5 mL DCE. Following centrifugation the volume of the aqueous phase was reduced to 100 μL.

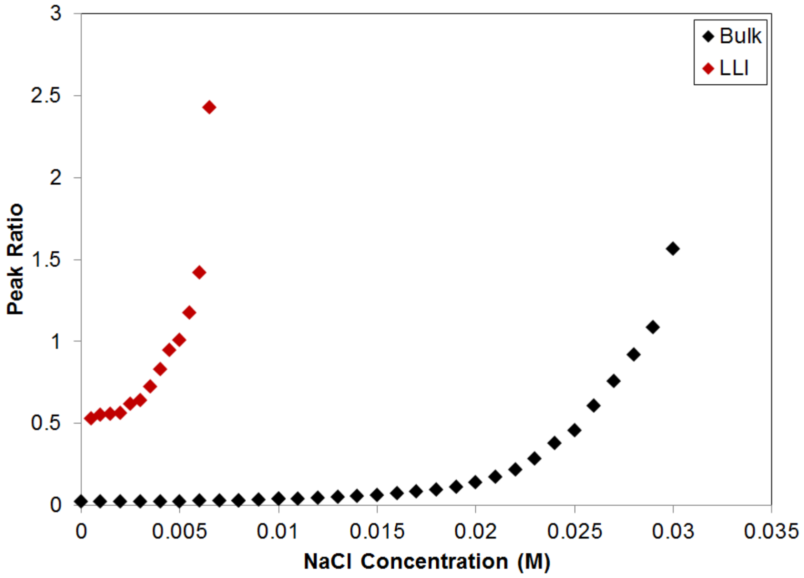

Figure 2.13 | Peak ratio between unaggregated and aggregated particles at the LLI (750nm/542nm) and in the bulk (630nm/520nm). Experimental conditions were the same as in Figure 2.12.

Nevertheless, the expected shift was not observed for MSA functionalized particles. Instead of red shifting, the relative strength of the peak at 750 nm increased compared to that of the 542 nm. This suggests that the particles at the interface are in 2 states, aggregated and separated, and increasing the NaCl concentration merely increases the number of aggregated particles. The ratios of aggregated peak intensity over unaggregated peak intensities can provide some information as to the relative stability of these particles at the interface in comparison to the bulk (Figure 2.13). It is clearly evident that aggregation occurs at lower NaCl concentration at the interface. This is attributed to forces other than van der Waals and electrostatic repulsion being introduced by the presence of the LLI (such as capillary forces from the deformation of the interface). This once again highlights the importance of particles that are stable with respect to aggregation to allow control over the inter-particle separation.

Although MSA contains 2 carboxyl groups per thiol, it was presumed that electrostatic repulsion by itself was insufficient to overcome the aggregating forces – van der Waals coupled with other compressive forces would ultimately dominate at short separations. In order to prevent particles from getting close enough to experience van der Waals, it was decided to use a spacer between the thiol and the carboxyl group. 12-mercaptododecanoic acid (MDDA) was chosen for this:

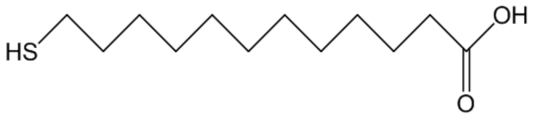

12- Mercaptododecanoic acid
(MDDA)

The effectiveness of this spacer was surprising in terms of stability – at no conditions tested, was irreversible aggregation observed. Even when dried out, these particles can be dispersed back into solution – this was in stark contrast to citrate stabilized or even MSA functionalized particles. Additionally, instead of the binary states of aggregation that MSA and citrate displayed, MDDA particles display a continuum of states from UV-Vis spectroscopy. More importantly, preliminary NaCl dependency on MDDA functionalized 16 nm particles experiments, qualitatively, gave rise to the expected trends from theory – both a red shift and peak broadening was observed for these samples from transmission spectroscopy (Figure 2.14).

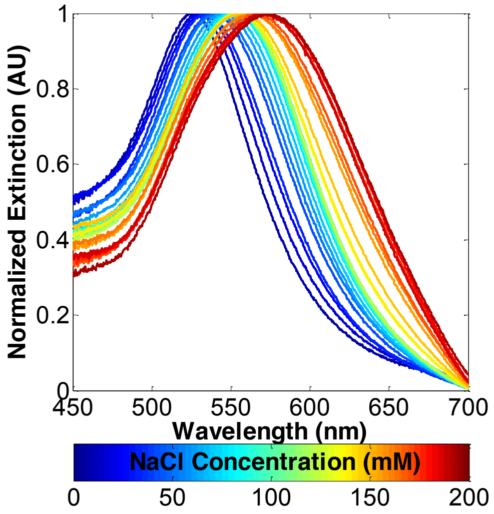

Figure 2.14 | Normalized extinction spectra of MDDA functionalized 16 nm NPs as a function of salt, assembled by centrifugation for 10 minutes at 9391 *g*, with a total number of NPs of 2.75x10^{11} in 1 mL of the aqueous phase together with 0.5 mL DCE. Reprinted with permission from Turek *et al*[24]. Copyright (2012) American Chemical Society.

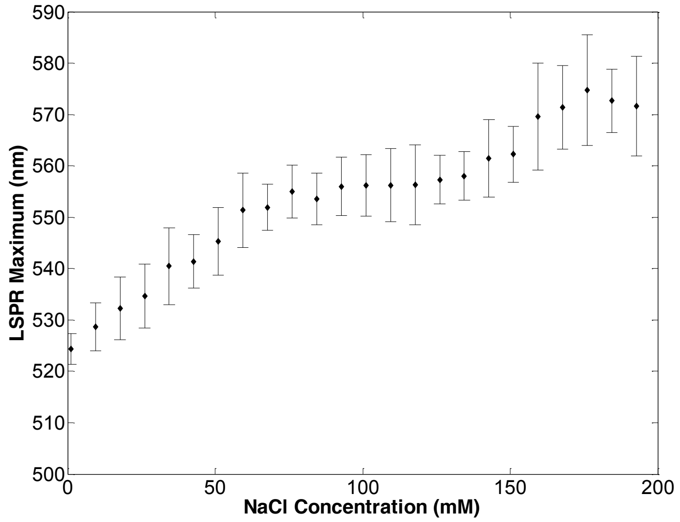

Figure 2.15 | LSPR maximum as a function of salt concentration. Experimental conditions are identical to Figure 2.14. Reprinted with permission from Turek *et al*[24]. Copyright (2012) American Chemical Society.

These results suggested that by centrifuging MDDA stabilized NPs to a water-DCE interface, it was possible to control the inter-particle separation and monitor this through transmission spectroscopy. This lead to a detailed study of this process, which was subsequently published in ACS Nano[24] and will be discussed in detail in Chapter 3.

2.9 X-ray diffraction of NPs at the LLI

Though the vast majority of the experimental evidence points to the fact that relatively ordered monolayers can be formed at the LLI, this evidence is mainly indirect. As already mentioned, the vast majority of characterization techniques are not suited to study particles sandwiched between two liquids, one of the few exceptions to this is XRD.

Beam-time was obtained at Diamond light source in the hopes of establishing and quantifying the actual separations between 16 nm MDDA functionalized NPs at the water-DCE interface as a function of NaCl concentration. One of the requirements for the XRD was an interface with a ≈ 10 cm diameter, therefore the standard 2 mL centrifugation tubes had to be replaced with 1 L ones. Transmission spectroscopy was much more challenging in such containers, but more importantly it was not needed – reflection spectroscopy is a more attractive way to extract spectral information as it offers the possibility of quantification of the intensities. Due to the large interfacial area of 1L tubes, curvature effects became less pronounced, therefore a reflection probe was used to obtain reflection spectra. Finally, despite the centrifuge tubes being designed for centrifugation, this was not an option for the assembly of NPs to the LLI (the large volumes meant that severe material limitations are placed on the tubes at higher RCFs) – the alternative of longer centrifugation times at reduced RCFs (hours) was deemed undesirable, instead emulsification was to be used (the use of emulsification to aid NP self-assembly will be discussed in more detail below).

Control experiments confirmed that even in larger tubes, with reflection spectroscopy and assembly by emulsification yielded comparable optical properties to those described in Chapter 3. However due to the large volumes of DCE that was needed and the perceived need for higher purities, 20 litres of fresh DCE at a 99.5% (in comparison to the 99.0% that was used prior to this) purity was bought. Unfortunately, the higher purity DCE was incompatible with the LLI (the impurities in these DCE batches contained an unidentified polymer/surfactant that not only aggregated the NPs at the interface, but also lead to the formation non-uniform interfaces) – a fact that was only determined during sample preparation at Diamond. Instead, in order not to waste the beam-time and obtain some quantitative information on NP behaviours at the LLI, the DCE was replaced by toluene.

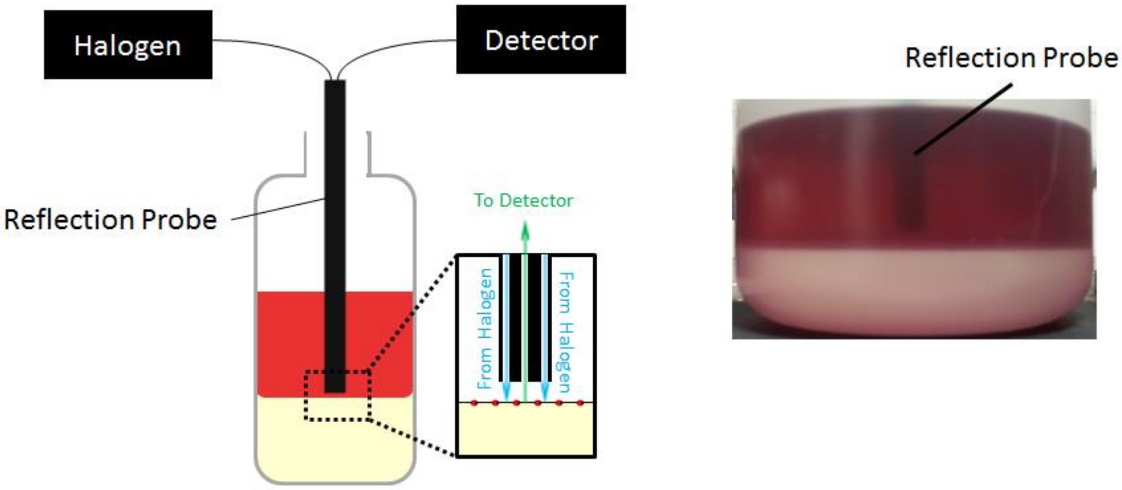

Figure 2.16 | Schematic of reflection probe and photograph of reflection probe immersed in aqueous NP solution.

Surprisingly, controlling the inter-particle separation of 16 nm MDDA functionalized particles could not be achieved at the toluene interface. All conditions tested, gave rise to a LSPR maximum at approximately 590 nm – even when no additional NaCl was added to the solution (*i.e*. at as made conditions). Reflection spectra suggested that 2D aggregation occurred whenever the particles adsorbed. The reason for such a difference compared to DCE is still not clear – it may be that the position of the NPs with respect to the interface changes leading to stronger capillary forces at the toluene-water interface. The interesting conclusion is that what 'looked like' 2D aggregation from the spectra obtained from reflection spectroscopy, XRD was able to confirm that this was indeed the case, suggesting that the spectral information can be used as an efficient tool to gauge structural information about the NP assembly.

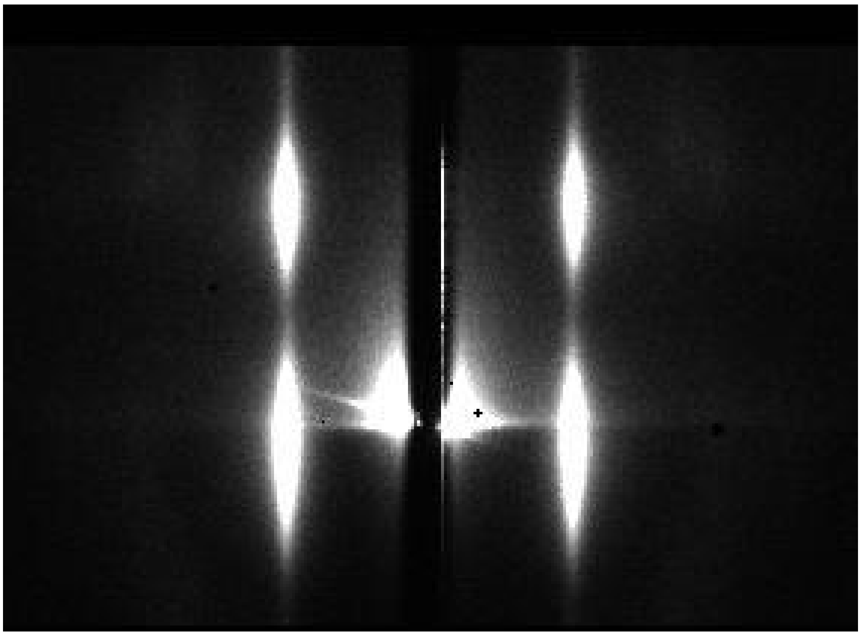

Figure 2.17 | GI-SAXS diffraction pattern of MDDA functionalized 16 nm NPs at a water-toluene interface. Image courtesy of Dr. Steve Roser.

The diffraction patterns obtained suggest that in all tested cases, the centre-centre inter-particle separation was ≈20 nm, the particles form a hexagonal, monolayer lattice, with a 'crystal' diameter of ≈1.5 μm (in other words, the order is observed over the distance of 1.5 μm).

2.10 Diffusion limited NP self-assembly at the LLI – application in SERS

Having established centrifugation as tool for controlling NP self-assembly to a water-DCE interface, it was noticed that particles also assemble spontaneously, if left in the presence of a LLI for long enough (usually overnight). This is not surprising as even in 1903, Ramsden noted the spontaneous formation of solid or highly viscous coatings of the free surface of colloidal solutions[18]. The challenge in relying on diffusion to adsorb particles is the painfully low diffusion coefficient of bulky objects such as particles. In fact, the use of centrifugation may do nothing more than simply speed up the formation of an array that would have been achieved if the mixtures were left to equilibrate (however it may also provide a force to overcome potential energy barriers, leading to a more dense assembly that would otherwise be formed, but the presence or absence of these energy barriers was not investigated).

One of the main industrial applications of particles at LLIs are emulsions. These are stable droplets of water-in-oil/oil-in-water that are stabilized by adsorbed particles/surfactants. Without the addition of surfactants, these emulsions separate out into distinctive phases. An example of this is spoiled milk separating into the more dense clear water phase and a coagulated protein/fat phase. Due to the small size of the droplets, an emulsion possess a vast interfacial area, but more importantly from a self-assembly point-of-view, the average distance that a particle has to diffuse to reach an interface is orders of magnitude smaller than when two distinct phases are present.

In other words, the formation of an emulsion between the aqueous nanoparticles and an organic phase is in principle an efficient way to speed up diffusion limited self-assembly. The fact that the NP concentrations that are generally used are small in comparison to those needed to form stable emulsions means that emulsion will separate back out into two distinct phases, while the particles will remain adsorbed. It is possible to achieve such an emulsion by sonication, however the resulting mixture was observed to separate out very slowly – several hours were usually required. Instead, and in fact a much simpler approach, is to simply shake the two phases for a few seconds. It is probable that the resulting droplets are much larger than those formed by sonication, however for the purposes of allowing NPs to diffuse to the interface, it was noticed that simply shaking the mixture could be used efficiently. The remarkable simplicity and speed of such an adsorption mechanism was subsequently discovered to be known in the literature – in fact one of the earliest papers on plasmonic NPs at the LLI used ‘shaking’ to assemble the particles[25].

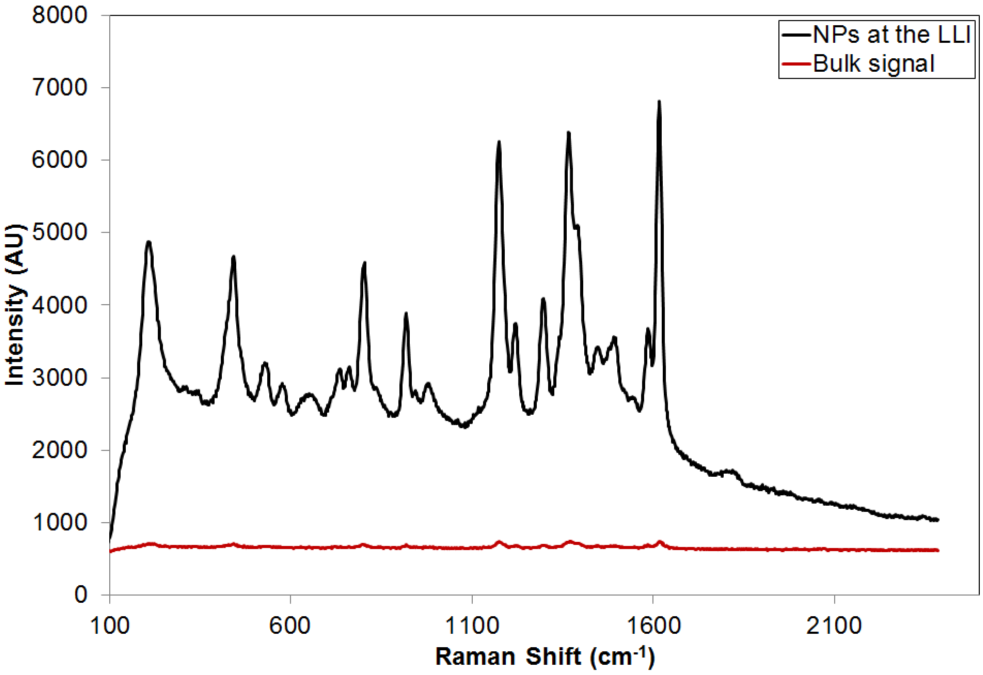

Figure 2.18 | Comparison of SERRS intensity between MGITC functionalized particles in bulk water and at the LLI. The aqueous phase contained 20 mM NaCl, 115 pmol MGITC, with a total number of particles available in the bulk of 1.74 ± 0.05 x 10^{10} in a 500 μL initial aqueous volume and 500 μL DCE volume. Following NP adsorption, the volume of the aqueous phase was reduced to 50 μL, followed by transferral to the coverslip. A 632.8 nm HeNe laser was used with an incident intensity of 8.5 mW.

In a collaborative effort with a then-PhD-student studying SERRS of malachite green isothiocyanate (MGITC) functionalized gold nanoparticles[26, 27] (Michael P. Cecchini), it was hypothesised that the plasmonic coupling between the NPs may lead to a sensitive detection platform. Given that the self-assembly process through shaking is trivial and extremely fast, as compared to many of the detection platforms utilizing SERS in the literature, it was decided to carry out a quick test on a home-built Raman setup[26, 27]. MGITC functionalized particles were assembled at a water-DCE interface then deposited on a glass coverslip similar to that shown in Figure 2.6 and the signal intensities between particles assembled at the interface were be compared to that of free, non-interacting particles in the bulk aqueous (Figure 2.18). The results were extremely positive – the coupling of the particles leads to a remarkable increase in signal intensity. More importantly however, is the fact that such a platform is easily self-assembled within seconds and is extremely versatile. The opportunity of SERS at the LLI was investigated in detail, leading to a patent submission, a publication in Nature Materials[28] and will be discussed in detail in chapter 5.

2.11 Conclusions

This chapter represents an overview of the project. Though most of the work described in this chapter is not publishable or is known in the literature (with the exception of the XRD study of NPs at the toluene-water interface), it nevertheless laid the groundwork for the rest of the PhD. The key results of this chapter include: the synthesis and characterization of citrate stabilized 16 and 43 nm gold NPs; establishing centrifugation as a means to assemble NPs to the LLI; preventing 2D aggregation of the NPs through the use of MDDA to functionalize the particles; emulsification as a means to speed up diffusion-limited NP self-assembly; possibility of obtaining SERS at the LLI; and finally XRD studies of MDDA functionalized particles at the water-toluene interface.

2.12 References

1. Wang, Z.; Ma, L. *Coordination Chemistry Reviews* **2009,** 253, (11-12), 1607-1618.
2. Daniel, M.-C.; Astruc, D. *Chemical Reviews* **2003,** 104, (1), 293-346.
3. Lee, P. C.; Meisel, D. *The Journal of Physical Chemistry* **1982,** 86, (17), 3391-3395.
4. Turkevich, J. *Discussions of the Faraday Society* **1951,** 11, 55.
5. Frens, G. *Nature* **1973,** 241, (105), 20.
6. Kimling, J.; Maier, M.; Okenve, B.; Kotaidis, V.; Ballot, H.; Plech, A. *The Journal of Physical Chemistry B* **2006,** 110, (32), 15700-15707.
7. Pong, B.-K.; Elim, H. I.; Chong, J.-X.; Ji, W.; Trout, B. L.; Lee, J.-Y. *The Journal of Physical Chemistry C* **2007,** 111, (17), 6281-6287.
8. Brust, M. *Journal of the Chemical Society. Chemical communications* **1994**, (7), 801.
9. Jana, N. R.; Gearheart, L.; Murphy, C. J. *The Journal of Physical Chemistry B* **2001,** 105, (19), 4065-4067.
10. Njoki, P. N.; Lim, I. I. S.; Mott, D.; Park, H.-Y.; Khan, B.; Mishra, S.; Sujakumar, R.; Luo, J.; Zhong, C.-J. *The Journal of Physical Chemistry C* **2007,** 111, (40), 14664-14669.
11. Lin, Y.; Skaff, H.; Emrick, T.; Dinsmore, A. D.; Russell, T. P. *Science* **2003,** 299, (5604), 226-229.
12. Binks, B. P.; Lumsdon, S. O. *Langmuir* **2000,** 16, (23), 8622-8631.
13. Su, B.; Abid, J.-P.; Fermín, D. J.; Girault, H. H.; Hoffmannová, H.; Krtil, P.; Samec, Z. *Journal of the American Chemical Society* **2003,** 126, (3), 915-919.
14. Abid, J.-P.; Abid, M.; Bauer, C.; Girault, H. H.; Brevet, P.-F. *The Journal of Physical Chemistry C* **2007,** 111, (25), 8849-8855.
15. Li, Y.-J.; Huang, W.-J.; Sun, S.-G. *Angewandte Chemie International Edition* **2006,** 45, (16), 2537-2539.
16. Younan, N.; Hojeij, M.; Ribeaucourt, L.; Girault, H. H. *Electrochemistry Communications* **2010,** 12, (7), 912-915.
17. Reincke, F.; Kegel, W. K.; Zhang, H.; Nolte, M.; Wang, D.; Vanmaekelbergh, D.; Mohwald, H. *Physical Chemistry Chemical Physics* **2006,** 8, (33), 3828-3835.

18. Ramsden, W. *Proceedings of the Royal Society of London* **1903,** 72, (ArticleType: research-article / Full publication date: 1903 - 1904 / Copyright © 1903 The Royal Society), 156-164.
19. Luo, M. X.; Song, Y. M.; Dai, L. L. *J Chem Phys* **2009,** 131, (19).
20. Lin, Y.; Böker, A.; Skaff, H.; Cookson, D.; Dinsmore, A. D.; Emrick, T.; Russell, T. P. *Langmuir* **2004,** 21, (1), 191-194.
21. Isa, L.; Lucas, F.; Wepf, R.; Reimhult, E. *Nat Commun* **2011,** 2, 438.
22. Boker, A.; He, J.; Emrick, T.; Russell, T. P. *Soft Matter* **2007,** 3, (10).
23. Tseng, T.-C.; McGarrity, E. S.; Kiel, J. W.; Duxbury, P. M.; Mackay, M. E.; Frischknecht, A. L.; Asokan, S.; Wong, M. S. *Soft Matter* **2010,** 6, (7), 1533-1538.
24. Turek, V. A.; Cecchini, M. P.; Paget, J.; Kucernak, A. R.; Kornyshev, A. A.; Edel, J. B. *ACS Nano* **2012,** 6, (9), 7789-7799.
25. Gordon, K. C.; McGarvey, J. J.; Taylor, K. P. *The Journal of Physical Chemistry* **1989,** 93, (18), 6814-6817.
26. Cecchini, M. P.; Hong, J.; Lim, C.; Choo, J.; Albrecht, T.; deMello, A. J.; Edel, J. B. *Analytical Chemistry* **2011,** 83, (8), 3076-3081.
27. Cecchini, M. P.; Stapountzi, M. A.; McComb, D. W.; Albrecht, T.; Edel, J. B. *Analytical Chemistry* **2011,** 83, (4), 1418-1424.
28. Cecchini, M. P.; Turek, V. A.; Paget, J.; Kornyshev, A. A.; Edel, J. B. *Nat Mater* **2013,** 12, (2), 165-171.

Chapter 3: A Plasmon Ruler at the Liquid-Liquid Interface

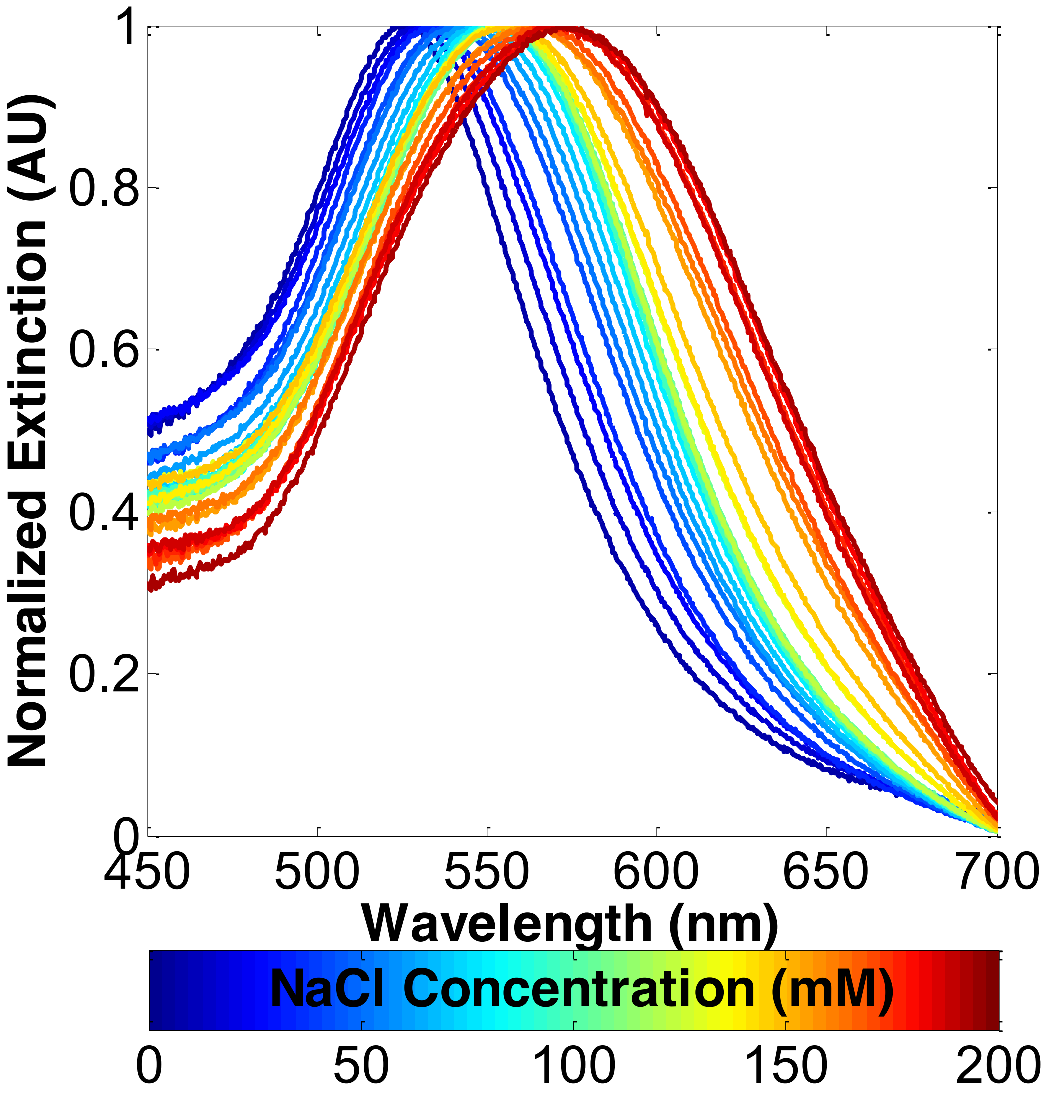

Reprinted with permission from Turek *et al*[1]. Copyright (2012) American Chemical Society.

3.1 Abstract

Having established centrifugation as a means to control NP adsorption at the LLI; MDDA as a suitable NP functionality; and transmission spectroscopy of aqueous droplets surrounded by DCE as a means to extract spectral information from the NP arrays, this chapter discusses control over the inter-particle separation. Tuneable inter-particle separation is established through control of the ionic strength of the aqueous solution, which in itself leads to novel optical properties of the NP assembly at the LLI. From comparisons between theory and simulations, this optical information is then used to estimate the inter-particle separation as well as study the effects of the NaCl concentration, centrifugation time, the centrifugal force and the effect of the interfacial area. Reversibility of NP adsorption to the LLI is (partially) demonstrated by changes in the pH of the solution. Finally, a study of the NP concentration dependence in the aqueous solution is shown to yield an unexpected result which will be covered in detail in Chapter 4.

Please note: The work described in this chapter was published and draws heavily from a publication in ACS Nano[1], with figures reprinted with permission.

3.2 Introduction

To date, the full potential of NPs at the LLI has yet to be realized. Despite the unique and attractive properties that the LLI offers to a wide range of fields[2-7], a relatively small number of practical applications exist that utilize NPs at the LLI. With the advent of nanotechnology, intense research efforts have focused on hierarchical self-assembly for the purposes of engineering macroscopic structures through nanoscale building blocks[8-10]. Through careful design of these building blocks, it is possible to generate unique material properties[11-15]. Though many techniques exist for hierarchical self-assembly, a common theme in achieving this is templating[16-18]. One of the simplest of templates is an interface. The most commonly used interface is that of a solid – a solid-liquid/solid-air interface allows for chemical modification of the surface to provide adhesion for analytes and/or the nanoscale building blocks[19, 20]. Despite the solid interface being the most widely used, there are some limitations of such an interface which should not be overlooked. Thin films formed at the solid interface are generally fragile – being highly susceptible to damage from, for example scratches, may be detrimental to the desired properties of thin films[21]. In addition, the fabrication of a truly smooth solid surface at the nanoscale can be challenging in and of itself[22]. The facile, intrinsically smooth[23] and 'self-healing'[24] properties that the LLI displays are therefore highly beneficial in this respect. Additionally, the LLI, much like the solid interface can also serve as a template for the self-assembly of nanoscale building blocks, however in many respects, the LLI is more suited to 2D self-assembly – adsorption to a LLI is a spontaneous and almost universal property of most nanoscale materials which requires no surface modification[25, 26].

Nevertheless, despite the aforementioned advantages of the LLI, the solid interface offers an important advantage. Obtaining structural information at the solid interface with sub-nanometer resolution is a trivial task that can be achieved within minutes through electron microscopy or scanning probe microscopy – while trying to determine the same information from the LLI is a dauntingly difficult challenge[27]. In fact, to the best of the authors' knowledge, a direct experimentally obtained image of NPs assembled at the LLI has yet to be demonstrated. Techniques that measure the 'average structure' [7, 13, 28-31] (such as the XRD of chapter 2 and the work described here), while highly useful are nevertheless not able to determine crucial parameters such as the three phase contact angle – one of the most important parameters for NPs at the LLI (although simulations can provide invaluable information on the adsorbed NPs).

Without a convenient means to characterize the assembly, control of the NP self-assembly at the LLI is challenging. The vast majority of research that deals with NPs at the LLI has therefore focused on uncontrolled assemblies in which the NPs are aggregated in 2D[32-34]. Though it may be likely that 2D aggregated NPs may form ordered and reproducible assemblies at the interface, it is important to realize however, that this is only a limiting case. For the purposes of harnessing the LLI for novel technological applications, control is important. In the simplest case, control of NP assemblies at the LLI needs to establish controlled adsorption, desorption and a controlled inter-particle separation.

In this chapter, such control is established. By increasing the resistance of the NPs to aggregation, through the use of 12-mercaptododecanoic acid (MDDA), it is shown that the inter-particle separation can be tuned through the ionic strength of the aqueous phase. The use of plasmonic nanoparticles results in a tuneable LSPR[35-37] which not only demonstrate novel optical properties, but also allows for an extremely quick and simple measurement to extract structural information. Centrifugation is demonstrated as a versatile tool to aid NP adsorption to the LLI and finally, similar to work carried out by Reincke[38] *et al.* pH modulation is shown to achieve desorption from 16 nm NPs.

3.3 Results and Discussion

Chapter 2 described the evolution of the project. The early stages were characterized by extremely time consuming experiments, which mainly yielded irreproducible results. The lack of control of NP assembly or convenient imaging techniques hindered experimental progression. Nevertheless, after countless variations in trying to obtain controlled separation between the NPs and extract optical information, a working system was finally established in the form of centrifugation of MDDA stabilized 16 nm gold particles to the water-DCE interface, with controlled adsorption and inter-particle separation mediated by the ionic strength of the solution.

The volumes were chosen to be 0.6 mL aqueous phase and 0.5 mL DCE. The actual volumes are not critical for controlled spacing; however it is of course critical that for comparative purposes, the volumes remain constant between experiments.

3.3.1 Centrifugation

It is important to understand some particulars of centrifugation. Firstly, the centrifuge that was used had a 45° tube angle. Figure 3.1, shows a schematic cross-sectional representation of the tube during an applied centrifugal force, when stationary and when the tube is extracted from the centrifuge. Due to the angle of the tube holder, the inserted tubes have a larger interfacial area (Figure 3.1 A and B) than when held vertically up right (Figure 3.1 C). Due to the hydrophobicity of the tube walls, significant curvature is observed in cases A and C. While the centrifugal force is applied (due to the DCE having a larger density that water), it is probable that the interface will adopt a vertical orientation (Figure 3.1 B), additionally the more pronounced effects of densities under a centrifugal force are likely to reduce the curvature of B compared to A, leading to a slight reduction in the area. When the centrifugal force is switched off, the interface will experience agitation as it is again rotated 90° to adopt a horizontal position. When the tubes are extracted and held upright the interface will contract to adopt a circular shape. The importance of this is that particles adsorbing to the interface during centrifugation have a larger interfacial area to which to do so, than when the tube are extracted and held up-right. Therefore, if during centrifugation, more particles adsorb than can be accommodated by the reduced area of the resting interface, one of three phenomena can be expected: desorption to reach equilibrium, compression of the particles – which may lead to aggregation or the particles migrating to stabilize the water-tube wall interface. Of these adsorption to the tube walls was predominantly seen in particles that had undergone 2D aggregation (*i.e.* citrate-stabilized particles at higher NaCl concentrations), however this was not observed for MDDA stabilized NPs. In order to limit adsorption to the walls, which can cause the particles at the interface to lose their confinement, thereby leading to greater disorder in the lattice structure, as well as allow a facile route to extract optical information through transmission spectroscopy, the volume of the aqueous phase was reduced to form a droplet.

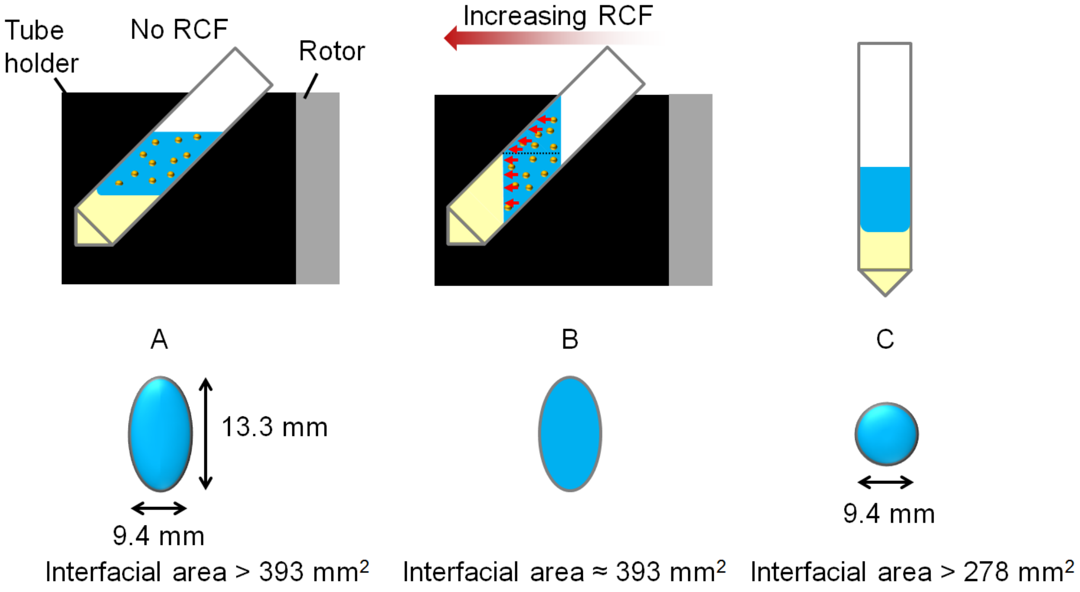

Figure 3.1 | Schematic of the cross-section of the tubes when stationary in the centrifuge (A), under an applied centrifugal force (B) and tubes that are extracted from the centrifuge (C). Below: interfacial area at these 3 positions.

Another aspect to consider for centrifugation with such a system is the migration of the particles under the applied centrifugal force. The direction of travel of the particles will be perpendicularly away from the rotor. Due to the 45° slant of the tubes and the likely re-orientation of the interface, some of the particles will not travel directly to the LLI, but rather the tube walls, following which, they are likely to migrate down the side to finally reach the interface. Interestingly, if Brownian motion is negligible and the particles are assumed to be infinitely small, then the particles above the dashed line in Figure 3.1 B will all converge at a single point of the LLI. Of course due to the fact that particles have a finite size, this point will be smeared. This concept has little implications for the current chapter, however may well be key to understanding chapter 4 as the larger aqueous volume used for that work (1 mL) means that approximately 60% of particles would converge to the same point at the interface.

3.3.2 Centrifugation as a means for NP assembly

Though of course, spontaneous NP adsorption to the LLI through diffusion can be achieved[39], the painfully long timescales and the lack of control of this assembly process makes it a non-optimal process in achieving tuneable properties of the self-assembled monolayers. Centrifugation is inherently a versatile and attractive tool in this respect – being applicable to the vast majority of particles as well as offering the opportunity of control over both the forces and timescales. It is therefore surprising that despite its simplicity, centrifugation had not been demonstrated as a way to control the assembly process in the literature. Though this fact was initially treated with caution (*i.e.* is there an inherent flaw with such an assembly mechanism?), it was later concluded that the very simplicity of centrifugation made it easy to overlook as a tool in facilitating NP adsorption to the LLI. Perhaps the main limitation of the work was the use of DCE together with the plastic centrifuge tubes. It was realized that the polypropylene carbonate that the tubes were made of has a limited stability to DCE, indeed if centrifugation was carried out over timescales that would be enough to raise the temperature of the system, then the plastic would show signs of physical deformation. Nevertheless, at moderate centrifugation times, at which the temperature of the tubes did not significantly increase (*i.e.* conditions for which this chapter describes), no detrimental effect was observed.

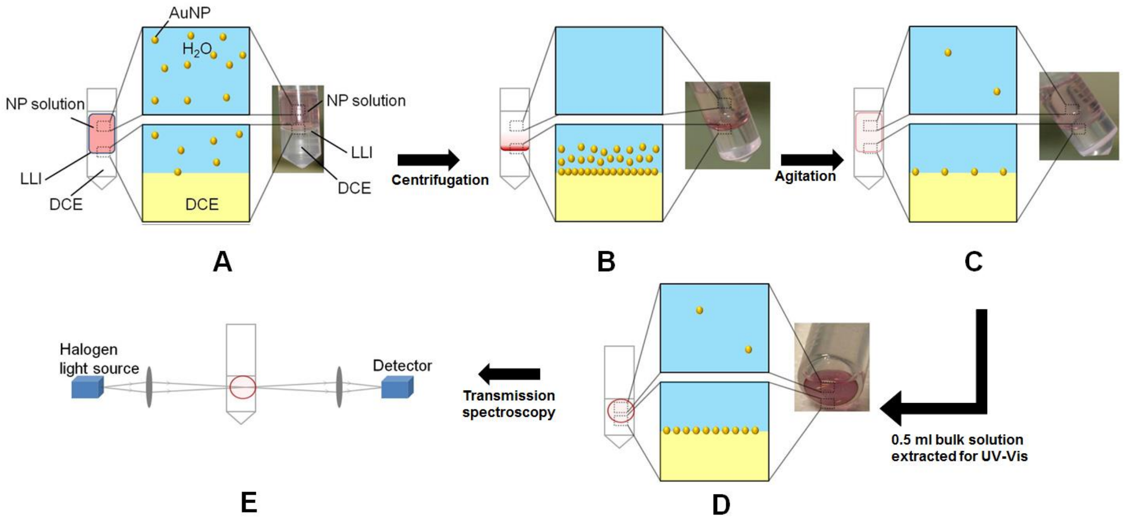

Figure 3.2 | Schematic of experimental procedure. (**A**) 0.6 mL Aqueous NP solution (containing $2.75\text{x}10^{11}$ 16 nm MDDA functionalized NPs at various NaCl concentrations) added to 0.5 mL DCE. (**B**) Centrifugation drives the NPs to the interface – depending on the NaCl concentration (or force/time of centrifugation) some particles adsorb to the LLI. (**C**) Agitation homogenizes the un-adsorbed particles in the aqueous phase. (**D**) Extraction of 0.5 mL of the aq. phase allows estimation of concentration of residual, un-adsorbed NPs (and hence the *adsorbed* particles) as well as induces the aq. phase to form a droplet. (**E**) Transmission spectroscopy is then performed directly on the droplet in the tubes, which through normalization allows the extraction of the LSPR maximum. Reprinted with permission from Turek *et al*[1]. Copyright (2012) American Chemical Society.

It was observed that when equilibrium of the adsorbed particles had been established through centrifugation, most of the particles remain close to LLI (if not adsorbed). One of the key pieces of information that is required in trying to determine the properties of the assembled NPs is the number of adsorbed particles – by comparing the maximum of the LSPR peak before and after centrifugation, it was realized that such numbers can be extracted. For this reason it was important to homogenize the aqueous phase (as most of the particles are close to the interface, simply pippeting out the aqueous phase would lead to unrepresentative concentrations). Rapid stirring or shaking can cause emulsification of the two phases[40], leading to additional NPs adsorbing to the interface in an uncontrolled manner, therefore the tubes were gently inverted 2-3 times to achieve such homogenization. During extraction of the aqueous phase, the adsorbed particles could be visibly seen to form a more optically dense film with a gradual red-shift. It is worth noting that below a critical volume (approximately 100 µL) an initial red-shift was seen, however within several seconds (or with additional agitation) the colour returned to the previous blue-shifted position that the 100 µL droplet displayed – it is highly likely that the initial red-shift is a result of compression of the NPs to a metastable level which subsequently leads to NP desorption. The general colour shift as a function of volume is in fact indicative that the particles remain unaggregated with clear inter-particle separation[41]. Aggregated particles display an increase in the intensity of the reflection when the volume is reduced, but show no change in colour. It is interesting to note that citrate stabilized particles assembled by emulsification also initially display a colour change when the volume is reduced – if carried out consecutively however, this shift is no longer seen. This suggests that even citrate stabilized particle can remain unaggregated at the LLI, but due to their poor stability are susceptible to 2D aggregation upon a compression of the interfacial area.

3.3.3 NP functionality

In fact functionality of the particles is perhaps the key parameter in achieving control of the inter-particle separation. As mentioned in chapter 2, MSA was also not successful in truly controlling the separation – this was due to the fact that MSA provides almost exclusively an electrostatic repulsion, which will eventually be overcome by the van der Waals (as well as the additional LLI-specific[42]) forces at close range. In order to achieve stable NPs it is therefore important to limit the extent of van der Waals forces between the gold cores. In the case of MDDA the use of an aliphatic backbone “spacer” between the thiol and carboxyl group was found to be extremely efficient in this respect. From a simple DLVO theory perspective, the reason why this stability was seen was because the radii of the two contributions are different – the radius of the van der Waals term of the gold core is ≈8 nm, while the radius of the electrostatic repulsion term is ≈9.5 nm.

The fact that citrate stabilized particles do initially lead to a visible red-shift upon a reduction of the volumes is interesting and deserves further studies, however as the main focus point was to achieve control, neither citrate nor MSA functionalized particles were used further in this respect. It was hypothesised that once a system that ‘works’ is established, then subsequent studies on other functionalities could be undertaken. Though it was established that the functionality is a key parameter, a detailed study of the functionality’s role was not performed.

3.3.4 NaCl dependence on NP adsorption

As mentioned in Chapter 2, the inter-particle separation was intended to be controlled through the ionic strength of the solution. The number of particles available in the aqueous solution was kept constant at $\approx 2.75\text{x}10^{11}$ NPs. The NaCl concentrations which were found to be most relevant were between 1 and ≈200 mM, however saturation of both the number of particles assembled as well as the red-shift occurred at ≈75 mM. Figure 3.3 shows the number of particles assembled as a function of the NaCl concentration. A constant RCF of 9391 g was applied for 10 minutes for these experiments. It can be clearly seen that the number of particles that the LLI can accommodate increases as a function of NaCl concentration. Assuming that repulsive forces dominate the inter-particle interactions, then this controlled adsorption is a direct of indication of tuneable inter-particle separation.

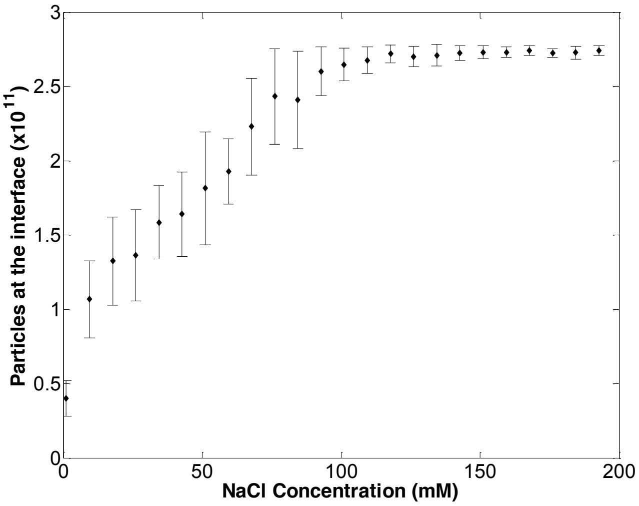

Figure 3.3 l Number of particles adsorbed at a water-DCE interface as a function of NaCl concentration. Centrifugation was carried out an RCF of 9391 g for 10 minutes, the total number of available particles in the solution was kept at 2.75x10^{11} NPs. N.B. Error bars denote 1 standard deviation from 12 repeated data sets. Reprinted with permission from Turek *et al*[1]. Copyright (2012) American Chemical Society.

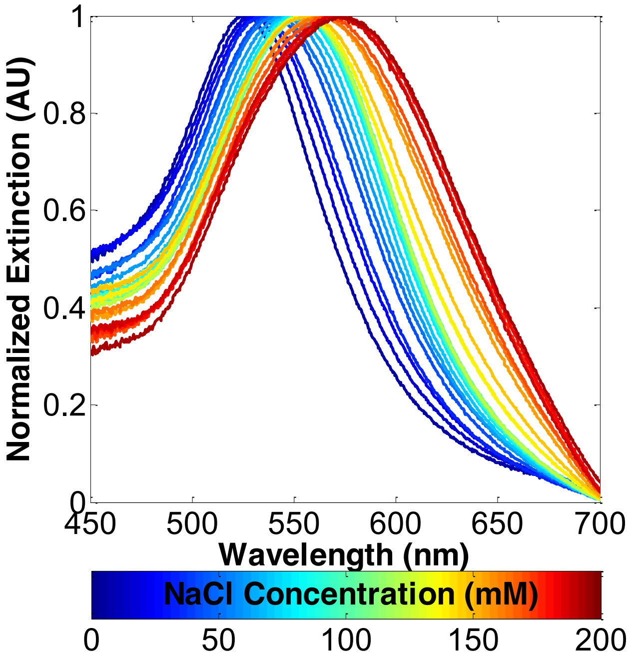

Figure 3.4 l Normalized extinction spectra of 16 nm MDDA functionalized gold NPs at the water-DCE interface as a function of NaCl concentration. Experimental conditions were identical to Figure 3.3. Reprinted with permission from Turek *et al*[1]. Copyright (2012) American Chemical Society.

As expected from tuneable inter-particle separations, a red-shift and peak broadening was observed from the transmission spectra of these samples (Figure 3.4). However, interestingly, the initial red-shift between 1-75 mM is followed by a plateau between 75-125 mM, which is followed by a further red-shift between 125 and 175 mM (Figure 3.5). Given that at 75 mM, almost all the particles in the solution are adsorbed, this further red-shifting is likely to be an indication of the particles losing their confinement, while further reducing localized inter-particle separation (though of course due to the constant number of particles at the LLI, the average separation between all the particles must be the same). In other words, between NaCl concentrations of 125 to 175 mM, the degree of inhomogeneity of the NP arrangement increases. This red-shift is followed by a second plateau above 175 mM. The hypothesis is that when the screening length is reduced to short enough distances, attraction between the particles will dominate. Due to a sum attraction between individual particles, they will form 2D clusters, in which, the separation cannot be reduced further due to steric confinement of the MDDA functionality.

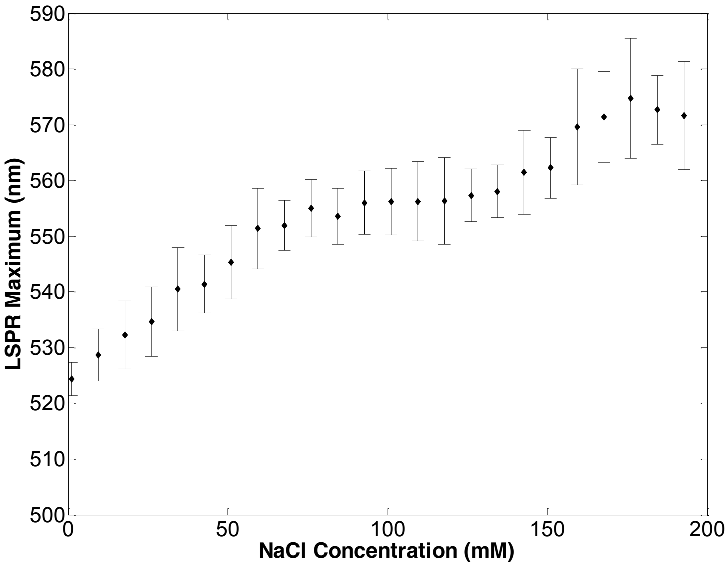

Figure 3.5 | LSPR Maximum of 16 nm MDDA functionalized gold nanoparticles as a function of NaCl concentration at a water-DCE interface. The onset of the plateau at 75 mM NaCl coincides with the conditions at which all the available particles are adsorbed to the LLI in Figure 3.3. N. B. Error bars denote 1 standard deviation from 12 repeated data sets. Reprinted with permission from Turek *et al*[1]. Copyright (2012) American Chemical Society.

Another useful source of information in trying to elucidate the behaviour of the particles at the interface lies in the peak broadness. Due to a larger spread of inter-particle separations in an unordered environment, the peak width is expected to increase when greater disorder is introduced. Aside from an indication of increasing inhomogeneity, theory predicts that as the inter-particle separation is reduced, the peak width will also broaden[6, 43]. An estimation of the true full width at half maximum (FWHM) was challenging due to the fact that the peak did not follow a normal distribution. Furthermore, a quantitative value of the FWHM was deemed less important than the qualitative trend of this width. From Figure 3.4, it is clear that assemblies made at higher NaCl concentrations have a distinctively broader peak than those prepared at lower concentrations; however it is also clear that the extinction of the assembly at wavelengths shorter than the peak maximum (*i.e.* at ≈ 450 nm) shows a clear decreasing trend as a function of NaCl concentration, while the sample prepared at the lowest NaCl concentration, doesn't reach the half maximum before the taper in the spectrum is observed. In order to side step this problem, the half-width at half maximum (HWHM) of the peak at longer wavelengths (*i.e.* red-shifted from the LSPR maximum) was extracted from the recorded spectra (Figure 3.6).

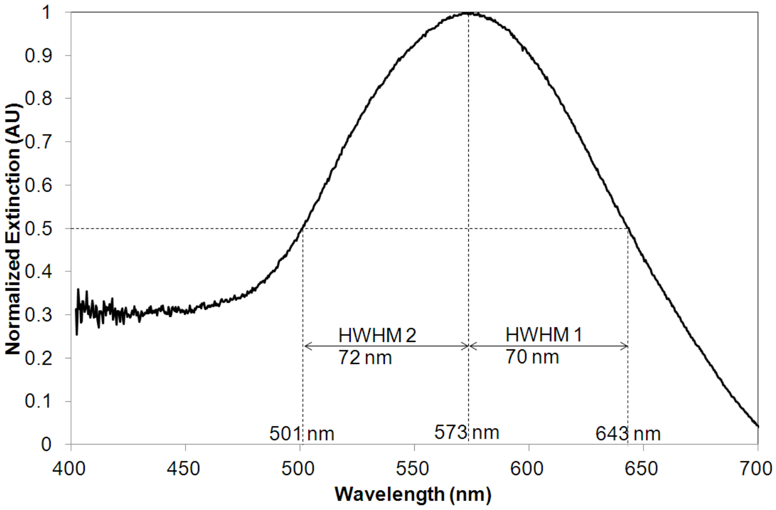

Figure 3.6 | The HWHM was extracted from the red-shifted shoulder of the LSPR peak (HWHM 1 rather than 2). Even though both are comparable in the example spectrum above, it is clear from Figure 3.4 that assemblies prepared at lower NaCl concentrations show that the two become less comparable, with HWHM 2>HWHM 1. Reprinted with permission from Turek *et al*[1]. Copyright (2012) American Chemical Society.

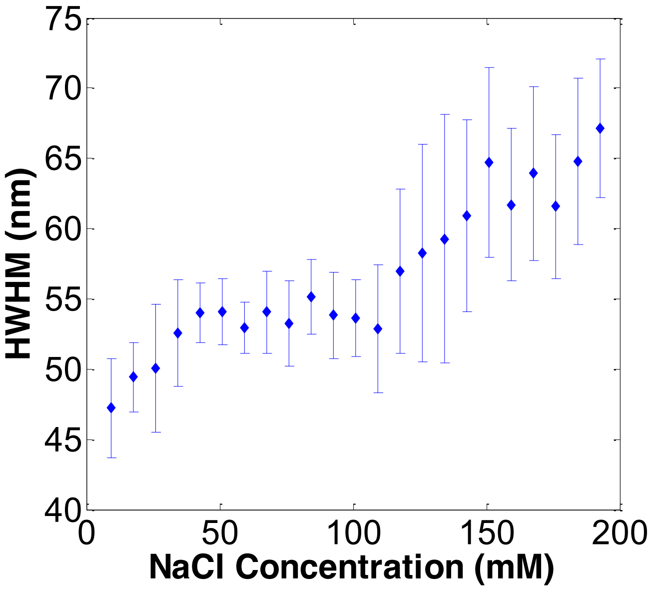

Figure 3.7 | HWHM of the LSPR of 16 nm MDDA functionalized gold nanoparticles at the water-DCE interface as a function of NaCl concentration. N. B. Error bars denote 1 standard deviation from 12 repeated data sets. Reprinted with permission from Turek *et al*[1]. Copyright (2012) American Chemical Society.

The HWHM as a function of NaCl concentration of these assemblies (Figure 3.7) show a similar trend as in Figure 3.5. That is, an increase, followed by a plateau, which is again followed by an increase and a final plateau. The NaCl concentration range of the initial increase in the HWHM, which is attributed to the reduced inter-particle separation, is surprising however. Despite evidence from both Figure 3.3 and Figure 3.5 that the inter-particle separation is controlled in the range of 0-75 mM NaCl, the HWHM only shows an increase between 0-50 mM NaCl. The reason why the plateau 'begins early' is not entirely understood. The plateau between 50 and 120 mM NaCl implies that there is no change between the inter-particle separation and no pronounced increase in inhomogeneity of the particle's arrangement. Though this is of course not quite true as going from 50 to 75 mM NaCl, approximately a third of the available NPs are assembled at the interface and a 15 nm red-shift of LSPR maximum is observed, indicating that the inter-particle separation does change between these salt concentrations. At NaCl concentrations above 120 mM two pronounced effects are clear, the first being a stark increase in peak broadness, while the second is the fact that the error bars become substantially larger than between 0 and 100 mM.

Both of these observations support the hypothesis that the arrangement of the particles becomes more disordered at salt concentrations between 100-150 mM. Interestingly, the second plateau in the HWHM, as with the first, is observed 25 mM ‘sooner’ than that in Figure 3.5. The plateau can be argued to occur at salt concentrations above 150 mM (though the large error bars and fluctuating data points make the existence of this plateau somewhat questionable).

Taking the observations from the number of particles adsorbed, the LSPR maximum and peak broadness as a function of NaCl concentration into account, the hypothesised ‘snapshot’ of the arrangement of the particle at the different NaCl concentrations is shown in Figure 3.8.

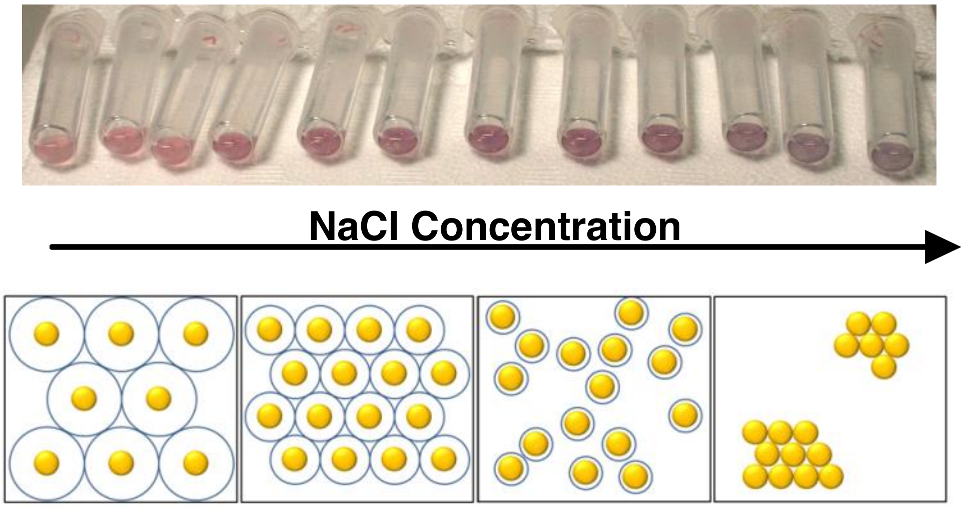

Figure 3.8 | Photographs of the droplets (above) and a top-down schematic of the hypothesised structure of the NPs arrangement (below) as a function of NaCl concentration. Reprinted with permission from Turek *et al*[1]. Copyright (2012) American Chemical Society.

At low ionic strengths of the solutions, the particles’ screening length and the effective area that the particles occupy at the interface is large; while the total interfacial area is smaller than the sum of the effective areas of all the particles (Figure 3.8 B i). As the effective area of particles is reduced, more particles are able to assemble at the interface and the average inter-particle separation is reduced, until a critical point where the sum of the effective areas of the particles becomes equal to the total interfacial area and all the available particles become adsorbed to the interface (Figure 3.8 B ii). As the screening length is reduced further, the interfacial area becomes larger than the effective area of all the available particles, leading to a loss in confinement, an increase in disorder and allows particles to move closer together (Figure 3.8 B iii). Finally, once the screening length is reduced to a critical point, aggregation starts to predominate and the particles form 2D clusters that possess some degree of short-range order, with fixed inter-particle separations (Figure 3.8 B iv).

A final indication that order is replaced by disorder as the NaCl concentration increases is observed in the reflection of the arrays. Below ≈100 mM NaCl the gold nanoparticle films appear reflective even to the eye, however above this, the films start taking on a dull matt appearance (Figure 3.8 A). This fact is confirmed in the reflection spectra of these arrays (Figure 3.10).

The reflection spectra were recorded with a reflection probe immersed in the aqueous solution, suspended approximately 1 mm away from the interface (Figure 3.9); while the particles were brought to the interface by emulsification. Though centrifugation was initially planned (hence the centrifuge tubes), it was subsequently realised not to be a suitable technique for such containers. The maximum RCF that such containers could withstand was 7100 *g*, while the larger distances that the particles would need to migrate through to the interface meant that centrifugation would need to be carried out for much longer timescales.

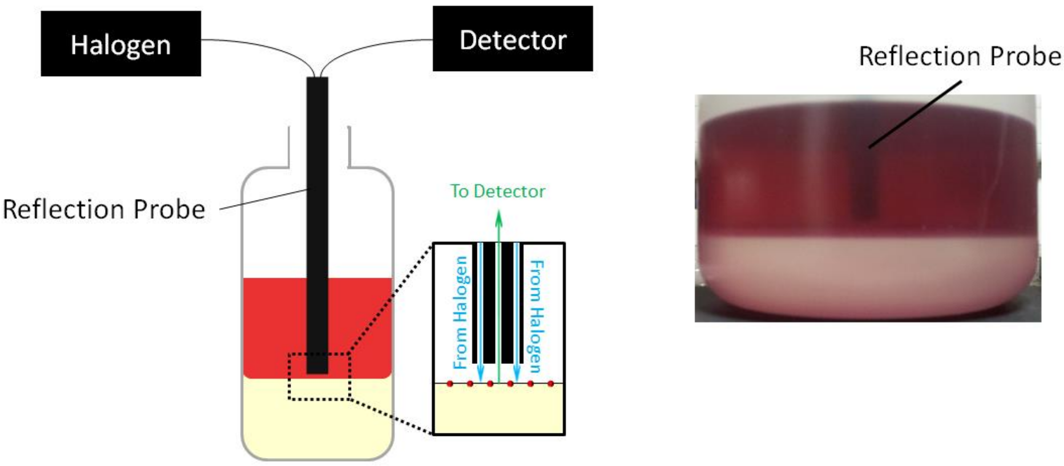

Figure 3.9 | Schematic of the reflection setup for measuring the reflection of gold nanoparticle arrays at the water-DCE interface. The interfacial area of the tubes was estimated to be approximately 75 cm^2.

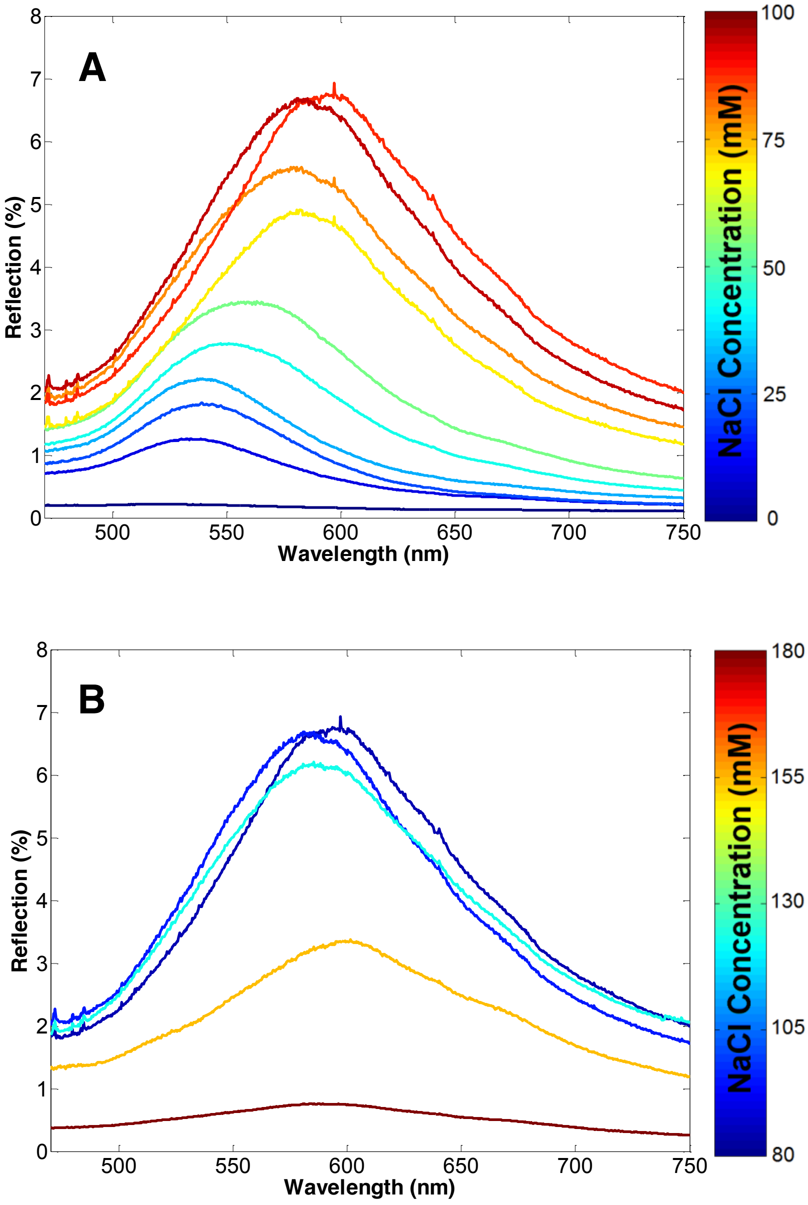

Figure 3.10 | Reflection spectra of 16 nm MDDA functionalized gold nanoparticles at the water-DCE interface as a function of NaCl concentration demonstrating an initial increase in reflectivity up to 100 mM NaCl (A), followed by a decreased reflectivity above 100 mM (B). NPs were assembled by vigorous shaking of the tubes for approximately 1 minute, after which the mixture was allowed to separate out and homogenize for a further 15 minutes. The total number of nanoparticles in the aqueous solution was 2.0×10^{14}, with an aqueous volume of 300 mL and the volume of DCE being 100 mL.

As expected the reflection spectra follow the red-shift that is indicative of reduced spacing as a function of NaCl. The spectra also show a clear increase in reflection intensity until 85-95 mM NaCl (Figure 3.10 A), at which a maximum of 7% reflection is seen, however this is followed by a decrease in the intensity at NaCl concentrations above 100 mM (Figure 3.10 B). Though this decrease may seem counter-intuitive at first – the inter-particle separation would be lower and the number of particles assembled would be higher at NaCl concentrations above 100 mM, this decrease is actually indicative that order in the assemblies is reduced at these conditions. Due to the fact that coherent scattering is reduced when disorder is introduced, the decrease in reflection intensity suggests that destructive interference of the scattered light predominates at these conditions.

Importantly, the peak magnitude of the reflection even at 85-95 mM NaCl does not agree with theoretical predictions. Theory predicts reflection coefficients approaching 20-30 % at these conditions, and a maximum reflection above 50%. Indeed, such high reflection coefficients were recently reported by Girault's group[14]. Therefore the question is why do the spectra in Figure 3.10 only show a maximum of 7%? The answer is likely to lie in disorder again. Theoretical predictions are made with a perfectly ordered system. The combined experimental results suggest that it is possible to control the average inter-particle separation and that there is relative order in the arrangement of the NPs at NaCl concentrations below 100 mM. However, this does not mean that the experimental system is perfectly ordered at these ionic strengths. In fact it is believed that the closest scenario to true order in the arrangement of NPs at the LLI is the limiting case where the particles aggregate in 2D, forming a close packed assembly. Nevertheless, it is hypothesised that the very reduction in magnitude of the reflection compared to theoretical predictions can be used to elucidate a more accurate representation of the arrangement of the particles at these interfaces, though this will be left for a separate study.

3.3.5 Control of the inter-particle separation at fixed NaCl concentrations

As mentioned previously, one of the main benefits of using centrifugation is the ability to control the number of particles assembled to the LLI. The previous section has demonstrated that at a fixed RCF and time of centrifugation, the concentration of NaCl can be used to control this parameter. However, the RCF and time of centrifugation can be employed equally well to control the number of particles at the interface, at a fixed NaCl concentration. Though of course, using of RCF or time of centrifugation to control this requires the system not to reach equilibrium. In other words, the maximum number of particles that can be adsorbed is governed by the effective area that each particle occupies at the interface, which is itself governed by the NaCl concentration, however through fine-tuning the RCF or time of centrifugation, it becomes possible to adsorb less particles. Under these conditions, these particles are expected to still experience a net repulsive force which will tune the inter-particle separation, but this repulsion will be weaker than at equivalent separations through control of the NaCl concentration. In effect, controlling the inter-particle separation through RCF or time of centrifugation allows one to tune the repulsive forces between the particles at the LLI.

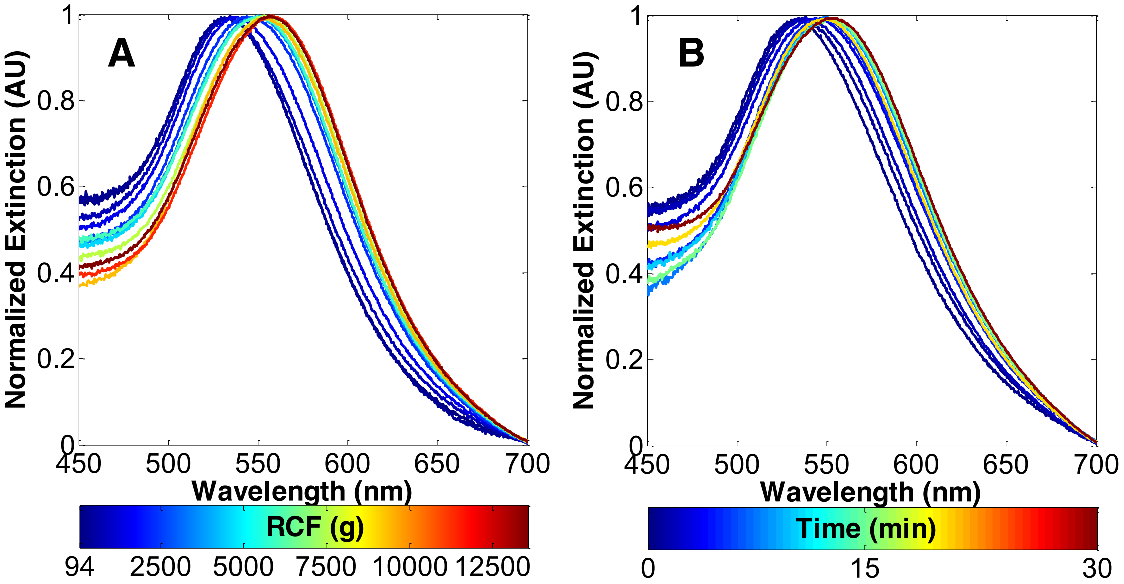

Figure 3.11 | Normalized extinction spectra of particles assembled as a function of RCF (A) and time of centrifugation (B). For both, the NaCl concentration was fixed at 75 mM; for varied RCF values the time of centrifugation was fixed at 10 minutes; while for varied times, the RCF was fixed at 9,391 *g*. Reprinted with permission from Turek *et al*[1]. Copyright (2012) American Chemical Society.

Unsurprisingly, both the RCF and time of centrifugation gave the expected red-shift indicative of tuneable inter-particle separations (Figure 3.11). Also, as expected the number of particles assembled at the interface followed a close correlation with the red-shift (Figure 3.12). The significance of these trends is perhaps less interesting in light of the tuneable inter-particle separation already demonstrated by controlling the NaCl concentrations. Nevertheless the ability to vary the separations at constant chemical conditions supports the hypothesis that the shifts that are seen in the transmittance spectra do in actual fact correspond to varied inter-particle separations. Additionally, these results demonstrate that controlling these separations can be achieved in more than one manner.

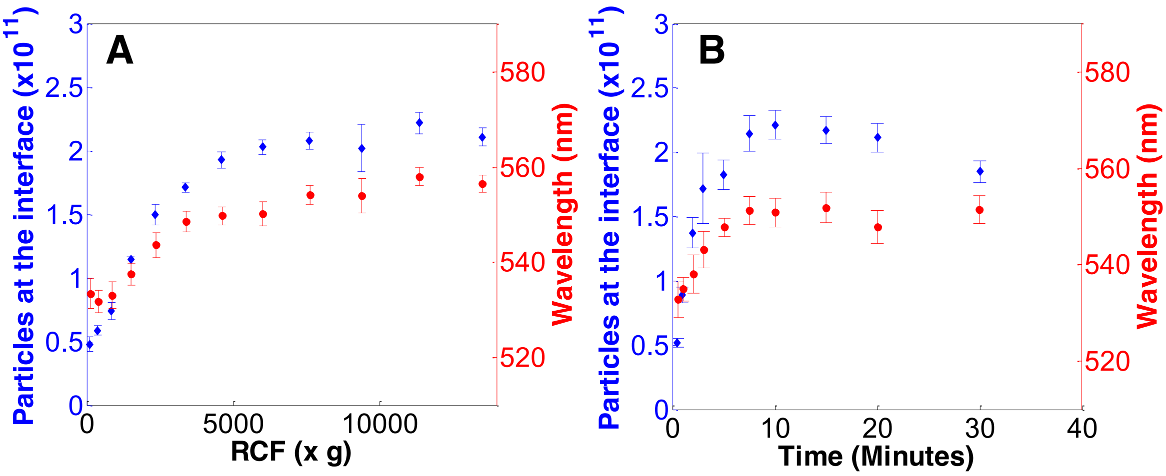

Figure 3.12 | Number of particles assembled at the interface (in blue) and LSPR Maximum (in red) as a function of RCF (A) and time of centrifugation (B). Reprinted with permission from Turek *et al*[1]. Copyright (2012) American Chemical Society.

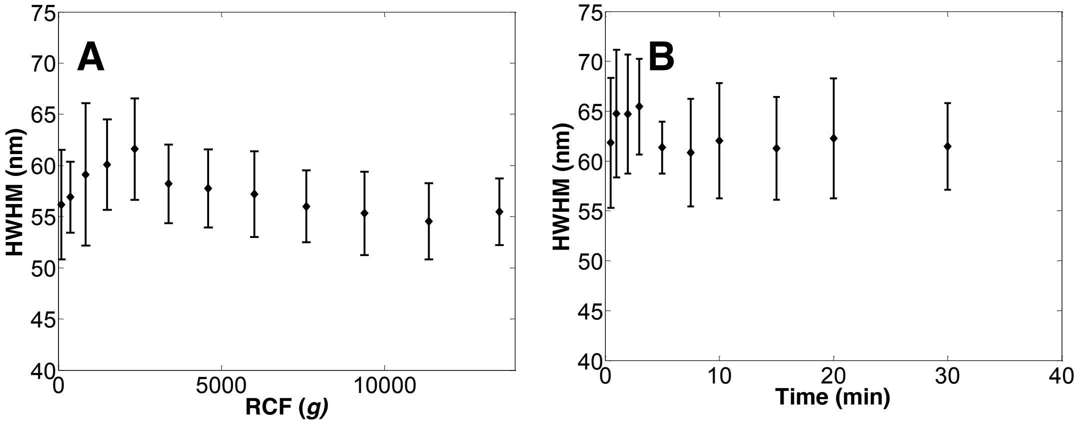

Figure 3.13 | HWHM of the LSPR of particles at the LLI assembled at varied RCF (A) and times of centrifugation (B). Reprinted with permission from Turek *et al*[1]. Copyright (2012) American Chemical Society.

Perhaps the most significant finding of these results lies in the LSPR peak broadness of these assemblies (Figure 3.13). As reasoned above, if the number of particles assembled at the interface is below the maximum that the interface can accommodate, then the particles will be repelled to distances further than what is observed at equivalent salt concentrations in Figures 3.3, 3.4 and 3.5. The lateral force between the particles at these extended distances will therefore be diminished, leading to greater disorder in the NPs' arrangement. This increased disorder is expected to appear as increased peak broadness at 'intermediate' RCFs and times of centrifugation. This broadness is then expected to tail off to equivalent HWHM as in Figure 3.7 once the interface starts approaching saturation with particles.

This effect is in actual fact seen in Figure 3.13 – at an RCF of 2348 *g* and, separately, at 3 minute centrifugation maxima are seen in the HWHM. As a greater force is applied or centrifugation allowed to carry on for longer, the HWHM reduce to 55.3 ± 4.1 and 60.9 ± 5.4 nm respectively. Both of these are within error of the 55.1 ± 2.6 nm HWHM of the 75 mM experiments from Figure 3.7. The interesting implication of this, as mentioned previously, is that the RCF/time of centrifugation allows one to tune the inter-particle forces at the LLI.

3.3.6 Volumetric dependence

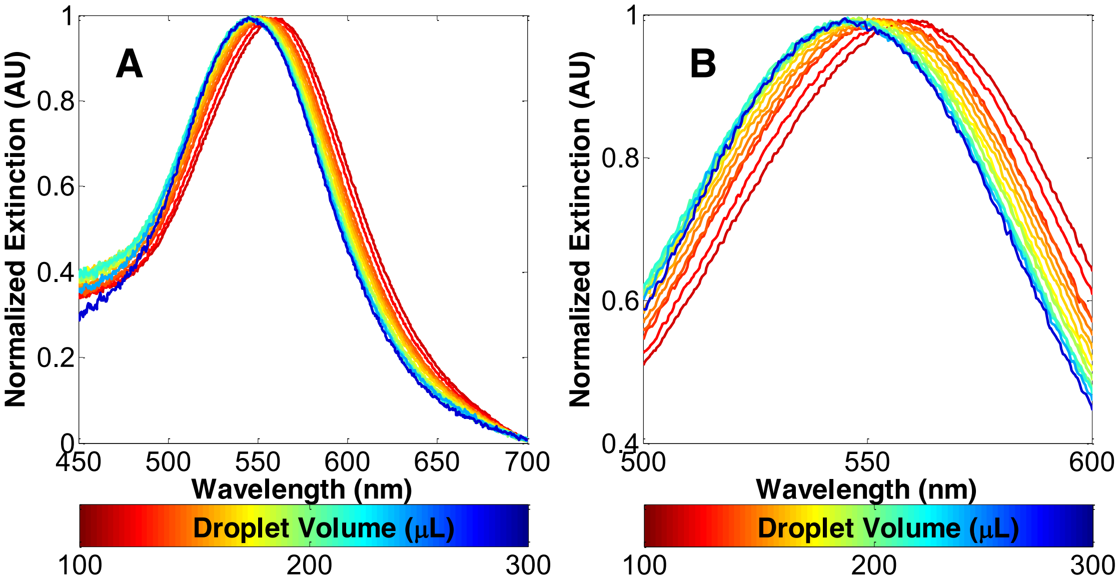

Figure 3.14 | Normalized extinction spectra of particles as a function of droplet volume. NPs assembled to the LLI by centrifugation at 9,391 *g* for 10 minutes in the presence of 75 mM NaCl, the volume of the droplet was subsequently controlled by addition of 75 mM NaCl solution. Reprinted with permission from Turek *et al*[1]. Copyright (2012) American Chemical Society.

The RCF/time experiments demonstrated an alternative to NaCl to tune the inter-particle separation. These experiments also suggest that at conditions when the interface is not saturated, the inter-particle interactions yield a net repulsive force, leading particles to more distant separations. It follows then that aside from reducing the number of assembled particles at a fixed interfacial area, increasing the interfacial area at a fixed number of particles should allow for another alternative control both the inter-particle separation and the inter-particle forces. The interfacial area was decided to be increased simply through an increase in the volume of the droplet. The benefit of controlling the assembly in this manner is that this allows one to tune the separations on any given assembly, whereas control through NaCl, RCF or centrifugation time is only available before the particles have assembled.

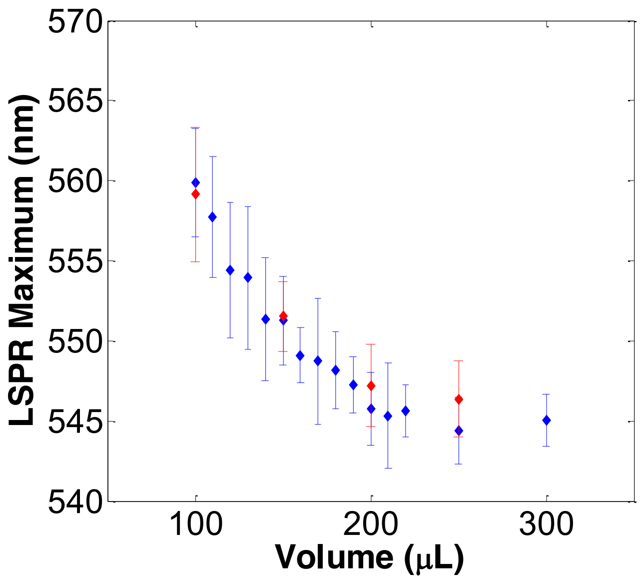

Figure 3.15 | LSPR maximum of the particles as a function of droplet volume. Blue data points correspond to an increasing volume, while the red data points are the recorded maxima when the droplet volume is subsequently reduced. Reprinted with permission from Turek *et al*[1]. Copyright (2012) American Chemical Society.

Predictably, Figure 3.14 shows a blue shift as the volume of the droplet is increased. The initial LSPR maximum of 559.9 ± 3.4 nm at 100 μL reaches a plateau of approximately 545.7 ± 2.3 nm at 200 μL – subsequent volume increases do not seem to affect the inter-particle separations. It is likely that the distances between the particles at this point become large enough that the inter-particle repulsion becomes comparable to thermal fluctuations and therefore negligible. Subsequent reductions in the volume of the droplets (red data points in Figure 3.15) show a negligible hysteretic behaviour in the LSPR maxima. Importantly, if the volume of the droplets is reduced below 100 μL, an initial colour change is observed by eye, it is hypothesised that at this stage, the interface becomes "super-saturated" with particles, leading to rapid desorption of the excess particles. This phenomenon is evidenced through the fact that the LSPR maximum equilibrates back to ≈560 nm and "excess" NPs are observed in the bulk aqueous phase after the volume reduction.

The HWHM of these particles remains roughly constant across the volumes. This is somewhat surprising, given that from Figure 3.13, it would be expected that the peak broadness should increase as the separation is reduced and greater disorder is introduced. This observation may be explained through the fact that there would be two competing processes – peak broadening from greater disorder and peak narrowing from greater inter-particle separations. It may therefore be that at these conditions, these two processes cancel out, leading to constant peak broadness.

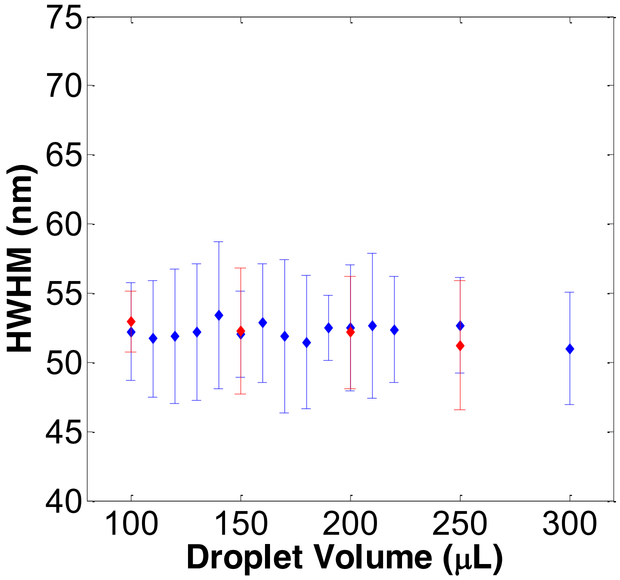

Figure 3.16 | HWHM of the LSPR as a function of droplet volume. Reprinted with permission from Turek *et al*[1]. Copyright (2012) American Chemical Society.

3.3.7 The ‘plasmon ruler’

It has been demonstrated in this chapter that tuning the inter-particle separations yields a shift in the LSPR maximum. This maximum can then be related to the actual separation. The question is how correlate these two parameters? Experimentally, the average inter-particle separation can be estimated from knowledge of the interfacial area and the number of assembled particles, then assuming that the particles are spaced as far away from each other as possible. This assumption is, of course, not valid if the net inter-particle interactions become either negligibly repulsive or attractive. Due to aggregation occurring at higher NaCl concentrations, it becomes challenging to extract an approximation for the inter-particle separation. In fact, experimental data at NaCl concentrations above 75 mM (it could be argued that NaCl concentration between 75 and 100 mM could still be valid, however the confinement of the particles is likely going to be diminished above 75 mM) becomes less valid and is therefore omitted. Meanwhile, the RCF/time of centrifugation results rely on the system not reaching equilibrium saturation – the fewer particles that are assembled in comparison to the equilibrium number, the smaller the effective repulsive force. In other words, the assumption that particles are spaced as far away from each other as possible becomes less valid for larger separations, therefore deviations from the NaCl dependency results are expected at larger inter-particle separations. Figure 3.17 shows the combined inter-particle separations against the LSPR maximum for the RCF/time of centrifugation (blue) and the NaCl dependency (green) results compared with theory (black) and simulations (red).

The simulations are plotted on a separate graph due to the fact that the conditions are different – these were run for a 2D array of particles in a vacuum[37]. This makes comparisons between the theory and experiments invalid when the axes are ‘LSPR maximum (nm)’ and ‘inter-particle separation (nm)’ (in other words λ_0 for the simulations cannot be assumed to be 525 nm). Additionally, the dielectric properties of the surrounding medium is challenging to describe theoretically (or measure experimentally) – parameters such as the three phase contact angle or even the ionic distribution around the particles remain unknown therefore even theory is not necessarily directly comparable to experiments. For a qualitative comparison however, both theory and simulation are plotted alongside experiments. The widely used plasmon ruler axes of $\Delta\lambda/\lambda_0$ against gap distance/diameter (Figure 3.17 B) is useful for more universal comparative purposes – these axes cancel out the effect of differently sized particles.

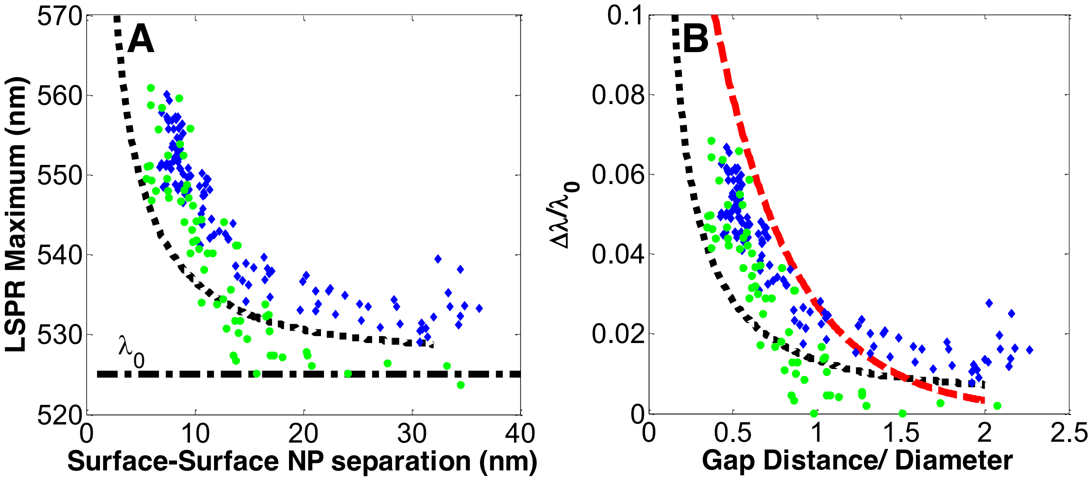

Figure 3.17 | LSPR maximum against surface-surface inter-particle separation (A) and the commonly used 'plasmon ruler' axes $\Delta\lambda/\lambda_0$ against gap distance/diameter (B). Blue points represent NaCl data from Figures 3.3 and 3.5 at NaCl concentrations below 75 mM; green points represent RCF/time experiments from figure 3.12; black dotted line represents theory; red dashed line represents simulations from Ben *et al.*[37]. Reprinted with permission from Turek *et al*[1]. Copyright (2012) American Chemical Society.

It is clear from Figure 3.17 that the experimental results from the NaCl experiments follow the expected qualitative trend that both theory and simulations do and in actual fact lie approximately between them at separations of 0.5-1.0 gap distance/diameter. Time/RCF experiments on the other hand show poor agreement to the NaCl experiments at separations above ≈12 nm, however agree well at shorter separations. As mentioned earlier, this deviation at longer separations is expected due to the assumptions made. Based on these results, it is likely that the average inter-particle separation for 16 nm MDDA functionalized nanoparticles at the water-DCE interface can be controlled in the region of 6-35 nm. However it is important to note that while these numbers are likely to be reasonable, a direct imaging technique (such as XRD) is required before truly meaningful comparisons can be made between experiments, theory and simulation.

3.3.8 Reversibility of adsorption

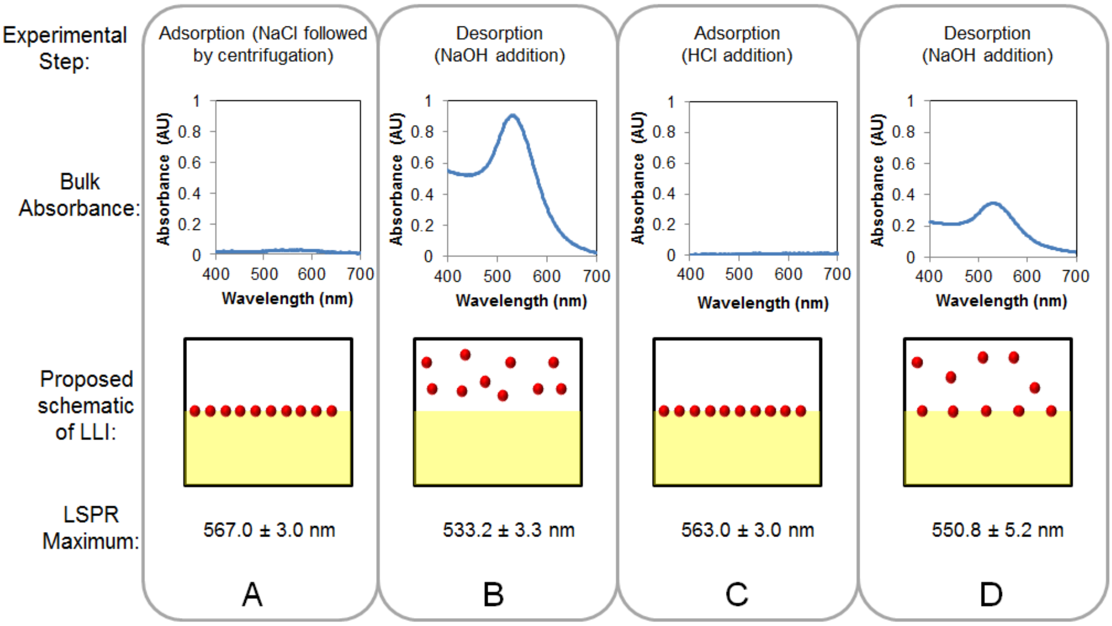

Figure 3.18 | Reversibility of adsorption of 16 nm MDDA functionalized Au NPs to the water-DCE interface. After centrifugation at a NaCl concentration of 165 mM for 10 minutes, the vast majority of the NPs are adsorbed to the interface (A), with a negligible bulk content. Followed by a 100 fold dilution of the NaCl concentration of the aqueous phase and the addition of 5 µL of 5 mM NaOH, most of the NPs desorb from the interface and are observed in the aqueous phase (B). Neutralization of the NaOH with 5 µL 5 mM HCl succeeds in re-adsorbing the NPs (C). A further desorption step through 5 µL 5 mM NaOH addition however only allows for partial desorption (D). Adapted with permission from Turek *et al*[1]. Copyright (2012) American Chemical Society.

Given that decreasing the volume of the droplet below 100 µL leads to desorption of the excess NPs from the interface, it was hypothesised that reversibility of adsorption of the particles should be possible. The reason for this desorption is due to the interfacial area being reduced below the effective area that the adsorbed NPs occupy. It should therefore be possible to achieve desorption by keeping the interfacial area constant, while increasing the effective area of the adsorbed NPs. If the NPs are initially assembled at the LLI, a reduction of the ionic strength of the solution should provide a route to desorption. This was tested by first centrifuging the particles at 165 mM NaCl (a high concentration was used to ensure that all available particles are assembled and that the bulk aqueous phase had a negligible NP content), followed by a 100-fold dilution of the aqueous phase with ultra-pure water (done by adding 900 μL water to the 100 μL of the aqueous phase, removing 900 μL, and another addition/removal step). Following the dilution, the particles did not seem to desorb, even when the droplet was left to equilibrate. It was reasoned that perhaps during the dilutions, the particles had lost some of their charge from re-association of the carboxyl groups, therefore the pH was adjusted with NaOH to ≈9. Though immediately after the addition of NaOH no visible change occurred, gentle agitation of the droplet succeeded in desorbing the NPs – it is probable that the agitation merely homogenized the solution thereby equilibrating the pH and dissociating the carboxyl groups. This effect is demonstrated in Figure 3.18.

Following centrifugation at 165 mM NaCl (Figure 3.18 A), almost no NPs are seen in the bulk aqueous phase, while the LSPR Maximum of the NPs at the interface is 567.0 ± 3 nm. Following dilution of the NaCl and addition of NaOH (Figure 3.18 B), almost complete desorption is seen, leading to an absorbance of ≈0.9 in the bulk and an LSPR maximum of the NPs at the interface of 533.2 ± 3.3 nm. Addition of HCl (Figure 3.18 C) in equimolar equivalents to the NaOH of step (Figure 3.18 B) leads to almost complete re-adsorption of the NPs with both the bulk absorbance and LSPR maximum returning to within experimental error of (Figure 3.18 A). Despite the fact that this effectively demonstrates a fully reversible cycle, subsequent desorption steps however (Figure 3.18 D), lead to only partial desorption with the bulk absorbance being ≈0.4 and the LSPR maximum of the NPs at the interface being 550.8 ± 5.2 nm. Re-adsorption remains efficient after the first cycle with a negligible bulk absorbance of the bulk, however a further red-shifted LSPR maximum of 570.0 ± 2.1 nm was observed. The desorption-adsorption cycle was repeated 2 further times, and both desorption steps gave identical results of Figure 3.18 D, while the LSPR maximum of the re-adsorbed step was in excess of 570 nm each time. The reason why subsequent cycles did not show complete desorption is not understood. It is likely to be a case of fine-tuning the chemical composition of the aqueous phase and alteration of the NaOH/HCl addition, however the reversibility of adsorption was not investigated in more detail. Given that full reversibility was observed in the first cycle, it is believed that ‘full’, indefinite reversibility of NP adsorption to the water-DCE inteface should be possible.

3.3.9 NP concentration dependence on adsorption to the LLI

At the time it was planned to study this reversibility in much more detail. Given that control of the spacing and number of nanoparticles adsorbed was achieved, full control of the desorption process was one of the remaining challenges to have full control of the NPs at the LLI (though Figure 3.18 demonstrates desorption it is carried out in an uncontrolled manner). However despite this intention, a side project arose as a result of an unexpected finding when studying the dependence on the NP concentration in the initial bulk aqueous phase on the adsorption and LSPR maximum of the LLI.

As can be seen from Figure 3.19, the number of particles "at the interface" plateaued at three different levels for the different NP contents in the initial aqueous phase. For the black points, the plateau occurs at ≈1.95x10^{11} particles – meaning that approximately 97.5 % of the available particles had assembled; for red, the plateau is 2.45x10^{11} particles, or 87.5%; while for blue the plateau was seen at approximately 3.10x10^{11} NPs, or 86.1%. This in and of itself is not surprising – it was hypothesised that by increasing the NP content, the plateau would be seen at different levels, while at high enough concentrations the number of particles at the interface would be independent of the concentration.

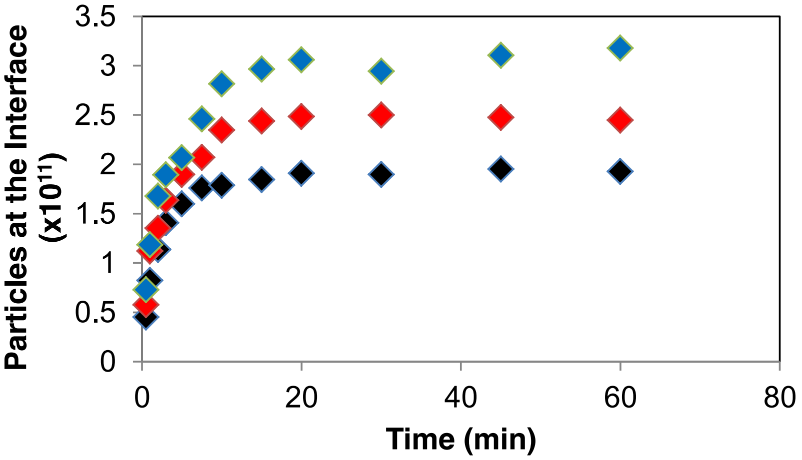

Figure 3.19 | "Number of particles at the interface" as a function of time of centrifugation at three different NP contents – Black = 2.0x10^{11} NPs; Red = 2.8x10^{11} NPs; Blue = 3.6x10^{11} NPs. The RCF was 9391 *g* at 75 mM NaCl.

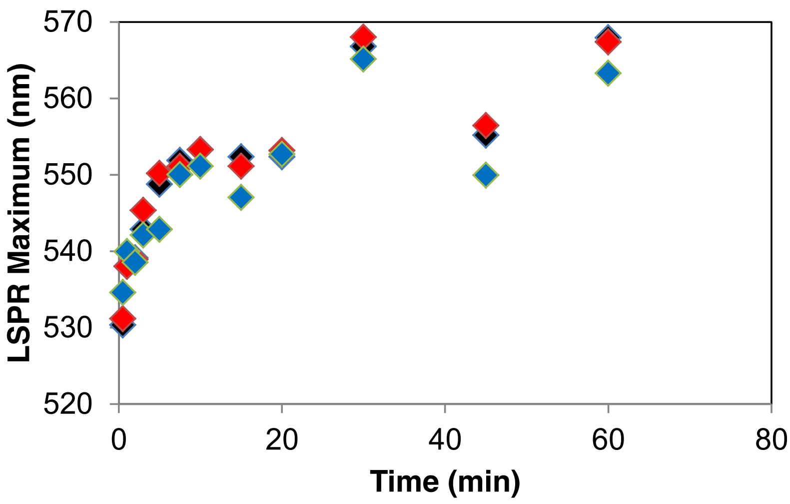

Figure 3.20 | LSPR maximum of NPs assembled at the interface as a function of time of centrifugation at three different NP contents – colours correspond to Figure 3.19.

The surprising aspect of the experiment is shown in Figure 3.20. Despite the 3 clearly different plateaus in terms of particles at the interface shown in Figure 3.19, the LSPR maxima are within experimental error of being identical, with no obvious trends as a function of NP concentration. If more particles are assembled at the interface at a given time, it should be expected that the separation should be reduced, thereby further red-shifting the LSPR. These results were initially interpreted as contradictory to the hypothesis that the inter-particle separation or the number of NPs assembled at the interface were indeed being controlled by this study.

As was subsequently discovered, the error in analysing these results was labelling the y-axis of Figure 3.19 as "particles at the interface" – this is an indirect measurement as what is actually being measured through UV-Vis of the bulk solution is the number of "particles missing" with respect to the initial concentration. This mistake arose from the assumption that all the particles that are not in the bulk are at the LLI (provided no aggregation or adsorption to the tube walls occurs). In reality, a more interesting mechanism can occur when the NP concentration exceeds a certain threshold – a small black spec can be seen to form at the bottom of the DCE. This spec is in actual fact an aqueous solution whose NP concentration is large enough to physically alter the density of water to levels exceeding that of DCE. At the conditions in Figure 3.19/3.20, this phenomenon was not immediately obvious (as the volumes of the high density aqueous solutions are extremely small), but if a substantially larger concentration of NPs are initially used, this effect becomes more apparent (Figure 3.21).

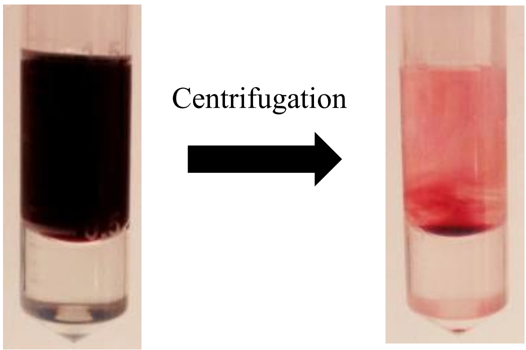

Figure 3.21 | When a concentrated NP solution is centrifuged in the presence of DCE, a black droplet containing the majority of the available NPs can be seen at the bottom of the organic phase.

The significance of this effect was not immediately apparent; however Chapter 4 is based on a study of this droplet. In terms of anomalous results of Figure 3.19 and 3.20, the reason for the discrepancy between number of particles missing and LSPR maximum, was because 2 competing process are causing the loss – adsorption to and ‘piercing’ of the interface.

3.4 Conclusions

This chapter has demonstrated novel optical properties of NPs adsorbed to the LLI. By controlling the inter-particle separation through the ionic strength of the aqueous phase, a controlled shifting of the LSPR maximum was observed, which subsequently allowed for the estimation of the separation. Importantly, centrifugation has been demonstrated as a versatile tool for studying NP adsorption to the LLI and transmission spectroscopy has been shown to be a fast and simple way to extract spectral informative spectral properties.

The significance of this work to the field lies primarily in the simple and versatile nature of the techniques demonstrated in studying NP adsorption to the LLI. Additionally, this work highlights that whilst controlling the inter-particle separation at the LLI is a challenging parameter to image directly, it is a relatively straightforward parameter to control – either through surface charge, interfacial area or the ionic strength of the aqueous solution.

Furthermore, NPs with tuneable separations can yield novel optical properties, when compared to 2D aggregated assemblies. It is hoped therefore that this work will both enable researchers in the field to gain a better understanding of NPs at the LLI as well as promote controlled self-assembly of more diverse macroscopic structures with novel properties.

3.5 References

1. Turek, V. A.; Cecchini, M. P.; Paget, J.; Kucernak, A. R.; Kornyshev, A. A.; Edel, J. B. *ACS Nano* **2012,** 6, (9), 7789-7799.
2. Nieminen, J. J.; Hatay, I.; Ge, P.; Mendez, M. A.; Murtomaki, L.; Girault, H. H. *Chemical Communications* **2011,** 47, (19).
3. Crossley, S.; Faria, J.; Shen, M.; Resasco, D. E. *Science* **2010,** 327, (5961), 68-72.
4. Boker, A.; He, J.; Emrick, T.; Russell, T. P. *Soft Matter* **2007,** 3, (10).
5. Edel, J. B.; Kornyshev, A. A.; Urbakh, M. *ACS Nano* **2013,** 7, (11), 9526-9532.
6. Flatté, M. E.; Kornyshev, A. A.; Urbakh, M. *The Journal of Physical Chemistry C* **2010,** 114, (4), 1735-1747.
7. Lin, Y.; Böker, A.; Skaff, H.; Cookson, D.; Dinsmore, A. D.; Emrick, T.; Russell, T. P. *Langmuir* **2004,** 21, (1), 191-194.
8. Blättler, T. M.; et al. *Nanotechnology* **2008,** 19, (7), 075301.
9. Whitesides, G. M.; Grzybowski, B. *Science* **2002,** 295, (5564), 2418-2421.
10. Seeman, N. C. *Annu Rev Biochem* **2010,** 79, 65-87.
11. Tessier, P. M.; Ong, K.; Christesen, S. D.; Lenhoff, A. M.; Kaler, E. W.; Velev, O. D. In *Assembly of gold nanostructured films templated by colloidal crystals and use in surface-enhanced Raman spectroscopy*, 2002; pp 53-64.
12. Muševič, I.; Škarabot, M.; Tkalec, U.; Ravnik, M.; Žumer, S. *Science* **2006,** 313, (5789), 954-958.
13. Hojeij, M.; Younan, N.; Ribeaucourt, L.; Girault, H. H. *Nanoscale* **2010,** 2, (9), 1665-1669.
14. Fang, P.-P.; Chen, S.; Deng, H.; Scanlon, M. D.; Gumy, F.; Lee, H. J.; Momotenko, D.; Amstutz, V.; Cortés-Salazar, F.; Pereira, C. M.; Yang, Z.; Girault, H. H. *ACS Nano* **2013,** 7, (10), 9241-9248.
15. Grzelczak, M.; Liz-Marzán, L. M. *Langmuir* **2013**.
16. Yang, J. K. W.; Lau, C. L., C. Y.; Duan, H. G.; Wang, F. K.; He, C. B.; Low, H. Y. *Langmuir* **2011,** 27, (7), 3355-3360.
17. Yan, H.; Park, S. H.; Finkelstein, G.; Reif, J. H.; LaBean, T. H. *Science* **2003,** 301, (5641), 1882-1884.
18. Cheng, J. Y.; Ross, C. A.; Smith, H. I.; Thomas, E. L. *Advanced Materials* **2006,** 18, (19), 2505-2521.
19. Parak, W. J.; Gerion, D.; Zanchet, D.; Woerz, A. S.; Pellegrino, T.; Micheel, C.; Williams, S. C.; Seitz, M.; Bruehl, R. E.; Bryant, Z.; Bustamante, C.; Bertozzi, C. R.; Alivisatos, A. P. *Chemistry of Materials* **2002,** 14, (5), 2113-2119.
20. Jiang, L.; Zou, C.; Zhang, Z.; Sun, Y.; Jiang, Y.; Leow, W.; Liedberg, B.; Li, S.; Chen, X. *Small* **2013**, n/a-n/a.
21. Hashimoto, A.; Suenaga, K.; Gloter, A.; Urita, K.; Iijima, S. *Nature* **2004,** 430, (7002), 870-873.
22. Diebel, J.; Löwe, H.; Samorí, P.; Rabe, J. P. *Appl Phys A* **2001,** 73, (3), 273-279.
23. Bresme, F.; Chacón, E.; Tarazona, P.; Tay, K. *Physical Review Letters* **2008,** 101, (5), 056102.
24. Yogev, D.; Efrima, S. *The Journal of Physical Chemistry* **1988,** 92, (20), 5754-5760.
25. Binks, B. P.; Lumsdon, S. O. *Langmuir* **2000,** 16, (23), 8622-8631.
26. Li, Y.-J.; Huang, W.-J.; Sun, S.-G. *Angewandte Chemie International Edition* **2006,** 45, (16), 2537-2539.
27. Isa, L.; Lucas, F.; Wepf, R.; Reimhult, E. *Nat Commun* **2011,** 2, 438.

28. Galletto, P.; Girault, H. H.; Gomis-Bas, C.; Schiffrin, D. J.; Antoine, R.; Broyer, M.; Brevet, P. F. *Journal of Physics: Condensed Matter* **2007,** 19, (37), 375108.
29. Younan, N.; Hojeij, M.; Ribeaucourt, L.; Girault, H. H. *Electrochemistry Communications* **2010,** 12, (7), 912-915.
30. Kutuzov, S.; He, J.; Tangirala, R.; Emrick, T.; Russell, T. P.; Boker, A. *Physical Chemistry Chemical Physics* **2007,** 9, (48), 6351-6358.
31. Wang, J.; Jiang, Z.; Lin, X. M.; Sprung, M.; Narayanan, S. *Nano Letters* **2010,** 10, (3), 799-803.
32. Park, Y.-K.; Yoo, S.-H.; Park, S. *Langmuir* **2007,** 23, (21), 10505-10510.
33. Duan, H.; Wang, D.; Sobal, N. S.; Giersig, M.; Kurth, D. G.; Möhwald, H. *Nano Letters* **2005,** 5, (5), 949-952.
34. Abbott, N. L.; Bai, Y. Q. *Langmuir* **2011,** 27, (10), 5719-5738.
35. Sonnichsen, C.; Reinhard, B. M.; Liphardt, J.; Alivisatos, A. P., A molecular ruler based on plasmon coupling of single gold and silver nanoparticles. 2005.
36. Yang, L.; Wang, H.; Yan, B.; Reinhard, B. r. M. *The Journal of Physical Chemistry C* **2010,** 114, (11), 4901-4908.
37. Ben, X.; Park, H. S. *The Journal of Physical Chemistry C* **2011,** 115, (32), 15915-15926.
38. Reincke, F.; Kegel, W. K.; Zhang, H.; Nolte, M.; Wang, D.; Vanmaekelbergh, D.; Mohwald, H. *Physical Chemistry Chemical Physics* **2006,** 8, (33), 3828-3835.
39. Du, K.; Glogowski, E.; Emrick, T.; Russell, T. P.; Dinsmore, A. D. *Langmuir* **2010,** 26, (15), 12518-12522.
40. McGorty, R.; Fung, J.; Kaz, D.; Manoharan, V. N. *Mater Today* **2010,** 13, (6), 34-42.
41. Kinnan, M. K.; Chumanov, G. *The Journal of Physical Chemistry C* **2010,** 114, (16), 7496-7501.
42. Bresme, F.; Oettel, M. *Journal of Physics: Condensed Matter* **2007,** 19, (41), 413101.
43. Kornyshev, A. A.; Marinescu, M.; Paget, J.; Urbakh, M. *Physical Chemistry Chemical Physics* **2012,** 14, (6).

Chapter 4: Ultra-Concentration of Nanoparticles

4.1 Abstract

Chapter 3 demonstrated control of the 2D inter-particle separation facilitated by the NaCl concentration and centrifugation. An investigation of the NP concentration dependence on adsorption to the LLI lead to a NP-rich droplet being observed at the bottom of the DCE at higher initial NP concentrations of the bulk aqueous phase. As was subsequently discovered, the droplet actually contains surprisingly high NP concentration. Though serendipitous, it follows nicely that NaCl concentration together with centrifugation and the liquid-liquid interface are actually able achieve controlled 3D inter-particle separations, which these droplets demonstrate. The high NP concentrations of these solutions lead to some remarkably altered physical properties of the solution – for example the highest reported density of an aqueous solution at room temperature is easily achievable, while the solution itself can contain ≈20% volume gold, with an optical density at 525 nm of up to 74,000 absorbance units. Due to the high NP concentration in these droplets with respect to smaller dissolved chemical species, it is demonstrated that the droplet formation mechanism has applications in NP purification, with a 10-15 minute step exceeding 99.9% purification efficiency. Finally, as with chemical purification, the encapsulation of the NPs is highly dependent on size (and therefore the sedimentation coefficient), it is also demonstrated that this can be used to separate NPs depending on size.

Please note: this work was published in ACS Nano and this chapter draws heavily from the publication[1].

4.2 Introduction

The anomalous results of Figures 3.19 and 3.20 in chapter 3, lead to a surprising observation – a high density aqueous droplet containing a large portion of the available NPs was seen to form at the bottom of the DCE following centrifugation. It follows that the NP content must be sufficiently high in such a solution to physically alter the properties of water. Though serendipitous, this phenomenon has extremely important consequences in the field of 'nanofluids'[2, 3]. Extensive studies have been conducted that demonstrate that solutions with high NP contents are able to enhance the properties of the carrier phase[4, 5]. The vast majority of research into nanofluids has focused on the effect of NP content on thermal transport[6]. This is an important area of research that aims to keep up with increasing miniaturization of electronic components and their heat dissipation demands. The thermal conductivities that nanofluids exhibit is in fact anomalous, with no current theoretical model being able to accurately predict these properties[7-9]. One of the main challenges with nanofluids is achieving a homogenous dispersion[10] – a task that is made all the more difficult by aggregation of NPs at high concentrations.

When taking the previously demonstrated NP contents into account, the seemingly trivial high density solution displays some remarkable properties. Nanofluids composed of gold NPs have been limited to below 2% (by volume)[11], it is probable that solutions with higher content have not been demonstrated due to either aggregation or an insufficient solubility of the NPs in the solvents – in this chapter, nanofluids containing 20% (by volume) gold are demonstrated, however it should be stressed that this value is highly unlikely to be limiting. The natural question about such solutions is whether or not aggregation occurs and whether the NPs are homogenously distributed in the solution. The surprising answer is that not only do the particles remain separated from their neighbours, but that this separation can be controlled. The inter-particle separation, similarly to chapter 3 is shown to be tuneable by the NaCl concentration of the solution during centrifugation, however unlike the 2D control in chapter 3, the separation in this chapter is controlled in 3 dimensions. This controlled self-assembly is made all the more remarkable by the fact that it is un-templated, macroscopic, requires only centrifugation to achieve and despite showing a crystalline diffraction pattern the product is a liquid. The resulting solution is therefore both a colloidal crystal[12, 13] and a liquid crystal, however to the best of the author's knowledge, no macroscopic 'crystal' has previously been demonstrated that combines the two types of materials[14].

The fundamental property of this solution that enables its formation is an increased density compared to water. Logically, the threshold density of the solution must not only exceed the 1.253 g/cm^3 of DCE, but also make the formation of the additional interfacial area more energetically favourable, though the exact minimum threshold has yet to be determined. The more interesting study is what the maximal value that the density of this solution can display. As mentioned above, the NaCl concentration is able to tune the screening length of the solution, thereby tuning the inter-particle separation and the effective volume that a single NP occupies in the solution. At higher NaCl concentrations, the fraction of the volume that the NPs occupy is therefore increased and with it, the density. At higher NaCl concentrations however, as chapter 3 demonstrated, more NPs will adsorb to the LLI which will reduce the interfacial tension. It was observed that at NaCl concentrations above ≈10 mM this has the effect of stabilizing the interfacial tension so much that a spherical droplet geometry was no longer preferable, which together with the low volumes of the solutions obtained made density measurements challenging. Nevertheless, at the limit of the tested densities, a value of 4.57 ± 0.26 g/cm^3 at room temperature was obtained. This value is itself remarkable when taking into account the fact that this is an aqueous solution (in other words the density of water is increased by ≈350% by the presence of the gold NPs), but more surprising is the fact that this density exceeds that of a saturated Clerici solution at room temperature (4.25 g/cm^3)[15]. The Clerici solution consists of 1:1 thallium formate and thallium malonate and having been first demonstrated in 1907[16] has remained one of the densest aqueous solutions known. It has found uses in mineralogy, however due to its toxic and corrosive nature, has been widely replaced with safer, though less dense alternatives[17, 18]. The fact that gold NPs are neither toxic nor corrosive, coupled with the fact that the room temperature density of the high density solution can exceed the Clerici solution makes it beneficial for mineralogical density determination. This is especially true when taking into account the fact that the solutions tested here were not optimized for the highest possible density – for example replacement of gold with a denser element such as Iriduim or Osmium, while keeping all other variables constant would lead to densities in excess of 5.1 g/cm^3, while using larger NPs or a shorter functionality than MDDA would increase this even further. While 'record-breakingly' high density solutions may have relatively limited direct applications, the ability to engineer the physical properties of liquids to previously unavailable values is perhaps the most intriguing prospect of this research. In addition to high densities, these solutions are shown to possess: surface areas of 103 m^2 per mL of solution; an optical density at 525 nm of 7.4x10^4; 3.7 grams of gold per mL of solution.

An additional and direct practical application of the droplet formation mechanism, is purification of NPs. Many of the applications that nanoparticles have require precise control over the chemical compositions of the solution. For example quantum dots have applications as optical surgical aids[19], however cadmium is commonly used for the quantum dot core and is highly toxic – the ZnS shell limits the toxicity of core, but any dissolved cadmium that is not used up during core synthesis must be purified. Another example relates to NPs with a non-spherical morphology – there have been countless types of particles[20-24] that have been demonstrated, many of which are substantially more suited to specific applications that their spherical counterparts, while remaining relatively simple to synthesise. Nevertheless, spherical gold/silver particles remain the most widely used in the literature. The main reasons for this is that non-spherical NP syntheses tend to use surfactants such as CTAB, as well as the formation of by-product particles that do not have the desired morphology, however both of these types of contaminants are challenging to remove[25-30].

It is expected that in order to be encapsulated in the droplet, the material must possess a large enough sedimentation coefficient – the large difference in size between NPs and chemical species means that NPs would be predominantly captured in the droplet. Given even a constant concentration of chemical 'contaminants' between the initial aqueous phase and the droplet, the simple fact that the concentration of NPs in these droplets can be easily increased $1x10^4$ fold means that once diluted to initial NP concentrations an extremely efficient purification of these contaminants is achieved. Additionally, it is shown that the same difference in the sedimentation coefficients between NPs of differing sizes allows for their size separation.

4.3.1 Results and discussion

It was soon realized that the black droplet contained NPs that had sedimented from the main aqueous phase – this was evidenced by the fact that contact with water promoted re-dispersion of the NPs, with little signs of irreversible aggregation. Even citrate stabilized particles could form the droplet and be re-dispersed into water again. A shift in the re-dispersed NPs' LSPR was occasionally observed through UV-Vis, especially with citrate stabilized particles or MDDA particles in which the droplet was left refrigerated overnight, however typically, the spectra between re-dispersed and as made particles were qualitatively identical – as shown in Figure 4.1.

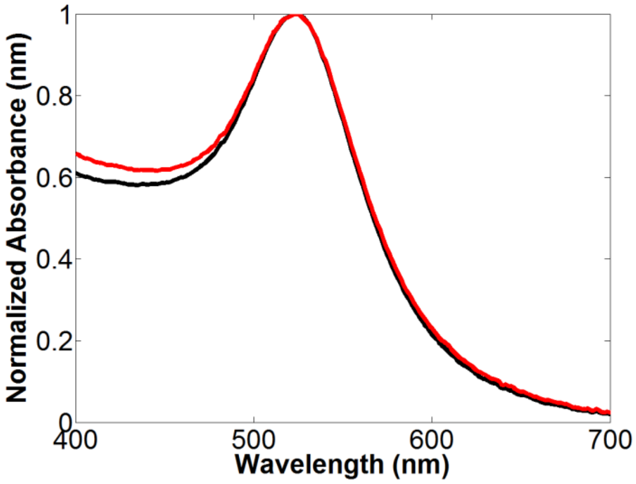

Figure 4.1 | Normalized absorbance spectra of as-made MDDA functionalized particles (red) and those re-dispersed from the droplet (black). Reprinted with permission from Turek *et al*[1]. Copyright (2013) American Chemical Society.

Due to the very low volumes of the droplets, it was not immediately obvious that they were in actual fact aqueous solutions – it was initially believed that these droplets consisted of reversibly agglomerated NPs that had sufficient energy to overcome the energy barrier for phase transfer into the DCE. Upon combination of approximately 60 droplets (Figure 4.2 A) and studying their behaviour however, it became apparent that this was not the case and that the NPs remained suspended in water – this was evidenced by the fact that it was possible to pipette out the solution (Figure 4.2 B).

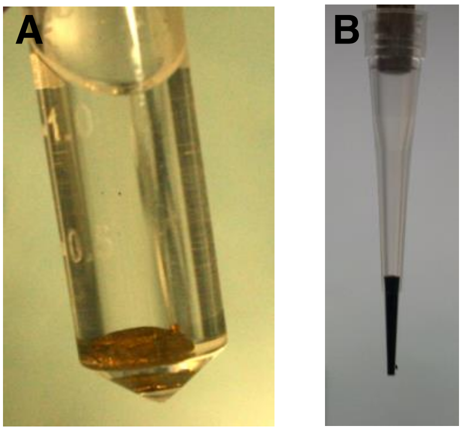

Figure 4.2 | Photographs of the high density nanoparticle solution. Combination of approximately 60 droplets (A) lead to more manageable volumes. It became apparent that in actual fact, the NPs remained dispersed in solution, as it could be pipetted out (B).

4.3.2 NP concentration dependence

It was observed that the droplet isn't formed at low NP concentrations, while at higher concentrations the droplets not only became larger but also contained a larger proportion of the available NPs in the initial solution. In order to characterize this effect, the content of the residual NPs in the supernatant was compared to the content of the droplets as a function of initial NP concentration. The ionic strength was kept at as-made conditions – the conductivity of the solution was 217 μS/cm or 2.5 mM NaCl equivalent ('equivalent' is used as NaCl is not the only species that contributes to this conductivity, citrate ions, as well as side-products of the citrate reduction of gold were also present in the solution). Figure 4.3 clearly demonstrates that while the number of particles confined to the droplet has a strong dependency on the available particles, the residual NPs in the supernatant follows a much weaker dependence (in fact, the number of residual particles was almost constant across the concentration ranges tested).

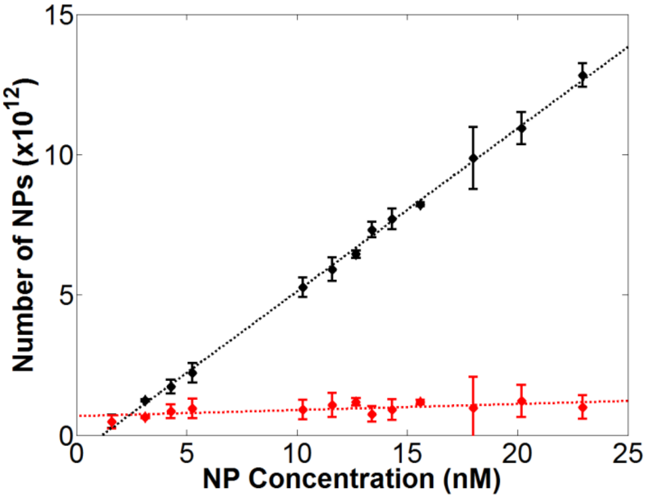

Figure 4.3 | Number of NPs as a function of NP concentration – red denotes number of residual NPs left over in the supernatant; while black represent the number of particles confined to the droplet. Experimental conditions: 1 mL aqueous NP solution at 2.5 mM NaCl equivalent; 0.5 mL DCE; centrifuged at 20,231 *g* for 10 minutes. Reprinted with permission from Turek *et al*[1]. Copyright (2013) American Chemical Society.

The almost constant number of residual NPs in the supernatant as a function of concentration range seems to represents a threshold value below which no droplet is formed. In reality, substantially larger concentrations are needed before the droplet becomes large enough to be visible (the volume of the droplet is dependent on the number of NPs confined and the ionic strength of the solution). In view of this, it is hypothesised that the general mechanism for the droplet formation is as shown in Figure 4.4.

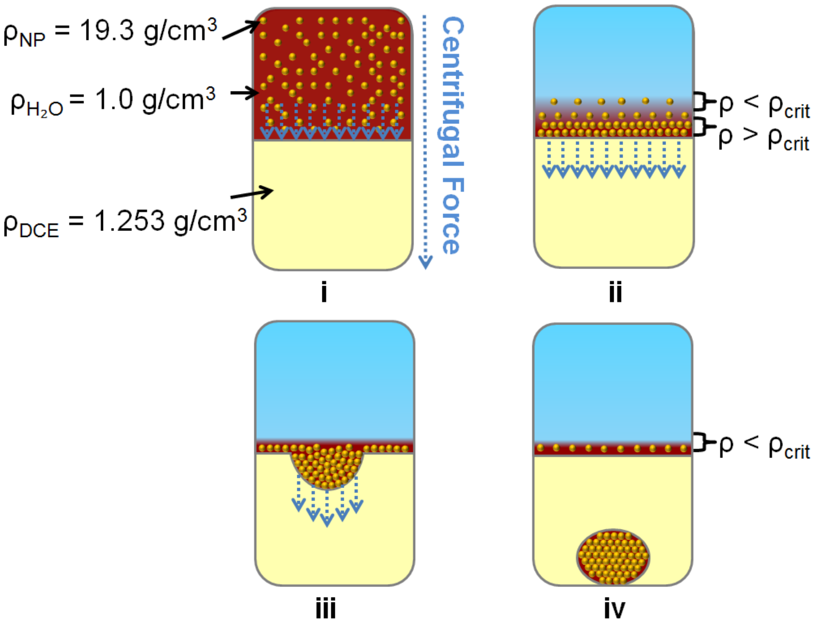

Figure 4.4 | Schematic of hypothesised mechanism for droplet formation. In the presence of a more dense organic phase, NPs in the aqueous phase are driven to the interface (i). Provided that the ionic strength is low enough to prevent adsorption, while the number of particles is high enough, a NP-rich film is believed to form close to the LLI (ii). If the density of aqueous phase reaches a critical threshold value, fluctuations may induce deformations of the interface (iii). These deformations will then break off from the main aqueous phase, sediment and finally merge as a high density solution at the bottom of the DCE (iv). Reprinted with permission from Turek *et al*[1]. Copyright (2013) American Chemical Society.

In the presence of an organic phase with a density greater than 1 g/cm^3, aqueous NPs are initially driven to the interface (Figure 4.4 i). Provided that there is a sufficient energy barrier to prevent phase-transfer of NPs, a layer close to the interface reaches a critical NP concentration (Figure 4.4 ii) at which the effective density of the aqueous phase exceeds a ‘critical’ density (it is probable that for DCE, the critical density needs to be somewhat higher than 1.253 g/cm^3 as the increased density would also need to energetically compensate for the formation of additional interfacial area). At this point, it is likely that fluctuations of the interface will arise, leading to a deformation of the interface that would collect the high density aqueous phase (Figure 4.4 iii). These fluctuations of the interface will ultimately break off from the main aqueous phase, yielding high density droplets that will sediment and merge at the bottom of the organic phase. It should be once again mentioned (as was discussed in Figure 3.1) that the formation of the film is unlikely to be a homogenous process across the entire interface – due to the volumes used it is believed that ≈60% of the available NPs in the solution will converge at a single point on the interface. This convergence may assist the formation of the droplets.

4.3.3 Density

It follows naturally, that in light of these aqueous solutions remaining at the bottom of the DCE, that they must possess a greater density than 1.253 g/cm^3. This fact in itself is quite remarkable as this process effectively raises the NP content of these solutions to levels where the physical properties of water become substantially different to standard conditions. It was therefore decided to measure the density of the solution at 1 mM NaCl equivalent (the as-made NPs were concentrated approximately 10-20 fold by conventional centrifugation and diluted with DI water). Lacking any sophisticated equipment for determining the density of very low volume solutions, it was decided that a simple 'measure the volume and measure the weight' technique would be used. Pipetting a set volume was not deemed possible as substantial errors are introduced with high density liquids in standard air pipettes. Instead, the volume in 10 µL pipette tip was calibrated as a function of the height of the top meniscus with DI water, followed by drawing in an arbitrary volume of the high density solution into the pipette tip. The volume that was actually pipetted was estimated by the calibration with water, while weighing the pipette tip with and without the solution to determine its mass. The resulting density was determined to be 2.08 ± 0.01 g/cm^3. This again is quite remarkable as the NP content of this solution more than doubled the density of water. Perhaps more interesting however are some of the implications of this value. Assuming that only NPs and water is present in the solution (*i.e.* a negligible contribution to the density from other dissolved species), this implies that the NP concentration of this solution is 2.75 x 10^{16} NPs per mL or 45.7 µM. Interestingly, if it is assumed that the NaCl equivalent concentration in this droplet remains ≈1 mM (though this is of course highly unlikely as the high concentration of NPs and their charged functionalities will increase the salt concentration) and that the MDDA functionality provides a ≈1.5 nm shell around the particles, then the NPs together with their screening lengths will occupy approximately 80% of the volume of the solution. Though of course the assumptions made when calculating this percentage are highly likely to overestimate this value, the fact that a very large portion of the solution 'feels' the NPs' charge suggests that the concentrations obtained with this method are limited by the ionic strength of the solution. To test this hypothesis, it was decided to study the effect of density of solution as a function of the equivalent NaCl concentration. Combining dozens of droplets enough to be able to accurately pipette the resulting solutions was deemed too time consuming to use as a density measurement method for a full data set, therefore a modified procedure was used to determine the volumes, as shown schematically in Figure 4.5. The droplets were placed on a pre-weighed coverslip of 140 µm thickness, the DCE that was transferred along with the droplet was allowed to evaporate off and the weight of the droplet on the coverslip was recorded. The coverslip was then placed between 2 other coverslips, followed 2 additional coverslips on top to bridge the 2 gaps and provide a fixed height, a final coverslip was then placed on the 3rd level to sandwich the droplet. At this point a photograph was taken from the top of the assembly and ImageJ was used to determine the area of the solution in contact with the slides. It was assumed that the sandwiched droplet was cylindrical in shape (in other words that the contact angles with the glass and the solution were 90° at all points) and that the area could simply be multiplied by the height (*i.e.* 140 µm) to obtain an estimate of the volume.

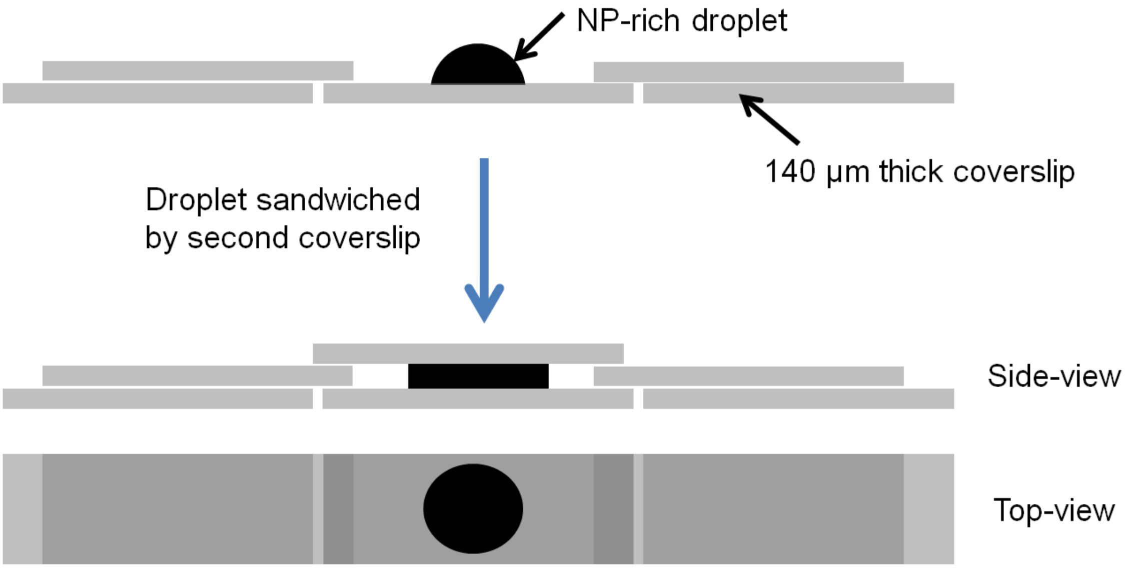

Figure 4.5 | Schematic of the method used to estimate the volume of the droplets. Reprinted with permission from Turek *et al*[1]. Copyright (2013) American Chemical Society.

The crudeness of this approach, meant that errors were more significant than with the pipette tip method, however a clear trend was observed in the densities of the solutions as a function of NaCl equivalent concentration (Figure 4.6).

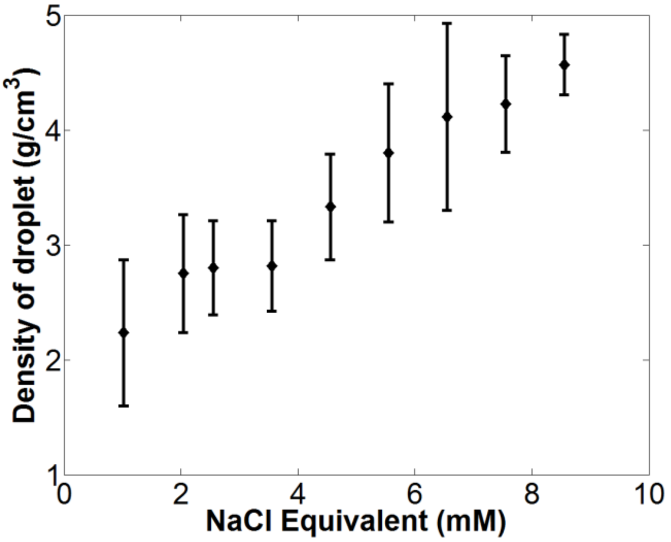

Figure 4.6 | Density of the resulting NP-rich solutions as a function of NaCl equivalent concentration. Reprinted with permission from Turek *et al*[1]. Copyright (2013) American Chemical Society.

As the NaCl equivalent was varied between 1.0-9.5 mM the densities increased from 2.24 ± 0.64 to 4.57 ± 0.26 g/cm^3. It is worth noting that at 4.57 ± 0.26 g/cm^3, the resulting solution is not only the most concentrated gold nanoparticle solution reported, but also shows the highest room temperature density of any aqueous solution – the Clerici solution is widely accredited to be the densest aqueous solution and when saturated this has a room temperature density of 4.25 g/cm^3. While interest in high density solutions by themselves is relatively low, the important fact about this finding is that the NPs are able to drastically alter the physical properties of water. Furthermore, the densities demonstrated in Figure 4.6 are not the limit with this method – above 9.5 mM NaCl equivalent it became challenging to measure the volume with the above method due to the fact that the volume of the droplet shrunk to levels where the top coverslip was unable to provide contact with the solution as well as the fact that NP adsorption to the LLI at higher NaCl concentrations lead to non-spherical droplets. Nevertheless droplets could be successfully made up to and including 50 mM (though at NaCl equivalent concentrations above 20 mM these droplets, if redispersed in water, showed a significant red-shift in the LSPR).

The density measurements of the droplets made at NaCl equivalent concentrations of 9.5 mM imply some fascinating other physical properties of these solutions: based on the density, 1 mL of this solution would contain 3.7 grams of gold or ≈ 20% gold by volume; converted into NPs, this would equate to $9.1\text{x}10^{16}$ particles/mL; if the MDDA functionality is viewed as the physical surface of the NPs (and once again assumed to be 1.5 nm long), then this implies an effective surface area of 103 m^2/mL (to put this value into perspective, an Olympic swimming pool (≈2500 m^3) filled with such a solution would contain a larger surface area ($2.58\text{x}10^5$ km^2) than the UK ($2.42\text{x}10^5$ km^2)); assuming an extinction coefficient[31] of $4.91\text{x}10^8$ $M^{-1}cm^{-1}$ (and no shift from plasmon coupling between NPs), then the optical density at 525 nm is expected to exceed $7.4\text{x}10^4$ (again for some perspective, if the solution thickness would be reduced to 100 nm, ≈52% of light at 525 nm would be absorbed).

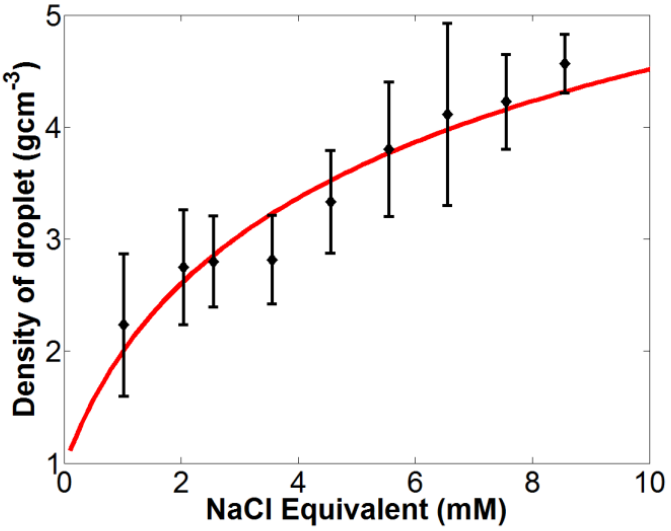

Figure 4.7 | Same plot as with Figure 4.6, however the red line is an estimate of the maximum density of the solution if the NPs, functionality and Debye screening length (calculated from the initial pre-centrifuged solution) are assumed to be hard, non-overlapping spheres. Adapted with permission from Turek *et al*[1]. Copyright (2013) American Chemical Society.

Though perhaps coincidental rather than insightful, if the gold core, MDDA shell and screening length of the initial solution (*i.e.* before centrifugation) are assumed to be a hard sphere (in other words the screening lengths do not overlap), then the estimated 'maximum' density at each NaCl equivalent concentration agrees surprisingly well with the experimental results of Figure 4.6 (shown in Figure 4.7). It is of course difficult to justify that the NPs and the screening length would act as a hard sphere or that the ionic strength will not change in the droplet with respect to the initial solution. Nevertheless, the fit and in fact the dependency of the resulting density of the solution on the ionic strength suggests that, similar to chapter 2, it is possible to control the inter-particle separation.

4.3.4 Controlled 3D inter-particle separation

The possibility of control of the inter-particle separation in this solution was decided to be tested through a similar technique as in chapter 3. Transmission of broadband light through the high density solution to obtain the absorbance was viewed as a logical method to extract spectral information of the LSPR. A key limitation of this method was the aforementioned extremely high absorbance of the resulting solutions. Figure 4.8 demonstrates schematically the technique that was employed in achieving resolvable transmitted signals.

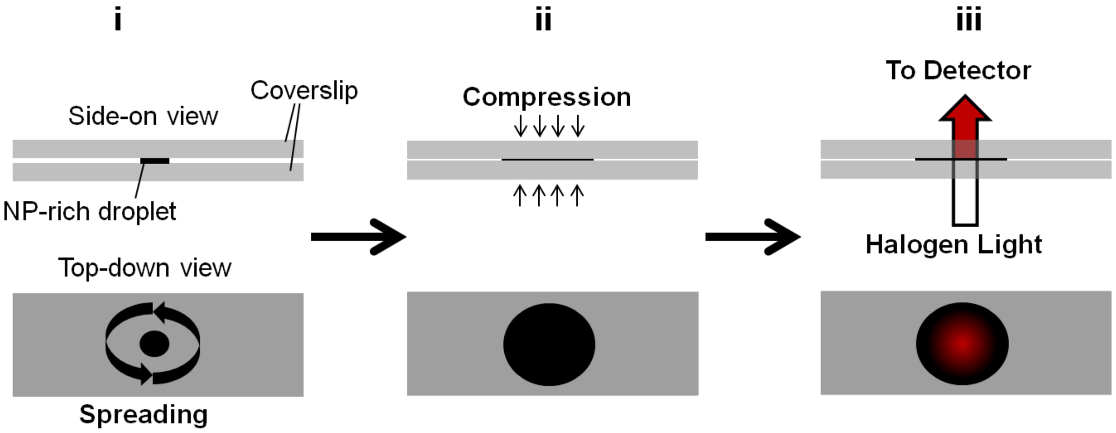

Figure 4.8 | Schematic of treatment of the high density solutions to achieve transmission measurements. The high density droplets were pipetted onto a glass coverslip and the residual DCE was allowed to evaporate, followed by sandwiching with a second coverslip. The solution was then spread to increase the contact area with the glass (i). This was usually insufficient to allow transmission of light, therefore the coverslips were manually compressed in the centre of the solution (ii). Following these procedures a dark red colouration could be seen in the centre of the solution, through which the halogen light was transmitted (iii). Reprinted with permission from Turek *et al*[1]. Copyright (2013) American Chemical Society.

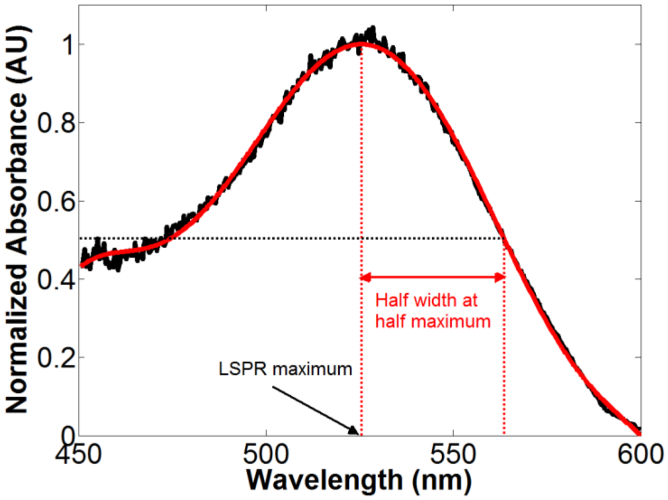

Figure 4.9 | The absorbance spectra of the high density solutions (black) had a poor signal-to-noise ratio, therefore a 6th order polynomial was fitted to the data – the LSPR maximum was then extracted from the polynomial fit (HWHM, as in chapter 3, were extracted from the red-shifted shoulder of the peaks). Reprinted with permission from Turek *et al*[1]. Copyright (2013) American Chemical Society.

The droplets were initially pipetted onto a coverslip and any residual DCE that was transferred over was allowed to evaporate. A second coverslip was then placed on top to sandwich the droplet between them. The coverslips were then rotated with respect to each other to spread the solution over a larger area (Figure 4.8 A). This was usually insufficient to transmit light therefore the slides were then manually compressed in the centre of the solution (Figure 4.8 B), after which a dark red coloration could be seen in the centre of the solution, through which the halogen light was directed (Figure 4.8 C) – note, that for solutions above 8.5 mM NaCl equivalent, it was not possible to obtain resolvable spectra even with this method. Despite these steps, the resulting absorbance spectra had a poor signal-to-noise ratio (due to the fraction of light that was transmitted being small). A 6th order polynomial was therefore fitted to the spectra in order to yield a smoothed spectrum (Figure 4.9), from which the LSPR maximum and HWHM were extracted.

As to be expected if the inter-particle separation was being controlled through the NaCl concentration, the spectra showed a red-shift at higher NaCl concentration (Figure 4.10). It should be noted however that the resulting shifts were small relative to those obtained in Chapter 3. There was also no noticeable dependence of the NaCl on the HWHM (Figure 4.11).

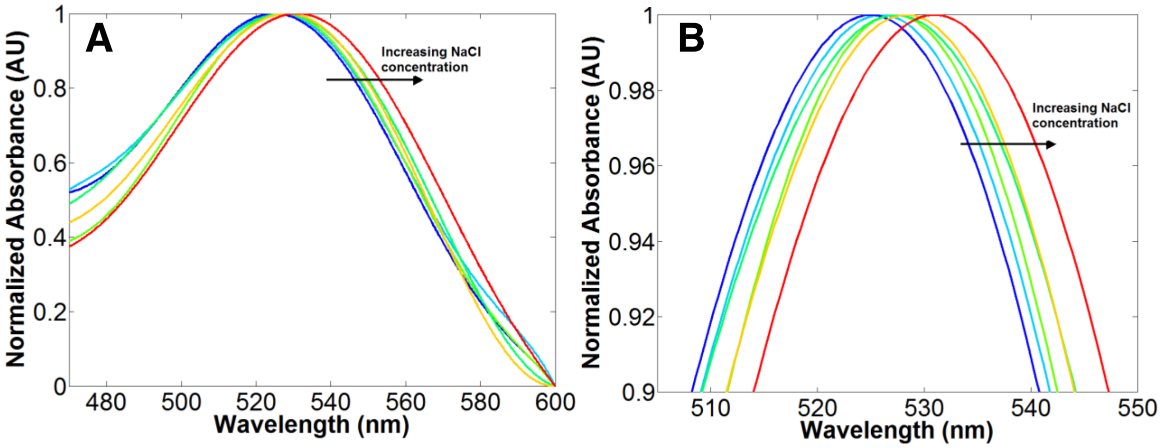

Figure 4.10 l Normalized fitted absorbance spectra of the high density solutions at different NaCl concentrations. As expected of controlled inter-particle separation, a shift is observed in the spectra, however the magnitude of this shift is much smaller than those demonstrated in Chapter 3, B therefore shows a close-up of the peak. Reprinted with permission from Turek *et al*[1]. Copyright (2013) American Chemical Society.

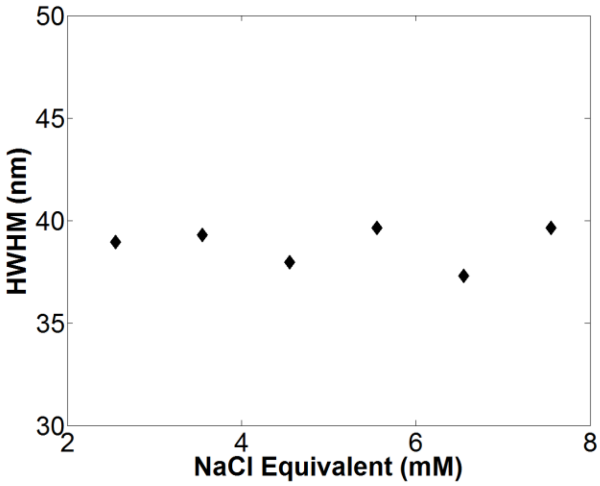

Figure 4.11 l HWHM of the fitted LSPR of the high density solutions as a function of NaCl equivalent concentrations. Reprinted with permission from Turek *et al*[1]. Copyright (2013) American Chemical Society.

By assuming that ‘the particles will be spaced as far away from each other as possible’, it was possible to estimate the average inter-particle separations from the density measurements. Based on this, Figure 4.12 shows the experimental results of inter-particle separation against

LSPR maximum compared with simulations of particles in a HCP lattice with tuned separations.

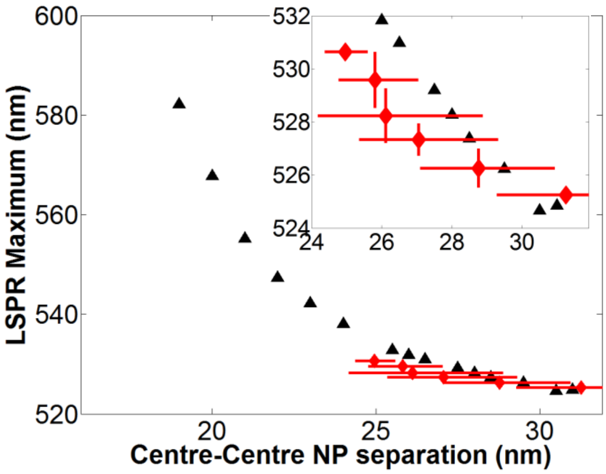

Figure 4.12 | LSPR maximum as a function of inter-particle separation of the high density solutions. Red are experimental results, while simulations are in black. Reprinted with permission from Turek *et al*[1]. Copyright (2013) American Chemical Society.

It is worth noting that experiments and simulations do not precisely agree with each other; however the range over which the experiment extends is quite small (25-30 nm). It is likely that using this technique it should be possible to control the separation over substantially larger distances, however if the separations are made larger no shift would be expected (the particles would be too far from each other to couple – in fact the data point at 31 nm separation already has a comparable maximum to λ_0), while alternative optical measurements would be need to extract spectral information at shorter separations.

The fact that control of the separation can be achieved, begs the question – is it merely the 'average' separation in a randomly orientated system, or is there order? If order exists, XRD should be able to verify this, allow extraction of the separations, as well as determine what type of lattice (if any) is present. The challenge with carrying out XRD on these solutions is that XRD is usually suited to probing order on a much smaller scale (the typical unit cell is 1-2 orders of magnitude smaller than the 25-30 nm centre-centre interparticle separation that the density results suggest). Due to the use of reciprocal space, larger structures would produce a smaller diffraction angle (Q) – the use of the beam stop to prevent saturation of the detector from the main beam means that much larger sample-to-detector path lengths need to be in place to resolve the diffraction and prevent the beam stop from adsorbing the diffraction.

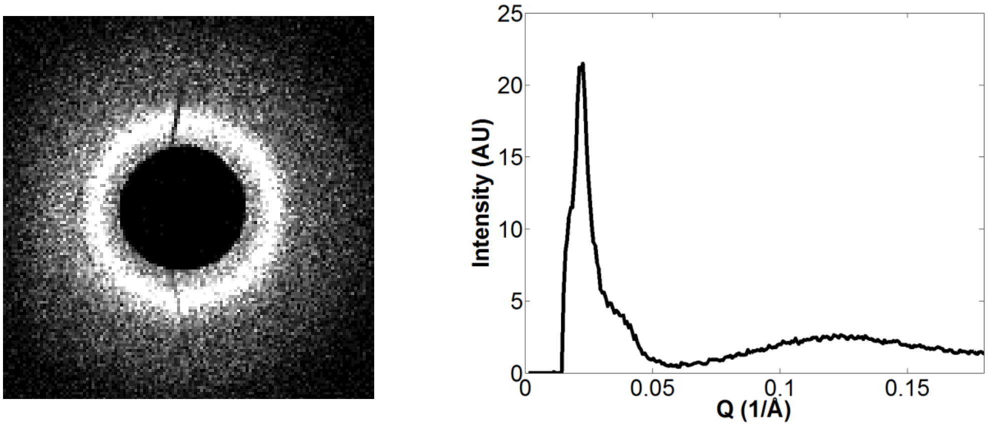

Figure 4.13 | Diffraction pattern of a high density solution prepared at 2.5 mM NaCl equivalent. Reprinted with permission from Turek *et al*[1]. Copyright (2013) American Chemical Society.

Available laboratory XRD setups proved to have an insufficient sample-detector path length, therefore facilities at Diamond light source were used instead. In order to prevent evaporation of the solutions, the droplets were allowed to remain surrounded by DCE and kept refrigirated. Figure 4.13 demonstrates the diffraction pattern obtained from a solution prepared at 2.5 mM NaCl equivalent. A peak can clearly be seen in the pattern. However, unlike truly crystalline materials, the absence of other peaks means that this corresponds to a positional correlation between the NPs – in other words there is an average separation between adjacent particles, but no long range order is present (an analogy would be marbles in a bag). Interestingly, this separation (from XRD) for the 2.5 mM NaCl equivalent sample was determined to be ≈29 nm (centre-centre), which is in excellent agreement of the 28.5 nm estimation from the density measurement.

Importantly, during a separate, repeat measurement, the same sample was measured at ESRF. For transportation safety reasons, it was not possible to leave the solution encapsulated by DCE, therefore the solution was extracted and but kept refrigerated. Unlike the measurement at Diamond however, this solution displayed clear Bragg peaks (Figure 4.14) – in other words long range order in the orientation of the NPs was observed, albeit with shorter (22 nm) inter-particle separation. The most feasible explanation for the discrepancy in the results between Figure 4.13 and 4.14 is the fact that some evaporation is likely to have occurred on route to ESRF. The reduced volume, together with an increase in the ionic strength, is believed to have induced shorter inter-particle separations as well as increasing the effective repulsive forces between the particles and hence promoting more ordered structures. The presence of both long range order and liquidity of these solutions means that they are effectively liquid colloidal crystals – however to the best of the author's knowledge, such systems have never been demonstrated on a macroscopic scale in 3D with gold nanoparticles. Additionally, unlike conventional crystals, the order in these solutions is promoted predominantly by repulsive electrostatic forces.

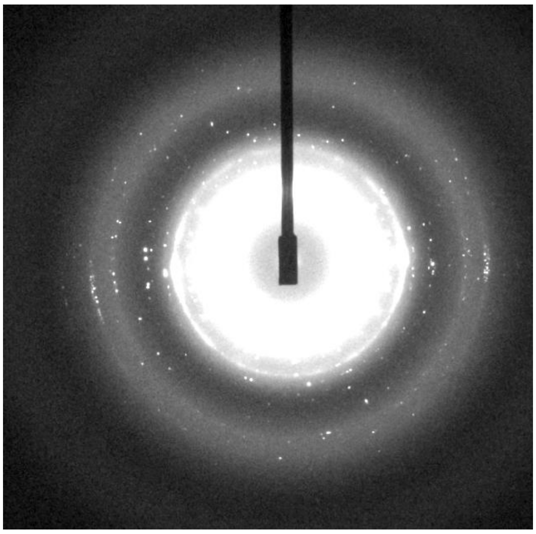

Figure 4.14 | XRD pattern obtained from the high density solution made at an initial NaCl concentration equivalent of 2.5 mM, that had subsequently been extracted from the DCE. It is probable that extraction of the droplet lead to some evaporation of the solution, which in turn lead to a more ordered NP arrangement, nevertheless despite the solution retaining its liquid properties, clear Bragg diffraction indicative of crystalline structure was seen. Image courtesy of Dr. Arwen I. I. Tyler and Prof. John Seddon.

4.3.5 Purification of chemical species

The fact that NPs are able to be concentrated by 3-4 orders of magnitude and then re-dispersed without notable signs of aggregation, naturally leads to applications in purification strategies. Conventional centrifugation is commonly used to purify particles of reaction side-products[32] or excess unattached functional groups, however the purification efficiency is usually limited by the amount of supernatant that can be removed and is typically irreproducible due to the manual separation process[28]. The present method is substantially more efficient in this respect – the volume of the pelleted NPs was usually below 0.3 µL (whereas using conventional centrifugation in 2 mL tubes, volumes of 50 µL are challenging to separate out), additionally, the separation of the supernatant and the pellet is inbuilt into the mechanism of this process, therefore manual errors are reduced and reproducibility substantially improved.

In order to test the purification efficiency, of conventional centrifugation and the method presented here, a dye (Rose Bengal) was introduced into the NP solution. One of the quickest and easiest ways to monitor the dye/NP content was through UV-Vis Spectroscopy. Figure 4.15 shows the normalized spectra of 'as-made' NPs, those contaminated with Rose Bengal (RB) and the 1st and 2nd conventional purification steps. It is clear that even after 2 purification steps (total purification efficiency of 99.5 ± 0.1 %), the normalized absorbance doesn't match the as-made particles. The absorbance is slightly higher to the red of the maximum, due to residual dye being present. A third purification is therefore needed for no detectable dye to be present in the solution through UV-Vis spectroscopy. A single purification step of the same solution as shown in red through the formation and re-dispersion of the high density solution, Figure 4.16, show that the normalized absorbance overlaps the as made NP solution almost perfectly. In fact the close fit of the two does not allow quantifiable purification efficiencies to be determined – but suggests that it is in excess of 99.9%.

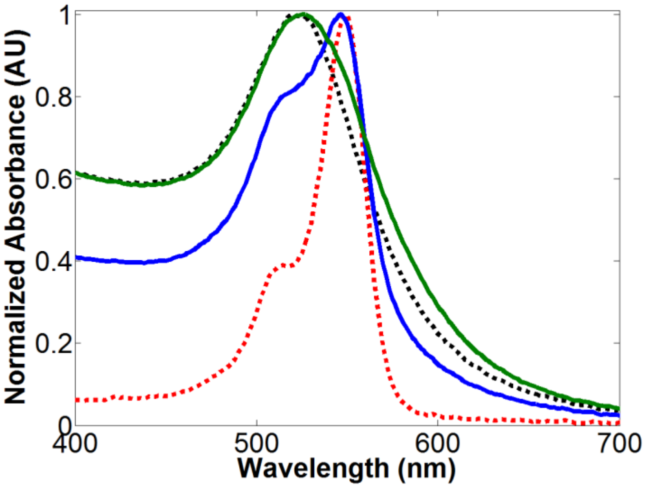

Figure 4.15 | Purification of RB contaminated 16 nm MDDA functionalized NPs with conventional centrifugation. The initial RB concentration was approximately 2 mM and centrifugation was performed at 20,238 *g* for 15 minutes. Red dashed line represents the normalized absorbance of the contaminated solution; black dashed line represents as-made un-contaminated NPs; blue line is after the 1st purification (95.2 ± 0.8% efficiency); green line is the second purification step (90.0 ± 3.0 % efficiency). Reprinted with permission from Turek *et al*[1]. Copyright (2013) American Chemical Society.

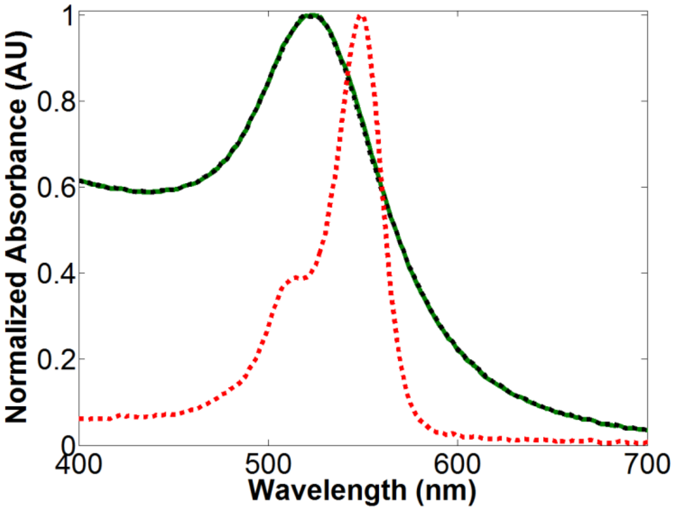

Figure 4.16 | Purification of RB contaminated MDDA functionalized 16 nm NPs through formation of the high density solution. Red and black dashed lines correspond to Figure 4.15; green line is a single purification through the high density solution. Reprinted with permission from Turek *et al*[1]. Copyright (2013) American Chemical Society.

4.3.6 Size separation of NPs

An interesting conclusion from the high purification efficiency of Figure 4.16, is that the purification with this method is dependent on a difference in the sedimentation coefficients of the two species – for 16 nm NPs and dyes, this is naturally very high. However the same principle can be applied to allow for the separation of NPs with differing sedimentation coefficients. To test this hypothesis, a mixture of 16 and 43 nm NPs (in a 1:1 vol:vol ratio which corresponds to ≈21.6 times more 16 nm NPs than 43 nm) was used.

Figure 4.17 A and B show TEMs of the mixture. After centrifugation of this solution in the presence of DCE for 10 minutes at 1,503 *g*, it was subsequently discovered that very few 16 nm particles remain in this solution. Figure 4.17 C and D shows that indeed only a relatively small number of 16 nm NPs are left. Through manual analysis of the electron micrographs of 5,000 separate particles, it was estimated that the separation efficiency of the 43 nm NPs is ≈99.5%. It is worth noting however that experimental parameters such as time of centrifugation and the RCF may need to be altered for other NP size compositions. Additionally, provided that a sedimentation coefficient difference exists, it is likely that this separation procedure may also be applicable to separate NPs of differing shapes. This may have important applications for synthesis of non-spherical NPs, many of which demonstrate either a multi-modal size distribution[25] or multiple NP morphologies[33] being formed. Nevertheless, despite many potentially interesting alternative size/shape separations being possible using this technique, this has yet to be studied in more detail.

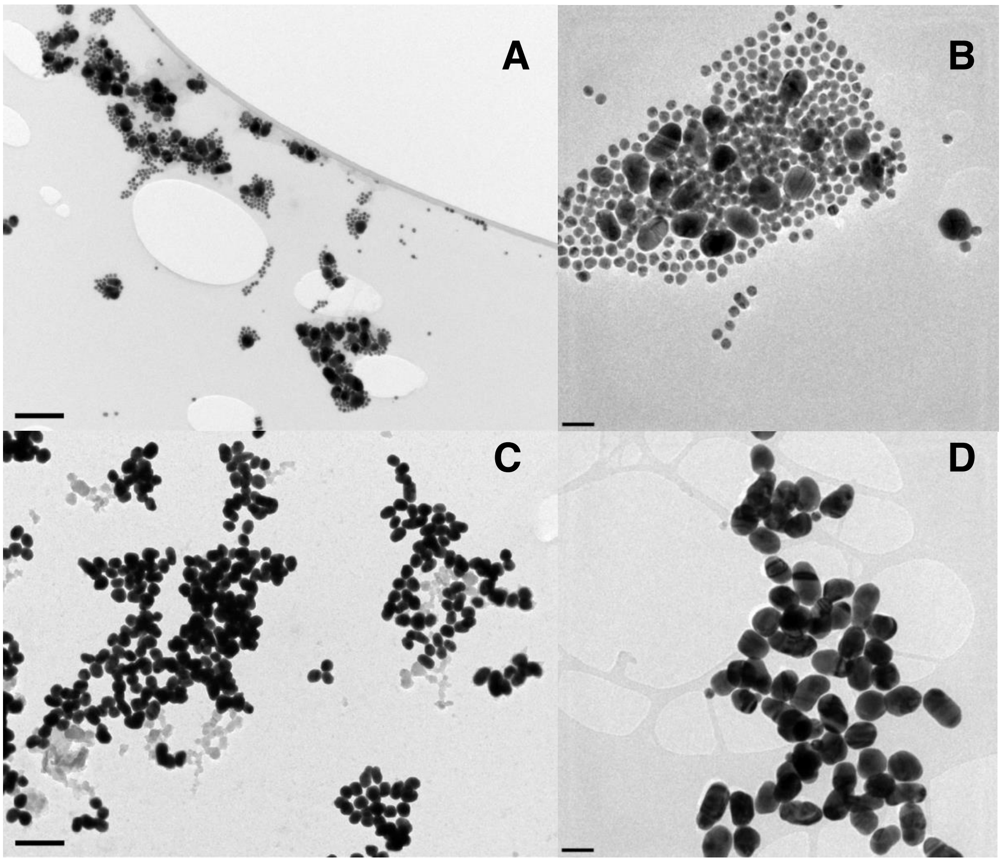

Figure 4.17 | TEM images demonstrating size separation of 43 nm NPs from a mixture of 16 and 43 nm. A and B represent a zoomed out and close-up image that is representative of the NP distribution in the mixture. C and D also represent a zoomed out and close-up image, however these are taken from the resuling droplet after a 10 minute centrifugation step at 1,503 *g*. The initial solution contained a 1:1 as made mixture of 16 and 43 nm particles (which corresponds to a ratio of 21.6:1 for 16:43), following centrifugation very few 16 nm particles are seen in the TEMs, suggesting that the droplet formation mechanism is very size-selective (in this instance a 99.5% separation is achieved for 43 nm particles). Reprinted with permission from Turek *et al*[1]. Copyright (2013) American Chemical Society.

4.4 Conclusions

This chapter is perhaps the most novel of the thesis. A simple alteration to the conditions of the work in Chapter 3 resulted in some fascinating results. The ability to quickly and easily assemble aqueous colloidal crystals on a large scale may enable engineering of advanced materials with previously unfeasible material properties. It is enough to say that despite being un-optimized many of the properties that have been demonstrated here are impressive, if not record-breaking. It is firmly believed however that if optimized, significantly enhanced properties would be possible. For example, if it would be possible to make a high density solution using 100 nm osmium/iridium nanoparticles, with a surface-surface inter-particle separation of ≈ 5 nm in a hexagonally close packed lattice, it may be possible to obtain room temperature liquid density levels exceeding that of mercury – though in principle this should be realistic to achieve, it is unclear whether or not such dense solutions would have any direct practical applications. In fact, despite an academic interest, perhaps the biggest limitation of this work is that lack of clear-cut practical applications of these liquid properties. Nevertheless, it is hoped that a more detailed investigation of additional physical properties, of these solutions will yield results that are more applicable in the real-world. In particular, it would be extremely interesting to conduct a thorough study into their thermal conductivities – at just 0.026 vol %, Patel *et al*. demonstrated a 21% thermal conductivity enhancement of water[34], the 3 orders of magnitude larger volume fraction nanofluids that this method can produce is therefore likely to dramatically increase this enhancement.

Unlike the physical properties, the NP purification/size separation aspect of this work has clear-cut applications. The purity levels obtained, combined with the speed, simplicity and versatility that this method is capable of makes it directly applicable to researchers working with NPs. The more significant application of this work however is a slightly altered system – if it is possible to almost exclusively separate NPs from contaminants, without affecting their functional groups, it should be possible to use this method to quickly and efficiently separate precious materials. For example, DNA, proteins or enzymes may be reversibly bound onto the surface of the NP in an inhomogenous medium (e.g. cell-lysate), which after centrifugation would lead to a high density droplet containing almost exclusively the analyte and the NPs. In principle this may provide an attractive route for the separation and/or purification of biomolecules.

4.5 References

1. Turek, V. A.; Elliott, L. N.; Tyler, A. I. I.; Demetriadou, A.; Paget, J.; Cecchini, M. P.; Kucernak, A. R.; Kornyshev, A. A.; Edel, J. B. *ACS Nano* **2013,** 7, (10), 8753-8759.
2. Yu, W.; France, D. M.; Routbort, J. L.; Choi, S. U. S. *Heat Transfer Engineering* **2008,** 29, (5), 432-460.
3. Özerinç, S.; Kakaç, S.; Yazıcıoğlu, A. *Microfluid Nanofluid* **2010,** 8, (2), 145-170.
4. Sundar, L. S.; Sharma, K. V.; Naik, M. T.; Singh, M. K. *Renewable and Sustainable Energy Reviews* **2013,** 25, (0), 670-686.
5. Wang, X.-Q.; Mujumdar, A. S. *International Journal of Thermal Sciences* **2007,** 46, (1), 1-19.
6. Trisaksri, V.; Wongwises, S. *Renewable and Sustainable Energy Reviews* **2007,** 11, (3), 512-523.
7. Eastman, J. A.; Choi, S. U. S.; Li, S.; Yu, W.; Thompson, L. J. *Applied Physics Letters* **2001,** 78, (6), 718-720.
8. Chon, C. H.; Kihm, K. D.; Lee, S. P.; Choi, S. U. S. *Applied Physics Letters* **2005,** 87, (15), -.
9. Sergis, A.; Hardalupas, Y. *Nanoscale Res Lett* **2011,** 6, (1), 1-37.
10. Saidur, R.; Leong, K. Y.; Mohammad, H. A. *Renewable and Sustainable Energy Reviews* **2011,** 15, (3), 1646-1668.
11. Jana, S.; Salehi-Khojin, A.; Zhong, W.-H. *Thermochimica Acta* **2007,** 462, (1–2), 45-55.
12. Stein, A.; Schroden, R. C. *Current Opinion in Solid State and Materials Science* **2001,** 5, (6), 553-564.
13. Lu, L.; Randjelovic, I.; Capek, R.; Gaponik, N.; Yang, J.; Zhang, H.; Eychmüller, A. *Chemistry of Materials* **2005,** 17, (23), 5731-5736.
14. Ravnik, M.; Alexander, G. P.; Yeomans, J. M.; Žumer, S. *Proceedings of the National Academy of Sciences* **2011,** 108, (13), 5188-5192.
15. Janlvs, R. H. **1939**.
16. Clerici, E. *Uendiconti reale Ac. Lincei Rom, 5a* **1907,** 16, 187.
17. Koroznikova, L.; Klutke, C.; McKnight, S.; Hall, S. *J. S. Afr. Inst. Min. Metall.* **2008,** 108, (1), 25-33.
18. Klutke, C.; Koromikova, L.; McKnight, S.; Hall, S.; AusImm, *The development of heavy suspension techniques for high density sink-float separations (Replacement of Clerici's Solution)*. Australasian Inst Mining & Metallurgy: Parkville Victoria, 2006; Vol. 2006, p 73-83.
19. Michalet, X.; Pinaud, F. F.; Bentolila, L. A.; Tsay, J. M.; Doose, S.; Li, J. J.; Sundaresan, G.; Wu, A. M.; Gambhir, S. S.; Weiss, S. *Science* **2005,** 307, (5709), 538-544.
20. Sau, T. K.; Murphy, C. J. *Langmuir* **2004,** 20, (15), 6414-6420.
21. Vigderman, L.; Zubarev, E. R. *Langmuir* **2012,** 28, (24), 9034.
22. Jana, N. R. *Small* **2005,** 1, (8-9), 875-882.
23. Liang, H.; Li, Z.; Wang, W.; Wu, Y.; Xu, H. *Advanced Materials* **2009,** 21, (45), 4614-4618.
24. Nehl, C. L.; Liao, H.; Hafner, J. H. *Nano Letters* **2006,** 6, (4), 683-688.
25. Akbulut, O.; Mace, C. R.; Martinez, R. V.; Kumar, A. A.; Nie, Z.; Patton, M. R.; Whitesides, G. M. *Nano Letters* **2012,** 12, (8), 4060-4064.
26. Mace, C. R.; Akbulut, O.; Kumar, A. A.; Shapiro, N. D.; Derda, R.; Patton, M. R.; Whitesides, G. M. *Journal of the American Chemical Society* **2012,** 134, (22), 9094-9097.
27. Limayem, I.; Charcosset, C.; Fessi, H. *Sep Purif Technol* **2004,** 38, (1), 1-9.
28. Hollamby, M. J.; Eastoe, J.; Chemelli, A.; Glatter, O.; Rogers, S.; Heenan, R. K.; Grillo, I. *Langmuir* **2009,** 26, (10), 6989-6994.
29. Sweeney, S. F.; Woehrle, G. H.; Hutchison, J. E. *Journal of the American Chemical Society* **2006,** 128, (10), 3190-3197.
30. Krieg, E.; Weissman, H.; Shirman, E.; Shimoni, E.; Rybtchinski, B. *Nat Nanotechnol* **2011,** 6, (3), 141-146.

31. Liu, X.; Atwater, M.; Wang, J.; Huo, Q. *Colloids and Surfaces B: Biointerfaces* **2007,** 58, (1), 3-7.
32. Balasubramanian, S. K.; Yang, L.; Yung, L.-Y. L.; Ong, C.-N.; Ong, W.-Y.; Yu, L. E. *Biomaterials* **2010,** 31, (34), 9023-9030.
33. Jana, N. R.; Gearheart, L.; Murphy, C. J. *The Journal of Physical Chemistry B* **2001,** 105, (19), 4065-4067.
34. Patel, H. E.; Das, S. K.; Sundararajan, T.; Sreekumaran Nair, A.; George, B.; Pradeep, T. *Applied Physics Letters* **2003,** 83, (14), 2931-2933.

Chapter 5: Surface Enhanced Raman Spectroscopy (SERS) at the LLI

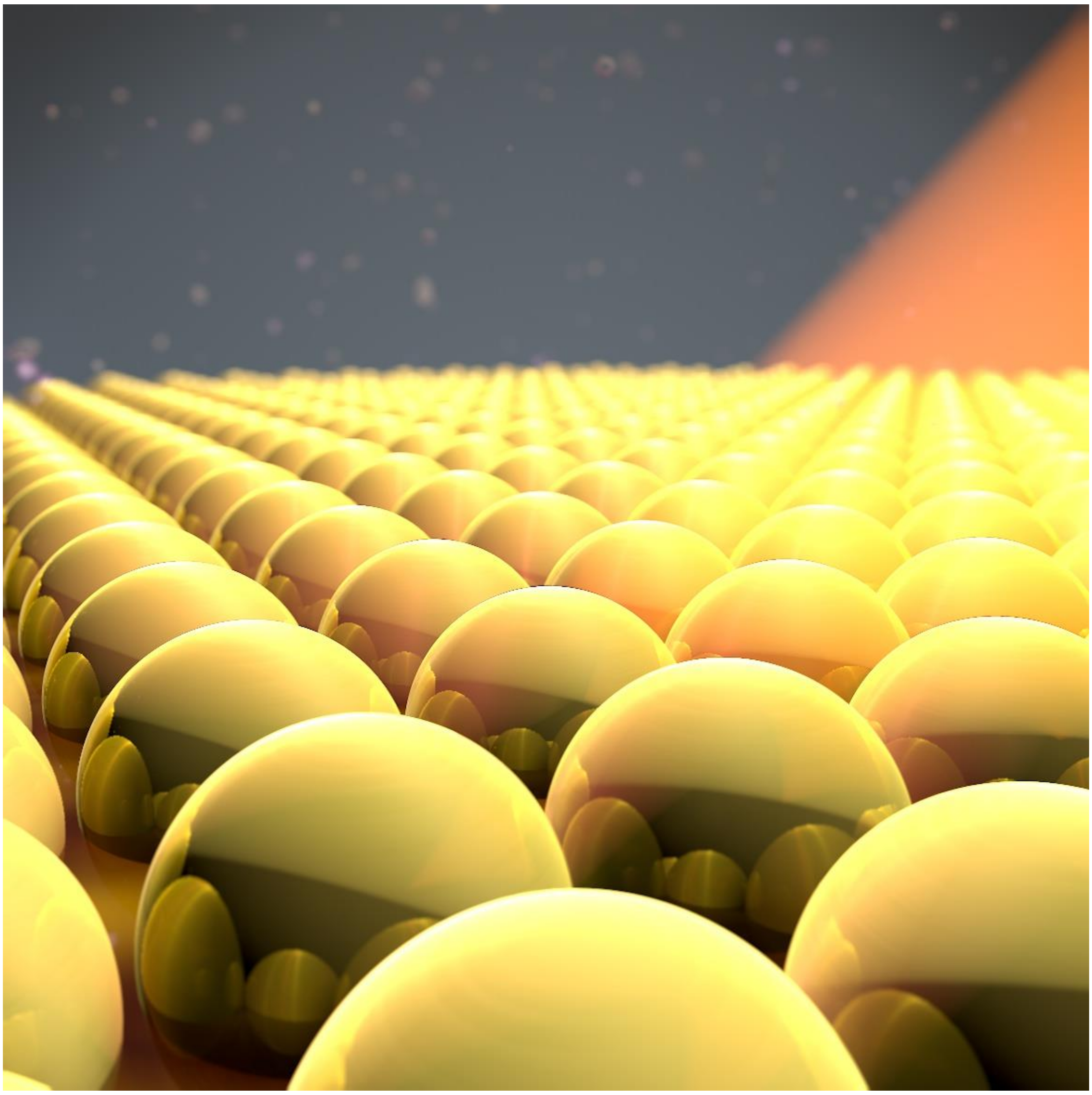

Image courtesy of Benjamin Miles

5.1 Abstract

While carrying out studies on the plasmon ruler, it was realized that aside from fundamental studies, the LLI is capable of ‘real-world’ applications. One of these side projects was using SERS to obtain spectral information on the analytes adsorbed to the NPs interface. The coupling at close enough inter-particle separations would form hot-spots and the allow spectra of the analytes to be recorded. By optimizing the assembly process for speed, simplicity and efficiency, this chapter initially reports on a versatile detection platform using SERS at the LLI, in a ‘proof-of-concept’ manner. It is demonstrated that analytes in aqueous, organic and air phases can be easily detected in quantities as low as fmole. The versatility of the detector in the first part of this chapter is built upon in the second part, in which the simulataneous, multi-phase analyte detection is key in achieving rapid, sensitive and specific detection of mercury.

Please note: the first part of this chapter was published in Nature Materials and draws heavily from this publication[1].

5.2.1 Introduction

SERS has been the focus of intense research in recent years[2-11]. Having established itself as a rapid and inexpensive technique capable of not only detection but also identification of single molecules, it is easy to understand the driving force behind this research[12-14]. Few techniques offer the potential to revolutionize modern-day detection capabilities in such a broad range of applications. A few examples include, but are not limited to: narcotics[15-18], water pollution[19, 20], pesticides[21-23], explosives[24-26] and even biological detection[27-29].

At its most basic, the SERS intensity increases as a fourth power of the electric field strength at the surface of a plasmonic material. In other words a relatively small increase in the field strength will have a dramatic effect on the intensity of the signal. Indeed it is this property that allows for single molecule sensitivity. Several strategies have been employed to achieve an increment in the field strength. Perhaps the easiest method is to simply aggregate NPs[12, 30-32] – the plasmonic coupling between aggregated NPs (the use of NPs ensures a large surface area for analyte capture) increases in a 'random' fashion leading to areas with dramatically increased field strengths, these are known as 'hot-spots'. Though aggregation in the bulk of a solution is a convenient strategy and can employed with a dual detection mode in the form of colorimetric assays[33, 34] (as NPs aggregate the colour change provides an instrument-free indication of analyte presence), it is an uncontrolled process which may lead not only to a large inter-measurement intensity distributions (as a result of the random distribution of hot-spots) but also to an ill-defined point of detection. For example the initial colour change of the solution as the NPs will start to aggregate will lead to nucleation followed by cluster formation throughout the bulk of the solution, at this point a SERS signal can be detected at any point in the solution and the focal point is not important, however after several seconds the clusters will start to fuse, reaching a critical size under which gravity will induce sedimentation, at this stage the focal point becomes extremely important but challenging predict. Therefore, despite the single molecule sensitivity and convenience that bulk aggregation may offer, it is not always an optimal detection strategy.

An interesting branch of nanotechnology has dealt with the synthesis of NPs with exotic morphologies; by eschewing the traditional spherical NPs and introducing sharp edges, it is possible to increase the electric field strength of a single non-coupling NP with respect to its spherical counterpart[35-37]. This provides the benefit of a homogenous signal distribution throughout the bulk of the solution, while making the focal point less important throughout the detection process. Perhaps the biggest limitation of this approach (as discussed in chapter 4) is the fact that the synthetic strategies that allow for exotic NP syntheses involve a form of directed growth, which is itself achieved by the functionalization of a facet of the NP with a strongly bound ligand (e.g. CTAB) that prevents the gold/silver ions from adsorbing to that face – post-synthesis however, it is challenging to desorb these ligands, meaning that the analyte will have a reduced surface area to adsorb onto as well as a potential contamination of the signal from these ligands[38]. Additionally, non-spherical NP syntheses tend to suffer from by-products (e.g. spherical particles together with nanorods), which may introduce inhomogeneity in signal intensity[39, 40]. It is also worthwhile mentioning that similarly to wet-chemistry individual nanostructures with high electric field strengths may be created by top-down approaches (such as e-beam lithography), however these are usually fabricated on solid substrates rather than in solution[41-44]. For fundamental studies, this approach is highly beneficial as it allows for extremely well-defined experimental parameters, making comparisons with theory and simulations especially informative. The fact that deposition occurs at a solid substrate also enables for an unambiguous focal point, ensuring reproducible signal intensities. Despite the many advantages of top-down fabricated structures, real world SERS detection applications of these are limited by the fact that they are not easily mass produced and the fact that for real-world applications a non-trivial cleaning step would need to be introduced[45] (as any adsorbed material will hinder further detection).

One final common approach that will be mentioned here involves a bottom-up assembly of a nano-engineered solid surface. A few examples of these include roughened electrodes[46-48], self-assembled NP films[49-51] and arrays prepared by lithographic techniques[52-54]. The main benefit of this strategy for SERS detection is that they generally attempt to demonstrate a detection platform that can be mass produced, while maintaining a regular distribution of plasmonic hotspots in a clearly defined plane of detection. While potentially less sensitive than other detection strategies, this approach provides robust and versatile detection platforms. Nevertheless, there are some limitations of these substrates. Lithographic techniques, can be relatively time consuming to fabricate; require a cleaning step (whereas a system that was cheap enough to be disposable would be advantageous); and finally, most solid substrates suffer from an inefficient analyte capture mechanism due to their relatively low surface area when compared to NPs.

5.2.2 SERS at the LLI

For real-world applications, the requirements of SERS substrates are: easy and quick fabrication; efficient analyte capture mechanism; a high density and uniform distribution of hot-spots; well-defined point/plane of detection; cheap material costs (preferentially the substrate should be disposable to avoid additional cleaning steps); versatile – analytes of interest are extremely diverse, therefore a substrate that can be optimized for different types of analyte with minimal effort would be preferential. Of the three types of detection platforms mentioned above, a self-assembled 2D substrate is most suited for these criteria. As mentioned in chapter 3, the LLI offers many advantages over the solid interface, which are often overlooked. In the case of SERS, these advantages become especially apparent. Firstly, NP adsorption to the LLI is a spontaneous process that can be achieved rapidly, as demonstrated in Chapter 2, simply emulsifying the mixture will reduce the distance that NPs need to diffuse to reach the interface. While drawing on the work of chapter 3, two further steps can ensure a greater NP density at the LLI – that is an increase in the ionic strength of the solution, as well as a reduction of the interfacial area[55]. It is therefore possible to within seconds achieve a regular (though ill-defined) self-assembled structure in which homogenous, uniform hotspots will exist. Secondly, the LLI provides for an easily identified plane of detection, while providing a common ‘meeting point’ for hydrophilic, hydrophobic and amphiphilic species. The aforementioned emulsification therefore serves a secondary purpose – not only does it reduce the distance that the NPs must diffuse, but also the distance that an analyte must diffuse to reach the interface and therefore the NPs. In effect the emulsification process provides for an efficient analyte capture mechanism from both the organic and aqueous phases, which subsequently (upon separation of the two phases) concentrates the analyte and the NPs at a common plane of detection. Thirdly, while prefabricated substrates would be convenient for in-the-field applications as no additional preparation steps would be required, prefabricated plasmonic structures would need to be protected from environmental adsorption of contaminants. Cleanliness however is not an easy aspect to ensure (even in laboratory conditions), as airborne contaminants have a propensity to adsorb onto clean surfaces[56]. One of the ways that this can be overcome is by preparing the substrate in-the-field, the preparation process must however be easy, fast and require minimal technical experience/equipment. Therefore one of the advantages of the work described here is that in order to fabricate the substrate only 2 quick and easy steps are required – shaking a vial of NP solution with DCE and pipetting the droplet onto a glass coverslip. Finally, the versatility of NPs thin-films at the LLI allows them to not only detect *either* hydrophilic or hydrophobic analytes but *both* simultaneously. The importance of this ability may not be immediately obvious, but will be shown to play a key role in the latter part of this chapter where specific Hg detection is demonstrated.

For completeness, some disadvantages of SERS detection at the LLI should also be mentioned. Perhaps the biggest limitation of this platform is the constraints that it places on the optical setup. The LLI provides a plane of detection, however without more sophisticated cell design, it may be difficult to predict where this plane would be with respect to the optics. This means that the sample stage must have either a z-axis translational stage or x/y control (the spherical nature of the droplet means that the interface can also be optically found at its edges). Translational stages are relatively easy to implement in optical setups, however the other aspect of this limitation is that the temporal resolution must also be quite high in order to get real-time intensity feedback and therefore optimize the focal length to focus on the actual interface. The other major limitation of SERS detection at the LLI is that other than plasmonic coupling from NPs it is unlikely that the interface will itself increase the enhancement factor, though it is likely to influence the position of the hot-spots[8]. In other words the sensitivity of the platform is unlikely to be improved in comparison to NP arrays at the solid interface. The final potential limitation is the fact that the detector is essentially a droplet which limits its stability, factors such as oscillations, evaporation and tilting of the sample will have adverse effects for detection purposes. Nevertheless it is believed that this limitation can be mitigated through careful sample handling.

5.2.3 Heavy metal ion detection

As mentioned already, SERS offers many advantages as a sensing mechanism. Requiring only a relatively cheap optical setup, with opportunities for portability[57] and in-field applications, coupled with high sensitivity, sample identification and a real-time readout make it a very promising strategy for next-generation sensors. There are however limitations with the type of sample that SERS could be used to identify. Primarily, due to the absence of a change in polarizability (as no bonding exists), monoatomic ions cannot produce a Raman spectrum. Despite this, many monoatomic ions/species are of great interest for detection purposes. Perhaps chief of which are heavy metals. In order to bypass this fundamental limitation and allow the detection of heavy metal ions with SERS, three general strategies have been used:

1. Aggregation of NPs through the addition of the heavy metal ion[58, 59]. This involves functionalization of NPs with specificity groups that allow complexation with the heavy metal ions. As the ions essentially chelate two NPs together, aggregation causes an increased plasmonic coupling and the electric field enhancement. This may then be investigated either through SERS or (more commonly) though a colorimetric assays [60-62]. The main limitation of this is that NPs are generally very susceptible to aggregation anyway and while in clean laboratories it is possible to ensure that aggregation-inducing contaminants are kept to a minimum, in-the-field applications will struggle to achieve such cleanliness. Strategies to increase NP stability to aggregation (such as the addition of spacer groups) are typically incompatible with this method as either the aggregates' coupling would be weaker (from a greater surface-surface inter-particle separation), leading to lower sensitivity, or the stabilizing mechanism will prevent aggregation all together and the system will become unresponsive to heavy metal ions.
2. A reduction of SERS signal through reporter displacement by heavy metal ions[33, 63-66]. This is perhaps the least preferential mechanism, but is nevertheless occasionally reported. The principle behind this route involves a decrease in the SERS intensity as the heavy metal ion concentration is increased. For example, through the displacement of a (strongly) SERS active analyte by heavy metal ions. The replacement of the surface functionality with an inactive species leads to a reduction in the recorded intensity of the spectra. Though an interesting scientific principle, the limitations of such an approach to real-world sensing applications are numerous – the decrease in signal intensity can be a result of other phenomena – e.g. substrate degradation, the sample being out of focus, a drop off in laser intensity and even binding of other chemical species with a lower SERS intensity. In fact for a substrate such as gold, Figures 5.9-5.12 demonstrate some of the functional groups that have affinity to gold – this means that achieving specificity using such a system is more challenging than even through aggregation. Additionally, signal intensity in Raman spectra is usually reported as arbitrary units – the intensity has uses for qualitative comparative purposes, however extracting quantitative information from the intensities is highly challenging.
3. A conformational change of a reporter molecule in the presence of a heavy metal ion, leading to a change in the SERS spectrum[67-72]. This is perhaps the most promising and widely used strategy to use for heavy metal ion detection through SERS. If the

> vibrational spectrum of a reporter becomes substantially different in the presence of a heavy metal ion, it becomes possible for true specificity to occur – though contaminants and impurities may be present in the sample, the conformation that the reporter adopts in the presence of the heavy metal ion will be indicative of its presence in the solution. The fact that such a route is not dependant on aggregation or a signal decrease is highly beneficial compared to other techniques. Nevertheless, a key challenge with this is in selecting the reporter molecule that displays both a high selectivity to specific heavy metal ions as well as a clearly identifiable spectral change in its presence. As heavy metal ions are almost exclusively water soluble, conventional detection strategies have been mostly limited to using hydrophilic species or functionalized surfaces.

It is clear that a conformational change of the reporter is the most desirable strategy for heavy metal detection with SERS. The main benefit that the LLI provides in this respect is that it overcomes the limitation of reporter solubility. This aspect of SERS at the LLI will be taken advantage of through the detection of Hg^{2+} ions dissolved in the aqueous phase by 1,8-diaminonaphthalene dissolved in the DCE, in the second part of this chapter.

5.3.1 Results and Discussion

It was mentioned in chapter 2 that one of the ways in which the initial experiments tried to characterize NP assemblies at the LLI was to first assemble them at the interface, followed by pipetting out the aqueous phase and evaporation to leave a dried NP film. Though it is clear that such structural studies are not representative of the structure at the interface, it was realized that similar to the plasmon ruler studies, particles that are ‘un-functionalized’ (citrate stabilized) would also couple, allowing for shorter inter-particle separations and greater field enhancement. Instead of trying to describe the NPs’ behaviour it was decided to try and obtain a SERS spectrum from the NP films while they are still at the interface (Figure 5.1).

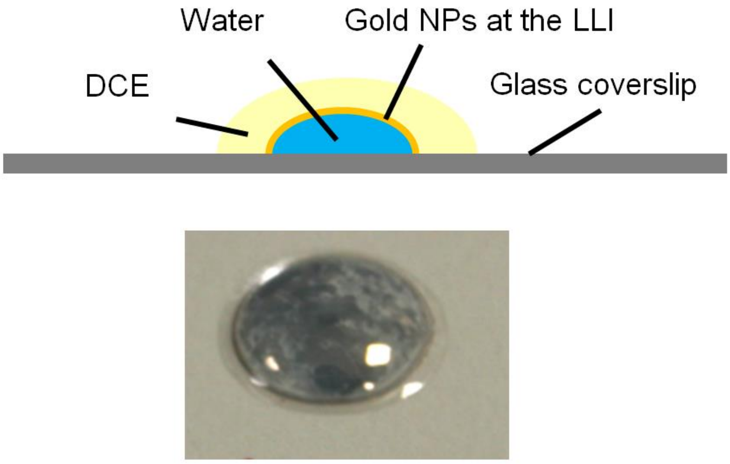

Figure 5.1 | Schematic and picture of gold NPs assembled at the LLI and subsequently transferred onto a glass coverslip for SERS.

A home-built high-temporal resolution Raman setup was constructed as part of a separate project (by Dr. Michael Cecchini) in which malachite green isothiocyanate (MGITC) functionalized gold NPs were studied through SERS[73-75]. MGITC has an absorbance band at ≈630 nm, while the LSPR of closely packed NPs is also expected to shift to have a strong resonance at this wavelength. The overlap between the resonance of the dye with the LSPR gives rise to surface enhanced resonant Raman scattering (SERRS) if an appropriate excitation wavelength is used.

For preliminary experiments, the spectra of MGITC functionalized NPs were recorded when assembled at the interface and in bulk solution for comparison. Figure 5.2 clearly demonstrates the increased signal that was seen when the particles are at the interface. It should be noted that even in the bulk aqueous phase, the signal remains clearly distinguishable, however the signal intensity is dramatically weaker. The increased intensity at the interface arises from a combination of factors including a shift in the LSPR to a more optimum wavelength for excitation with a 632.8 nm laser; an increased effective NP concentration at the point of detection; as well as the plasmonic hot-spots as a result of plasmon coupling.

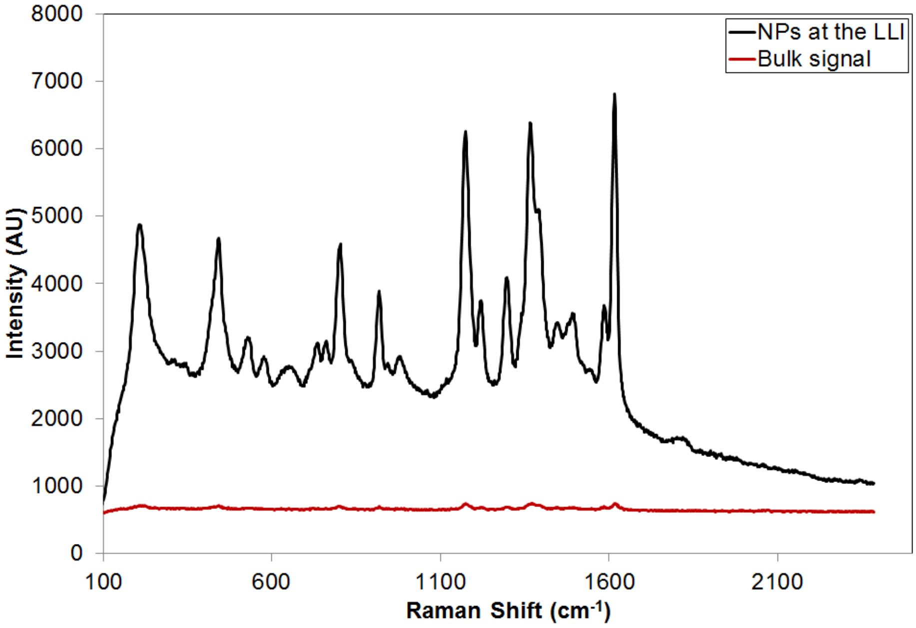

Figure 5.2 | Comparison of SERRS obtained at the interface and in bulk solution. Experimental conditions as highlighted in Figure 2.18.

It was noticed that MGITC is soluble in water at low concentrations, however when an organic phase is introduced, it undergoes a phase transfer to preferentially the organic phase. The facile nature of analyte capture meant that it was not necessary to have 'pre-functionalized' NPs. Instead the ability to be dissolved in both aqueous and organic phases allowed for the investigation of limits of detection with this platform from both of these phases. In order to assemble the NPs to the interface, emulsification[76] (through vigorous shaking) was chosen (Figure 5.3). The dependency of the assembly process on the salt concentration was already known, however to prevent aggregation from occurring the bulk of the aqueous phase, an increased NaCl concentration of 20 mM was used. When the particles assembled (usually within 10-20 seconds of shaking), the mixture was allowed to separate out again into 2 distinct phases, followed by a reduction in the volume of the aqueous phase. This reduction is believed to play a key role as the reduced interfacial area at a constant number of adsorbed NPs increases the effective coverage, thereby allowing both a more uniform substrate, as well as an increased concentration of plasmonic hotspots. The aqueous droplet, together with the adsorbed NPs and a portion of the DCE was then transferred onto a glass coverslip and imaged. The total time needed between sample preparation and signal acquisition was a few minutes (though the entire procedure could be accomplished within about 1 minute if optimized for speed).

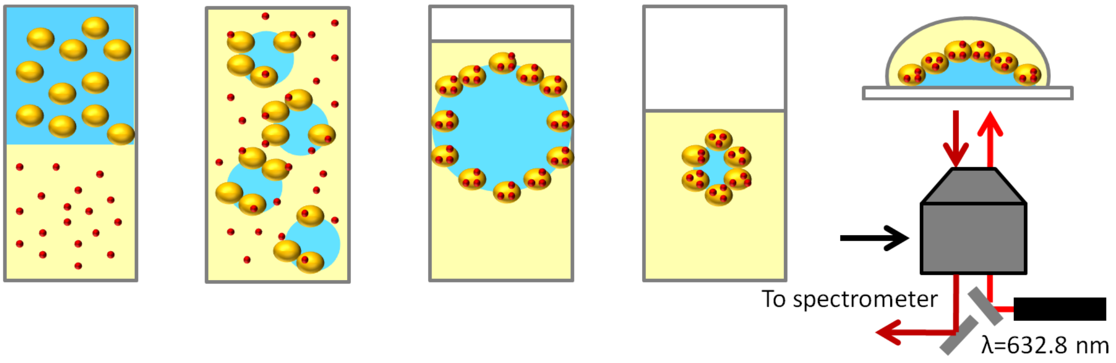

Figure 5.3 | Schematic of sample preparation. A NP solution (0.5 mL containing 1.74×10^{10} 43 nm citrate stabilized Au NPs at a NaCl concentration of 20 mM) was added to the organic DCE phase (0.5 mL) containing the analyte (A) (please not the analyte could also be dispersed in water, however the volumes of both phases were kept at 0.5 mL throughout the work). Upon vigorous shaking, an emulsion is formed in the tubes (B) which reduces the path length that both the NPs and the analyte have to diffuse to reach the interface. When left unaggitated for several seconds, the emulsion separates back out into 2 distinct phases (C). The volume of the aqueous phase is reduced to 50 µL to increase the effective concentration of both the NPs and the analyte at the interface (D). The aqueous phase together with a small amount of DCE is then transferred onto a coverslip and spectra are recorded (E). Adapted with permission from Cecchini *et al*[1].

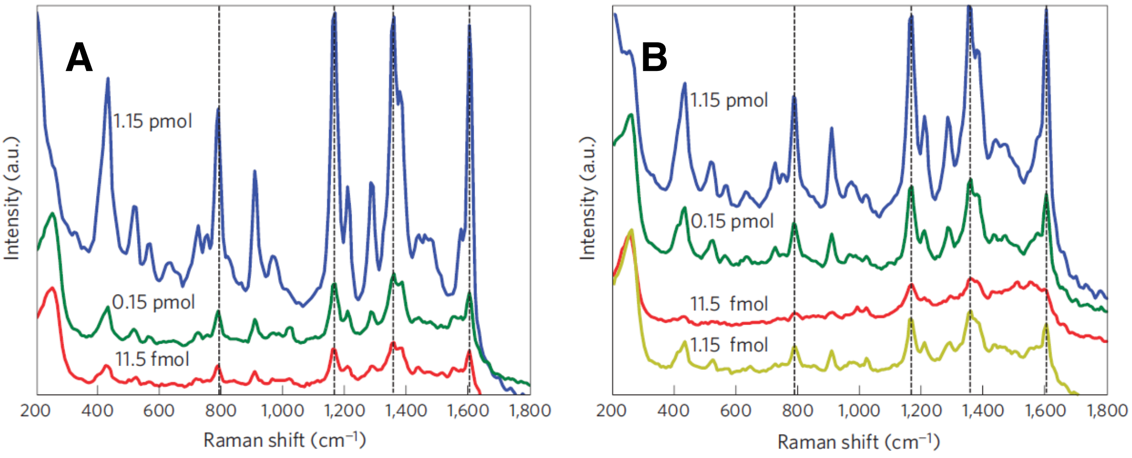

Figure 5.4 | Spectra of MGITC detection at the LLI, initially dissolved in DCE (A) and in water (B). Reprinted with permission from Cecchini *et al*[1].

It was found that the reproducible limits of detection of MGITC were an order of magnitude lower when dissolved in water compared to DCE. Though it should be noted that occasionally detection limits in both water and DCE reached ≈100 amol, however due to the inconsistency in obtaining spectra from these samples, the detection limits are reported as ≈1 fmol in water and ≈10 fmol in DCE. The order of magnitude increased sensitivity in water is likely a product of the analyte having direct access to the NPs for adsorption prior to emulsification – in other words if dissolved in DCE, the NPs will first need to adsorb on to the interfaces, followed by which MGITC will be able to reach the NPs' surface in sufficient quantities, whilst if dissolved in water MGITC will be able to reach the NPs through the sample preparation process.

Of course, MGITC is an 'ideal' case – most real world analytes will not have an absorbance band that matches both the LSPR of the NPs as well as the laser. For this reason, the limits of detection from both the aqueous and organic phase were decided to be tested with 'real' analytes. That is, hydrophilic in water and hydrophobic in the organic phase, which do not have a resonance at 633 nm. The chosen analytes were methoxy-α-toluenethiol (MATT) as the hydrophobic analyte and 2-mercapto-5-nitrobenzimidazole (MNBI) as the hydrophilic analyte. Figures 5.5 and 5.6 demonstrate the spectra obtained at the lowest detectable analyte contents.

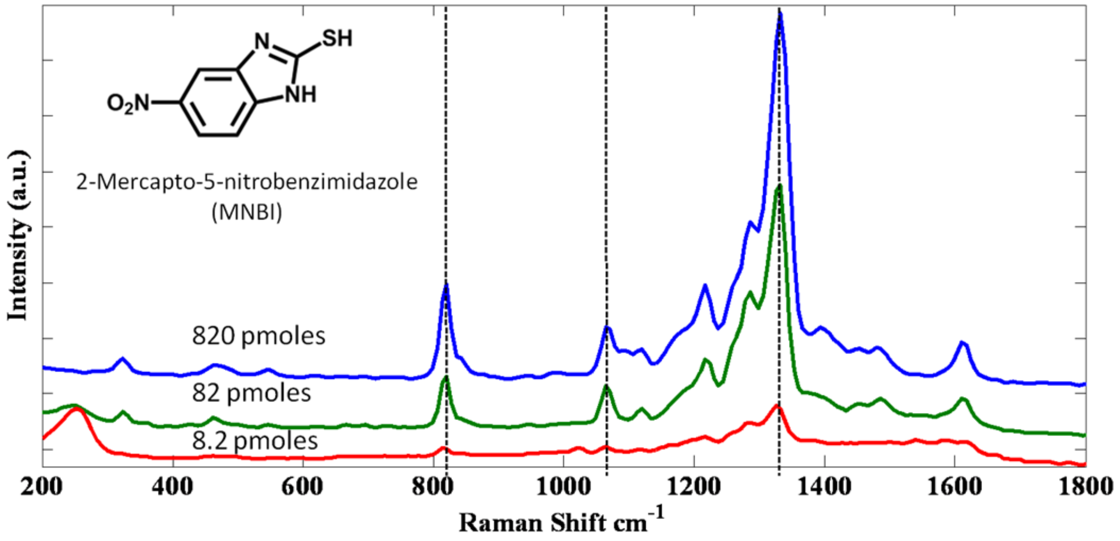

Figure 5.5 | Spectra of MNBI at the LLI initially dissolved in the aqueous phase. Reprinted with permission from Cecchini *et al*[1].

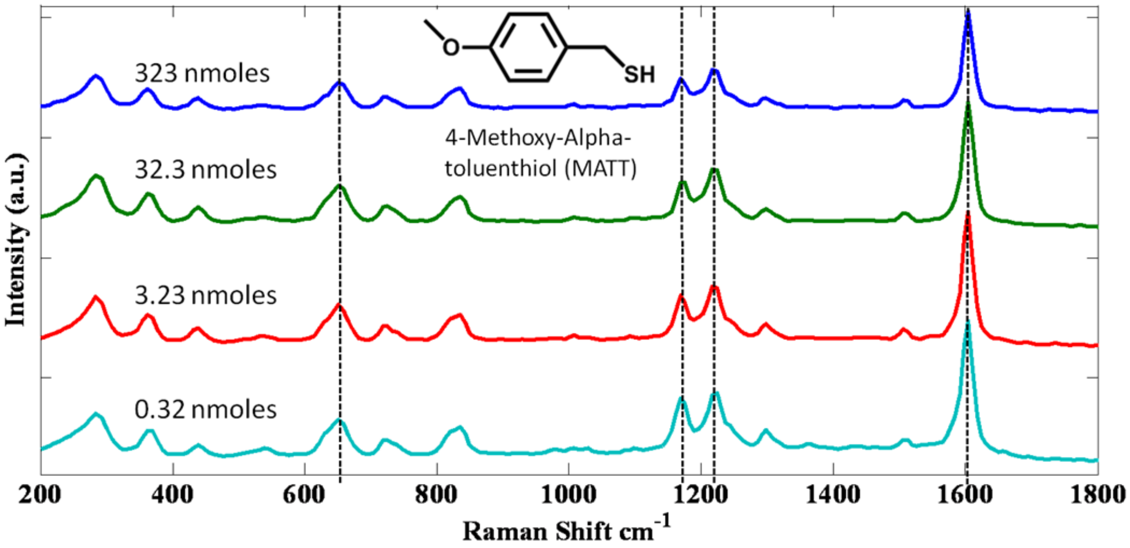

Figure 5.6 | Spectra of MATT at the LLI initially dissolved in DCE. Reprinted with permission from Cecchini *et al*[1].

It is clear that similar to the detection limits of MGITC that the limits of detection of analytes dissolved in the organic phase is between 1-2 orders of magnitude higher (*i.e.* higher concentrations are needed of the hydrophobic analytes) compared to those in water. It is also worthwhile noting that in comparison to the resonant MGITC spectra, non-resonant analytes such as MATT and MNBI have 3-4 orders of magnitude higher detection limits in their respective phases. As mentioned above, the main importance of this result is not the sensitivity of NPs at the LLI for SERS, but their versatility – with no modification, the same platform was able detect both types of analytes.

5.3.2 Simultaneous Dual-phase detection

Given this fact that no modification is required to the platform, an obvious test was to determine whether the detection platform also allows for simultaneous dual-phase sensing. The higher sensitivity of the platform to analytes dissolved in the aqueous phase could potentially overpower any detection capabilities of analytes dissolved in the organic phase, thereby limiting the practically of the sensor. Figure 5.7 shows the recorded spectra at 3 different MNBI:MATT ratios.

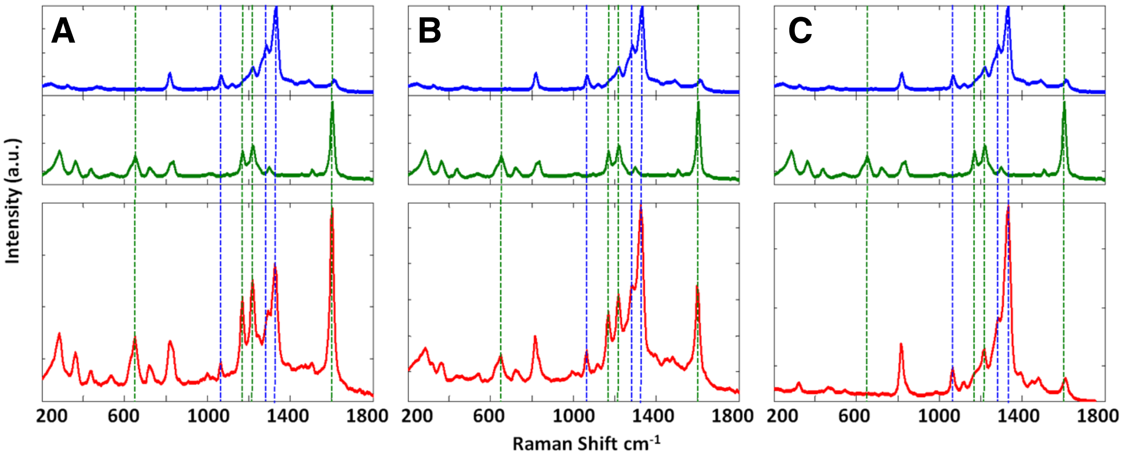

Figure 5.7 | Simultaneous dual-phase detection of MNBI and MATT (red) at three different mole ratios: A is 20:1 MATT:MNBI; B is 2:1 MATT:MNBI; and C is 1:5 MATT:MNBI. For clarity, the spectra and key peaks of pure MNBI and pure MATT is shown above in blue and green respectively. The absolute number of moles for the lowest concentration analyte was kept as 82 pmol (*i.e*. 20:1 MATT:MNBI represents 82 pmole MNBI and 1.64 nmole MATT). Reprinted with permission from Cecchini *et al*[1].

It was found that the ratio between MNBI and MATT had a direct effect on the resulting spectra. Due to its more efficient binding mechanism, MNBI was observed at all tested ratios, with the relative intensity of MATT increasing as the fraction of MATT is higher. In effect, this suggests that the detection platform is capable of simultaneous dual-phase sensing and that the preferred sensitivity of aqueous analytes will not hinder detection of hydrophobic species. Furthermore, the relative peak intensities create an opportunity for some interesting functionality studies – dual functionalization can be achieved and estimated on a particle's surface. For example, if the calibration curves are performed, a knowledge of the concentration of one analyte may allow for estimation of the concentration of the other. Figure 5.8 shows an example of such a calibration curve – the peak intensities of the strongest MNBI peak was compared to the strongest MATT peak at various MATT:MNBI fractions.

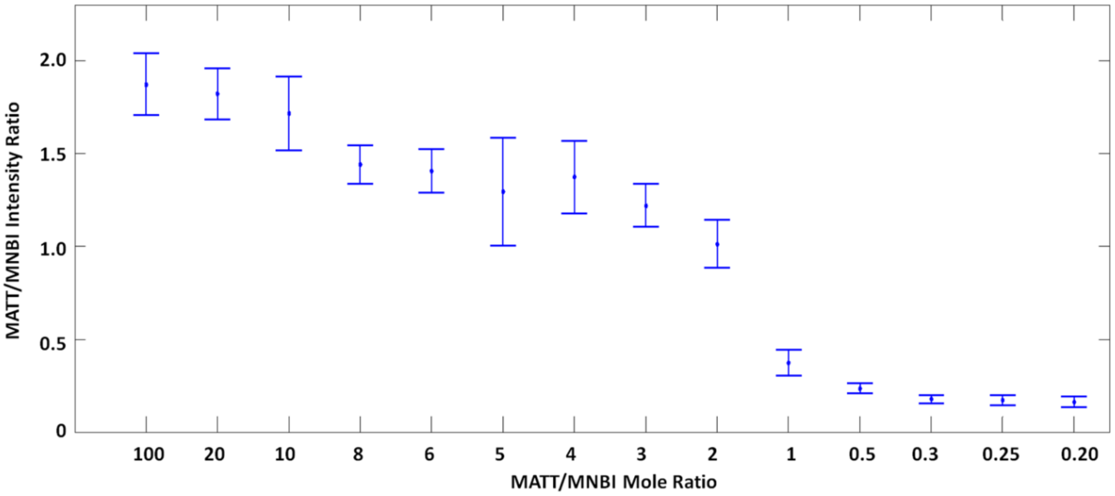

Figure 5.8 | MATT:MNBI signal intensity ratio against MATT:MNBI fraction. Reprinted with permission from Cecchini *et al*[1].

The ability to estimate concentrations of one species in comparison to another is particularly useful in the context of dual-functionality – though many reports of dual-functionality NPs exist in the literature, it is often extremely challenging to quantify, with any precision, the actual fraction of one functional group in comparison to the other[34, 77, 78]. Additionally, for the purposes of a one-off measurement, it is challenging to relate the SERS intensity to concentration – calibration curves would need to be performed at different analyte concentrations on the same instrument at the same conditions prior to estimating an unknown concentration. The peak ratios on the other hand provide for a more convenient concentration estimation method as these will be independent of the actual intensity. Though it could be argued that the LLI is perhaps unnecessary for these purposes and that more conventional SERS substrates are capable of achieving this, it should be highlighted that the speed and ease of obtaining SERS spectra at the LLI make it an attractive platform for general studies using SERS.

5.3.3 Versatility

As mentioned previously, the reported detection platform is versatile. So much so, that the same procedure, with minimal/no modification has successfully been applied to the detection of over 50 different chemicals during the project. Almost every molecule that was tested produced a SERS spectrum from the NPs at the LLI (the main exceptions to this were molecules that were insoluble in either the aqueous or organic phases or highly fluorescent molecules that were not fully bound onto the gold). The presence of a thiol is generally beneficial when working with gold NPs, however it should be stressed that gold has an affinity to many other functionalities that are more common in random molecules – carboxyl, phosphate, amine, nitro and others. To demonstrate some of these detection capabilities, the spectra of 4 different molecules at 2 different concentrations were acquired at the LLI possessing differing functional groups, these are demonstrated in Figures 5.9-5.12. Additionally, some spectra of other tested chemicals at a single content of 1 µmol are shown in Figures 5.13 and 5.14.

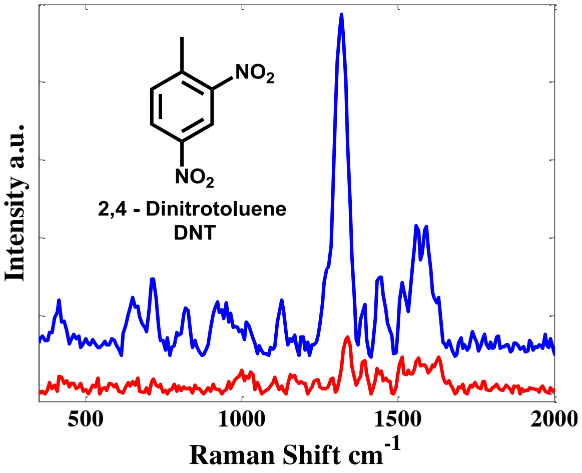

Figure 5.9 | Spectra of 2,4-dinitrotoluene at the LLI at 1 µmol (blue) and 10 nmol (red) contents. The affinity to the gold's surface is provided by the nitro groups. Reprinted with permission from Cecchini *et al*[1].

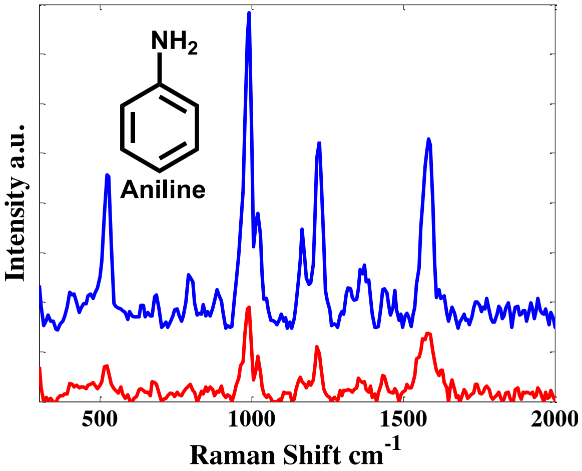

Figure 5.10 | Spectra of aniline at the LLI at 1 µmol (blue) and 10 nmol (red) contents. The affinity to the gold's surface is provided by amine groups. Reprinted with permission from Cecchini *et al*[1].

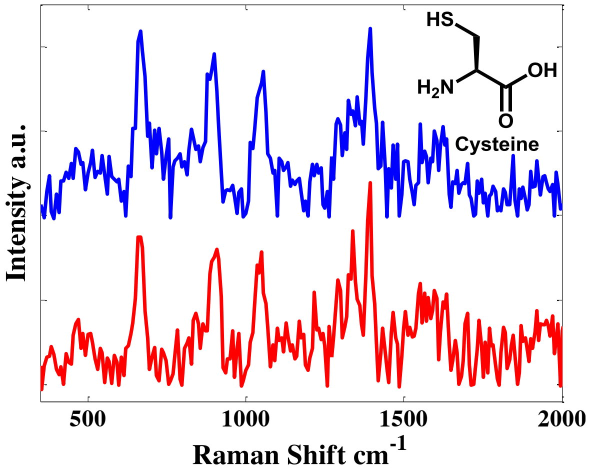

Figure 5.11 I Spectra of cysteine at the LLI at 1 μmol (blue) and 10 nmol (red) contents. Though a thiol is present in cysteine which allows for high gold affinity, the absence of an aromatic ring leads to a low Raman cross-section of this molecule thereby lowering signal-to-noise when compared with aromatic compounds. Reprinted with permission from Cecchini *et al*[1].

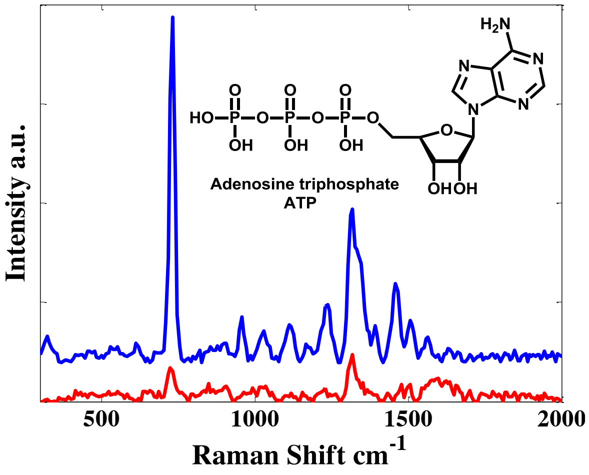

Figure 5.12 I Spectra of ATP at the LLI at 1 μmol (blue) and 10 nmol (red) contents. The phosphate and amine of ATP provides affinity to the gold surface. Reprinted with permission from Cecchini *et al*[1].

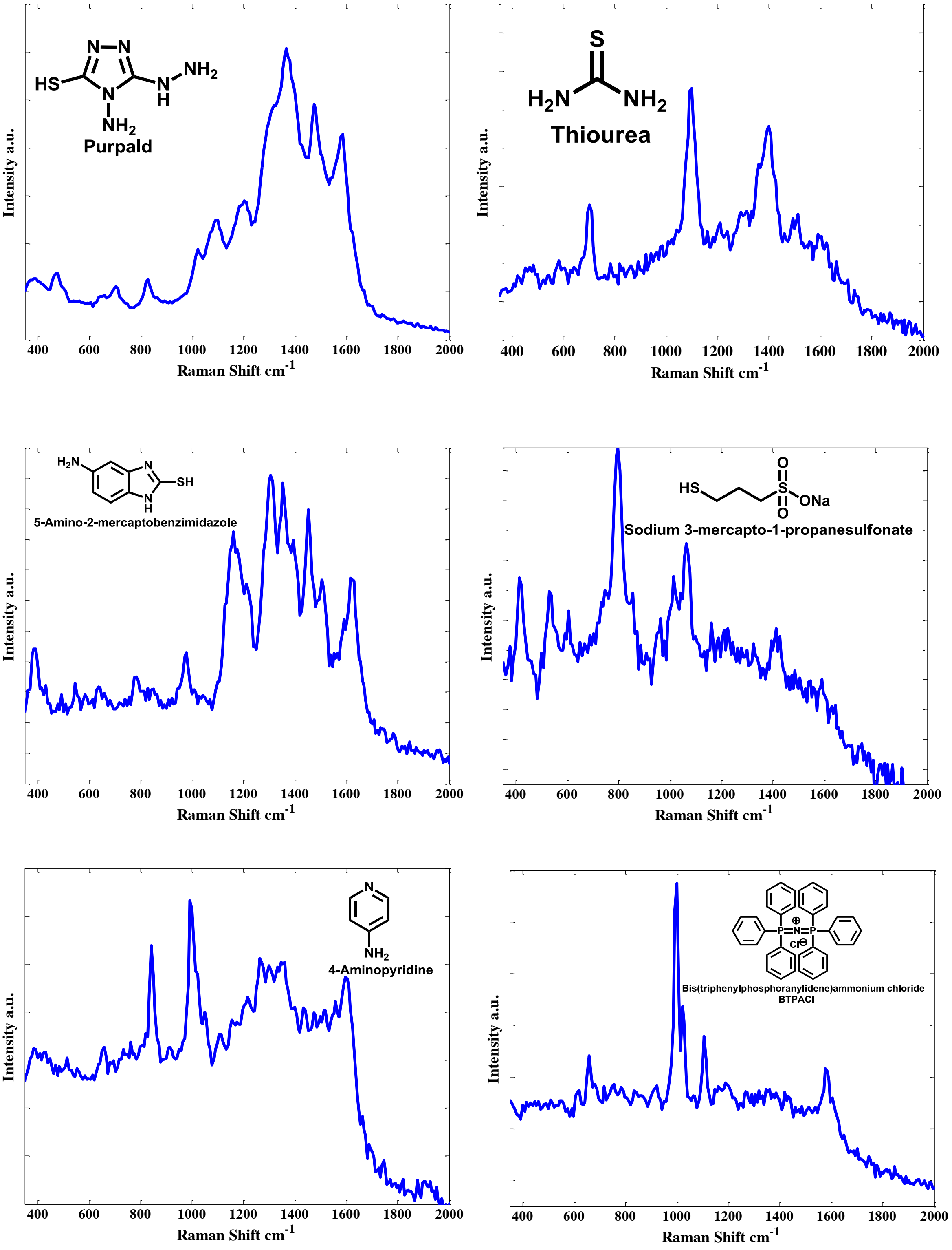

Figure 5.13 | Versatility of SERS detection at the LLI (part 1).

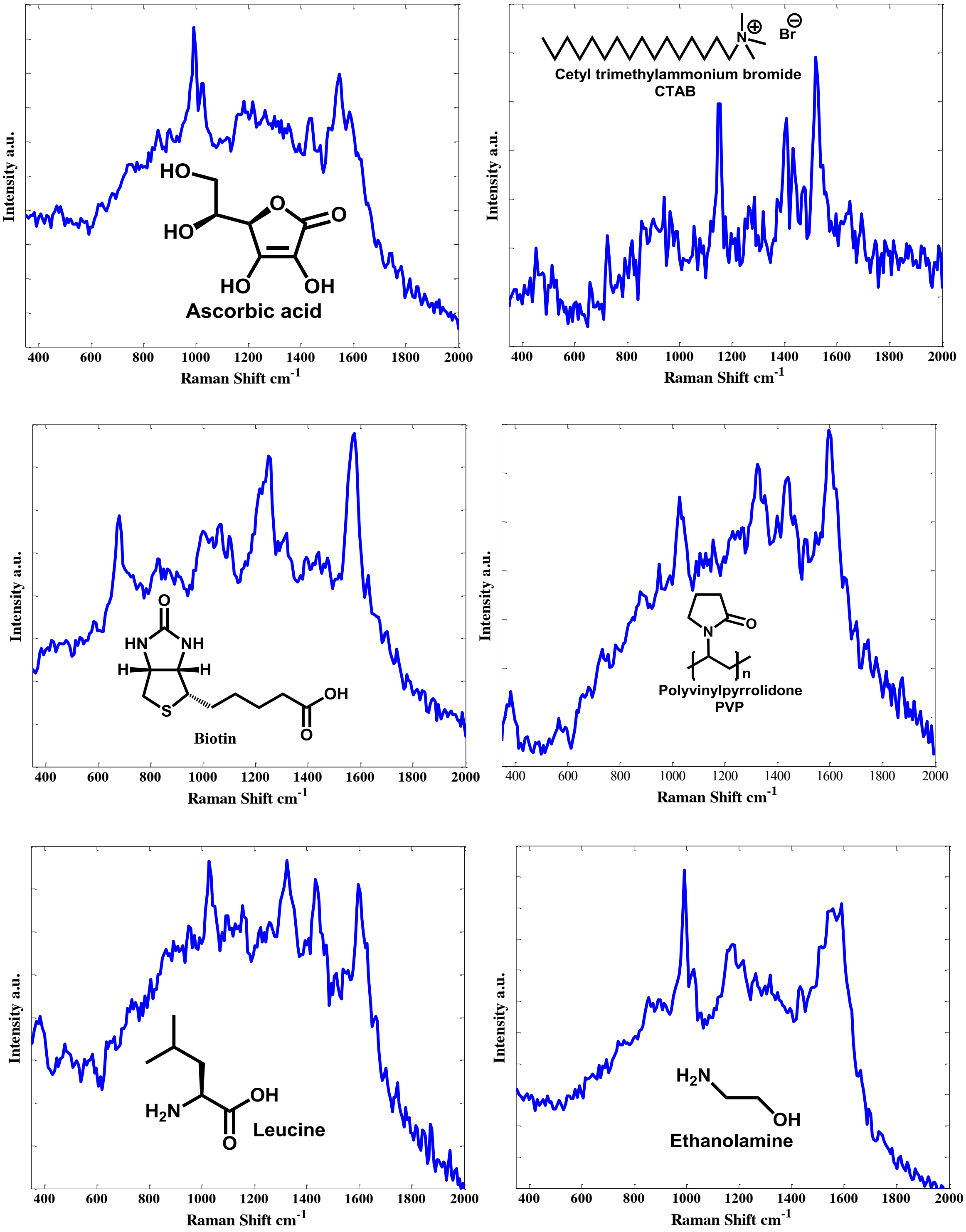

Figure 5.14 | Versatility of SERS detection at the LLI (part 2). Figures 5.13 and 5.14 demonstrate some of the various chemicals with different functional groups that can be detected through SERS at the LLI. In all cases the analytes were dissolved in the aqueous phase with a total content of 1 µmol.

5.3.4 Airborne Detection

While working with MATT, it was noticed that it had a strong smell. During control experiments, the spectra of NPs at the LLI in the absence of added analytes was recorded. Additionally, the Raman spectrum of pure MATT was recorded for comparison with the SERS, for speed and consumable saving purposes, a droplet of MATT was placed on the same coverslip as the blank NPs at the interface – though physical contact of the two droplets was avoided. After an initial acquisition of blank NPs, the Raman spectra of MATT was recorded, which was again followed by a repeat measurement of the blank NPs at the liquid-air interface (during acquisition of the MATT spectra, the residual DCE had evaporated, exposing the NPs to the air). Surprisingly, the spectrum of MATT was observed during the second acquisition.

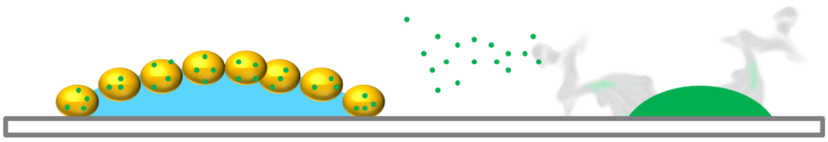

Figure 5.15 | Schematic of airborne detection.

It was quickly realized that evaporation of MATT into the air (hence the strong smell) and the close proximity of the MATT to the particles allowed for airborne detection (Figure 5.15). It was therefore decided to investigate this effect by recording the time evolution of the spectrum of MATT. Figure 5.16 demonstrates that as the MATT droplet is introduced onto the coverslip (the droplet was placed 1.5 cm from the edge of the NPs at the liquid-air interface (LAI) and both were encapsulated in a petri dish with a detection window cut out underneath the NPs at the LLI) the signal intensity experienced a ≈10 second lag, followed by a steady increase, which is itself followed by a plateau after ≈60 seconds. The plateau is likely indicative of saturation of the NPs' surface with the analyte. It is worthwhile noting that the rate of the steady increase is most probably related to airborne analyte concentration and though it is believed that such concentrations could be estimated from calibration curves, quantitative determination of this was achieved. The reason for this being the significant complexity of controlling airborne concentrations, as well as the need of secondary detection equipment for comparative purposes, which was unavailable.

The opportunity for airborne detection from NPs adsorbed at the LAI complements the already versatile detection platform that the LLI provides and means that essentially the same platform is able to detect hydrophobic, hydrophilic, amphiphilic and airborne analytes.

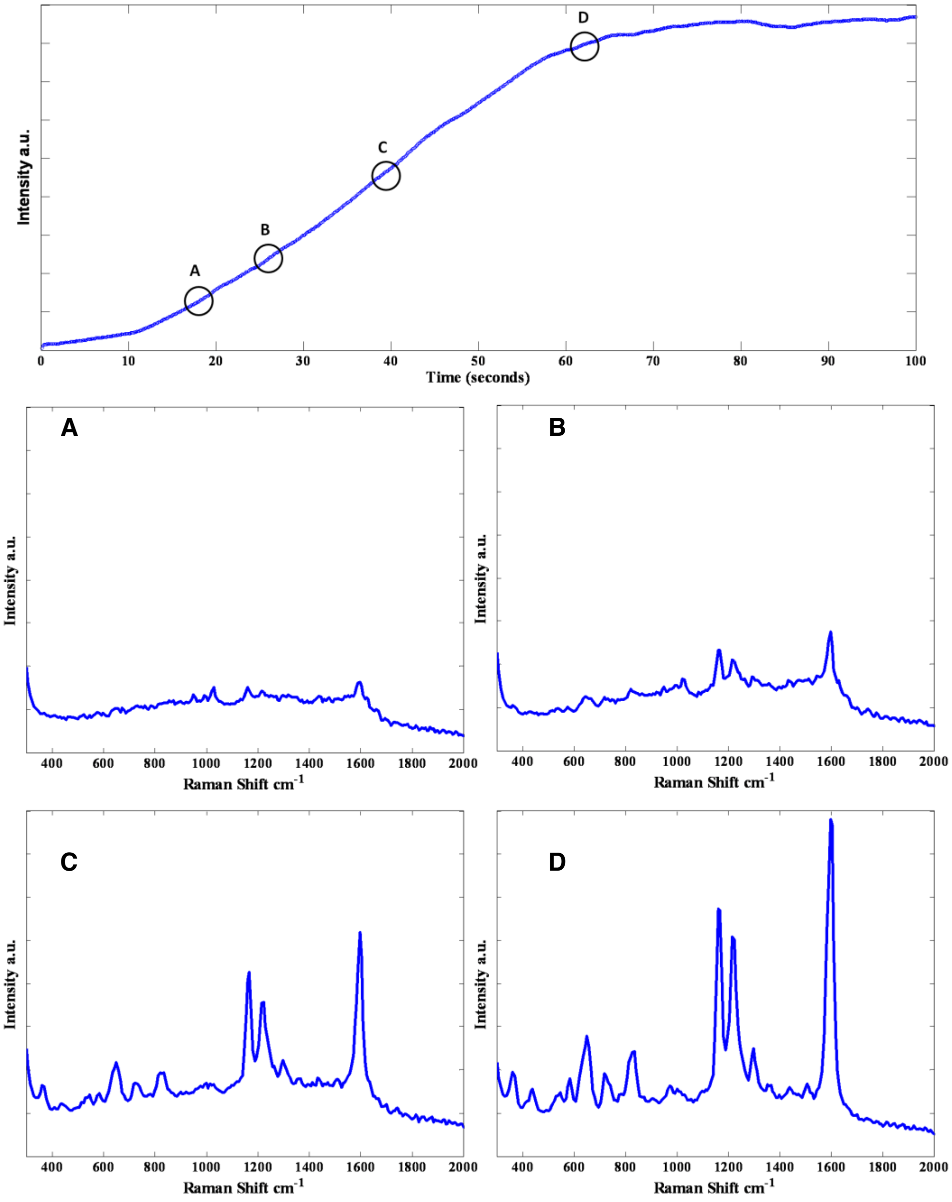

Figure 5.16 l Time evolution of the MATT spectrum through airborne SERS detection at the LAI. Reprinted with permission from Cecchini *et al*[1].

Due to the proof-of-principle nature of this work as well as the specialized equipment that would be required for a detailed study of airborne detection, this aspect of the detector was not studied in more detail. Nevertheless, the potential that airborne detection at the LAI offers warrants a separate study of its own.

5.4.1 Part 2: Heavy metal detection through SERS at the LLI

The results presented in part 1 of this chapter demonstrated a useful and versatile sensor. Nevertheless, the individual detection of hydrophilic, hydrophobic and airborne analytes with SERS is not by itself unique to the LLI and has been demonstrated countless times in the literature[79-81]. While the main novelty of SERS at the LLI is that it is possible to carry out all of these measurements through a single cheap and fast to fabricate platform. Simultaneous dual-phase detection however, *is* a unique aspect of SERS at the LLI. The reason why this may have important applications is demonstrated in this part of the chapter.

5.4.2 Selection of the reporter molecule

Unlike previously reported work that aimed to detect heavy metal ions through a reporter molecule by SERS, the solubility of the reporter was not limiting at the LLI. The diversity of chemical species that have an affinity to gold NPs meant that the main limiting factor was specificity and affinity of the reporter molecule to a heavy metal ion. In fact, the freedom of choice in the reporters was initially overwhelming, but in an effort to prevent a needle-in-a-haystack search, some ‘Ionophores’ (from Sigma Aldrich) were the first choice of reporters. Due to their known affinity to heavy metal ions and their existing use in the literature, this seemed like a logical first choice. 5 reporter molecules were first chosen – these were morin[82] (Al^{3+} ionophore), pyrithione[83] (Zn^{2+} ionophore), 4,4′,4″,4‴-(porphine-5,10,15,20-tetrayl)tetrakis(benzoic acid)[84] (PTTBA) (Ni^{2+} ionophore), 1,10-dibenzyl-1,10-diaza-18-crown-6[85] (DBDAC) (Hg^{2+} ionophore) and 1,8-diaminonpathalene[86] (1,8-DAN) (VO^{2+} ionophore). Quite unlike other molecules that usually are extremely easily detectable with SERS at the LLI, significant problems arose when dealing with these ionophores. One of the few classes of molecules that are challenging to detect through SERS at the LLI are dyes which do not have a strong affinity to gold, due to swamping of the SERS signal with fluorescence – as it turned out, morin and 4,4′,4″,4‴-(porphine-5,10,15,20-tetrayl)tetrakis(benzoic acid) are in this class of compounds (it was believed that the fact that their absorbance maxima were ≈400 nm that fluorescence could be avoided, but this was not the case). An obvious way to overcome such fluorescence would be through a reduction of the working concentrations with these molecules, however due to promising results with mercury detection with 1,8-diaminonaphthalene, it was decided to focus on mercury. Additionally, 1,10-dibenzyl-1,10-diaza-18-crown-6 was almost undetectable through SERS, the absence of appropriate functional groups meant that affinity to gold was extremely poor, though there is an increased band strength at 287 cm^{-1} (Figure 5.18) in the presence of Hg^{2+}, the low signal-to-noise in these spectra make it a poor reporter. Of the remaining two reporters pyrithione did showed some changes in the vibrational spectrum (Figure 5.19), however this change was relatively minor and showed little-to-no specificity (Figure 5.20), therefore once again, this was deemed unsuitable for ion detection. It is probable that the lack of selectivity of pyrithione arises from the fact that the thiol will chemisorb onto the gold surface, thereby making it unavailable to interact with ions. The remaining 1,8-diaminonaphthalene (1,8-DAN) however, was quite successful in VO^{2+} detection – a substantially altered spectra was observed in the presence of the ion (Figure 5.21).

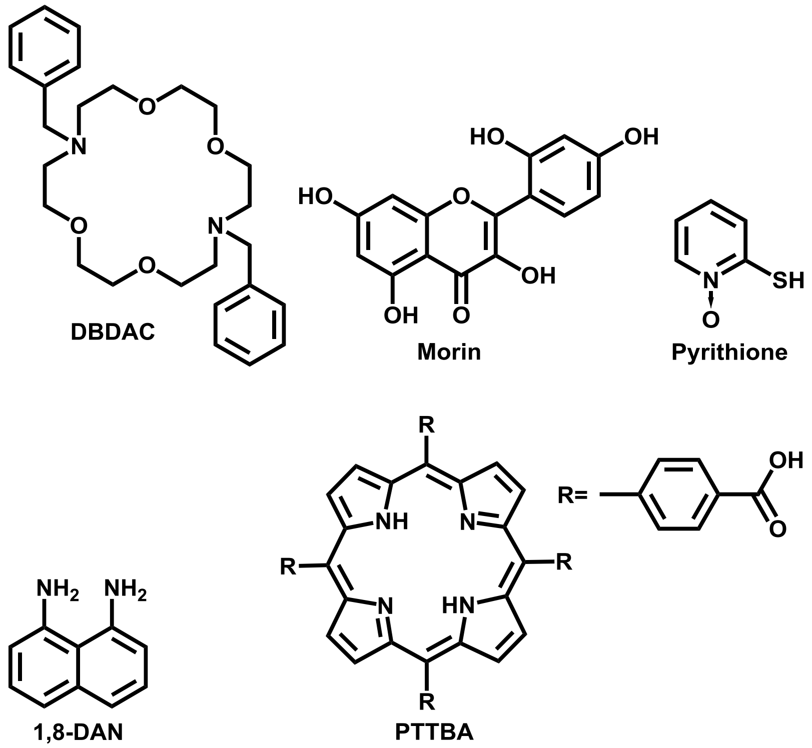

Figure 5.17 | Chemical structures of the "ionophores" tested.

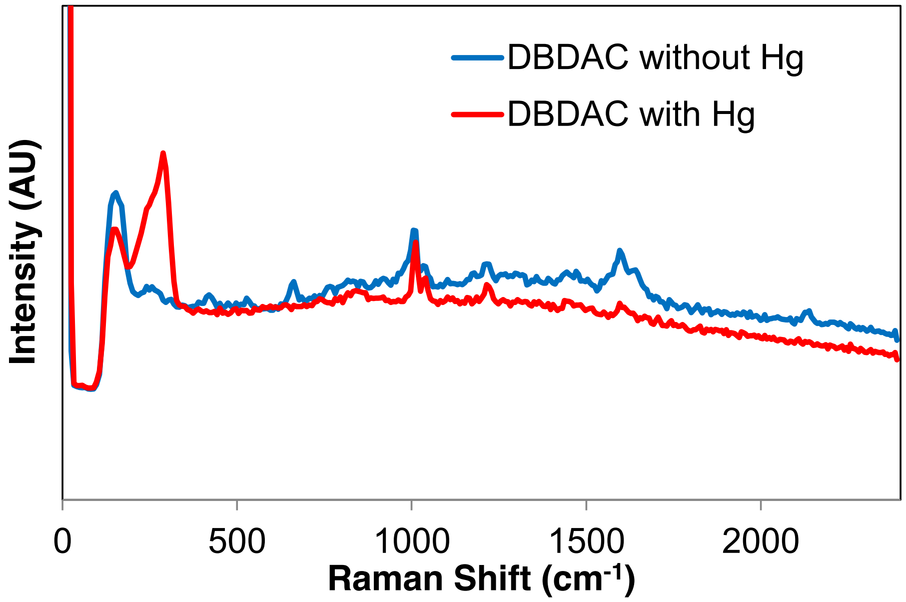

Figure 5.18 | DBDAC SERS spectra at the LLI in the presence and absence of Hg^{2+}. The samples contained 1 µmole of both DBDAC (dissolved in DCE) and $HgCl_2$ (dissolved in the aqueous phase).

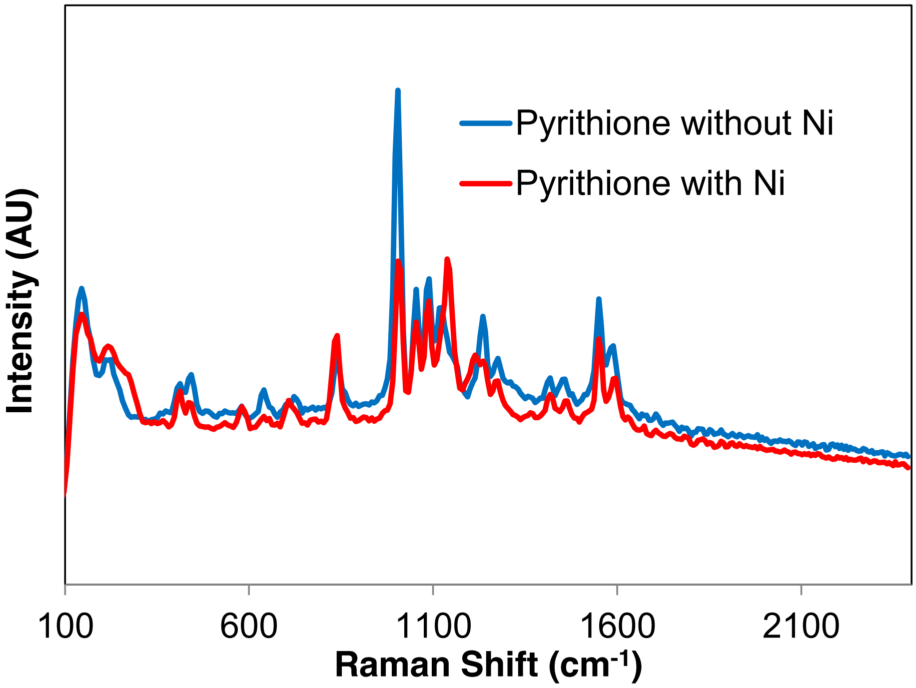

Figure 5.19 | SERS spectra of pyrithione in the presence and absence of Ni^{2+}. The sample contained 1 µmole of both pyrithione (dissolved in DCE) and $NiCl_2$ (dissolved in the aqueous phase).

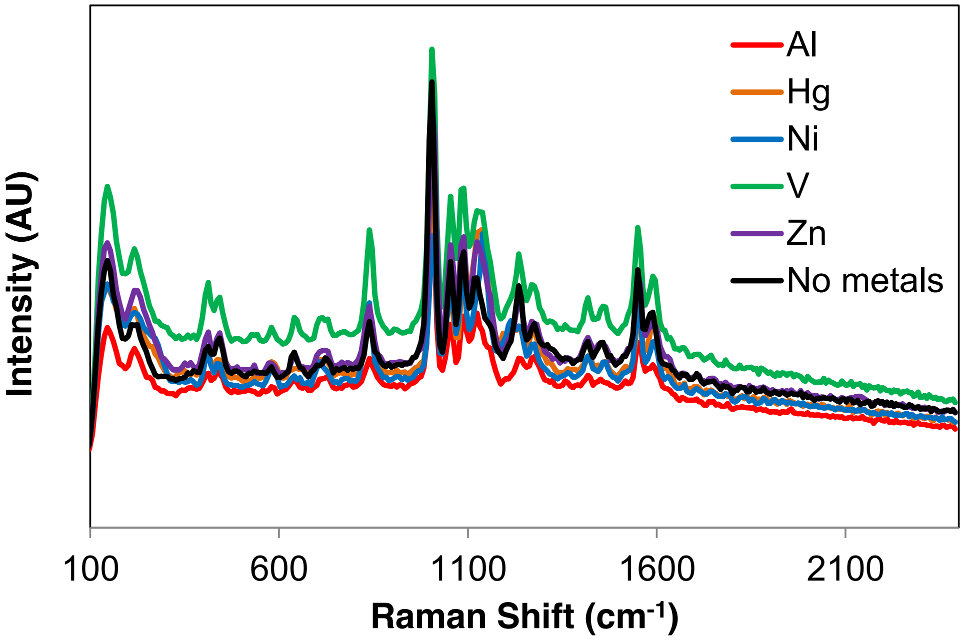

Figure 5.20 l Selectivity of pyrithione to other metal ions. It is clear that the changes are relatively minor and show very little specificity. 1 µmole of pyrithione (dissolved in DCE) and all of the ions (dissolved in the aqueous phase) was used.

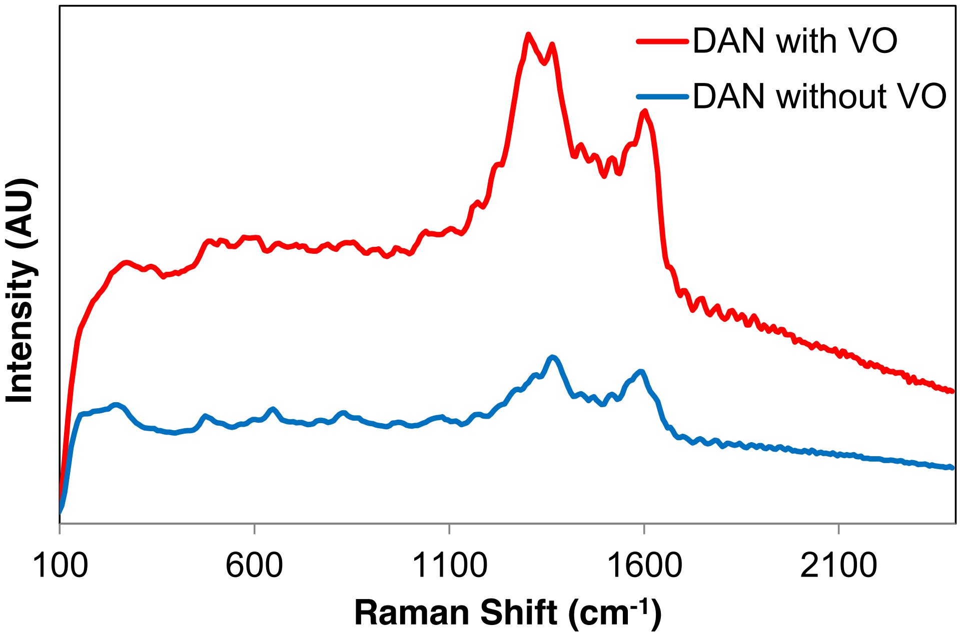

Figure 5.21 l Spectra of 1,8-DAN in the presence and absence of VO^{2+}. The samples contained 1 µmole of both 1,8-DAN (dissolved in DCE) and Vanadium(IV) oxide (dissolved in the aqueous phase).

However, the change observed with VO^+ was overshadowed by the change in the presence of Hg^{2+}. In fact the spectrum was not only altered, but the intensity of the signal increased by orders of magnitude with respect to 1,8-DAN in the absence of metal ions (Figure 5.22).

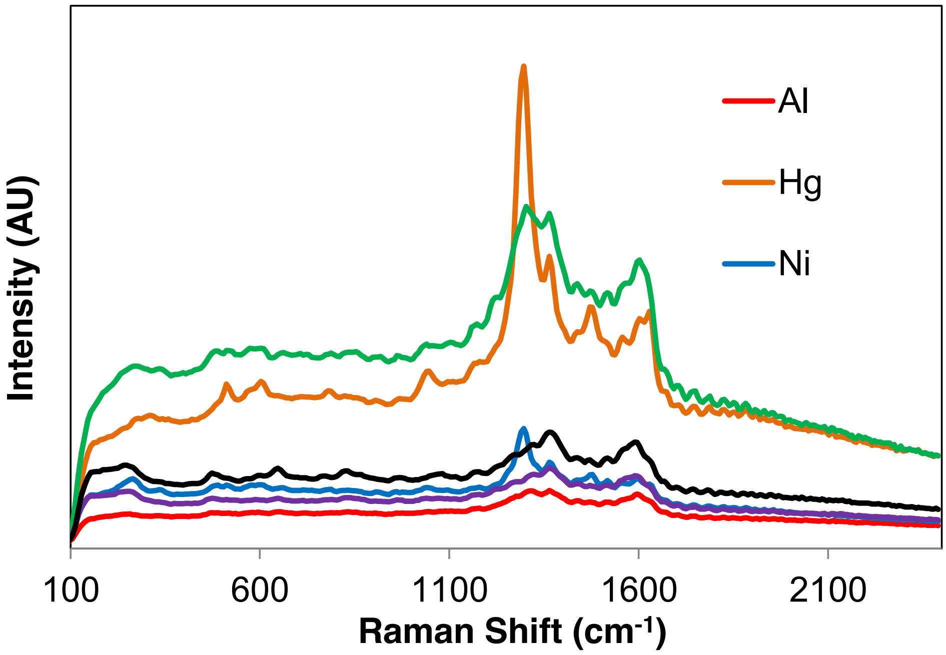

Figure 5.22 | Selectivity of 1,8-DAN to some metal ions. 1 µmole of both 1,8-DAN (dissolved in DCE) and the metal ions (dissolved in the aqueous phase) was used.

Raman Shift (cm^{-1})	Intensity	Assignment
272	vw	βC-NH2
511	w	Au-N
610	w	γNH2
788	vw	γCH ring
824	vw	skeletal bend
1046	w	γNH2 (wagg.)
1186	w	β NH2 (rock.)
1303	vs	C-N
1364	m sh	ring stretching
1471	m	C-H bend
1517	m	ring stretching
1556	w	NH2 (sciss.)
1628	m br	ring stretching

Table 5.1 | Peak assignement of 1,8-DAN in the presence of mercury ions.

Importantly, the spectrum of DAN in the presence of Hg^{2+} is not only drastically increased in intensity and displays different vibrations to DAN in the absence of metal ions, but the spectrum is different enough even to other metal ions, such that differentiation between for example Hg^{2+} and VO^{+} is trivial. From this limited selectivity/sensitivity test it was concluded that 1,8-DAN is a good candidate for the detection of Hg^{2+} ions through SERS at the LLI.

5.4.3 Sensitivity of 1,8-DAN to Hg

Interestingly, the intensity that was recorded in Figure 5.20 is actually quite weak for the Hg/1,8-DAN complex. A concentration dependence on 1,8-DAN/Hg (Figures 5.23 and 5.24) indicates that (counterintuitively) an increase in intensity is observed as the Hg^{2+} content is decreased from 1 µmole to 1 nmole, whereas a reverse (and more intuitive) trend is seen as function of 1,8-DAN content, that is a decreased signal intensity as the 1,8-DAN concentration is lowered.

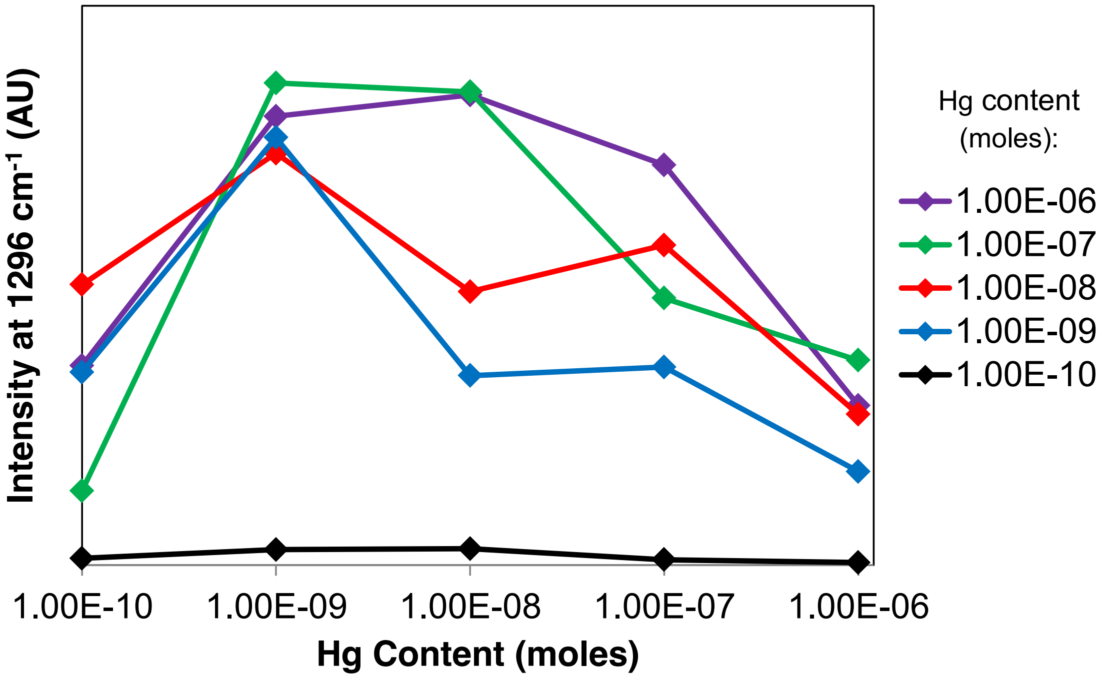

Figure 5.23 | SERS intensity at 1296 cm^{-1} as a function of Hg content at various 1,8-DAN contents.

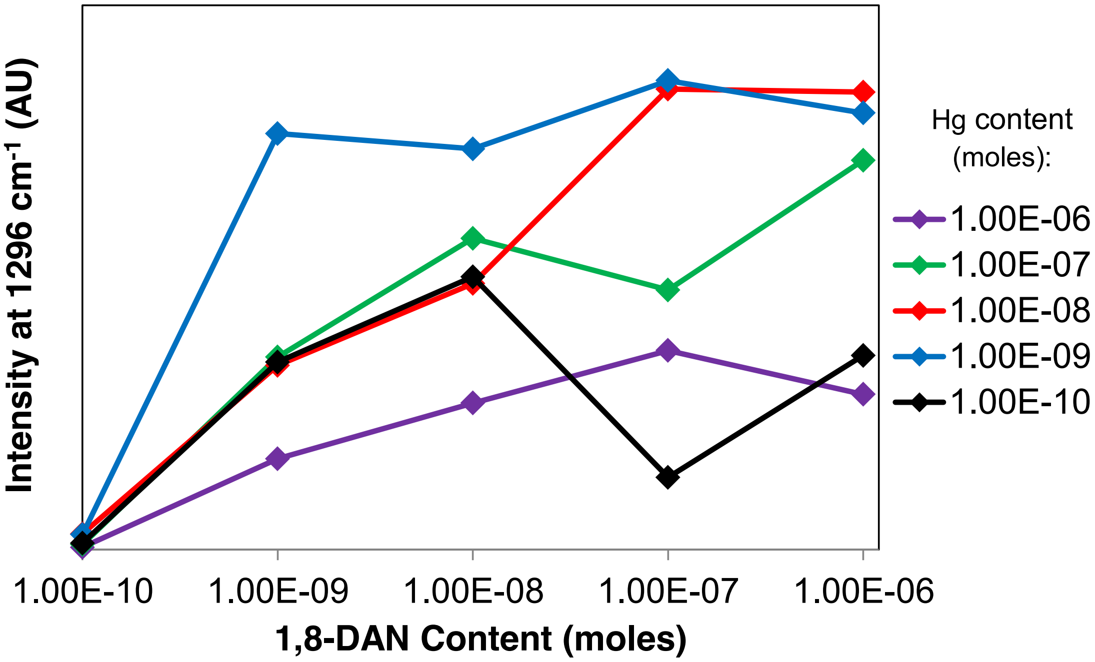

Figure 5.24 | SERS intensity at 1296 cm^{-1} as a function of 1,8-DAN content at various Hg concentrations.

It should of course be highlighted that while DAN appears to be extremely sensitive to Hg^{2+}, the lack of a clearly defined relationship between Hg concentration and intensity, as well as the fact that intensity is arbitary makes quantification of precise Hg concentrations challenging. Therefore the Hg detection that this system offers is a true/false type of measurement on the presence of Hg ions in the solution. An interesting observation about the intensity of the signal of the 1,8-DAN/Hg complex is not apparent from Figures 5.23/5.24. While working with MGITC, at the highest concentrations tested, the laser power would occasionally need to be attenuated 10 fold in order to prevent saturation of the detector. This is of course to be expected of SERRS, the intensity of which is sometimes enough for single molecule detection. DAN in the presence of Hg on the other hand, at the highest intensities (that is at 1 nmole Hg and 1-1000 nmole 1,8-DAN), required a 100 fold laser attenuation to prevent saturation of the detector. It remains unclear as to what is causing the intensity to increase so dramatically, however for the purposes of Hg detection this is highly beneficial as the magnitude of the intensity provides an immediate indication of the presence/absence of Hg ions.

5.4.4 Selectivity of 1,8-DAN to Hg

Nevertheless, sensitivity is perhaps less important than selectivity for the purposes of heavy metal ion detection through SERS. The indirectness of the measurement means that without selectivity it is impossible to identify what ion is being detected. The selectivity tests demonstrated in Figure 5.22 are promising, however these were carried out for only 5 species. A greater range of ions is therefore needed for a more conclusive test. For this purpose a further 15 ions were tested: Mg^{2+}, Mn^{2+}, Ni^{2+}, Pb^{2+}, Ti^{2+}, Co^{2+}, Ca^{2+}, Hg^{2+}, Al^{3+}, Zn^{2+}, Cr^{2+}, Fe^{2+}, Fe^{3+}, Ag^{+} and Cd^{2+}. For clarity, the intensity of the peak maximum of 1,8-DAN in the presence of the analytes was divided by the intensity of the maximum of pure 1,8-DAN. The ratios extracted are effectively the sensitivity of 1,8-DAN to the ions tested and are shown in Figure 5.25.

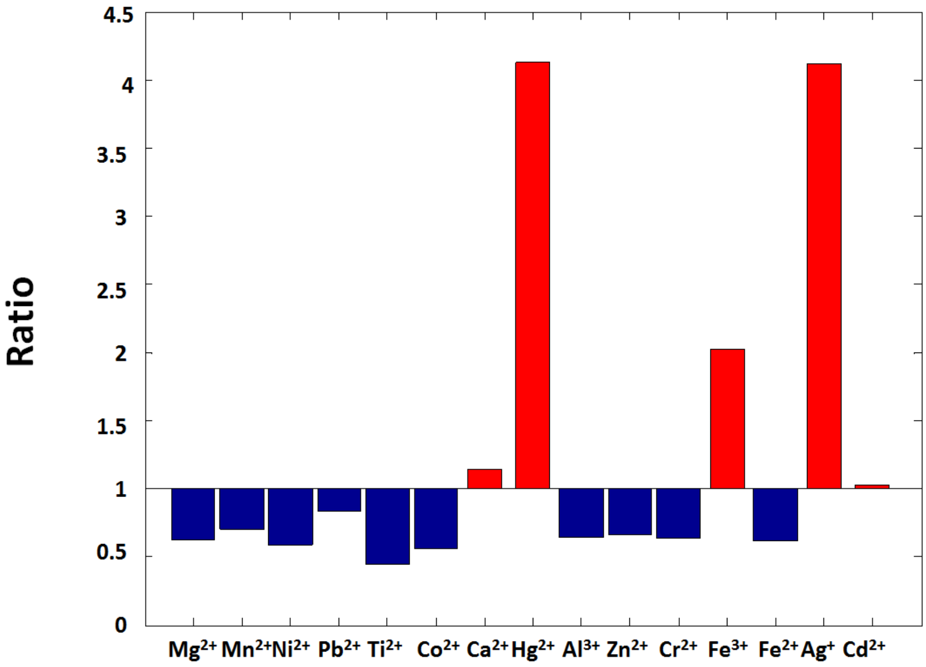

Figure 5.25 | Selectivity of 1,8-DAN to various ions.

It is clearly visible from Figure 5.25 that 3 main ions also give a dramatic increase in the SERS intensity – that is Hg^{2+}, Ag^{+} and to a lesser extent Fe^{3+}. Though 1,8-DAN is not exclusively selective to Hg, the result is nevertheless promising for detection applications with 1,8-DAN. A large portion of Fe^{3+} containing compounds are notoriously insoluble, while Ag^{+} is easily reduced – in other words, depending on the sample, these 2 ions may not be present in large enough quantities to give false positives. Nevertheless, the fact that 1,8-DAN is also sensitive to these ions is an important limitation. It should also be mentioned that an additional ion tested, Cu, gave rise to a green precipitate that fell out of solution, this observation is consistent with previously reported literature[87].

5.4.5 Airborne Hg detection

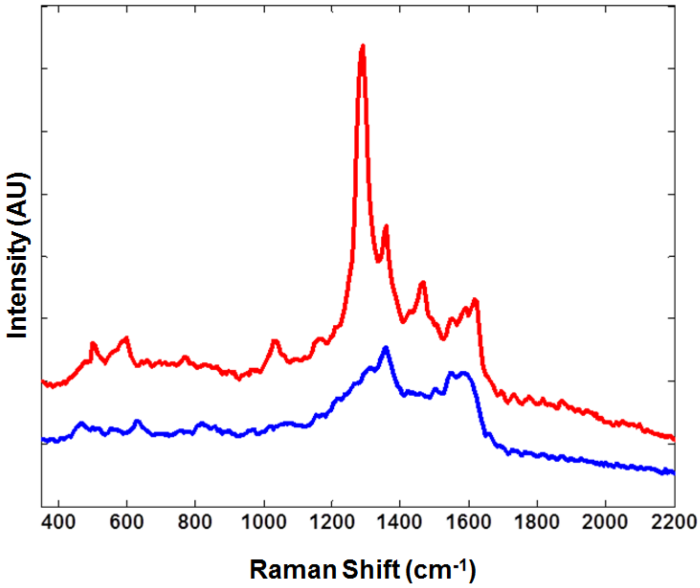

Figure 5.26 | Airborne Hg detection – the blue line represents NPs at the LAI (with the organic phase having evaporated); while the red line represents the same system, enclosed in a petri dish for 15 minutes in the presence of a non-contacting mercury droplet.

As was already demonstrated, upon evaporation of the organic phase, the LAI can serve as an airborne sensor. In line with those experiments, it was decided to test whether or not detection of airborne Hg is possible. It was found that after a 15 minute exposure of the NPs at the LAI, encapsulated in a petri dish, to a non-contacting mercury droplet, that the characteristic 1,8-DAN/Hg complex spectrum was seen (Figure 5.26). Additionally, it was found that if the NPs were initially allowed to dry onto the coverslip (*i.e.* at the solid-air interface) then no change in the spectrum occurred at the same experimental conditions. These results are surprising, as the airborne mercury will not be an ion but in its ground state (*i.e.* Hg(0) instead of Hg(II)) suggesting that the complex formation with 1,8-DAN is independent of the charge on mercury. Another implication of the lack of signal from the dried NP array is that the complex formation needs to occur in solution to give rise to a SERS spectrum. Despite it remaining unclear as to the mechanism by which this detection is possible, to the best of the author's knowledge, not only has airborne detection of Hg never been done with SERS, but in fact airborne detection of Hg with any method remains a challenging task with highly specialized equipment being required[88, 89].

5.4.6 Mechanism

1,8-DAN with gold NPs at the LLI/LAI has shown some fantastic opportunities for mercury detection, the system benefits from being highly sensitive, (with few exceptions) selective, cheap and fast. It is also (at this point) uniquely capable of providing airborne mercury detection. However as mentioned previously, the question of why DAN with gold NPs at the LLI is able to elucidate a drastically increased and altered SERS spectrum remains unanswered. Though some work has been carried out on a DAN/metal ion extraction technique[90-93], the literature remains scarce, with only a single publication carrying out SERS of DAN (although the aim of this paper was to investigate its polymerization at an electrode)[87]. In an attempt to understand the significance of 1,8-DAN, some analogues have been tested (Figures 5.27-5.29). These reporters fall into 3 categories – four of the tested analogues (Figure 5.27) displayed a dramatic increase and change in the spectrum in the presence of Hg, the spectra with and without Hg for these are shown; another 4 analogues (Figure 5.28) showed moderately increased/altered spectrum in the presence of Hg; however the majority of the analogues (Figure 5.29) showed no change in the presence of mercury.

The investigation of the mechanism of the spectral change of the DAN analogues in the presence of mercury is an ongoing research effort however, from Figures 5.27-5.29, it appears that some general trends can be deduced:

- The amine functionality is crucial
- The 1 position is preferential for the amine than the 2 position
- The amine must be directly attached to an aromatic ring
- The aromatic structure should contain more than 1 ring

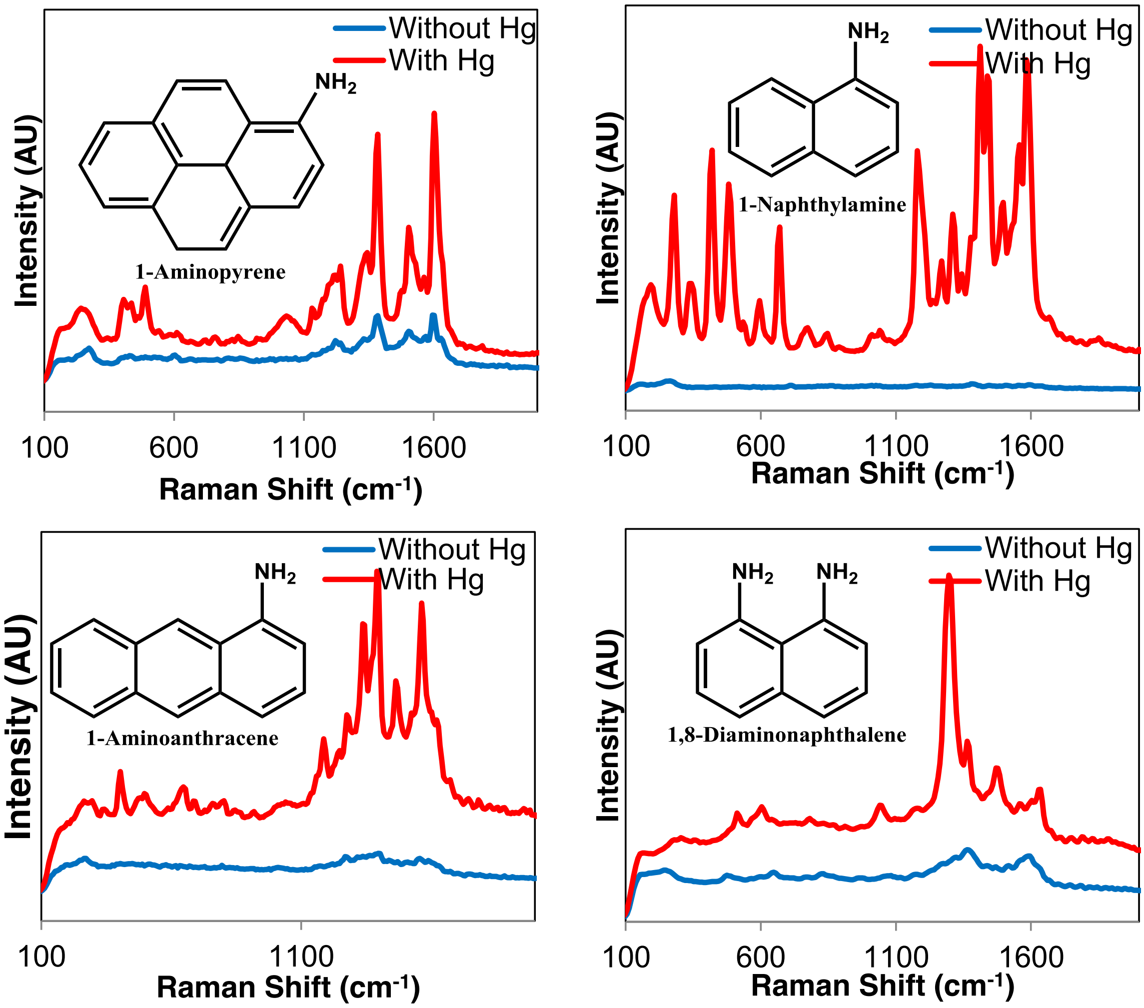

Figure 5.27 | Spectra in the presence and absence of Hg of some 1,8-DAN analogues with high sensitivity to Hg. For all compounds 1 µmole was used – all 1,8-DAN analogues were dissolved in DCE, while $HgCl_2$ was dissolved in the aqueous phase.

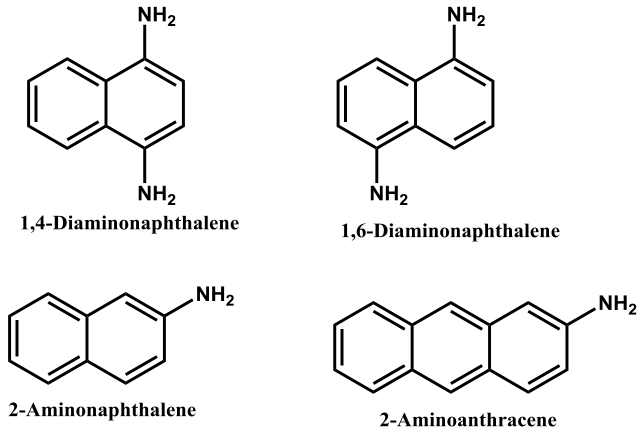

Figure 5.28 | 1,8-DAN analogues with moderate sensitivity to Hg.

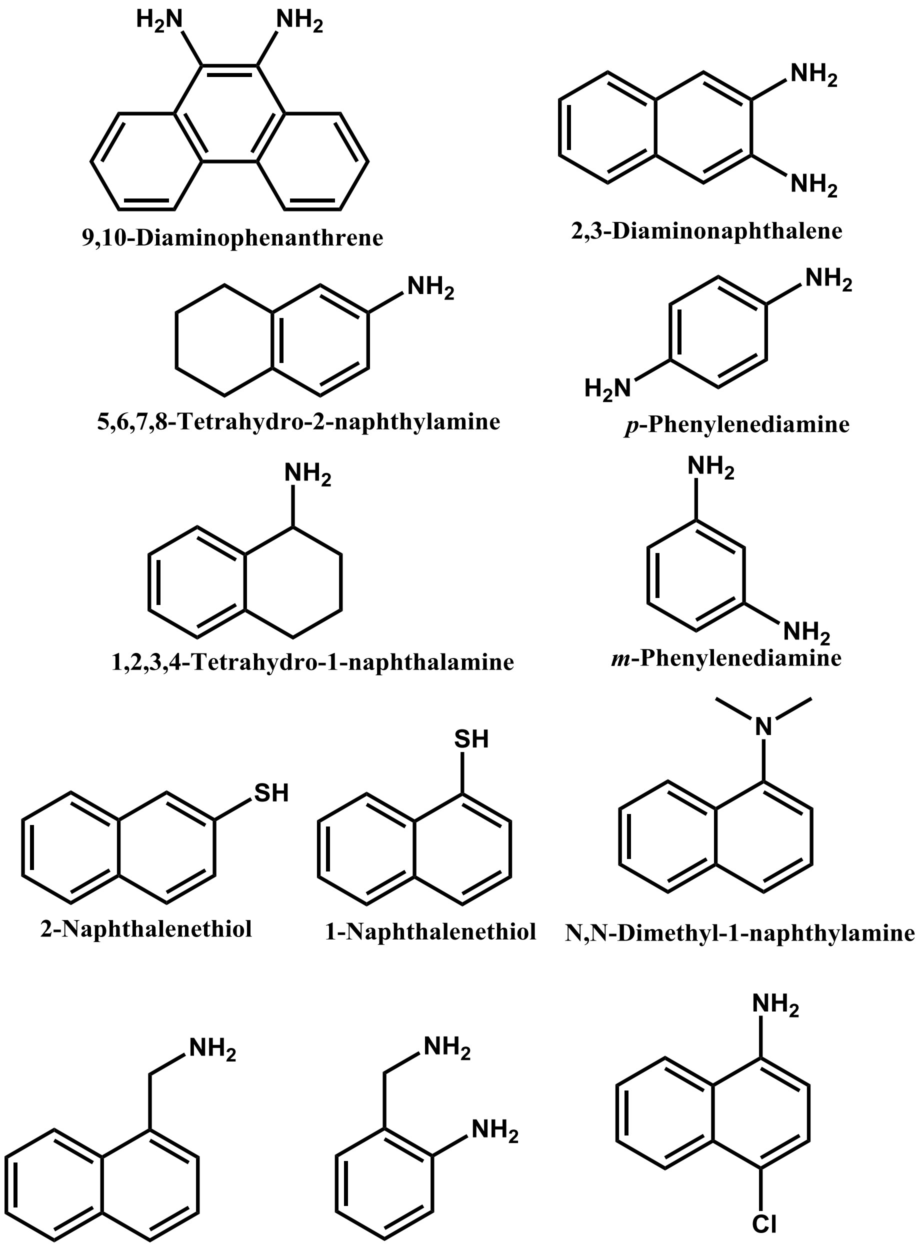

9,10-Diaminophenanthrene
2,3-Diaminonaphthalene
5,6,7,8-Tetrahydro-2-naphthylamine
p-Phenylenediamine
1,2,3,4-Tetrahydro-1-naphthalamine
m-Phenylenediamine
2-Naphthalenethiol
1-Naphthalenethiol
N,N-Dimethyl-1-naphthylamine
1-Naphthylmethylamine
2-Aminobenzylamine
1-Amino-4-chloronaphthalene

Figure 5.29 | 1,8-DAN analogues with little/no sensitivity to Hg.

There are currently 3 main hypotheses which are under investigation:

1. The adsorption of the DAN-analogues on the surface of the gold is promoted by Hg^{2+} through metallo-organic bonding and π-π stacking to achieve a greater density of the reporters, thereby not only increasing their effective concentration at the (hence the

signal increase), but also altering the molecular vibrations (hence the difference in the SERS spectra). The difference in the positions of amines with respect to the aromatic ring may induce some conformational constraints on the supramolecular assembly.

2. Mercury forms an amalgam with the gold, thereby changing the plasmonic properties of the NPs to yield an increased density of hotspots at the interface, leading to a drastic increase in the SERS intensity.
3. The mercury serves as a catalyst/reactant for the formation of a complex which has a resonance with the laser, leading to SERRS. The structure of the DAN-analogues may therefore influence the absorbance of the resulting molecule, leading to non-resonant SERS if mismatched. This hypothesis is at least partially supported by the formation of the green copper – 1,8-DAN precipitate, however no such precipitate was observed between Hg – DAN even at higher concentrations.

The π-π stacking/metallo-organic bonding hypothesis is perhaps the most convincing argument for the differences in the selectivity of the DAN-analogues to mercury, however it does not explain the dramatic signal intensity increase. The amalgam formation on the other hand could explain the difference in intensities, however it doesn't explain the selectivity. Though the formation of a complex that gives rise to SERRS could potentially explain both the signal intensity increase as well as the selectivity, control experiments in which 1,8-DAN in DCE was mixed with Hg^{2+} ions in the aqueous phase failed to show any species that had an absorbance in the visible spectrum. It may be that a combination of these factors (or an entirely different process altogether) contribute to observed sensitivity of 1,8-DAN at the LLI to Hg, however without additional evidence it is difficult to draw concrete conclusions about the mechanism.

5.5 Conclusions

The first part of this chapter demonstrated SERS from NPs at the LLI as a versatile, rapid, cheap (if the NPs are synthesised rather than bought commercially) and easy to fabricate detection platform that is capable of simultaneous-multiphase dual-analyte sensing, as well as detecting hydrophilic, hydrophobic, amphiphilic and airborne analytes. Despite the proof-of-principle nature of this work, it performed with real-world applications in mind and it is therefore hoped that it would find practical applications.

The second part of this chapter has introduced 1,8-DAN as a powerful reporter molecule for the detection of mercury. The fact that 1,8-DAN is hydrophobic, while mercury ions are hydrophilic means that NPs at the LLI/LAI are (as of this writing) uniquely capable of such detection. Additionally, to the best of the author's knowledge, the first airborne mercury detection using SERS has been demonstrated. Nevertheless, questions about the mechanism behind this detection remain unanswered and are currently under investigation.

5.6 References

1. Cecchini, M. P.; Turek, V. A.; Paget, J.; Kornyshev, A. A.; Edel, J. B. *Nat Mater* **2013,** 12, (2), 165-171.
2. Campion, A. *Chemical Society Reviews* **1998,** 27, (4), 241.
3. Katrin, K.; Harald, K.; Irving, I.; Ramachandra, R. D.; Michael, S. F. *Journal of Physics: Condensed Matter* **2002,** 14, (18), R597.
4. Doering, W. E.; Nie, S. *Analytical Chemistry* **2003,** 75, (22), 6171-6176.
5. Wustholz, K. L.; Henry, A.-I.; McMahon, J. M.; Freeman, R. G.; Valley, N.; Piotti, M. E.; Natan, M. J.; Schatz, G. C.; Duyne, R. P. V. *Journal of the American Chemical Society* **2010,** 132, (31), 10903-10910.
6. Talley, C. E.; Jackson, J. B.; Oubre, C.; Grady, N. K.; Hollars, C. W.; Lane, S. M.; Huser, T. R.; Nordlander, P.; Halas, N. J. *Nano Letters* **2005,** 5, (8), 1569-1574.
7. Tao, A.; Kim, F.; Hess, C.; Goldberger, J.; He, R.; Sun, Y.; Xia, Y.; Yang, P. *Nano Letters* **2003,** 3, (9), 1229-1233.
8. Yang, Z.; Chen, S.; Fang, P.; Ren, B.; Girault, H. H.; Tian, Z. *Physical Chemistry Chemical Physics* **2013**.
9. Alvarez-Puebla, R. A.; Agarwal, A.; Manna, P.; Khanal, B. P.; Aldeanueva-Potel, P.; Carbó-Argibay, E.; Pazos-Pérez, N.; Vigderman, L.; Zubarev, E. R.; Kotov, N. A.; Liz-Marzán, L. M. *Proceedings of the National Academy of Sciences* **2011,** 108, (20), 8157-8161.
10. Lim, D.-K.; Jeon, K.-S.; Hwang, J.-H.; Kim, H.; Kwon, S.; Suh, Y. D.; Nam, J.-M. *Nat Nanotechnol* **2011,** 6, (7), 452-460.
11. Rodríguez-Lorenzo, L.; Álvarez-Puebla, R. n. A.; Pastoriza-Santos, I.; Mazzucco, S.; Stéphan, O.; Kociak, M.; Liz-Marzán, L. M.; García de Abajo, F. J. *Journal of the American Chemical Society* **2009,** 131, (13), 4616-4618.
12. Kneipp, K.; Wang, Y.; Kneipp, H.; Perelman, L. T.; Itzkan, I.; Dasari, R. R.; Feld, M. S. *Physical Review Letters* **1997,** 78, (9), 1667.
13. Nie, S.; Emory, S. R. *Science* **1997,** 275, (5303), 1102-1106.
14. Kneipp, K.; Kneipp, H.; Kartha, V. B.; Manoharan, R.; Deinum, G.; Itzkan, I.; Dasari, R. R.; Feld, M. S. *Physical Review E* **1998,** 57, (6), R6281-R6284.
15. Bell, S. E.; Sirimuthu, N. M. *The Analyst* **2004,** 129, (11), 1032-6.
16. Kawano, R.; Osaki, T.; Sasaki, H.; Takinoue, M.; Yoshizawa, S.; Takeuchi, S. *Journal of the American Chemical Society* **2011,** 133, (22), 8474-8477.
17. Carter, J. C.; Brewer, W. E.; Angel, S. M. *Appl Spectrosc* **2000,** 54, (12), 1876-1881.
18. Li, P.-W.; Zhang, J.; Zhang, L.; Mo, Y.-J. *Vibrational Spectroscopy* **2009,** 49, (1), 2-6.
19. Mulvihill, M.; Tao, A.; Benjauthrit, K.; Arnold, J.; Yang, P. *Angewandte Chemie* **2008,** 120, (34), 6556-6560.
20. BurmáKyong, J.; KyuáLee, E. *Analyst* **2005,** 130, (7), 1009-1011.
21. Shende, C.; Gift, A.; Inscore, F.; Maksymiuk, P.; Farquharson, S. In *Inspection of pesticide residues on food by surface-enhanced Raman spectroscopy*, Providence, RI, USA, 2004; Bennedsen, B. S.; Chen, Y.-R.; Meyer, G. E.; Senecal, A. G.; Tu, S.-I., Eds. SPIE: Providence, RI, USA, pp 28-34.

22. Lee, D.; Lee, S.; Seong, G. H.; Choo, J.; Lee, E. K.; Gweon, D.-G.; Lee, S. *Appl Spectrosc* **2006,** 60, (4), 373-377.
23. Alak, A. M.; Vo-Dinh, T. *Analytica Chimica Acta* **1988,** 206, (0), 339-344.
24. Sylvia, J. M.; Janni, J. A.; Klein, J. D.; Spencer, K. M. *Analytical Chemistry* **2000,** 72, (23), 5834-40.
25. Xu, J. Y.; Wang, J.; Kong, L. T.; Zheng, G. C.; Guo, Z.; Liu, J. H. *Journal of Raman Spectroscopy* **2011,** 42, (9), 1728-1735.
26. Yang, L.; Ma, L.; Chen, G.; Liu, J.; Tian, Z. Q. *Chem-Eur J* **2010,** 16, (42), 12683-12693.
27. Sengupta, A.; Mujacic, M.; Davis, E. J. *Analytical and Bioanalytical Chemistry* **2006,** 386, (5), 1379-1386.
28. Grubisha, D. S.; Lipert, R. J.; Park, H.-Y.; Driskell, J.; Porter, M. D. *Analytical Chemistry* **2003,** 75, (21), 5936-5943.
29. Premasiri, W. R.; Moir, D. T.; Klempner, M. S.; Krieger, N.; Jones, G.; Ziegler, L. D. *The Journal of Physical Chemistry B* **2004,** 109, (1), 312-320.
30. Nikoobakht, B.; El-Sayed, M. A. *The Journal of Physical Chemistry A* **2003,** 107, (18), 3372-3378.
31. Schwartzberg, A. M.; Grant, C. D.; Wolcott, A.; Talley, C. E.; Huser, T. R.; Bogomolni, R.; Zhang, J. Z. *The Journal of Physical Chemistry B* **2004,** 108, (50), 19191-19197.
32. Moskovits, M. *Journal of Raman Spectroscopy* **2005,** 36, (6â 7), 485.
33. Duan, J.; Yang, M.; Lai, Y.; Yuan, J.; Zhan, J. *Analytica Chimica Acta* **2012,** 723, (0), 88-93.
34. Lu, W.; Arumugam, S. R.; Senapati, D.; Singh, A. K.; Arbneshi, T.; Khan, S. A.; Yu, H.; Ray, P. C. *ACS Nano* **2010,** 4, (3), 1739-1749.
35. Vigderman, L.; Zubarev, E. R. *Langmuir* **2012,** 28, (24), 9034.
36. Aroca, R. F.; Alvarez-Puebla, R. A.; Pieczonka, N.; Sanchez-Cortez, S.; Garcia-Ramos, J. V. *Advances in Colloid and Interface Science* **2005,** 116, (1–3), 45-61.
37. Jurasekova, Z.; Sanchez-Cortes, S.; Tamba, M.; Torreggiani, A. *Vibrational Spectroscopy* **2011,** 57, (1), 42-48.
38. Zijlstra, P.; Paulo, P. M.; Orrit, M. *Nat Nanotechnol* **2012,** 7, (6), 379-382.
39. Sharma, V.; Park, K.; Srinivasarao, M. *Proceedings of the National Academy of Sciences* **2009,** 106, (13), 4981-4985.
40. Jana, N. R.; Gearheart, L.; Murphy, C. J. *The Journal of Physical Chemistry B* **2001,** 105, (19), 4065-4067.
41. Banholzer, M. J.; Millstone, J. E.; Qin, L.; Mirkin, C. A. *Chemical Society Reviews* **2008,** 37, (5), 885-897.
42. Gunnarsson, L.; Bjerneld, E. J.; Xu, H.; Petronis, S.; Kasemo, B.; Kall, M. *Applied Physics Letters* **2001,** 78, (6), 802-804.
43. Lu, Y.; Liu, G. L.; Kim, J.; Mejia, Y. X.; Lee, L. P. *Nano Letters* **2004,** 5, (1), 119-124.
44. Li, K.; Clime, L.; Cui, B.; Veres, T. *Nanotechnology* **2008,** 19, (14), 145305.
45. Lin, X.-M.; Cui, Y.; Xu, Y.-H.; Ren, B.; Tian, Z.-Q. *Analytical and bioanalytical chemistry* **2009,** 394, (7), 1729-1745.
46. Zou, S. Z.; Chen, Y. X.; Mao, B. W.; Ren, B.; Tian, Z. Q. *Journal of Electroanalytical Chemistry* **1997,** 424, (1–2), 19-24.
47. Sauer, G.; Brehm, G.; Schneider, S. *Journal of Raman Spectroscopy* **2004,** 35, (7), 568-576.
48. Kudelski, A. *Chemical Physics Letters* **2005,** 414, (4–6), 271-275.
49. Theiss, J.; Pavaskar, P.; Echternach, P. M.; Muller, R. E.; Cronin, S. B. *Nano Letters* **2010,** 10, (8), 2749-2754.
50. Sánchez-Iglesias, A.; Aldeanueva-Potel, P.; Ni, W.; Pérez-Juste, J.; Pastoriza-Santos, I.; Alvarez-Puebla, R. A.; Mbenkum, B. N.; Liz-Marzán, L. M. *Nano Today* **2010,** 5, (1), 21-27.
51. Chen, A.; DePrince, A. E.; Demortière, A.; Joshi-Imre, A.; Shevchenko, E. V.; Gray, S. K.; Welp, U.; Vlasko-Vlasov, V. K. *Small* **2011,** 7, (16), 2365-2371.

52. Cintra, S.; Abdelsalam, M. E.; Bartlett, P. N.; Baumberg, J. J.; Kelf, T. A.; Sugawara, Y.; Russell, A. E. *Faraday Discussions* **2006,** 132, 191-199.
53. Mahajan, S.; Baumberg, J. J.; Russell, A. E.; Bartlett, P. N. *Phys. Chem. Chem. Phys.* **2007,** 9, (45), 6016-6020.
54. Li, W.-D.; Ding, F.; Hu, J.; Chou, S. Y. *Opt. Express* **2011,** 19, (5), 3925-3936.
55. Turek, V. A.; Cecchini, M. P.; Paget, J.; Kucernak, A. R.; Kornyshev, A. A.; Edel, J. B. *ACS Nano* **2012,** 6, (9), 7789-7799.
56. Smith, T. *Journal of Colloid and Interface Science* **1980,** 75, (1), 51-55.
57. XuanáQuang, L.; HunáSeong, G.; JunáDo, K. *Lab on a Chip* **2008,** 8, (12), 2214-2219.
58. Li, F.; Wang, J.; Lai, Y.; Wu, C.; Sun, S.; He, Y.; Ma, H. *Biosensors and Bioelectronics* **2012**.
59. Yuan, Y.-X.; Ling, L.; Wang, X.-Y.; Wang, M.; Gu, R.-A.; Yao, J.-L. *Journal of Raman Spectroscopy* **2007,** 38, (10), 1280-1287.
60. Wu, S.-P.; Chen, Y.-P.; Sung, Y.-M. *Analyst* **2011,** 136, (9), 1887-1891.
61. Chai, F.; Wang, C.; Wang, T.; Li, L.; Su, Z. *Acs Appl Mater Inter* **2010,** 2, (5), 1466-1470.
62. Liu, C.-W.; Hsieh, Y.-T.; Huang, C.-C.; Lin, Z.-H.; Chang, H.-T. *Chemical Communications* **2008**, (19), 2242-2244.
63. Wang, G.; Lim, C.; Chen, L.; Chon, H.; Choo, J.; Hong, J.; deMello, A. *Analytical and Bioanalytical Chemistry* **2009,** 394, (7), 1827-1832.
64. Wang, Y.; Irudayaraj, J. *Chemical Communications* **2011,** 47, (15), 4394-4396.
65. Luo, Y.; Li, K.; Wen, G.; Liu, Q.; Liang, A.; Jiang, Z. *Plasmonics* **2012,** 7, (3), 461-468.
66. Ren, W.; Zhu, C.; Wang, E. *Nanoscale* **2012,** 4, (19), 5902-5909.
67. Zamarion, V. M.; Timm, R. A.; Araki, K.; Toma, H. E. *Inorg Chem* **2008,** 47, (8), 2934-2936.
68. Lee, S. J.; Moskovits, M. *Nano Letters* **2010,** 11, (1), 145-150.
69. Crane, L. G.; Wang, D.; Sears, L. M.; Heyns, B.; Carron, K. *Analytical Chemistry* **1995,** 67, (2), 360-364.
70. Sheng, C.; Zhao, H.; Gu, F.; Yang, H. *Journal of Raman Spectroscopy* **2009,** 40, (9), 1274-1278.
71. Tan, E.; Yin, P.; Lang, X.; Zhang, H.; Guo, L. *Spectrochimica Acta Part A: Molecular and Biomolecular Spectroscopy* **2012,** 97, (0), 1007-1012.
72. Wang, X.; Shen, Y.; Xie, A.; Chen, S. *Materials Chemistry and Physics* **2013,** 140, (2–3), 487-492.
73. Cecchini, M. P.; Hong, J.; Lim, C.; Choo, J.; Albrecht, T.; deMello, A. J.; Edel, J. B. *Analytical Chemistry* **2011,** 83, (8), 3076-3081.
74. Cecchini, M. P.; Stapountzi, M. A.; McComb, D. W.; Albrecht, T.; Edel, J. B. *Analytical Chemistry* **2011,** 83, (4), 1418-1424.
75. Cecchini, M. P.; Wiener, A.; Turek, V. A.; Chon, H.; Lee, S.; Ivanov, A. P.; McComb, D. W.; Choo, J.; Albrecht, T.; Maier, S. A. *Nano letters* **2013,** 13, (10), 4602-4609.
76. Gordon, K. C.; McGarvey, J. J.; Taylor, K. P. *The Journal of Physical Chemistry* **1989,** 93, (18), 6814-6817.
77. Kim, J.; Lee, J. E.; Lee, J.; Jang, Y.; Kim, S.-W.; An, K.; Yu, J. H.; Hyeon, T. *Angewandte Chemie* **2006,** 118, (29), 4907-4911.
78. Liong, M.; Lu, J.; Kovochich, M.; Xia, T.; Ruehm, S. G.; Nel, A. E.; Tamanoi, F.; Zink, J. I. *ACS Nano* **2008,** 2, (5), 889-896.
79. Piorek, B. D.; Lee, S. J.; Santiago, J. G.; Moskovits, M.; Banerjee, S.; Meinhart, C. D. *Proceedings of the National Academy of Sciences* **2007,** 104, (48), 18898-18901.
80. Andreou, C.; Hoonejani, M. R.; Barmi, M. R.; Moskovits, M.; Meinhart, C. D. *ACS Nano* **2013,** 7, (8), 7157-7164.
81. Xie, Y.; Wang, X.; Han, X.; Xue, X.; Ji, W.; Qi, Z.; Liu, J.; Zhao, B.; Ozaki, Y. *Analyst* **2010,** 135, (6), 1389-1394.
82. Gupta, V. K.; Jain, A. K.; Maheshwari, G. *Talanta* **2007,** 72, (4), 1469-1473.
83. Nolan, E. M.; Jaworski, J.; Racine, M. E.; Sheng, M.; Lippard, S. J. *Inorg Chem* **2006,** 45, (24), 9748-9757.

84. Singh, L.; Bhatnagar, J. *Sensors-Basel* **2003,** 3, (9), 393-403.
85. Gupta, V. K.; Chandra, S.; Agarwal, S. *INDIAN JOURNAL OF CHEMISTRY SECTION A* **2003,** 42, (4), 813-818.
86. Akbari, A.; Mousavi, M. F.; Shamsipur, M.; Rahmanifar, M. S. *Talanta* **2003,** 60, (4), 853-859.
87. Palys, B. J.; Bukowska, J.; Jackowska, K. *Journal of electroanalytical chemistry* **1997,** 428, (1–2), 19-24.
88. Bahns, J. T.; Lynds, L.; Stwalley, W. C.; Simmons, V.; Robinson, T.; Bililign, S. *Optics Letters* **1997,** 22, (10), 727-729.
89. Nerentorp, M.; Kyllonen, K.; Wängberg, I.; Kuronen, P. *E3S Web of Conferences* **2013,** 1, 27003.
90. Rutkowska, J.; Kilian, K.; Pyrzynska, K. *Eur Polym J* **2008,** 44, (7), 2108-2114.
91. Kilian, K.; Pyrzynska, K. *Reactive and Functional Polymers* **2008,** 68, (5), 974-980.
92. Ismail *, T. M. A. *J Coord Chem* **2005,** 58, (2), 141-151.
93. Pałys, B. J.; Skompska, M.; Jackowska, K. *Journal of electroanalytical chemistry* **1997,** 433, (1–2), 41-48.

Chapter 6: Conclusions and Outlook

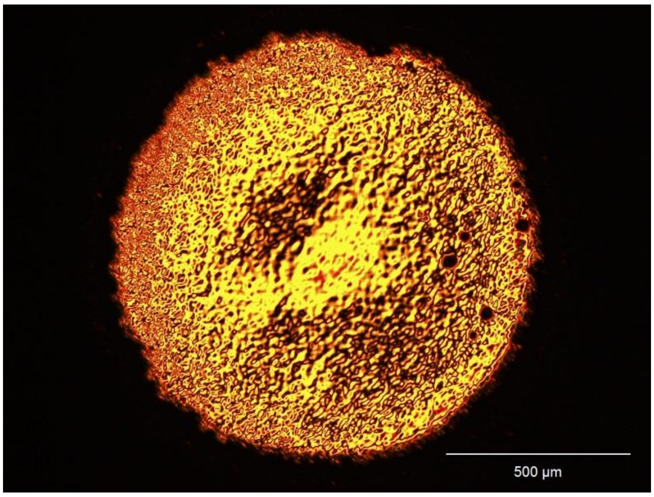

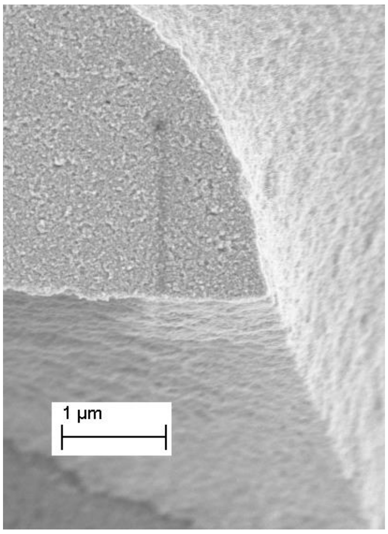

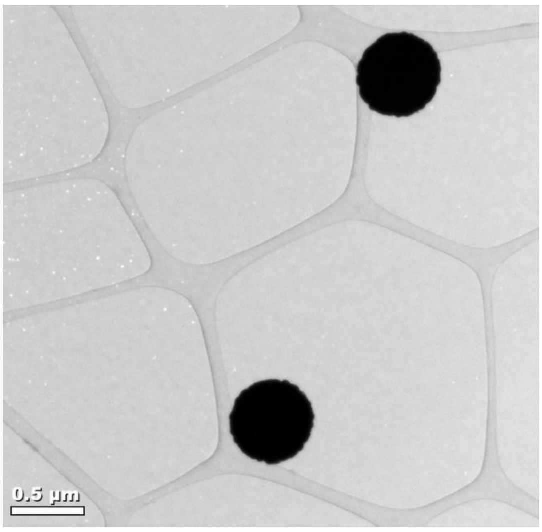

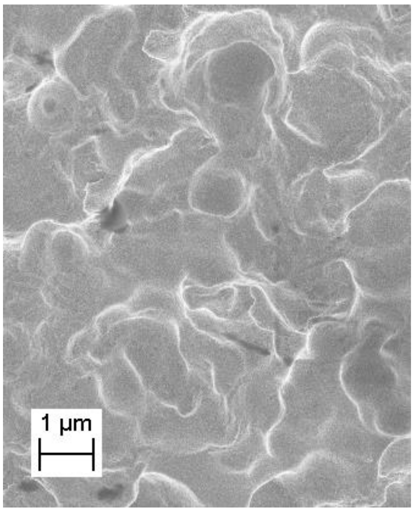

6.1 Controlled inter-particle separation

The initial project aim of studying the optical properties of NP arrays at the LLI with controlled coverage and inter-particle separations was partially successful. Centrifugation was demonstrated as a (surprisingly) novel method to aid the spontaneous self-assembly of the particles. The benefit of using centrifugation for NP adsorption is predominantly for time saving purposes. However, in principle, due to the controlled universal force that is acting on the particles, centrifugation may allow for some interesting fundamental studies. For example, it may be possible to study whether or not an energy barrier exists for NP adsorption – this is likely to be negligible at low particle coverage, however is likely to increase as more particles adsorb. Additionally, it may be possible to study whether or not a centrifugal force is able to desorb the particle – in other words, if the NPs are first adsorbed onto a LLI with a less dense organic phase (e.g. toluene instead of DCE), centrifugation may promote desorption from the interface and redispersion of the NPs into the aqueous phase.

Additionally, it was demonstrated that there is a dependence of inter-particle separation on the ionic strength of the solution. From an experimental perspective this presents several avenue of further exploration. It would be interesting to determine what effect bivalent/trivalent cations/anions have on the separation and particle adsorption. Importantly, the system is highly dependent on the functionality of the particles – the aliphatic backbone of the 12-MDDA is believed to play a key role in the ability of the particles to remain unaggregated. An obvious further experiment would therefore be to study the importance of this. For example, by changing the length of the spacer group it is likely that the stability of the particles will be altered. Furthermore, Chapter 3 demonstrated controlled separation of 16 nm gold particles, attempts to control the separation of MDDA stabilized 43 gold particles where not successful – 2D aggregation was observed for these. It may therefore be informative to study the adsorption and LSPR peaks of NPs as a function of size as well as ionic strength.

Finally, Chapter 3 demonstrated novel optical properties of plasmonic particles at the LLI. Through the plasmon ruler, the inter-particle separations were estimated. This may have important consequences for researchers in the field as it demonstrates an easy way to extract structural information from NPs directly at the LLI. The fast, simple, intuitive and inexpensive technique of simply transmitting a halogen light source through a droplet coated with NPs may add to the arsenal of experimentalists working on understanding the behaviour of NPs at the LLI.

There are however, some aspects of the work that have yet to be clarified. Firstly, theoretical predictions of the reflection coefficients are an order of magnitude higher[1, 2] than what was experimentally observed. The recent publication by Fang *et al*[3]. reported reflectivities of gold particles at the LLI of as high as 40%. This was however carried out using 60 nm particles at the water-(heptane+DCE) interface at a 65° incident angle in which the particles are likely to be in 2D close-packed arrangement, therefore the two systems may not be directly comparable. Nevertheless, it would interesting to carry out a more detailed study on the reflectivities. Finally, the main challenge that remains for this work is to accurately correlate the LSPR maximum as a function of the experimentally determined inter-particle separation. The estimation of this parameter for the work made several potentially inaccurate assumptions that may mean that the actual separations would be substantially altered. This is aimed to be established in a repeat experiment at Diamond later on in the year.

6.2 High density aqueous solutions

Perhaps the most novel aspect of the work is in the high density aqueous solution. It was demonstrated that aqueous densities exceeding 4.5 g/cm^3 can be easily achieved using centrifugation of an aqueous NP solution and a more dense organic phase. It is interesting to note that this value is very unlikely to be limiting. Though already mentioned, by using 100 nm Ir/Os NPs with a 5 surface-surface inter-particle separation density above mercury could, in principle, be achieved. In other words rather than the densest aqueous phase at room temperature, this technique could potentially allow a new record of liquid densities.

The main challenge that this work faces is however finding practical applications. Despite demonstrating novel material properties, it is not immediately apparent what uses such properties may have. Though high density solutions may potentially have uses for mineralogy, the main limitations would be associated costs (though these could be pushed down by using less expensive particles – e.g. if monodispersity is not essential, milled gold particles are substantially cheaper or perhaps even a different chemical composition altogether could be used (such as tungsten)). Though the high densities of such solutions is established, their main application may lie in nanofluids. The high gold fraction (which could be made substantially higher) together with a potential rigidity between the particles and a homogeneous dispersion may enable some fascinating studies on their thermal conductivities.

Finally the NP purification and size separation by this method has been shown to be extremely efficient. This is in and of itself a practical application of these solutions, however a more interesting story may be in a subtly altered study. Instead of purifying the particles, from contaminants it may be more worthwhile using the particles to purify a precious material. An obvious example of this would be to attempt to purify DNA from cell-lysate. Specificity groups would of course need to be introduced to the gold particles, however if successful, this may have the potential to revolutionize DNA/protein extraction.

6.3 SERS at the LLI

The demonstration of the LLI as a versatile, cheap, simple and effective SERS platform was performed. The simple fact of a SERS signal at the LLI is of course not in and of itself novel – in fact this was reported simultaneously with the seminal 'MELLF' paper that was the first demonstration of plasmonic nanoparticles at the liquid-liquid interface by Yogev and Efrima[4]. Nevertheless, the main novelty of the work demonstrated in chapter 5 is that it was realized that the simultaneous detection of aqueous and organic chemicals was possible. In addition, the evaporation of the organic phase leads to a facile airborne detector. Coupled with an efficient analyte capture and concentration mechanism, the detection platform is directly suitable for real-world applications. The lack of mechanical rigidity of the LLI is not a significant issue, provided that a relatively small aqueous droplet wets a glass coverslip – the effects of gravity under these conditions are not necessarily important, if handled with care.

Finally, the simultaneous dual-phase detection capabilities were exploited for the detection of aqueous and airborne mercury. The use of 1,8-DAN (and a few of its analogues) dissolved in the organic phase with mercury ions in the aqueous phase led to a dramatic increase in SERS intensity as compared to 1,8-DAN without mercury. In addition, the system shows reasonable selectivity for mercury. Aside from demonstrating the benefits of using a LLI/LAI as a SERS platform, the first (to the best of the authors knowledge) SERS based airborne detection of mercury was achieved. This system therefore has an opportunity to establish itself as a versatile, sensitive and selective route to real-world mercury detection applications. However, perhaps more important, is the general approach – by taking advantage of the LLI it is possible to tap into some otherwise inaccessible chemistry. One such system that would be worth investigating in more detail is catalysis.

6.4 References

1. Kornyshev, A. A.; Marinescu, M.; Paget, J.; Urbakh, M. *Physical Chemistry Chemical Physics* **2012,** 14, (6).
2. Flatté, M. E.; Kornyshev, A. A.; Urbakh, M. *The Journal of Physical Chemistry C* **2010,** 114, (4), 1735-1747.
3. Fang, P.-P.; Chen, S.; Deng, H.; Scanlon, M. D.; Gumy, F.; Lee, H. J.; Momotenko, D.; Amstutz, V.; Cortés-Salazar, F.; Pereira, C. M.; Yang, Z.; Girault, H. H. *ACS Nano* **2013,** 7, (10), 9241-9248.
4. Yogev, D.; Efrima, S. *The Journal of Physical Chemistry* **1988,** 92, (20), 5761-5765.

Plasmonic Ruler at the Liquid−Liquid Interface

Vladimir A. Turek, Michael P. Cecchini, Jack Paget, Anthony R. Kucernak, Alexei A. Kornyshev,* and Joshua B. Edel*

Department of Chemistry, Chemical Physics Section, Imperial College London, Exhibition Road, South Kensington, London, SW7 2AZ, United Kingdom

ABSTRACT We report on a simple, fast, and inexpensive method to study adsorption and desorption of metallic nanoparticles at a liquid/liquid interface. These interfaces provide an ideal platform for the formation of two-dimensional monolayers of nanoparticles, as they form spontaneously and are defect-correcting, acting as 2D "nanoparticle traps". Such two-dimensional, self-assembled nanoparticle arrays have a vast range of potential applications in displays, catalysis, plasmonic rulers, optoelectronics, sensors, and detectors. Here, we show that 16 nm diameter gold nanoparticles can be controllably adsorbed to a water/1,2-dichloroethane interface, and that we can control the average interparticle spacing at the interface over the range 6−35 nm. The particle density and average interparticle spacing are experimentally assessed by measuring the optical plasmonic response of the nanoparticles in the bulk and at the interface and by comparing the experimental data with existing theoretical results.

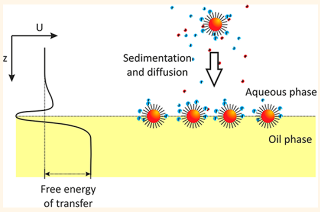

KEYWORDS: liquid−liquid interface · plasmonic ruler · nanoparticles · self assembly · centrifugation

Nanoparticle (NP) adsorption at liquid−liquid interfaces (LLIs) is a well-established phenomenon that was first reported independently more than a century ago by Ramsden and Pickering.[1,2] More recently, plasmonic NPs at LLIs have been reported to possess novel "metal liquid like" properties[3] that have sparked a renewed interest. Driven by the growing need for cheap, fast and reproducible bottom-up assembly for nanotechnological applications, the unique optical,[4] magnetic,[5] electrical,[6] and chemical[7] properties of such films has attracted intensive research in a rapidly growing field.

NP assemblies at the LLI hold great promise in diverse fields ranging from electrovariable optics[8] to templates for hierarchical self-assembly,[9] and plasmonic rulers.[10] One of the main benefits of localizing NPs at a LLI for these applications is the aforementioned self-assembly.[11] Currently, most technological applications of nanoassemblies are based around solid-state fabrication. Although the control that the solid interface offers is unparalleled, it does have several drawbacks when compared to a LLI. One such drawback is topological defects which can emerge either during or post-manufacturing and are extremely difficult to correct. In fact, it is often easier to fabricate a new device rather than attempting to repair defects. Inversely, a LLI system has the ability to self-correct without any external manipulation.[12]

An additional drawback of a solid state system becomes clear when introducing the exciting concept of a plasmonic ruler.[13−15] Precise NP spatial information can be extracted through localized plasmon coupling. This concept has been demonstrated for 2D arrays,[10] particle dimers[14] at solid interfaces and tethered NPs in bulk solution.[16] The plasmonic ruler has even recently been demonstrated to provide 3-dimensional structural information.[17] The use of plasmonic particles at the LLI should therefore provide information on the structural characteristics of these assemblies. The large body of work on plasmonic NPs at LLIs has typically focused on close packed arrays and is broadly divided into spectroscopic studies for sensing[18,19] (e.g., SERS and SPR) or use of the LLI as a template for 2D self-assembly.[20]

Despite our growing theoretical understanding of these assemblies,[21] there are numerous questions that remain unanswered. It has become evident through theory,[22,23] simulation,[24,25] and key experiments[26−28] that the simple electrostatic and van der Waals forces that DLVO (Derjaguin−Landau−Verwey−Overbeek) theory considers for NPs in bulk solution is not sufficient to explain the stability of NPs at the LLI. NP interactions at the LLI are governed by interfacial tension stabilization,[8] long-range dipole−dipole interactions resulting from an asymmetric counterion cloud,[29] hydration forces for the NP immersed in the two fluids,[30] capillary forces

* Address correspondence to
a.kornyshev@imperial.ac.uk,
joshua.edel@imperial.ac.uk.

Received for review April 22, 2012
and accepted August 19, 2012.

10.1021/nn302941k

resulting from deformations of the interface,[31] van der Waals forces that differ to those in the bulk,[32] as well as thermal fluctuations.[33] It is beyond the scope of this work to give a detailed account of these forces, especially when comprehensive review articles have been published on these interactions.[11,34,35] However, for clarity the balance of forces and a pictorial representation of NP adsorption to the LLI are shown in Figure 1.

From an experimental perspective, characterizing these interfaces can be a challenging task. For example, invaluable insight has come from experiments utilizing grazing-incidence small-angle X-ray scattering to study the assembly of small CdSe nanocrystals at a toluene–water interface[36] in which it was determined that the particles form a close packed, but disordered liquid-like structure. Furthermore, fluorescence loss induced by photobleaching and fluorescence recovery after photobleaching on the same system revealed that the lateral diffusion of these assemblies is four orders of magnitude slower than its bulk counterpart.[36] Second harmonic generation,[37] surface plasmon resonance,[38] and ellipsometry[39] have also been shown as characterization methods for NPs at the LLI. More recently, freeze-fracture shadow-casting cryo SEM has been performed with single-particle resolution.[40] However, most of these techniques are time-consuming and require specialized equipment. Therefore a need exists for a fast, *in situ* technique that would extract, with nanometer resolution, the structural characteristics of these films.

In this paper we develop techniques for characterizing and controlling the spacing of NPs at a LLI. To use the plasmon ruler at these interfaces, one needs to first control the adsorption of NPs to the LLI and prevent aggregation-induced close packing. Diffusion-driven, electrochemical,[41] and ethanol-induced[42] adsorption to the liquid interface are among the most widely used strategies. Out of these techniques, spontaneous self-assembly is the most convenient for the plasmon ruler; however, the assembly time is generally limited by diffusion. We build on this by using centrifugation as a means to adsorb a 2D array of 16 nm Au NPs to a water/1,2-dichloroethane (DCE) LLI. Spectroscopic techniques are used to characterize the plasmonic properties of the NPs by controlling the centrifugal force, centrifugation time, salt concentration, interfacial area, and pH. The methods utilized are simple, fast, and inexpensive and can be used to characterize and control the properties of NPs at the LLI.

RESULTS AND DISCUSSION

Centrifugation as a Means of Kinetic Control of NP Assembly at the LLI. The simplicity and flexibility of centrifugation makes it an ideal technique to control particle adsorption to the LLI. We will forego a comprehensive study on the effects of centrifugation of the NPs, focusing instead on the experimental observation arising from NP assembly, disassembly, and controlled spacing at the LLI. The reader is referred to the Supporting Information for a detailed discussion on the physical background behind centrifugation speed and time dependence on NP adsorption.

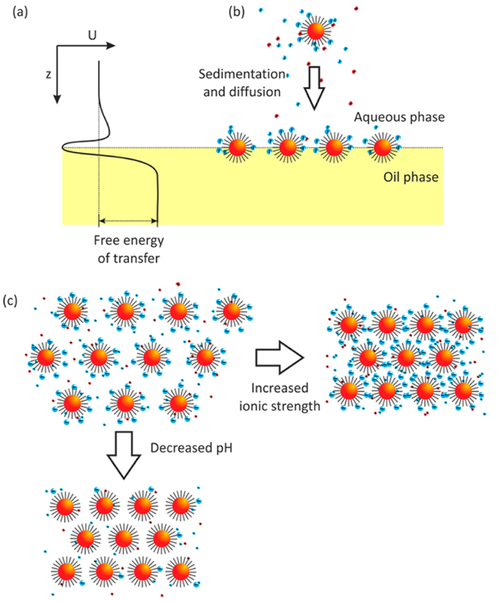

Figure 1. The main factors that influence localization of NPs functionalized by charged ligands at the LLI. (a) The free energy profile, *U*(*z*), for a single NP at the LLI is dominated by an interfacial stabilization well caused by the reduction of the system free energy when the NP blocks some parts of the energetically unfavorable interface between the aqueous and organic phases. For highly charged NPs, the combination of interfacial stabilization and Born resolvation may give rise to a barrier on the aqueous side separating the well. The ratio of the height of the barrier to the depth of the well should grow with the size of the NP, as long as the amount of charge on an NP scales as its surface area. (b) The particles reside on the interface driven by the interfacial stabilization, but they feel this force at the distances of the order of their size. (c) NPs at the water/oil interface with a viewpoint normal to it. The interparticle separation is controlled by the ionic strength of the solution and also the charge on the particles, which is controlled by the pH of the solution, and ligand functionality.

Unless otherwise stated, the procedure for NP assembly describing all the steps is shown in Tables 1 and 2. A general experimental schematic of the protocol for assembly and the detection of the NPs at the LLI are shown in Figure 2. After centrifugation, all but 100 μL of the aqueous solution was removed. This resulted in the 100 μL solution forming a droplet with the assembled NPs at the DCE/aqueous boundary. Notably, a distinct red coloration close to the interface could be seen post-centrifugation, indicating that the NPs have successfully migrated to the LLI (Figure 2b). The NPs are known to provide an interfacial tension stabilization between the oil and water,[43] this stabilization also prevents the particles from crossing the LLI and

TABLE 1. Point by Point Summary of Experimental Procedures for the Assembly of NPs to the LLI and Measuring LSPR Maxima

experimental step	DCE volume (μL)	aqueous volume (μL)	description
(1) DCE saturation with H_2O	500	100	H_2O is added to DCE aliquot and emulsified by vigorous shaking.
(2) NP/NaCl solution preparation	0	1000	Separately, 500 μL NP solution is added to 500 μL NaCl solution (for NP/NaCl concentrations see Table 2).
(3) addition of NP solution to water-saturated DCE	500	600	500 μL of solution (2) is added to mixture (1) [the remainder of (2) is used to estimate the bulk NP concentration by UV–Vis spectroscopy].
(4) centrifugation	500	600	Mixture (3) is centrifuged, followed by gentle inverting to homogenize the bulk concentration of NPs.
(5) estimation of the number of NPs adsorbed at LLI	500	100	500 μL of mixture (4) is removed and used for UV–Vis to measure the residual bulk NP concentration, which allows estimation of the number of adsorbed NPs.
(6) background transmission measurement	500	100[a]	Mixture (1) is used to measure background transmission spectrum.
(7) LSPR at LLI measurement	500	100	The mixture remaining after stage (5) is used to measure LSPR of the NPs adsorbed to the LLI by transmission spectroscopy.[b]

[a] For transmission of droplets with a volume greater than 100 μL, the background was measured with the greater volume. [b] For volume- and pH-dependent experiments, these steps were initially carried out, followed by additional procedures as highlighted in the main text.

TABLE 2. Experimental Conditions, the Number of NPs, the NaCl Concentration, RCF, Time of Centrifugation, Aqueous Droplet Volume, and pH, for the Results Shown in Figures 3, 4, 6, and 7

experimental variable	total NPs in solution	NaCl concn (mM)	centrifugation speed - RCF (g)	centrifugation time (min)	aq. droplet volume (μL)	pH
NaCl concentration	2.75×10^{11}	(1–193)	9391	10	100	5.5
RCF	2.75×10^{11}	75	(93–13523)	10	100	5.5
centrifugation time	2.75×10^{11}	75	9391	(0.5–30)	100	5.5
droplet volume	2.75×10^{11}	75	9391	10	(100–300)	5.5
pH	2.75×10^{11}	165	9391	10	100	(2–9)

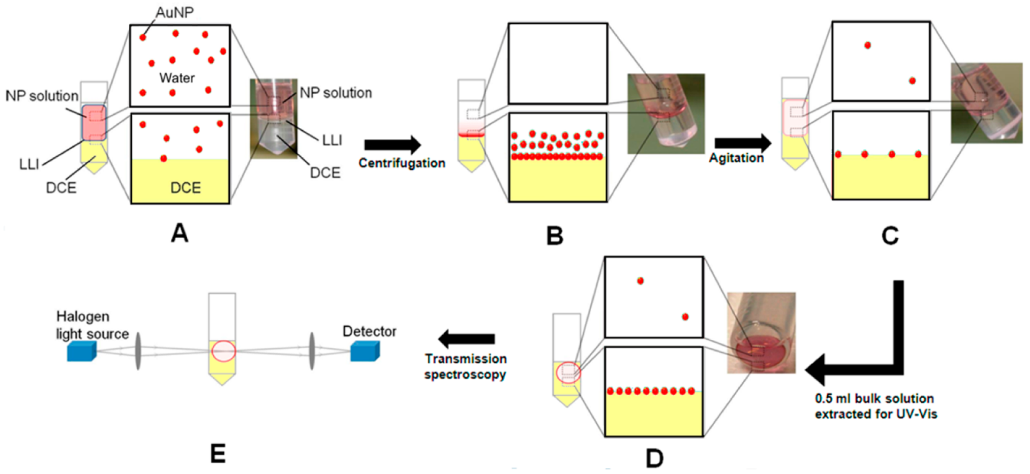

Figure 2. Schematic of the experimental procedure. All experiments were carried out with a 0.5 mL DCE and a 0.6 mL aq NP solution (A). Upon centrifugation (B), the centrifugal driving force provided a means to speed up NP adsorption at the LLI. (C) A total of 0.5 mL of the aqueous phase was then removed from the tubes, followed by gentle agitation of the remaining phases, readdition of the removed aq. phase followed again by removal of 0.5 mL aq phase for UV–Vis measurements (D). Remaining 100 μL droplet was then imaged by transmission spectroscopy in the geometry shown in (E).

sedimenting at the bottom of the DCE. However, as described, nanoparticles are charged and repel each other electrostatically unless this repulsion is substantially screened.[8] Consequently, these NPs could be visibly redispersed back into the bulk by gentle agitation at NaCl concentrations below 50 mM, while no visible change in the bulk occurred at NaCl concentrations above 50 mM. The NaCl concentration had a large effect on the visual appearance of the LLI. Between approximately 40–150 mM a highly glossy reflective film was observed at the LLI, at concentrations above 150 mM a matt appearance was observed while at concentrations below 40 mM only faint coloration was observed. It should be stressed that the transitions do not have clear boundaries.

The remaining 100 μL of the aqueous phase formed a truncated oblate ellipsoid droplet whose surface area was estimated to be 1.071 ± 0.01 cm^2 in the cell holder (see Supporting Information for more details). Optical transmission spectra of the NPs at the aqueous droplet/DCE interface (Figure 2e) were measured to determine the localized surface plasmon resonance (LSPR) maxima, with a beam diameter of 1.5 mm at the sample interface. Before each reading, the sample height was adjusted so that the incident light would pass at approximately normal incidence; this was monitored by the intensity of the collected light, which decayed rapidly at non-normal incidences. The tube holder was tilted to approximately 5°, which minimized variations in the droplet shapes in the set of performed experiments. This tilt also helped to pin the droplets by buoyancy to an approximately constant position with respect to the incident light.

NP Functionality. It was found that functionalization groups play a large role in controlling the assembly of NPs at the LLI shown schematically in Figure 1c. The critical role of the functionality is well documented, with several works focusing on the role of the particle's surface chemistry on adsorption and behavior at the LLI.[44−46] For example, 12-mercaptododecanoic acid (MDDA)-functionalized particles do not spontaneously assemble in large quantities at the LLI at low salt concentrations. This is evidenced from the fact that the centrifugation and homogenization process leaves the vast majority of the NPs in the bulk solution. On the other hand, performing an identical experiment with citrate stabilized particles results in the majority of the available NPs adsorbed to the LLI. Unfortunately agglomeration readily occurs for citrate stabilized particles; therefore, they were not used for further experiments. The MDDA functionality prevents the adsorbed NPs from agglomerating as the carbon chain provides approximately a 1.5 nm steric coating that circumvents short-range van der Waals interactions which induce aggregation. Furthermore, the dissociated carboxyl groups at the end of the carbon chain provide a Coulombic repulsion. This stabilizing technique was extremely successful, so much so that no irreversible aggregation was observed at any conditions tested. The stabilizing effect of steric repulsion for particle suspensions is consistent with the literature.[47] It is known that purely electrostatically stabilized gold particles aggregate at salt concentrations greater than 20 mM.[48] Above these salt concentrations the Debye screening length is reduced such that the electrostatic repulsion can no longer overcome the van der Waals attraction forces between the NPs causing aggregation. However, due to the interplay of the additional forces that takes place at the LLI, as well as the interface-caused modification of electrostatic and van der Waals interactions, the signatures of the bulk aggregation cannot be directly used to extrapolate the salt effect on the electrostatic repulsion at a LLI.[34,49] It is beyond the scope of this work to further investigate this interplay as well as accurately describe the local ionic concentration surrounding NPs at the LLI. However, invaluable insight can be found in other works.[34,50] As for the effects of the steric and electrostatic stabilization, provided by the MDDA functionality, in comparison with a predominantly electrostatic stabilization by mercaptosuccinic acid for NPs at the LLI, they are qualitatively compared in Figure S3 of the SI.

Salt Concentration Dependence on NP Adsorption and Plasmon Resonance. The effect of ionic strength on the number of particles assembled at the LLI is shown in Figure 3a−d. This value can be assessed from both the residual NPs in the aqueous phase (Figure 3b) and the LSPR spectra (Figure 3a). A clear red shift was observed as the NaCl concentration was increased gradually from 1 to 200 mM. Between these NaCl concentrations, the Debye screening is reduced from approximately 9.6 to 0.7 nm. It should be noted that the Debye screening may not only affect the NP population at the interface, but their precise position relative to the boundary.

Two potentially competing sources of red-shifting can be attributed to the experimental observations. The first is a change in the dielectric constant of the surrounding medium of the NPs, while the second is plasmon coupling. The dielectric constant of pure water and a 2 M NaCl solution is 1.78 and 1.80, respectively. Therefore, even if the local salt concentration at the interface in the electrical double layer is 10 times that of the bulk, a negligible positional change of the LSPR maximum would be observed. DCE on the other hand has a dielectric constant of 2.09; therefore, a more substantial effect could result from the NPs position shifting from the aqueous to DCE phases. However, the shift in the position of the LSPR would be minor in contrast to the shift caused by the resulting change of the distance between the NPs at the LLI. As a result, the observed shift can be attributed to distant dependent plasmon coupling.

With no addition of NaCl (i.e., intrinsic ionic strength equivalent to 1 mM NaCl), the number of NPs that could be adsorbed to the LLI under an RCF of 9391 g in 10 min was 4.0 ± 0.1 × 10^{10} NPs from a bulk aqueous solution containing a total of 2.75 × 10^{11} NPs. The low ionic strength of the solution means that the electrostatic repulsion acts over a longer distance inhibiting oncoming particles from adsorbing to the interface. At these conditions, the LSPR maximum was 524 ± 3 nm, which corresponds to the LSPR maximum of the NPs in the bulk aqueous solution. This suggests that little to no plasmonic coupling occurs due to a large separation between NPs. Based on both the empirical plasmon ruler equation as well as mean-field theory, the spacing

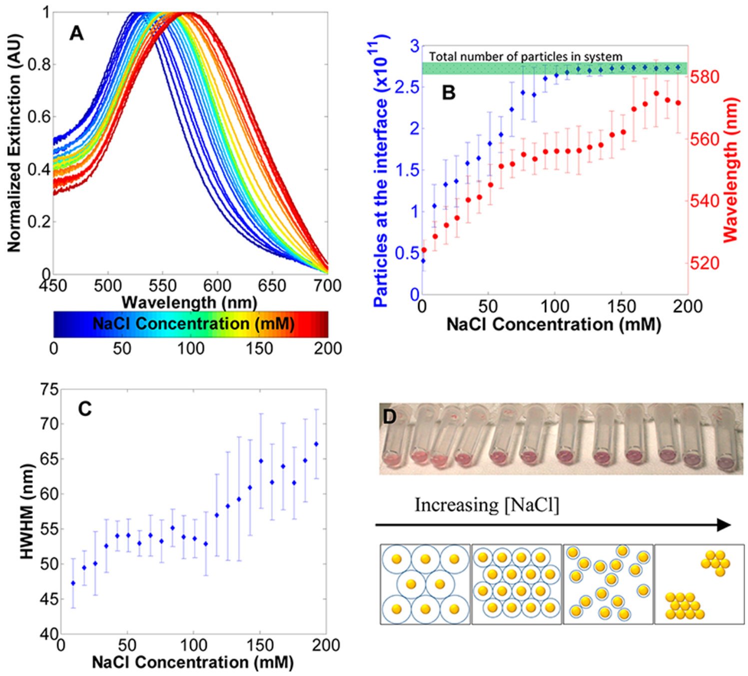

Figure 3. Dependence on plasmonic properties of 16 nm diameter gold NPs. (A) Full normalized spectra of samples. The spectra show a red-shift and peak broadening as the [NaCl] is increased. For clarity, the plasmon maximum with the number of particles adsorbed to the interface and half width at half-maximum are plotted in (B) and (C), respectively. A photograph of the samples (D) shows the effect of increasing the salt concentration on the NP color. Also included is a schematic showing the effect of increasing salt concentration on the nanoparticle spacing/arrangement.

is expected to be larger than 30 nm (Figure 5).[51,52] Increasing the salt concentration decreases the effective distance over which electrostatic repulsion takes place. As a result, a greater number of particles can be accommodated at the LLI. Because the surface area of the droplet and total number of particles in solution are roughly uniform, the spacing between NPs can be directly controlled by the addition of salt. This leads to a linear red-shift in the plasmonic response and a linear increase in the number of NPs adsorbed to the LLI between 1 and 75 mM NaCl. Between 75 and 125 mM NaCl both the LSPR maxima and the number of adsorbed particles plateaus at ≈555 nm and ≈2.75 × 10^{11} particles, respectively. This is due to all of the particles in the solution being collected at the interface. Under these conditions the average interparticle spacing remains constant. Finally, at concentrations above 150 mM NaCl, a further red-shift is observed. As the number of particles at the interface is already saturated, the red-shift is attributed to inhomogeneities and clustering of the NPs. This is supported by observing an increase in broadening of the plasmon spectra, Figure 3c. At lower salt concentration (1−50 mM) a linear dependence on the hwhm is observed, which is followed by a plateau between 50 and 110 mM and, finally, a second increase at concentrations >110 mM. By taking these observations into account along with the LSPR maxima and NP surface coverage, a possible explanation of these trends is shown in Figure 3d. As the NaCl is increased, NP coverage at the LLI will gradually go from a relatively ordered state to a disordered agglomerated state. This is further supported by the visual appearance of the LLI that, at low/moderate salt concentrations, appears golden mirror-like, which becomes matt in appearance at higher concentrations. The qualitative trends for red-shifting and peak broadening are as expected from the literature although broadening at higher NaCl concentrations is likely to be a combination of closer spacing and irregularities in the structure of the monolayer of NPs.[8,53]

In summary, based on the experimental results, NaCl concentrations of 1−75 mM give rise to controlled spacing with a relatively homogeneous NP distribution; the observed LSPR maximum at 75 mM NaCl is 555 ± 5 nm, which corresponds to a $\Delta\lambda/\lambda_0$ of ≈0.057. Coupled dipole approximation (CDA) simulations[52] suggest that a $\Delta\lambda/\lambda_0$ of 0.057 correlates to a gap distance/diameter of ≈0.65 which corresponds to ≈10 nm surface−surface NP separation in a hexagonal lattice (preferred packing geometry for a two-dimensional array of NPs with predominantly repulsive interactions). While mean-field theory[51] suggests that LSPR maximum of 555 nm corresponds to ≈4 nm. Our experimental data at these conditions suggests a surface−surface NP separation of ≈6 ± 1 nm (or a gap distance/diameter of ≈0.37), which lies between simulations and theory (Figure 5). Taking the

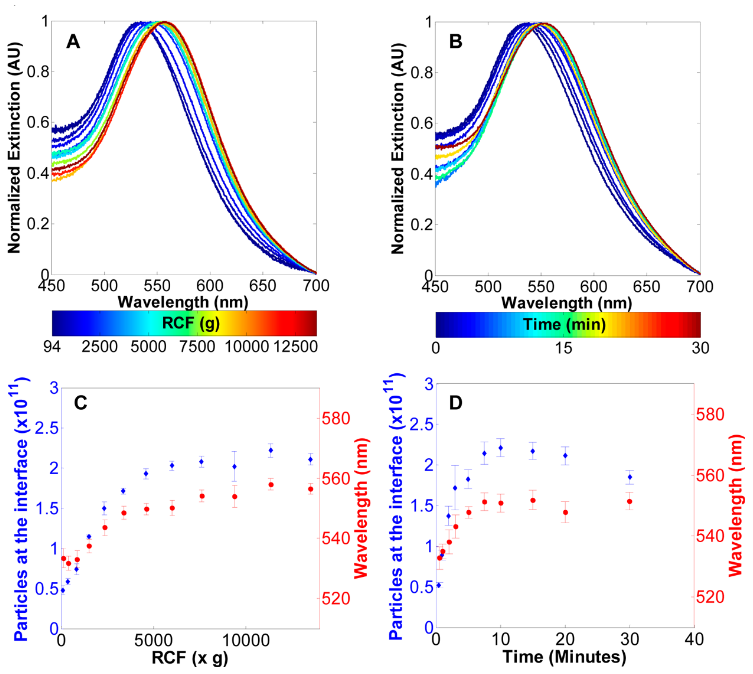

Figure 4. Transmission spectra as a function of RCF and centrifugation time are shown in (A) and (B). Corresponding LSPR maxima and number of particles adsorbed to the LLI are shown in (C) and (D) respectively.

steric coating of MDDA to be $\approx$1.5 nm and the Debye screening length to be 1.1 nm, then the minimum separation between 2 NPs is expected to be 5.2 nm; this is within experimental uncertainty of the experimentally determined values for NP separations at 75 mM.

Centrifugation Speed and Time Dependence on NP Adsorption and Plasmon Resonance. Centrifugation speed and time can also be used to control adsorption and the plasmonic properties of the NPs at the LLI (Figure 4). In Figure 4a,c the only parameter that was changed when compared to the NaCl results was the centrifugal force. The data shows very predictable behavior with a strong correlation between particle adsorbed to the interface and the plasmon red-shift. Both parameters increased until a plateau is reached which is a result of all particles being adsorbed to the interface. For example, the plasmon maximum at a RCF of 13523 g is 556 $\pm$ 2 nm ($\Delta\lambda/\lambda_0 \approx 0.059$), which corresponds to a 30 nm red-shift. Based on the plasmon ruler equation, $\Delta\lambda/\lambda_0 \approx 0.059$ suggests a $\approx$0.64 gap distance/diameter (or a $\approx$10 nm gap), while mean-field theory predicts a LSPR max of 556 nm corresponding to $\approx$4 nm surface–surface NP separation (Figure 5a,b).

The time-dependent studies (Figure 4b,d) show that, at short centrifugation times, a sharp increase in the number of particles adsorbed at the LLI is observed. This is followed by a plateau after 10 min where $2.2 \pm 0.1 \times 10^{11}$ NPs are adsorbed to the LLI. This is followed by a gradual decrease to a value of $1.8 \pm 0.2 \times 10^{11}$ NPs at 30 min is observed. This decrease could be attributed to heating of the samples that takes place during centrifugation, as dissociation is believed to be more efficient at higher temperatures, although further experiments are needed to verify this (*cf.* Figure 4d).

Combining the experimental data from Figures 3 and 4 (1–75 mM NaCl data), a plot of surface–surface NP separation can be drawn as a function of plasmon maximum (Figure 5a). Results from Figure 3 at NaCl concentrations of >75 mM were excluded due to the evidence of an inhomogeneous NP environment. The data presented is compared to two models. One of them was developed by Ben *et al.*[52] where a coupled dipole approach was used to calculate the plasmon frequency of an ordered 2D array of dipole scatterers. The results of these numerical calculations were then fit to a simple exponential function. However, one must be aware that the model cannot be directly applied to our system, because it was developed for an array of nanoparticles in vacuum; therefore, only the medium-independent $\Delta\lambda/\lambda_0$ can be used to compare qualitative trends (Figure 5b). In addition, we compare the results with a simple mean-field quasi-static dipolar theory developed by Kornyshev *et al.*[51] where we numerically determine the position of the plasmon resonance as a function of the distance between NPs (Figure 5a,b). The experimentally observed general trend is very similar to that predicted by both models. It is worth noting that deviation between the predictions of the mean-field theory and experimental RCF/time data becomes significant at larger interparticle separation due to a breakdown of the "continuous film" representation of the nanoparticle array.[51] The combined results from

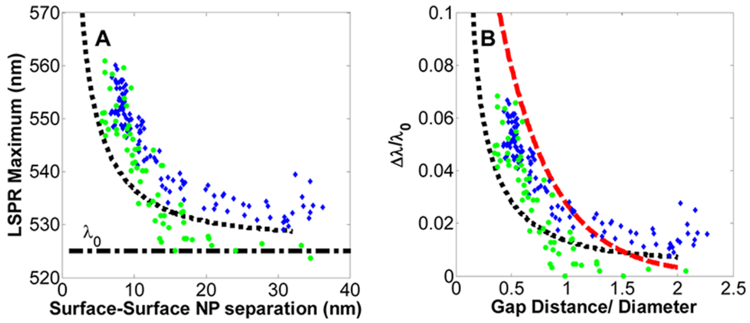

Figure 5. Demonstration of the plasmon ruler at the LLI for time- and RCF-dependent experiments (blue diamonds). NaCl-dependent experiments for concentrations ≤75 mM are also shown (green circles). The results from mean-field theory are shown as a black dotted line (A). Experimental results and theory are compared to CDA simulations (red dashed line). The LSPR shift is given as $\Delta\lambda/\lambda_0$, making the results applicable to Au NPs in any medium. The *x*-axis shows the dimensionless *a*/2*R*, the surface-to-surface separation divided by the diameter. λ_0 was taken to be 525 nm, as this represents the LSPR maximum of NPs in bulk water for the experimental results (B).

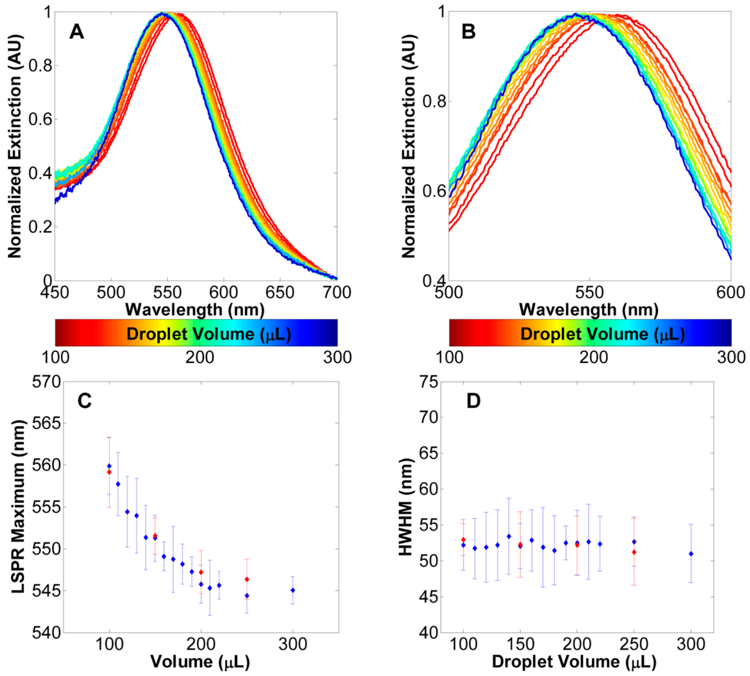

Figure 6. Volume dependence on transmission spectra (A, B), LSPR (C), and hwhm (D). Increasing the droplet volume leads to a blue shift (blue points). Importantly, the shift is reversible and a reduction of the volume (red points) results in the LSPR maxima going back to its original value.

the RCF and time-dependent studies suggest that the surface-to-surface separation between NPs can be precisely controlled between 7 and 30 nm, solely based on the centrifugation speed and time.

Volumetric Dependence on NP Adsorption and LSPR. Given that the results obtained from Figures 3 and 4 suggest that controlled spacing can be achieved, it follows naturally that one would expect to find a dependence on the LLI interfacial area for a constant total number of NPs at the interface. If the NPs' Coulombic as well as the long-range dipole−dipole repulsion lead to the NPs being spaced as far away from each other as possible at the LLI, then spacing should increase if the LLI area also increases. To verify this hypothesis, experiments were performed, increasing or decreasing the total aqueous droplet volume by pipetting fluid in or out of the droplet (Figure 6). The results suggest a clear dependence on the LSPR maximum with respect to the volume within a range of 100−200 μL. This is followed by a plateau at higher volumes. As expected, increasing the volume of the droplet causes a blue-shift in the LSPR maximum. For example, the LSPR maximum within a 100 μL was found to be 560 ± 3 nm, while 200 μL droplets had plasmon maxima of 546 ± 2 nm.

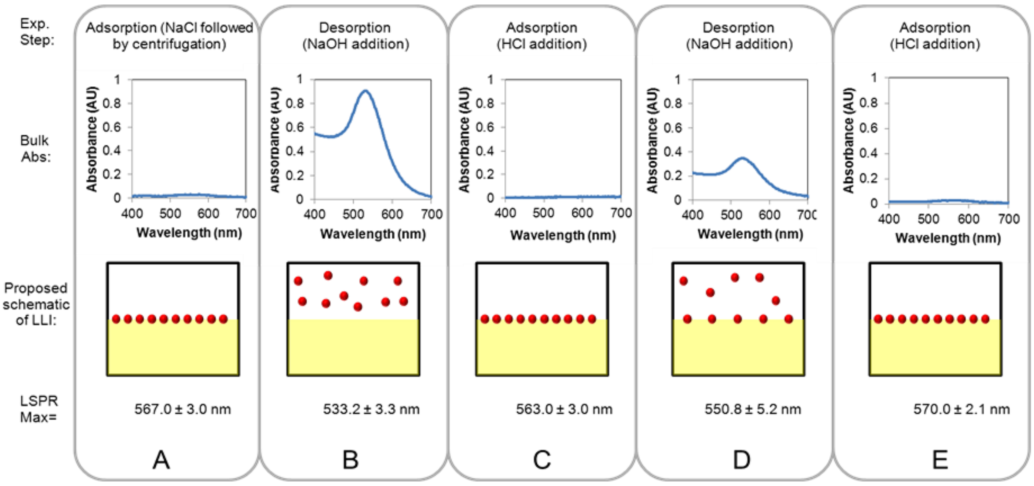

Figure 7. Demonstration of reversibility of NP adsorption/desorption. After assembly, the bulk salt was diluted in the aqueous phase 100× (A). Addition of 5 μL of 5 mM NaOH, followed by removal and combination of 5 μL from each of the 24 samples (B), with the position of the plasmon maximum shifting from 567.0 ± 3.0 to 533.2 ± 3.3 nm and the bulk absorption from UV−vis of ≈0.9. After the addition of 10 μL of 5 mM HCl, vigorous shaking of the sample and removal of 10 μL of the aqueous phase (C), the LSPR maximum from transmission returns to approximately the same value as the first adsorption step, while the bulk absorbance is negligible. Subsequent HCl/NaOH additions (D) and (E) show only partial reversibility.

The comparison of our experimental data with both models suggest that the surface-to-surface separation between NPs lies in the range of 6−13 nm. The decrease in the droplet volume, which results in a decrease in the LLI surface area, causes a red-shift in the LSPR maximum. It is important to note what happens when the volume is reduced below the initial 100 μL volume: the compression experienced by the particles initially leads to the expected red-shift, both visually and by transmission measurements; however, if the system is allowed to reach an equilibrium either by agitation or by waiting for a short period of time, then desorption of the "excess" NPs occurs. This is evidenced by both the LSPR maximum returning to ≈560 nm (*i.e.* same as for 100 μL) and the fact that after homogenization the NP in the bulk aqueous phase is greater than before homogenization. This is in marked contrast to close packed citrate stabilized arrays which are known to form `3D interfaces' and show buckling when the area of 2D NP array becomes larger than the area of the LLI.[54,55]

Reversibility of NPs at the LLI. NP adsorption at the LLI is impeded by electrostatic repulsion between the particles. For highly charged NPs there may be a barrier for individual NPs caused by resolvation. Both factors depend on the square of the charge of the NPs. Therefore we investigated the effect of changing the charge on the NPs to facilitate adsorption/desorption (Figure 7). NPs were assembled as described in Table 2. At this point, UV−Vis spectroscopy showed a negligible bulk absorbance (Figure 7a). The LSPR maximum was measured to be 567 ± 3 nm (consistent with the value at 165 mM NaCl from Figure 3b). To achieve desorption, 5 μL of 5 mM NaOH was added to the droplet, resulting in a final pH of approximately 9. This resulted in complete desorption of NPs from the LLI, which was evidenced by an increase in the bulk absorbance at 530 nm (Figure 7b). A blue-shift of the LSPR maximum (533 ± 3 nm) was also observed, which corresponds to the peak maxima for NPs in the bulk (530 nm).

Subsequent acidification of the aqueous solution with 10 μL of 5 mM HCl to a pH of approximately 2 and removal of the 10 μL "excess" aqueous phase (to ensure a constant volume) results in almost complete readsorption of the NPs (Figure 7c). The LSPR maximum returned to 563 ± 3 nm with UV−vis confirming that there was a negligible NP concentration in the bulk. Though this adsorption−desorption−adsorption cycle essentially suggests that full reversibility can be achieved, subsequent cycles could only demonstrate partial reversibility. The following desorption steps lead to a LSPR maximum of only 550.8 ± 5.2 nm and a bulk absorbance at 530 nm of ≈0.4, while the adsorption steps lead to negligible bulk NP concentration and an LSPR maximum of 570 ± 2 nm. This demonstrates an important step forward towards control of NP assemblies at the LLI, with the goal of coupling reversible adsorption with the plasmonic ruler by electrochemical means, that is, applying voltage across the ITIES, as suggested previously.[8]

CONCLUSIONS

We have demonstrated novel plasmonic properties of NPs localized at a LLI. Experimental results suggest that these properties arise from controlled spacing and that this spacing is affected by a set of controlled parameters. This was observed *indirectly* by normalized transmission spectroscopy. Importantly, experimental results qualitatively agree with mean-field theory, as well as the empirical plasmon ruler equation. The unique properties of homogeneous, controlled, submonolayer coverage NP assemblies at the LLI open routes for many potential applications ranging from plasmonic rulers to detectors and electro-variable optics.

Whereas, the *indirect* imaging is, as demonstrated, a fast and convenient way to probe the structural properties of these assemblies, further experiments with *direct* imaging will be crucial to prove/disprove the spacing hypothesis as well as to provide a relatable reference point for the exact spacing. We believe that the results that we presented in this paper give motivation and framework to such studies. Aside from demonstrating a novel centrifugation-based assembly method and a noninvasive, *in situ* optical characterization of the forming assemblies, we have also shown reversibility of the adsorption of 16 nm diameter gold particles. Finally, we have obtained results suggesting that the structural properties of NPs that are already localized to the LLI can be fine-tuned by varying the interfacial area.

It is hoped that, due to the simplicity of the experimental procedure developed here to achieve adsorption, desorption, and controlled spacing, this work will provide convenient techniques to study the details of these assemblies, as well as pave the way to control these features *via* electrochemical means.

EXPERIMENTAL SECTION

Equipment used include the following: UV−Vis measurements to quantify the number of particles assembled at the inerface were performed with a Nanodrop 2000c spectrometer using PMMA cuvettes. An Eppendorf 5424 centrifuge was used to aid in self-assembly of Au nanoparticles using 2 mL polypropylene centrifuge tubes. A FA-45−24−11 rotor with a radius of 8.4 cm was used and is capable of holding 24 × 2 mL centrifuge tubes at an angle of 45° with a maximum relative centrifugal force (RCF) of 20238 g (14680 rpm). A Beckmann Coulter DelsaNano C dynamic light scattering machine was used for hydrodynamic particle sizing and zeta potential measurements. Broadband transmission spectra were obtained with a home-built optical setup, with the core components consisting of a miniature fiber optic spectrometer (Ocean Optics, S2000) and a Tungsten halogen light source (Micropack, HL-2000). This setup was used to measure the LSPR spectra and approximate the interparticle spacing. It is important to note that due to the geometry of the setup, the incident light passed through two NP interfaces (i.e., the interface was elliptical). A Leo Gemini 1525 FEGSEM scanning electron microscope was used to size the NPs as well as provide evidence of monolayer formation (rather than multilayers). A Mettler-Toledo SevenGo Duo pro pH/ion/conductivity meter was used for conductivity measurements.

In all cases, ultrapure water with a resistivity of 18.2 MΩ·cm was used. All chemicals were purchased from Sigma-Aldrich U.K. and used without further purification. Chemicals used include the following: $HAuCl_4 \cdot {\approx}3H_2O$ (f.w. 339.79 (anhydrous), 99.999% trace metal basis); trisodium citrate dihydrate (f.w. 294.10, ≥99%); 12-mercaptododecanoic acid (MDDA, f.w. 232.38, 99%); ethanol (molecular biology, absolute grade); methanol (MeOH, CHROMASOLV, HPLC grade, ≥99.9%); sodium chloride (f.w. 58.44, ≥99.5%); 1,2-dichloroethane (DCE; ACS reagent, ≥99.0%).

MDDA Stabilized Gold Nanoparticle Synthesis. Gold NPs were synthesized based on the Turkevich-Frens recipes:[56,57] 8.6 mg $HAuCl_4 \cdot 3H_2O$ (5 mg gold) was dissolved in 95 mL of H_2O and brought to 100 °C. Under stirring, 5 mL of 13.6 mM sodium citrate solution was then added to the refluxing mixture. The initially faint-yellow solution gradually turned dark-blue, followed by wine-red over a period of 10 min. At this point, the NPs were measured to have a hydrodynamic diameter, electrophoretic mobility, and zeta potential of 20 ± 4 nm, -3.60×10^{-4} $cm^2/(V\ s)$, and −47.0 mV, respectively. The size of the particles was verified to be ≈16 ± 3 nm using a SEM. Once the reaction had gone to completion (typically less than 15 min), the temperature was reduced to 60 °C. This was followed by the addition of MDDA (5 mg) dissolved in MeOH (0.5 mL). The functionalization was allowed to continue for at least 1 h to ensure complete monolayer coverage, after which the mixture was allowed to slowly cool under stirring for at least an extra hour. The excess MDDA precipitated out and was removed by filtration. The functionalized NP typically had a hydrodynamic diameter of 26 ± 7 nm, a conductivity of 217 $\mu S/cm$, electrophoretic mobility of -4.37×10^{-4} $cm^2/(V\ s)$ and a zeta potential of −57.0 mV. The concentration of the NPs was then increased by centrifugation to the desired value. The "as-made" NP solution used for the experiments had an absorption of 0.890 at 525 nm. Taking an extinction coefficient of 4.92×10^8 M^{-1} cm^{-1}[58], the concentration of NPs was determined to be 1.8 nM or 1.09×10^{12} NPs/mL.

Conflict of Interest: The authors declare no competing financial interest.

Acknowledgment. We are thankful to Michael Urbakh, Michael Flatte, and Monica Marinescu for useful discussions. J.B.E. thanks the European Research Council starting grant scheme for financial support. A.A.K. also acknowledges support provided by FP7 EU grant "Nanodetector."

Supporting Information Available: A discussion of centrifugation, SEM images of dried nanoparticle arrays, the effects of the dielectric constant on the LSPR maximum, a comparison between mercaptosuccinic acid and MDDA, and details of the calculation of the interfacial area and HWHM. This material is available free of charge *via* the Internet at http://pubs.acs.org.

REFERENCES AND NOTES

1. Ramsden, W. Separation of Solids in the Surface-Layers of Solutions and Suspensions (Observations on Surface-Membranes, Bubbles, Emulsions, and Mechanical Coagulation): Preliminary Account. *Proc. R. Soc.* **1903**, *72*, 156–164.
2. Pickering, S. U. Emulsions. *J. Chem. Soc.* **1907**, *91*, 2021.
3. Yogev, D.; Efrima, S. Novel Silver Metal Liquidlike Films. *J. Phys. Chem.* **1988**, *92*, 5754–5760.
4. Kelly, K. L.; Coronado, E.; Zhao, L. L.; Schatz, G. C. The Optical Properties of Metal Nanoparticles: The Influence of Size, Shape, and Dielectric Environment. *J. Phys. Chem. B* **2002**, *107*, 668–677.
5. Duan, H.; Wang, D.; Sobal, N. S.; Giersig, M.; Kurth, D. G.; Möhwald, H. Magnetic Colloidosomes Derived from Nanoparticle Interfacial Self-Assembly. *Nano Lett.* **2005**, *5*, 949–952.
6. Younan, N.; Hojeij, M.; Ribeaucourt, L.; Girault, H. H. Electrochemical Properties of Gold Nanoparticles Assembly at Polarised Liquidliquid Interfaces. *Electrochem. Commun.* **2010**, *12*, 912–915.
7. Crossley, S.; Faria, J.; Shen, M.; Resasco, D. E. Solid Nanoparticles that Catalyze Biofuel Upgrade Reactions at the Water/Oil Interface. *Science* **2010**, *327*, 68–72.

8. Flatté, M. E.; Kornyshev, A. A.; Urbakh, M. Electrovariable Nanoplasmonics and Self-Assembling Smart Mirrors. *J. Phys. Chem. C* **2010**, *114*, 1735–1747.
9. Rotello, V. M.; Patra, D.; Malvankar, N.; Chin, E.; Tuominen, M.; Gu, Z. Y. Fabrication of Conductive Microcapsules *via* Self-Assembly and Crosslinking of Gold Nanowires at Liquid-Liquid Interfaces. *Small* **2010**, *6*, 1402–1405.
10. Kinnan, M. K.; Chumanov, G. Plasmon Coupling in Two-Dimensional Arrays of Silver Nanoparticles: II. Effect of the Particle Size and Interparticle Distance. *J. Phys. Chem. C* **2010**, *114*, 7496–7501.
11. Boker, A.; He, J.; Emrick, T.; Russell, T. P. Self-Assembly of Nanoparticles at Interfaces. *Soft Matter* **2007**, *3*, 1231–1248.
12. Benjamin, I. Theoretical Study of the Water/1, 2-Dichloroethane Interface: Structure, Dynamics, and Conformational Equilibria at the Liquid−Liquid Interface. *J. Chem. Phys.* **1992**, *97*, 1432.
13. Sonnichsen, C.; Reinhard, B. M.; Liphardt, J.; Alivisatos, A. P. A Molecular Ruler Based on Plasmon Coupling of Single Gold and Silver Nanoparticles. *Nat. Biotechnol.* **2005**, *23*, 741–745.
14. Jain, P. K.; Huang, W.; El-Sayed, M. A. On the Universal Scaling Behavior of the Distance Decay of Plasmon Coupling in Metal Nanoparticle Pairs: A Plasmon Ruler Equation. *Nano Lett.* **2007**, *7*, 2080–2088.
15. Su, K. H.; Wei, Q. H.; Zhang, X.; Mock, J. J.; Smith, D. R.; Schultz, S. Interparticle Coupling Effects on Plasmon Resonances of Nanogold Particles. *Nano Lett.* **2003**, *3*, 1087–1090.
16. Yang, L.; Wang, H.; Yan, B.; Reinhard, B. R. M. Calibration of Silver Plasmon Rulers in the 1−25 nm Separation Range: Experimental Indications of Distinct Plasmon Coupling Regimes. *J. Phys. Chem. C* **2010**, *114*, 4901–4908.
17. Liu, N.; Hentschel, M.; Weiss, T.; Alivisatos, A. P.; Giessen, H. Three-Dimensional Plasmon Rulers. *Science* **2011**, *332*, 1407–1410.
18. Gordon, K. C.; McGarvey, J. J.; Taylor, K. P. Enhanced Raman Scattering from Liquid Metal Films Formed from Silver Sols. *J. Phys. Chem.* **1989**, *93*, 6814–6817.
19. Wang, L.; Sun, Y.; Che, G.; Li, Z. Self-Assembled Silver Nanoparticle Films at an Air−Liquid Interface and Their Applications in SERS and Electrochemistry. *Appl. Surf. Sci.* **2011**, *257*, 7150–7155.
20. Zhang, J.; Coulston, R. J.; Jones, S. T.; Geng, J.; Scherman, O. A.; Abell, C. One-Step Fabrication of Supramolecular Microcapsules from Microfluidic Droplets. *Science* **2012**, *335*, 690–694.
21. Flatte, M. E.; Kornyshev, A. A.; Urbakh, M. Nanoparticles at Electrified Liquid−Liquid Interfaces: New Options for Electro-Optics. *Faraday Discuss.* **2009**, *143*, 109–115.
22. Pieranski, P. Two-Dimensional Interfacial Colloidal Crystals. *Phys. Rev. Lett.* **1980**, *45*, 569–572.
23. Hurd, A. J. The Electrostatic Interaction between Interfacial Colloidal Particles. *J. Phys. A* **1985**, *18*, L1055.
24. Tay, K. A.; Bresme, F. Wetting Properties of Passivated Metal Nanocrystals at Liquid−Vapor Interfaces: A Computer Simulation Study. *J. Am. Chem. Soc.* **2006**, *128*, 14166–14175.
25. Luo, M. Effects of Methanol on Nanoparticle Self-Assembly at Liquid-Liquid Interfaces: A Molecular Dynamics Approach. *J. Chem. Phys.* **2009**, *131*, 194703.
26. Reincke, F.; Kegel, W. K.; Zhang, H.; Nolte, M.; Wang, D.; Vanmaekelbergh, D.; Mohwald, H. Understanding the Self-Assembly of Charged Nanoparticles at the Water/Oil Interface. *Phys. Chem. Chem. Phys.* **2006**, *8*, 3828–3835.
27. Vermant, J.; Grzelczak, M.; Furst, E. M.; Liz-Marzan, L. M. Directed Self-Assembly of Nanoparticles. *ACS Nano* **2010**, *4*, 3591–3605.
28. Park, B. J.; Pantina, J. P.; Furst, E. M.; Oettel, M.; Reynaert, S.; Vermant, J. Direct Measurements of the Effects of Salt and Surfactant on Interaction Forces between Colloidal Particles at Water−Oil Interfaces. *Langmuir* **2008**, *24*, 1686–1694.
29. Park, B. J.; Vermant, J.; Furst, E. M. Heterogeneity of the Electrostatic Repulsion between Colloids at the Oil−Water Interface. *Soft Matter* **2010**, *6*, 5327–5333.
30. Flatté, M. E.; Kornyshev, A. A.; Urbakh, M. Understanding Voltage-Induced Localization of Nanoparticles at a Liquid−Liquid Interface. *J. Phys.: Condens. Matter* **2008**, *20*, 073102.
31. Boneva, M. P.; Danov, K. D.; Christov, N. C.; Kralchevsky, P. A. Attraction between Particles at a Liquid Interface Due to the Interplay of Gravity- and Electric-Field-Induced Interfacial Deformations. *Langmuir* **2009**, *25*, 9129–9139.
32. Williams, D. F.; Berg, J. C. The Aggregation of Colloidal Particles at the Air−Water Interface. *J. Colloid Interface Sci.* **1992**, *152*, 218–229.
33. Lehle, H.; Oettel, M. Importance of Boundary Conditions for Fluctuation-Induced Forces between Colloids at Interfaces. *Phys. Rev. E* **2007**, *75*, 011602.
34. Bresme, F.; Oettel, M. Nanoparticles at Fluid Interfaces. *J. Phys.: Condens. Matter* **2007**, *19*, 413101.
35. Singh, P.; Joseph, D. D.; Aubry, N. Dispersion and Attraction of Particles Floating on Fluid-Liquid Surfaces. *Soft Matter* **2010**, *6*, 4310–4325.
36. Lin, Y.; Böker, A.; Skaff, H.; Cookson, D.; Dinsmore, A. D.; Emrick, T.; Russell, T. P. Nanoparticle Assembly at Fluid Interfaces: Structure and Dynamics. *Langmuir* **2004**, *21*, 191–194.
37. Galletto, P.; Girault, H. H.; Gomis-Bas, C.; Schiffrin, D. J.; Antoine, R.; Broyer, M.; Brevet, P. F. Second Harmonic Generation Response by Gold Nanoparticles at the Polarized Water/2-Octanone Interface: from Dispersed to Aggregated Particles. *J. Phys.: Condens. Matter* **2007**, *19*, 375108.
38. Hojeij, M.; Younan, N.; Ribeaucourt, L.; Girault, H. H. Surface Plasmon Resonance of Gold Nanoparticles Assemblies at Liquid−Liquid Interfaces. *Nanoscale* **2010**, *2*, 1665–1669.
39. Zang, D.; Stocco, A.; Langevin, D.; Wei, B.; Binks, B. P. An Ellipsometry Study of Silica Nanoparticle Layers at the Water Surface. *Phys. Chem. Chem. Phys.* **2009**, *11*, 9522–9529.
40. Isa, L.; Lucas, F.; Wepf, R.; Reimhult, E. Measuring Single-Nanoparticle Wetting Properties by Freeze-Fracture Shadow-Casting Cryo-Scanning Electron Microscopy. *Nat. Commun.* **2011**, *2*, 1–9.
41. Su, B.; Abid, J.-P.; Fermín, D. J.; Girault, H. H.; Hoffmannová, H.; Krtil, P.; Samec, Z. Reversible Voltage-Induced Assembly of Au Nanoparticles at Liquid−Liquid Interfaces. *J. Am. Chem. Soc.* **2003**, *126*, 915–919.
42. Li, Y.-J.; Huang, W.-J.; Sun, S.-G. A Universal Approach for the Self-Assembly of Hydrophilic Nanoparticles into Ordered Monolayer Films at a Toluene/Water Interface. *Angew. Chem., Int. Ed.* **2006**, *45*, 2537–2539.
43. Du, K.; Glogowski, E.; Emrick, T.; Russell, T. P.; Dinsmore, A. D. Adsorption Energy of Nano- and Microparticles at Liquid−Liquid Interfaces. *Langmuir* **2010**, *26*, 12518–12522.
44. Isa, L.; Amstad, E.; Schwenke, K.; Del Gado, E.; Ilg, P.; Kroger, M.; Reimhult, E. Adsorption of Core-Shell Nanoparticles at Liquid−Liquid Interfaces. *Soft Matter* **2011**, *7*, 7663–7675.
45. Stefaniu, C.; Chanana, M.; Ahrens, H.; Wang, D.; Brezesinski, G.; Mohwald, H. Conformational Induced Behaviour of Copolymer-Capped Magnetite Nanoparticles at the Air/Water Interface. *Soft Matter* **2011**, *7*, 4267–4275.
46. D'Souza Mathew, M.; Manga, M. S.; Hunter, T. N.; Cayre, O. J.; Biggs, S. Behavior of pH-Sensitive Core Shell Particles at the Air−Water Interface. *Langmuir* **2012**, *28*, 5085–5092.
47. Reed, K. M.; Borovicka, J.; Horozov, T. S.; Paunov, V. N.; Thompson, K. L.; Walsh, A.; Armes, S. P. Adsorption of Sterically Stabilized Latex Particles at Liquid Surfaces: Effects of Steric Stabilizer Surface Coverage, Particle Size, and Chain Length on Particle Wettability. *Langmuir* **2012**, *28*, 7291–7298.
48. Meyer, M.; Le Ru, E. C.; Etchegoin, P. G. Self-Limiting Aggregation Leads to Long-Lived Metastable Clusters in Colloidal Solutions. *J. Phys. Chem. B* **2006**, *110*, 6040–6047.
49. Isa, L.; Amstad, E.; Textor, M.; Reimhult, E. Self-Assembly of Iron Oxide-Poly(ethylene glycol) CoreShell Nanoparticles at Liquid Liquid Interfaces. *Chimia* **2010**, *64*, 145–149.

50. Starov, V. M. *Nanoscience: Colloidal and Interfacial Aspects*; CRC: Boca Raton, FL, 2010.
51. Kornyshev, A. A.; Marinescu, M.; Paget, J.; Urbakh, M. Reflection of Light by Metal Nanoparticles at Electrodes. *Phys. Chem. Chem. Phys.* **2012**, *14*, 1850–1859.
52. Ben, X.; Park, H. S. Size Dependence of the Plasmon Ruler Equation for Two-Dimensional Metal Nanosphere Arrays. *J. Phys. Chem. C* **2011**, *115*, 15915–15926.
53. Zhao, L.; Kelly, K. L.; Schatz, G. C. The Extinction Spectra of Silver Nanoparticle Arrays: Influence of Array Structure on Plasmon Resonance Wavelength and Width. *J. Phys. Chem. B* **2003**, *107*, 7343–7350.
54. Tseng, T.-C.; McGarrity, E. S.; Kiel, J. W.; Duxbury, P. M.; Mackay, M. E.; Frischknecht, A. L.; Asokan, S.; Wong, M. S. Three-Dimensional Liquid Surfaces through Nanoparticle Self-Assembly. *Soft Matter* **2010**, *6*, 1533–1538.
55. Aveyard, R.; Clint, J. H.; Nees, D.; Quirke, N. Structure and Collapse of Particle Monolayers under Lateral Pressure at the Octane/Aqueous Surfactant Solution Interface. *Langmuir* **2000**, *16*, 8820–8828.
56. Turkevich, J. A Study of the Nucleation and Growth Processes in the Synthesis of Colloidal Gold. *Discuss. Faraday Soc.* **1951**, *11*, 55.
57. Frens, G. Controlled Nucleation for the Regulation of the Particle Size in Monodisperse Gold Suspensions. *Nature* **1973**, *241*, 20.
58. Liu, X.; Atwater, M.; Wang, J.; Huo, Q. Extinction Coefficient of Gold Nanoparticles with Different Sizes and Different Capping Ligands. *Colloids Surf., B* **2007**, *58*, 3–7.

A Plasmonic Ruler at the Liquid-Liquid Interface

Vladimir A. Turek, Michael P. Cecchini, Jack Paget, Anthony R. Kucernak, Alexei A. Kornyshev*, and Joshua B. Edel*

Department of Chemistry, Chemical Physics Section, Imperial College London, Exhibition Road, South Kensington, London, SW7 2AZ, United Kingdom

*Corresponding authors: a.kornyshev@imperial.ac.uk, joshua.edel@imperial.ac.uk

ESI

Charge on nanoparticles, the effect of resolvation energy, and other abilities of centrifugation

For highly charged nanoparticles the issue of overcoming the barrier before getting trapped in the well at the LLI, schematically depicted in Figure 1(a), may be important. Does the centrifugation force help not only to come to the foot of the barrier, but also to overcome it? If we make calculations along the lines that have been made to generate the nonpolarized-interface "0"- curve of Figure 2 in Ref. [1], we will get the maximal force (at the inflection point) against which the gold NPs of 20 nm radius has to climb the barrier $1.4 \cdot \mathrm{pN}$. The centrifugal force acting on the same particle is $0.3 \cdot \mathrm{pN}$, i.e. some four times smaller. Note however that curves in that figure where calculated for the surface charge concentrations on NPs close to the 'maximal'one - when every second ligand acid group is assumed to be dissociated and for nanoparticles more than two times larger than in the present paper. In fact we do not know the exact value of the surface charge density on nanoparticles and it can easily be substantially smaller; moreover the Born resolvation energy term is $q^2 / R^{\,2}$ and if q R^2 it scales as R^3. Thus since Svedberg coefficient scales as R^2, making the particle two times smaller will change the balance of forces two times in favour of the centrifugation, and had we just 2 times less charges on NPs, the centrifugal force will be enough to drive the NPs over the barrier.

The charge on NPs may be reduced not only by controlling pH. In fact the terminal anions may spontaneously re-associate with the protons when an NP is approaching the surface; when it pierces the surface, the 'dark side of the moon' – the surface area of NP exposed to oil may get fully neutralized. Thus the made estimates show that the centrifugal force can be of substantial assistance in overcoming the expected barrier on the way to the capillary trap at the LLI. Had the barrier been a bit higher, the centrifugal force would still bring the NPs to the foot of the barrier, after which it will get into the well with the help of the corresponding interface fluctuation, in the spirit of the mechanisms analyzed in Refs. [3], in the context of the transport of simple ions, which could be extended with the corresponding rescaling on the case of the transport of much larger particles.

Note that in the systems considered in this paper the amount of charge on the NP may be order of magnitude lower, and then the barrier will vanish or will not be an issue.

The population of NPs at the LLI can also be controlled kinetically. For example, centrifugation can be used to drive NPs to the LLI. Without this, the NPs would be limited by Brownian motion and it would take $\tau_d \approx \frac{L^2}{D} \sim 10^7$ s or 4 months for the NPs to completely cover the LLI, where L is the characteristic thickness of the aqueous layer ($L = 0.1$ cm), and D is the diffusion coefficient of NPs ($D = 10^{-8}\mathrm{cm}^2\mathrm{s}^{-1}$). Centrifugation is commonly used to separate gold nanospheres and nanorods. This is possible as the sedimentation velocity of nano-objects depends on both the objects' size and shape [4]. Sedimentation is usually described with the Svedburg co-efficient, S, which is the terminal velocity normalised by the angular acceleration. For a nanosphere $S = \frac{2}{9}(\rho_{NP} - \rho_w)\frac{R^2}{\mu}$, where $\rho_i$is the density of material i, R is the NP radius and μ the kinematic viscosity. The velocity of sedimentation can then be calculated as $v_{\mathrm{sed}} = GS$ where G is the applied angular acceleration. At the low NP concentrations the hydrodynamic interactions between particles are negligible and thus not considered. However, at high NP concentrations, reducing the charge on the NPs will lead to reduced electrostatic repulsion between NPs, which in turn increases the sedimentation velocity. Using the Svedburg co-efficient and defining the mean length of the aqueous phase to be 0.1 cm, the sedimentation time without centrifugation for the NPs we use is of the order of 2.5×10^5 s or ~70 h. This value is reduced to 40 s when a median centrifuge speed of G~6,400 g is used.

SEM Images of dried monolayers

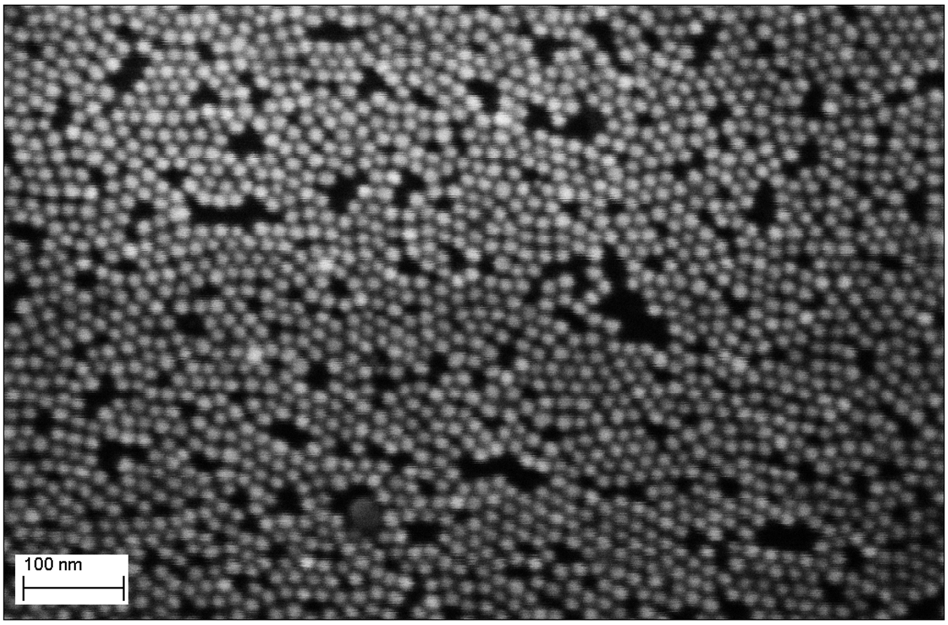

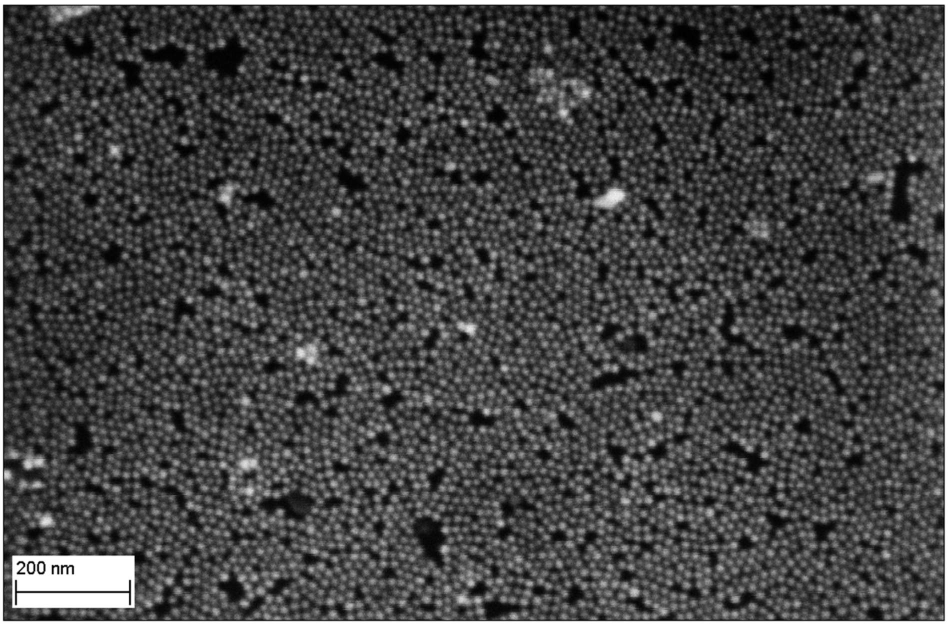

Fig. S1 SEM images of dried 16 nm MDDA functionalized gold NP monolayers from the LLI

Fig. S1 demonstrates that although gaps and particles sitting on top of the dried NP assembly can be clearly seen, the predominant structure is a *mono*-layer. It is reasoned that if 3D clusters or multi-layers were present at the LLI, then drying the film would intensify this effect. The absence of these supports the notion that this does not happen at the LLI and that it can be assumed that monolayers are the predominant structures for NPs at the LLI.

Dielectric Effects of local environment

The effect of the dielectric constant of the surrounding medium and plasmon coupling is compared for 16 nm particle from the mean-field quasistatic approximation in Fig. S2. Based on the discussion in the main text, a dielectric shift of less than 0.02 is expected when changing the NaCl concentration. The dielectric constant of pure water and a 2M NaCl solution is 1.78 and 1.80 respectively. It is evident from the figure below that the dielectric shift is not enough to fully account for the 30 nm LSPR maximum shift.

DCE on the other hand has as dielectric constant of 2.09. Therefore a most substantial effect could result from the NPs position going from the aqueous to DCE phases. However previous work has suggested that the position of a particle with respect to the interface is, at most, only mildly affected by the change in the concentration of NaCl, meaning that the effect of the change of the effective dielectric constant will be minor between these samples. Even if the three phase contact angle does change for these experiments, based on the hydrophilic nature of the NPs, it is unlikely that they should sit predominantly in the DCE, therefore it is likely that the limiting cases are between 50:50 water-DCE (90° contact angle) to 75:25 (30° contact angle – this is likely the lower limit as at this three phase contact angle, the desorption energy of the NPs starts reaching k_BT when an interfacial tension of 28.1 mN/m (20°C) is assumed for water-DCE). If we assume that the dielectric constants of the two phases can be averaged to determine the dielectric constant of the medium (i.e. dielectric constant of these two cases would be approximately 1.85 and 1.93), the expected plasmon shift would be ≈ 3 nm.

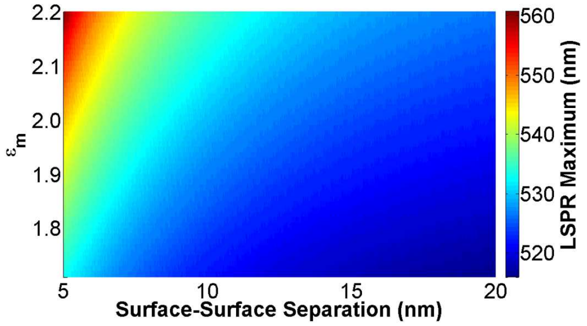

Fig. S2 LSPR maximum vs dielectric constant of the surrounding medium, ε_m, and surface-surface NP separation. Calculated using the mean-field quastatic approximation of reference[5].

Electrostatic vs Electrostatic and Steric stabilization

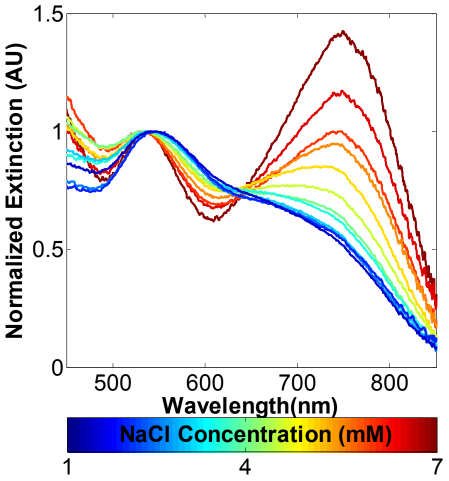

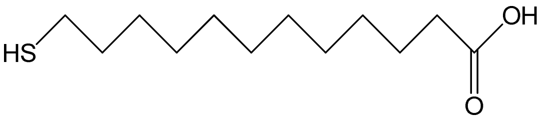

12- Mercaptododecanoic acid
(MDDA)

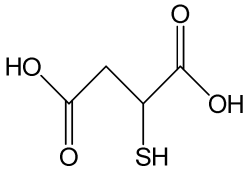

Mercaptosuccinic acid
(MSA)

Fig. S3 Normalized Transmission Spectra for MSA stabilized 16 nm particles at the LLI as a function of NaCl.

Reducing the carbon chain length between the thiol and the carboxylic acid that the MDDA functionality provides has a drastic effect on the plasmonic properties of NP assemblies at the LLI. It can be seen from Fig. S3 that unlike the spectra in Figures 3, 4 and 6 of the main text, there are two distinct peaks. These plasmonic properties could be compared to aggregate formation in the bulk aqueous solution, where 2 peaks are also seen – one corresponding to single particles (in the region of 520 nm), while the other arises as a result of intense plasmon coupling of aggregates (around 630 nm). It is probable therefore, that a similar effect occurs at the LLI and that increasing the NaCl concentration leads to 2 dimensional aggregation of the MSA functionalized particles. Another important observation is that the ranges of NaCl concentrations within which the aggregation of the studied NPs occurs at the LLI appear to be substantially lower than in the bulk. Indeed, while they are relatively stable in the bulk of the aqueous phase at ≈15 mM concentration, at the LLI a distinctive aggregate shoulder is already seen at 1 mM. For MDDA, the plasmon shifts gradually with increase of the concentration of [NaCl] and at no conditions were 2 peaks seen in the spectra, suggesting the strength of the plasmonic coupling is more or less uniform across the sample. The salt concentrations under which the MDDA functionalized particles were stable in the bulk of the aqueous phase were also an order of magnitude higher as compared to MSA. This suggests that the steric separation between the plasmonic cores afforded by MDDA plays a crucial role in the high stability of these particles both in aqueous solution and at the LLI.

Calculating the Surface Area of the LLI

The surface area of the interface was approximated as follows, leading to a value that was used in the main text of 1.071 ± 0.01 cm^2.

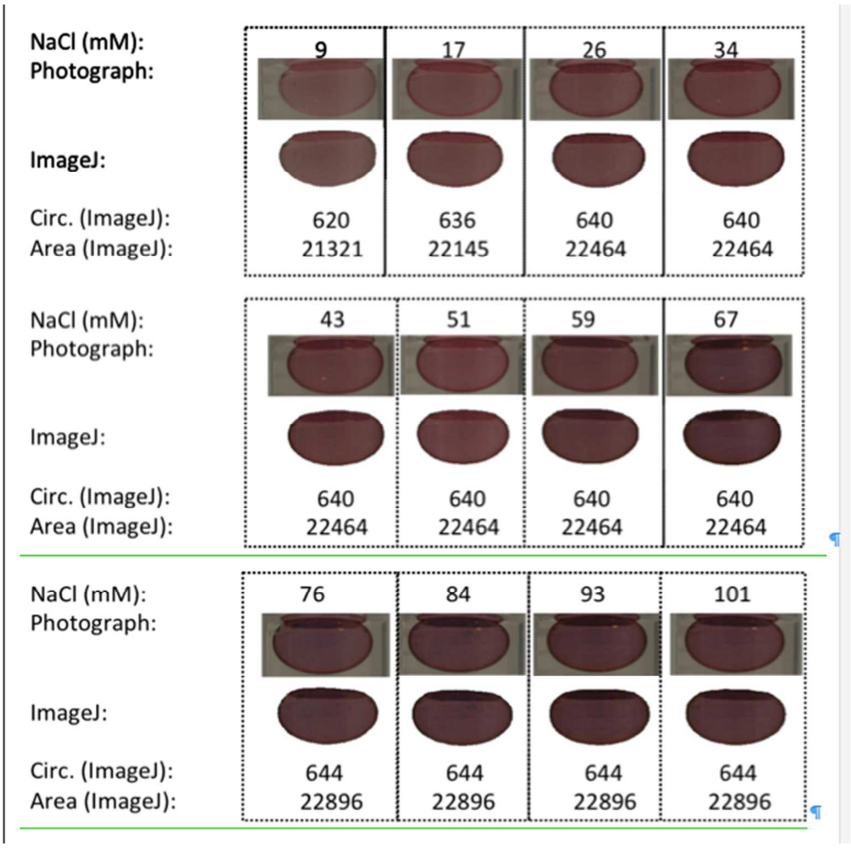

NaCl (mM):	9	17	26	34
Photograph:				
ImageJ:				
Circ. (ImageJ):	620	636	640	640
Area (ImageJ):	21321	22145	22464	22464

NaCl (mM):	43	51	59	67
Photograph:				
ImageJ:				
Circ. (ImageJ):	640	640	640	640
Area (ImageJ):	22464	22464	22464	22464

NaCl (mM):	76	84	93	101
Photograph:				
ImageJ:				
Circ. (ImageJ):	644	644	644	644
Area (ImageJ):	22896	22896	22896	22896

Fig. S4 – Photographs of droplets at 12 NaCl concentrations – ImageJ was used to crop out the aqueous droplet then estimate the circumference and area (both in arbitrary units) of the droplets.

If we assume that the above 2D images of the droplets are the cross section of an ellipsoid and the images above are themselves ellipses, then it is possible to calculate the dimensions of the oblate ellipsoid (i.e. b=c>a) in arbitrary units, knowing the volume of this ellipsoid, we can then use the arbitrary a and b units to calculate a conversion factor, x, to determine absolute values. Finally, using an approximation for the surface area of an ellipsoid, we can determine the surface area of the droplets.

From the approximation,

$$C \approx \pi\sqrt{2(a^2+b^2)-0.5(a-b)^2} \qquad \text{Eq.1}$$

And a second approximation,

$$C \approx \pi\left(3(a+b)-\sqrt{(a+3b)(3a+b)}\right) \qquad \text{Eq. 2}$$

We get,

$$a=\frac{2\sqrt{6}+12\sqrt{2}A}{C} \qquad \text{or} \qquad a=\frac{1.98814A}{C} \qquad \text{Eq. 3}$$

Where A is the area and C is the circumference. This allows the values for a, b and c (in arbitrary units). Given that $V=10^{-7}$ m^3 then from,

$$V=4\pi abcx^3 \qquad \text{Eq. 4}$$

The conversion factor, x, can be determined to convert a, b and c from arbitrary units into metres. Then from the approximation for the surface area of an ellipsoid,

$$S \approx 4\pi\left(\frac{a^p b^p+a^p c^p+b^p c^p}{3}\right)^{\frac{1}{p}} \qquad \text{Eq. 5}$$

Where $p \approx 1.6075$, we can estimate the surface area of the droplets:

NaCl (mM)	Area (AU)	Circumference (AU)	a (AU)	b (AU)	c (AU)	x (10^-5)	a (mm)	b (mm)	c (mm)	Surface Area (cm^2)
9	21321	620	68.37	99.26	99.26	3.28	2.25	3.26	3.26	1.070
17	22145	636	69.23	101.83	101.83	3.22	2.23	3.27	3.27	1.072
26	22464	640	69.78	102.47	102.47	3.19	2.23	3.27	3.27	1.071
34	22464	640	69.78	102.47	102.47	3.19	2.23	3.27	3.27	1.071
43	22464	640	69.78	102.47	102.47	3.19	2.23	3.27	3.27	1.071
51	22464	640	69.78	102.47	102.47	3.19	2.23	3.27	3.27	1.071
59	22464	640	69.78	102.47	102.47	3.19	2.23	3.27	3.27	1.071
67	22464	640	69.78	102.47	102.47	3.19	2.23	3.27	3.27	1.071
76	22896	644	70.68	103.11	103.11	3.17	2.24	3.27	3.27	1.070
84	22896	644	70.68	103.11	103.11	3.17	2.24	3.27	3.27	1.070
93	22896	644	70.68	103.11	103.11	3.17	2.24	3.27	3.27	1.070
101	22896	644	70.68	103.11	103.11	3.17	2.24	3.27	3.27	1.070

Table S1 – Tabulated values of parameters of Eq.(5), that allows to evaluate the surface area of the droplets shown in fig. S4 . Based on this data, in the main text the average droplet surface area was estimated to be 1.071 ± 0.001 cm^2.

Half Width at Half Maximum determination

The "HWHM" values were determined by finding the point at which the intensity of the plasmon decays to 0.5 on the red-shifted shoulder. Assuming that the width between the plasmon maximum and this point is the half width half maximum (HWHM). An example is shown in Fig. S5, from which it can be seen that both the half width half maxima are comparable, however the blue shifted shoulder (HWHM 2) was not used in the reported HWHM. This was done because of the fact that certain spectra did not intersect 0.5 on the blue-shifted shoulder, as a result of peak asymmetry. This example shows that 70 nm is a reasonable approximation to the HWHM, though it may not be the absolute value.

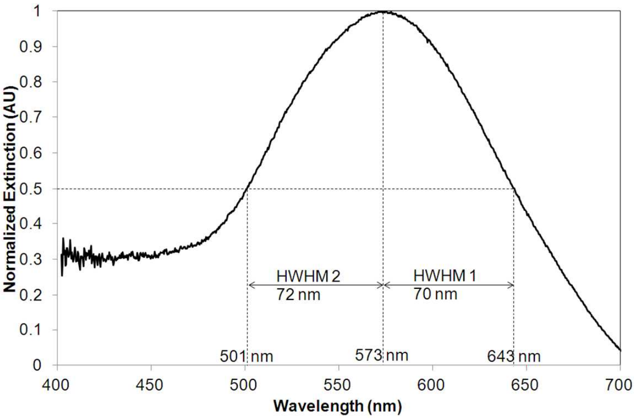

Fig. S5 HWHM were calculated by finding the separation between the peak maximum and the half maximum of the red-shifted shoulder half width half maximum (HWHM 1 above). E.g. in this example, the HWHM was assumed to be 70 nm rather than 71 or 72 nm.

1. Flatté, M. E.; Kornyshev, A. A.; Urbakh, M., Electrovariable Nanoplasmonics and Self-Assembling Smart Mirrors. *The Journal of Physical Chemistry C* **2010,** *114* (4), 1735-1747.
2. Flatté, M. E.; et al., Understanding voltage-induced localization of nanoparticles at a liquid–liquid interface. *Journal of Physics: Condensed Matter* **2008,** *20* (7), 073102.
3. (a) Marcus, R. A., On the theory of ion transfer rates across the interface of two immiscible liquids. *The Journal of chemical physics* **2000,** *113* (4), 1618-1629; (b) Kornyshev, A. A.; Kuznetsov, A. M.; Urbakh, M., Coupled ion--interface dynamics and ion transfer across the interface of two immiscible liquids. *The Journal of chemical physics* **2002,** *117* (14), 6766-6779; (c) Verdes, C. G.; Urbakh, M.; Kornyshev, A. A., Surface tension and ion transfer across the interface of two immiscible electrolytes. *Electrochemistry Communications* **2004,** *6* (7), 693-699.
4. (a) Sharma, V.; Park, K.; Srinivasarao, M., Shape separation of gold nanorods using centrifugation. *Proceedings of the National Academy of Sciences* **2009,** *106* (13), 4981-4985; (b) Potekaev, A.; Bubenchikov, M., Sedimentation of nanoparticles in the field of centrifugal forces. *Russian Physics Journal* **2011,** *54* (2), 211-220.
5. Kornyshev, A. A.; Marinescu, M.; Paget, J.; Urbakh, M., Reflection of light by metal nanoparticles at electrodes. *Physical Chemistry Chemical Physics* **2012,** *14* (6).

Self-Assembly and Applications of Ultraconcentrated Nanoparticle Solutions

Vladimir A. Turek, Laura N. Elliott, Arwen I. I. Tyler, Angela Demetriadou, Jack Paget, Michael P. Cecchini, Anthony R. Kucernak, Alexei A. Kornyshev, and Joshua B. Edel*

Department of Chemistry, Imperial College London, South Kensington Campus, London, SW7 2AZ United Kingdon

ABSTRACT We demonstrate a highly efficient method for concentrating, purifying and separating gold nanoparticles. The method relies on localized density gradients that can be formed at an aqueous | organic phase interface. We show that this method is able to concentrate aqueous gold nanoparticles to the point where confinement leads to variable interparticle separations. Furthermore, the physical properties of the resulting solution are drastically altered when compared to water. For example, densities higher than 4.5 g/cm^3 could be generated without nanoparticle aggregation. As far as we are aware, this is one of the highest reported densities of an aqueous solution at room temperature. Finally, the compositions of the solutions generated are highly dependent on parameters such as particle size and background analyte making this technique highly advantageous for the separation of multimodal NP populations and chemical purification, with 99.5% and >99.9% efficiency, respectively.

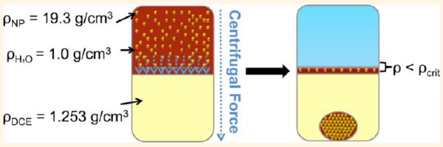

KEYWORDS: liquid−liquid interface · centrifugation · nanoparticles · purification · size separation · plasmon ruler

Nanoparticles (NPs) hold great promise in a vast number of fields including sensing,[1−3] catalysis,[4] medicine,[5,6] water treatment,[7] electronics,[8] solar cells[9] and optics.[10] Most of these applications require precise control over the NPs themselves in terms of size, shape, concentration, monodispersity and the medium in which they are suspended. Furthermore, there has been intense research focused on the synthesis of ever more complex particles with unique properties,[11] such as complex nonspherical geometries,[12] or even NPs with unique surface chemistries.[13] However, some of the common chemicals used in these processes such as surfactants,[14] dyes,[15] and polymers[16] are difficult to remove completely and can be detrimental in some applications. The synthesis of nonspherical NPs generally also suffer from broad size and/or geometry distributions.[17] Finally, the NP concentration is an overlooked physical property of NP solutions. So called 'nanofluids' (colloidal solutions with a high nanoparticle content) display remarkably varied physical properties as a function of NP concentration; however, very few techniques exist that can efficiently increase the concentration without inducing irreversible aggregation.[18] There is therefore a need for efficient methods that will achieve size/shape separation and purify the NPs from chemical contaminants, as well as increase the concentration of NPs without aggregation. Here, we present a method which allows for the rapid formation of ultraconcentrated gold NP aqueous solutions. As far as we are aware, this is the highest density aqueous NP solution known to date. We also show that this method can lead to highly efficient chemical purification and size separation of NPs.

The general operating mechanism is as follows: In the presence of a denser organic phase, aqueous NPs can be driven to the liquid−liquid interface (LLI), or in our case aqueous|1,2-dichloroethane interface, by a centrifugal force. Provided that the difference in solvation energies[19,20] are high enough to prevent a transfer of NPs across the interface, this leads to an increase in the concentration of particles directly adjacent to the interface.The concentration gradient also gives rise to a density gradient which upon reaching a critical density, may induce instabilities at the interface, leading to the

* Address correspondence to joshua.edel@imperial.ac.uk.

Received for review June 20, 2013 and accepted September 26, 2013.

10.1021/nn403131e

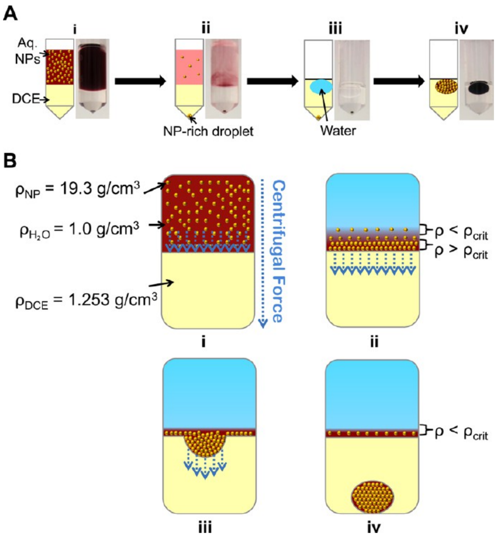

Figure 1. Schematic and mechanism of ultraconcentration. (A) Centrifugation of an aqueous nanoparticle solution in the presence of DCE (i) leads to an extremely concentrated NP droplet being formed at the bottom of the DCE (ii). The supernatant can be easily removed and replaced with pure water (iii), if contact is made with this phase the droplet can be redispersed (iv). (B) The centrifugal force acts on the NPs (i) and drives them to the interface (ii) above a critical threshold density, the interface is deformed (iii) and eventually a NP-rich droplet breaks off from the main aqueous phase (iv).

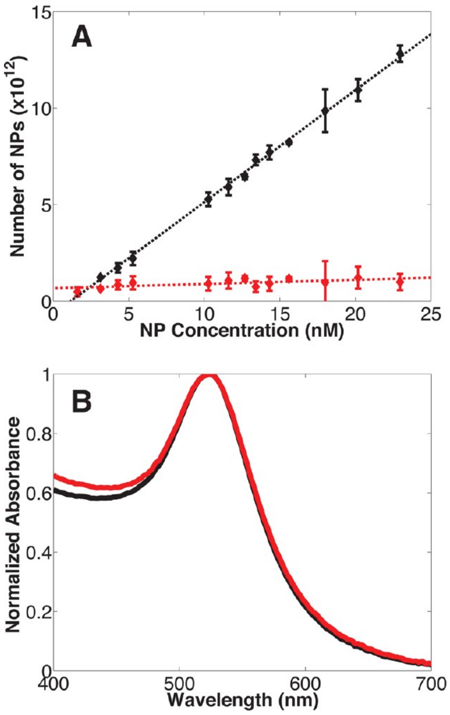

Figure 2. Characterization of the initial NP concentration dependence on the NP-rich droplet formation and the stability of the ultraconcentrated NPs. (A) Initial NP concentration dependence on the number of NPs in the droplet (black) and residual particles in the supernatant (red) at an initial NaCl equivalent concentration of 2.5 mM, centrifuged at 20 238*g* for 15 min. The constant residual NPs in the supernatant represents a threshold, below which no droplet is formed, while the NPs in the droplet follow a $y = 0.58x - 0.68$ dependency. (B) Comparison of the normalized absorbance of as made NPs (red) and a 20 000-fold dilution of the NP-rich droplet (black). The fact that no red-shifted 'shoulder' is seen in the spectrum of the diluted sample suggests that the method does not induce aggregation.

formation of NP rich droplets which sediment and merge at the bottom of the centrifuge tube (Figure 1A). It should be noted that droplet generation ensures that the particles remain dispersed in an aqueous environment, in other words, phase transfer does not occur. The critical density for this process is related to the following: the difference in density between the organic and aqueous phase, and the interfacial tension (a water|1,2-dichloroethane (DCE) interface has an interfacial tension of 28.1 mN/m at 20 °C; the DCE has a density of 1.253 g/cm^3 at 20 °C). The NP concentration in these droplets is high enough that electrostatic repulsion, screened by the ions of electrolyte, may induce local, short-range order. The interparticle spacing can be further controlled through the concentration of electrolyte, the increase of which will decrease the screening length. The resulting NP concentration levels at appropriate ionic strengths can exceed 3.7 g of Au/mL of solution, reaching densities of 4.5 g/cm^3

RESULTS AND DISCUSSION

Nanoparticle-Rich Droplet Formation and Concentration. Recently Turek *et al.* have demonstrated that centrifugation can be used to facilitate NP adsorption at a LLI made up of an aqueous solution consisting of NaCl and 16 ± 2.4 nm Au NPs functionalized with 12-mercaptododecanoic acid (MDDA) and DCE.[10] The particles adsorbed at the interface were characterized as a function of the ionic strength of the solution, relative centrifugal force, centrifugation time, pH, and the interfacial area. We build on this by operating with low ionic strength aqueous solutions (NaCl equivalent concentration of 1.0–8.5 mM) to limit NP adsorption and facilitate a concentration gradient at the LLI. By doing so, an aqueous droplet containing an extremely high NP concentration can be formed at the bottom of the DCE layer. Experimentally this was performed in a 2 mL centrifuge tube, consisting of 0.5 mL of DCE and 1 mL of NP solution, with a total number of NPs between 9.4×10^{11} and 1.4×10^{13}. To determine how many NPs transfer from the bulk to the droplet, the initial NP concentration in the bulk aqueous phase was varied between 1.5 and 23 nM (Figure 2B). A seemingly linear relationship was observed for the number of particles confined to the droplet with increasing initial concentration in the bulk of the aqueous phase; the percentage of the initial NPs confined to the droplet increased from 50% at 1.5 nM to 93% at 23 nM as determined through UV−Vis spectroscopy. However, the number of residual particles in the supernatant remained approximately constant, at a value of ≈9.4 × 10^{11} NPs irrespective of the initial concentration. This constant value is a threshold for the minimum number of NPs needed for this method to work—below this, no droplet is formed. On the basis of these observations, the mechanism that is proposed for the droplet generation is shown in Figure 1B. Upon centrifugation the NPs in the aqueous phase are driven to the interface (Figure 1B i), if the initial number of particles is above the threshold value, then the local density of the aqueous side of the interface is increased (Figure 1B ii) to the point where it is energetically more favorable to generate "extra" interfacial area (Figure 1B iii). Once the density gradient is established, the droplets break away from the interface and sediment at the bottom of the DCE phase (Figure 1B iv). At this point, the residual particles in the supernatant are insufficiently concentrated to obtain a sufficient density gradient for this process to be repeated.

Since the formed droplet is an extremely concentrated gold NP solution, we need to significantly dilute the sample to recover the absorbance. The droplet, formed from an aqueous solution containing an equivalent of 1 mM NaCl (as assessed from conductivity measurements), revealed the absorbance at 525 nm to be 20 300 ± 19%. When an extinction coefficient of 4.916 × $10^8 M^{-1}$ cm^{-1} was used,[21] the NP concentration in the droplet was determined to be ≈41.3 μM or 2.49 × 10^{16} ± 4.70 × 10^{15} NPs/mL. Given a weight per nanoparticle of 4.40 × 10^{-17} ± 1.94 × 10^{-17} g, the total gold content of this solution is 1.10 ± 0.53 g Au/mL. Interestingly, the density of this solution was determined to be 2.24 ± 0.64 g/cm^3 (*cf.* Supporting Information). It should be noted that the density and dilution values are in agreement on the estimated NP concentrations, *i.e.*, from the density (assuming a negligible density contribution from the ions and NP functionality) the weight of gold in the solution would be 1.30 ± 0.67 g/mL.

It was decided to test whether the salt concentration can control the concentration of NPs by altering the screening length. It then follows that an increase of the ionic strength leads to higher NP concentrations. This was verified by monitoring the density of the resulting solution as a function of the ionic strength of the initial preconcentrated solution (1.0−8.5 mM equivalent NaCl). As shown in Figure 3A, a strong effect of NaCl content on the concentration of NPs in the droplet is observed. Surprisingly, at an initial NaCl concentration of 8.5 mM, the resulting NP-rich droplet has a density of 4.57 ± 0.26 g/cm^3 and is therefore higher than even a saturated Clerici solution at room temperature.[22] This density corresponds to a solution which is composed of almost 20 vol % gold. To the best of the authors' knowledge, this is the highest density aqueous solution that has been demonstrated at room temperature; however, it should be stressed that higher densities still are likely to be accessible with this method. Furthermore, the NP concentration of this solution is 9.09 × 10^{16} NPs/mL or 3.76 g of gold/mL; the optical density at 525 nm is therefore expected to

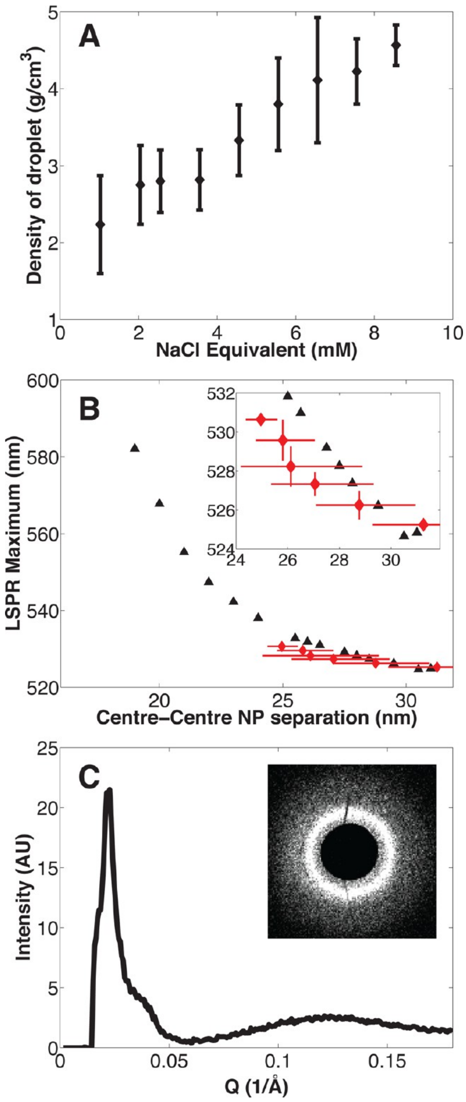

Figure 3. Tunable properties of the NP-rich droplet as a function of salt concentration. (A) Density of the resulting NP-rich droplet as a function of the ionic strength. There is a strong dependence between the density of the resulting droplet on the NaCl concentration, due to more efficient screening of the NPs' charge, reaching a density of 4.57 ± 0.26 g/cm^3 at an NaCl equivalent of 8.5 mM. (B) Experimental results (red) and simulations (black) of the LSPR maximum of the NP-rich droplet as function of the interparticle separations agree well with each other (note: experimental separations are approximated from the density). This indicates that the position of the NPs with respect to each other can be tuned by the ionic strength. (C) Low angle X-ray diffraction pattern of a solution made at 4.5 mM equivalent NaCl confirms there is positional correlation between the NPs, with a center−center separation of 29 nm.

be in excess of 74 000. Taking the surface of the MDDA as the edge of the physical radius of NPs (and assuming this functionality to provide a 1.5 nm steric coating), then this colloidal solution has an active surface area of 73 m^2/mL.

The strong dependence of the density on the NaCl concentration suggests that the separation between the particles is dictated by the ionic screening. If metallic NPs get close enough to each other, the coupling of localized plasmons in each of them leads to a red shift of the localized surface plasmon resonance (LSPR). Transmission measurements (see Supporting Information) of the resulting solutions (Figure 3B) made between 2.0 and 8.5 mM equivalent NaCl confirms that a red-shift between 525.2 ± 0.3 and 530.6 ± 0.2 nm is observed as the NaCl concentration is increased. From the densities of the solutions at these NaCl concentrations, the interparticle separations were estimated by assuming the particles reside as far away from each other as possible and a negligible contribution from the counterions and functionality to the overall density of the solution. A comparison of spectra obtained from Finite Integration Techniques (FIT) computer simulations (see Supporting Information) suggests that these LSPR maxima correspond to gold surface/gold surface separations between neighboring NPs of 10−15 nm.

These figures are supported further by X-ray diffraction (Figure 3C). A NP-rich droplet made at 4.5 mM NaCl equivalent shows a sharp interference peak in the small angle region which was interpreted as the first order peak of the particle−particle structure factor. This peak indicates that the average center−center interparticle separation is ≈29 nm. Working back from the density, the estimated center−center separation for this sample is 28.5 nm, which is in excellent agreement. Further experimentation is needed to fully characterize this, but there is strong evidence that this method is capable of concentrating NPs to levels at which the interparticle separations are controlled in 3 dimensions. The lack of long-range order in these samples is attributed to a relaxation of the compressive force when centrifugation is stopped; nevertheless the physical confinement and electrostatic repulsion give rise to short-range order.

Surprisingly, despite such high concentrations, there is no evidence of aggregation. Figure 2B shows a comparison between the normalized spectra of 'as-made' NPs and a 20 000-fold diluted sample from a NP-rich droplet made at 1 mM NaCl. Given even mild aggregation, the broadness of the dipole peak should increase; however, this is not observed in the diluted NPs' absorbance spectra. The lack of aggregation is likely due to the exceptional stability of MDDA stabilized NPs as described elsewhere.[10] Perhaps more surprising is that even citrate stabilized particles can be concentrated in this manner without initial aggregation. However, it should be noted that citrate stabilized NPs have a short-lived stability and aggregate irreversibly within approximately 30 min of droplet formation. Despite this, it is hypothesized that the initial stability of citrate particles at these concentrations is due to the fact that the forces acting on the NPs with this method are the same as during conventional centrifugation. Consequently if the NPs do not aggregate during conventional centrifugation, the probability that the NPs will be stable in the high density droplet is greater; however, this stability may be short-lived. Naturally, the versatility of this method can be extended to systems other than Au NPs as long as the NPs to have a sufficiently high sedimentation coefficient.

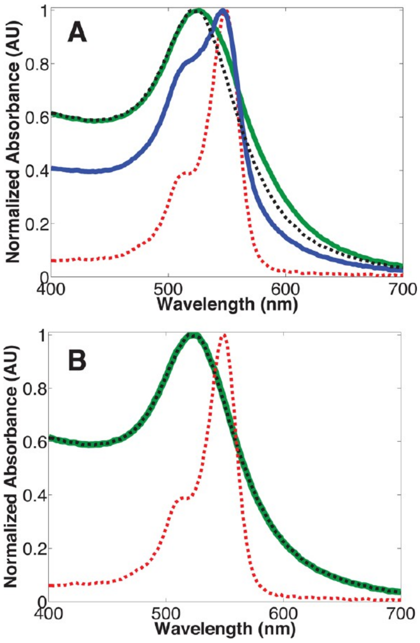

Figure 4. Comparison between conventional centrifugation and this method for the purification of NPs in the presence of a dye. (A) After a single step, conventional centrifugation (blue) is able to purify 95.2 ± 0.8% of the dye Rose Bengal (red dotted), while the second step (green) purifies an additional 90.0 ± 3.0% of the dye to a final purity of 99.5 ± 0.1%; when compared to as-made particles (black dotted), a clear shift in the absorbance spectrum can still be seen. (B) After a single step forming the NP-rich droplet, and redispersing in water (green) in excess of 99.9% of the dye is removed. So much so, that there is a negligible difference in the absorbance spectrum between the as-made and purified NPs. For both comparisons, the NP solutions were contaminated with 2 mM Rose Bengal and centrifugation was carried out at 20 238*g* for 15 min.

An interesting question related to this is why the functionalized NPs are in principle able to come at such close surface-to-surface separations in electrolytic solutions while not fusing? This could be understood using the Donnan equilibrium, which potentially manifests itself here due to a spontaneous increase salt concentration as the NPs are pushed into close proximity.

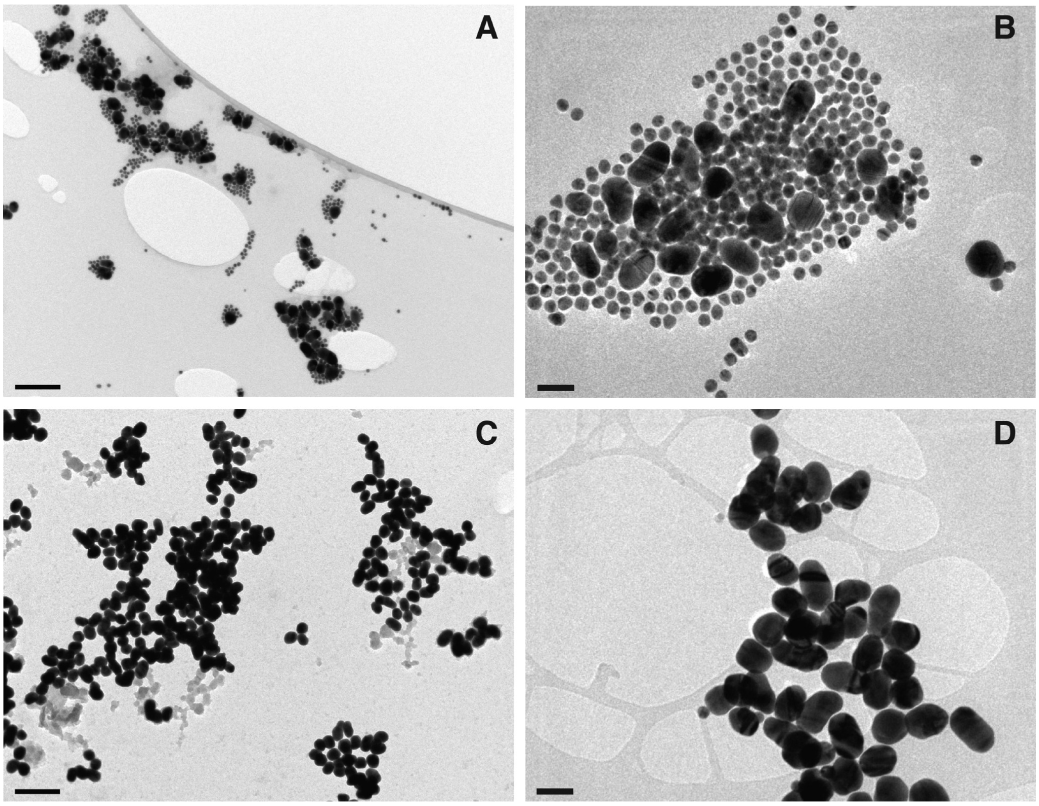

Figure 5. Demonstration of size separation of NP solutions. (A and B) Mixture of 16 and 43 nm gold particles. (C and D) Separated 43 nm particles after 15 min at 1503*g*. On the basis of the analysis of over 5000 NPs, there is a 99.5% removal of 16 nm NPs and a 210-fold enrichment of 43 nm particles. Scale bar for (A) and (C) is 200 nm, for (B) and (D) it is 50 nm.

Nanoparticle Purification and Size Separation. Dilution of the concentrated droplet back to as-made concentrations with DI water effectively acts as a purification mechanism. The LLI confines the particles to the droplet, which together with the high density of this solution makes its separation from the supernatant trivial. To test the levels of purification that can be achieved, a dye (Rose Bengal) was added to the aqueous NP solution (with a total of 8.9×10^{12} NPs) at a concentration of 2 mM. Conventional centrifugation was compared to the droplet generation method, as is shown in Figure 4. After a single step, conventional centrifugation removed 95.2 ± 0.8% of the dye, while the second step removed a further 90.0 ± 3.0%, to give a total purity of 99.5 ± 0.1% after 2 steps. Conversely, a single purification step with our method leads to purity levels that could not be accurately measured by UV−visible spectroscopy (due to an almost perfect overlap between the purified and uncontaminated NPs), but is in excess of 99.9%. This purification can also be applied to reducing the ionic strength of the NP solution. For example, the conductivity of the initial NP solution was 217 μS/cm while diluting the droplet with ultrapure water back to the as-made concentrations leads to a reduced conductivity of 1.4 μS/cm. Reducing the ionic strength aids stabilization of the nanoparticles through the increase in Debye screening length.

The efficiency of the purification relies on a difference in the sedimentation coefficient of the particles and dissolved species. Because of a large difference between the size of the nanoparticles and chemical species, this process proves to be extremely efficient. However, the same principle can be applied to separate NPs of differing sizes. For example, Figure 5A shows a mixture of 16 nm MDDA and 43 nm citrate gold particles, mixed in a 1:1 (v/v) ratio of as-made solutions; this equates to approximately 6.0×10^{11} 16 nm and 3.1×10^{10} 43 nm NPs per mL. Centrifuging the mixture at 1503*g* for 15 min results in the formation of a droplet consisting predominately of 43 nm NPs, Figure 5B. It is worth noting that optimizing the RCF may maximize the separation efficiency; however, this was not investigated in detail. Analysis of electron microscopy images of over 5000 particles (done by manually counting the particles from SEM) showed that the ratio of 16:40 nm particles was 21.57 for the initial mixed solution, and 0.10 in the separated NP-rich droplet. This suggests a ≈210 enrichment of the 43 nm NPs. This has important implications in NP synthesis where multimodal size distributions are present. This is a common problem with more advanced NP syntheses, where despite numerous reports in the literature describing nanometer control over the dimensions of nanoparticles, secondary nanostructures also arise. As an example, the "standard" gold nanorod synthesis[14] has exquisite control over the aspect ratio of the rods,[23] however 3 distinct particle populations are present − rods as well as large and small spheres.[24] Because of the properties of NPs being extremely size and shape specific,[25] these secondary particle contaminants are extremely deleterious to many of the applications that NPs promise. Indeed, one of the most time-consuming elements of many nonspherical nanoparticle syntheses is purification and size separation of the desired product. Naturally, the droplet formation process demonstrated here is a nonuniversal separation technique as only the larger particles (or those with a higher sedimentation coefficient) may be confined to the droplet. Furthermore, as Figure 2A demonstrated, a constant number of particles need to act as the 'sacrificial' particles for the critical density for droplet formation to be reached. If the smaller particles act as these sacrificial particles, then the separation efficiency is likely to be optimum, however if the concentration of the smaller particles becomes large enough to also form a droplet, then separation efficiencies are expected to be reduced. Nevertheless, if the conditions for separation are appropriately chosen, then this technique can be remarkably efficient for size separation. The speed, simplicity and efficiency that this technique offers are therefore highly pertinent to researchers working with NPs.

CONCLUSIONS

In conclusion, it has been demonstrated that by centrifuging a NP solution in the presence of a denser, insoluble phase (in this case water and DCE) after a single step, gold NP concentrations in excess of 3.7 g of gold/mL can be rapidly achieved. The density of the resulting aqueous phase can be tuned by the ionic strength and can exceed even the Clerici solution. At 8.5 mM NaCl equivalent, the density was determined to be 4.57 ± 0.26 g/cm^3 and is, to the best of the authors' knowledge, the highest density aqueous phase that has yet been demonstrated. Moreover, in this concentration the interparticle separation can be controlled in three dimensions. In addition, this method has also been shown to be extremely efficient in the purification and size separation of NPs, with an efficiency of >99.9% and 99.5%, respectively. It should be noted that the minimum weight/size of the NPs that is needed for this method to work is likely to be dependent on specifics of individual equipment/instruments rather than a universal property. Provided that the effective density of the solution directly adjacent to the interface is sufficiently large, then there is no obvious reason to expect any fundamental constraints on particle size. The simplicity, versatility, speed and efficiency of this technique allow it to be widely used for NP handling, while the remarkable physical properties of the resulting solutions will find applications as novel advanced materials. Of particular interest would be to determine the thermal conductivities of such solutions as the confinement of the NPs may significantly enhance the conductivity as compared to water.

EXPERIMENTAL SECTION

Equipment Used. UV−vis measurements were performed with a Nanodrop 2000c spectrometer using PMMA cuvettes. An Eppendorf 5424 centrifuge with a FA-45-24-11 rotor with a radius of 8.4 cm was used, capable of holding 24 × 2 mL centrifuge tubes at an angle of 45° with a maximum relative centrifugal force (RCF) of 20 238*g* (14 680 rpm). A Beckmann Coulter DelsaNano C dynamic light scattering machine was used for hydrodynamic particle sizing and zeta potential measurements. A Leo Gemini 1525 FEGSEM scanning electron microscope and a JEOL 2010 transmission electron microscope were used to size the NPs and demonstrate size separation. A Mettler-Toledo SevenGo Duo pro pH/ion/conductivity meter was used for conductivity measurements.

In all cases, ultrapure water with a resistivity of 18.2 MΩ·cm was used. All chemicals were purchased from Sigma-Aldrich UK and used without further purification. Chemicals used were the following: $HAuCl_4 \cdot \approx 3H_2O$ (fw 339.79 (anhydrous), 99.999% trace metal basis); trisodium citrate dihydrate (fw 294.10, ≥99%); 12-mercaptododecanoic acid (MDDA, fw 232.38, 99%); methanol (MeOH, CHROMASOLV, HPLC grade, ≥99.9%); 1,2-dichloroethane (DCE) (ACS reagent, ≥99.0%).

MDDA stabilized 16 nm gold nanoparticles were prepared as described previously.[10] Briefly, 8.6 mg of $HAuCl_4 \cdot 3H_2O$ (5 mg gold) was dissolved in 95 mL of H_2O and brought to 100 °C. Under stirring, 5 mL of 13.6 mM sodium citrate solution was then added to the refluxing mixture. The initially faint-yellow solution gradually turned dark-blue followed by wine-red over a period of 10 min. At this point the NPs were measured to have a hydrodynamic diameter, electrophoretic mobility, and zeta potential of 20 ± 4 nm, -3.60×10^{-4} cm^2/(V s), and −47.0 mV, respectively. The size of the particles was verified to be 16.3 ± 2.4 nm using an SEM and TEM. Once the reaction had gone to completion (typically 15 min), the temperature was reduced to 60 °C. This was followed by the addition of MDDA (5 mg) dissolved in MeOH (0.5 mL). The functionalization was allowed to continue for at least 1 h to ensure complete monolayer coverage, after which the mixture was allowed to slowly cool with continuous stirring for at least an extra hour. The excess MDDA precipitated out and was removed by filtration. The functionalized NP typically had a hydrodynamic diameter of 26 ± 7 nm, electrophoretic mobility of -4.37×10^{-4} cm^2/(V s), and a zeta potential of −57.0 mV. The solution typically had a conductivity of 217 μS/cm.

The 43 nm gold particles were synthesized as above with the exception of adding 5 mL of 6.39 mM sodium citrate solution to the refluxing gold salt solution. These particles were not subsequently functionalized with MDDA. After synthesis, the concentration of the citrate ions in the solution was adjusted to be equivalent to that of the 16 nm solution. The final particles had a hydrodynamic diameter of 64.7 ± 30.5 nm, while SEM showed an average particle size of 43 ± 4 nm.

In all experiments, a 2 mL centrifuge tube, with 0.5 mL of DCE and 1 mL of NP solution, was used. To pellet the 16 nm particles, the maximum RCF setting on the centrifuge of 20 238*g* for 15 min was applied. In the size-separation experiments, a 1:1 (vol/vol) mixture of 16 and 43 nm particles was used and centrifuged at 1503*g* (a lower RCF was chosen to limit aggregation of the citrate stabilized 43 nm NPs) for 15 min. The pellets were extracted by pipetting out the residual aqueous phase, followed by extraction of the pellet encapsulated in a small amount of DCE which was then allowed to evaporate off.

X-ray experiments were carried out on the high brilliance beamline I22 at Diamond Light Source (DLS), U.K. The synchrotron X-ray beam was tuned to a wavelength of 0.688 Å (E = 18 keV), having beam dimensions of approximately 320 × 250 μm, and had a typical flux of 10^{12} photons s^{-1}. The distance between the sample and detector was set at 2.2 m, and the 2-D diffraction patterns were recorded on a Pilatus 2M detector. Silver behenate (a = 58.38 Å) was used to calibrate the low-angle X-ray diffraction data. Diffraction images were analyzed using the IDL-based AXcess software package, developed in-house by Dr A. Heron.[26] The measured X-ray spacings are accurate to $\pm$0.1 Å.

Conflict of Interest: The authors declare no competing financial interest.

Supporting Information Available: Scanning electron micrographs of size separation, technique for density and LSPR measurements and details on FIT simulations. This material is available free of charge *via* the Internet at http://pubs.acs.org.

Acknowledgment. This work was funded in part by an ERC starting investigator grant and EPSRC grants EP/G00465X and EP/H046593/1. The authors would like to thank Professor John Seddon for useful discussions regarding the XRD diffraction experiments and to Christopher Wood for performing the TEMs. AAK and AD would like to thank EU FP7 'Nanodetector' grant (NMP4-SE-2012-280478).

REFERENCES AND NOTES

1. Cecchini, M. P.; Turek, V. A.; Paget, J.; Kornyshev, A. A.; Edel, J. B. Self-Assembled Nanoparticle Arrays for Multiphase Trace Analyte Detection. *Nat. Mater.* **2013**, *12*, 165–171.
2. Cecchini, M. P.; Hong, J.; Lim, C.; Choo, J.; Albrecht, T.; deMello, A. J.; Edel, J. B. Ultrafast Surface Enhanced Resonance Raman Scattering Detection in Droplet-Based Microfluidic Systems. *Anal. Chem.* **2011**, *83*, 3076 3081.
3. Cecchini, M. P.; Stapountzi, M. A.; McComb, D. W.; Albrecht, T.; Edel, J. B. Flow-Based Autocorrelation Studies for the Detection and Investigation of Single-Particle Surface-Enhanced Resonance Raman Spectroscopic Events. *Anal. Chem.* **2011**, *83*, 1418–1424.
4. Wilton-Ely, J. D. E. T. The Surface Functionalisation of Gold Nanoparticles with Metal Complexes. *Dalton Trans.* **2008**, 25–29.
5. Cheong, K. H.; Yi, D. K.; Lee, J.-G.; Park, J.-M.; Kim, M. J.; Edel, J. B.; Ko, C. Gold Nanoparticles for One Step DNA Extraction and Real-Time PCR of Pathogens in a Single Chamber. *Lab Chip* **2008**, *8*, 810–813.
6. Llevot, A.; Astruc, D. Applications of Vectorized Gold Nanoparticles to the Diagnosis and Therapy of Cancer. *Chem. Soc. Rev.* **2012**, *41*, 242–257.
7. Abid, A. D.; Kanematsu, M.; Young, T. M.; Kennedy, I. M. Arsenic Removal from Water Using Flame-Synthesized Iron Oxide Nanoparticles with Variable Oxidation States. *Aerosol Sci. Technol.* **2012**, *47*, 169–176.
8. Garnett, E. C.; Cai, W.; Cha, J. J.; Mahmood, F.; Connor, S. T.; Greyson Christoforo, M.; Cui, Y.; McGehee, M. D.; Brongersma, M. L. Self-Limited Plasmonic Welding of Silver Nanowire junctions. *Nat. Mater.* **2012**, *11*, 241–249.
9. Brown, M. D.; Suteewong, T.; Kumar, R. S. S.; D'Innocenzo, V.; Petrozza, A.; Lee, M. M.; Wiesner, U.; Snaith, H. J. Plasmonic Dye-Sensitized Solar Cells Using Core– Shell Metal– Insulator Nanoparticles. *Nano Lett.* **2011**, *11*, 438.
10. Turek, V. A.; Cecchini, M. P.; Paget, J.; Kucernak, A. R.; Kornyshev, A. A.; Edel, J. B. Plasmonic Ruler at the Liquid–Liquid Interface. *ACS Nano* **2012**, *6*, 7789–7799.
11. Vigderman, L.; Zubarev, E. R. Starfruit-Shaped Gold Nanorods and Nanowires: Synthesis and Sers Characterization. *Langmuir* **2012**, *28*, 9034.
12. Grzelczak, M.; Perez-Juste, J.; Mulvaney, P.; Liz-Marzan, L. M. Shape Control in Gold Nanoparticle Synthesis. *Chem. Soc. Rev.* **2008**, *37*, 1783–1791.
13. Ahammed, S.; Saha, A.; Ranu, B. C. Hydrogenation of Azides over Copper Nanoparticle Surface Using Ammonium Formate in Water. *J. Org. Chem.* **2011**, *76*, 7235–7239.
14. Jana, N. R.; Gearheart, L.; Murphy, C. J. Wet Chemical Synthesis of High Aspect Ratio Cylindrical Gold Nanorods. *J. Phys. Chem. B* **2001**, *105*, 4065–4067.
15. Faulds, K.; Littleford, R. E.; Graham, D.; Dent, G.; Smith, W. E. Comparison of Surface-Enhanced Resonance Raman Scattering from Unaggregated and Aggregated Nanoparticles. *Anal. Chem.* **2003**, *76*, 592–598.
16. Sun, Y.; Xia, Y. Shape-Controlled Synthesis of Gold and Silver Nanoparticles. *Science* **2002**, *298*, 2176–2179.
17. Jin, R.; Charles Cao, Y.; Hao, E.; Metraux, G. S.; Schatz, G. C.; Mirkin, C. A. Controlling Anisotropic Nanoparticle Growth through Plasmon Excitation. *Nature* **2003**, *425*, 487–490.
18. Li, Y.; Zhou, J.; Tung, S.; Schneider, E.; Xi, S. A Review on Development of Nanofluid Preparation and Characterization. *Powder Technol.* **2009**, *196*, 89–101.
19. Bresme, F.; Oettel, M. Nanoparticles at Fluid Interfaces. *J. Phys.: Condens. Matter* **2007**, *19*, 413101.
20. Flatté, M. E.; Kornyshev, A. A.; Urbakh, M. Understanding Voltage-Induced Localization of Nanoparticles at a Liquid–Liquid Interface. *J. Phys.: Condens. Matter* **2008**, *20*, 073102.
21. Liu, X.; Atwater, M.; Wang, J.; Huo, Q. Extinction Coefficient of Gold Nanoparticles with Different Sizes and Different Capping Ligands. *Colloids Surf., B* **2007**, *58*, 3–7.
22. Koroznikova, L.; Klutke, C.; McKnight, S.; Hall, S. The Use of Low-Toxic Heavy Suspensions in Mineral Sands Evaluation and Zircon Fractionation. *J. South. Afr. Inst. Min. Metall.* **2008**, *108*, 25–33.
23. Jana, N. R. Gram-Scale Synthesis of Soluble, near-Monodisperse Gold Nanorods and Other Anisotropic Nanoparticles. *Small* **2005**, *1*, 875–882.
24. Akbulut, O.; Mace, C. R.; Martinez, R. V.; Kumar, A. A.; Nie, Z.; Patton, M. R.; Whitesides, G. M. Separation of Nanoparticles in Aqueous Multiphase Systems through Centrifugation. *Nano Lett.* **2012**, *12*, 4060–4064.
25. Chithrani, B. D.; Ghazani, A. A.; Chan, W. C. W. Determining the Size and Shape Dependence of Gold Nanoparticle Uptake into Mammalian Cells. *Nano Lett.* **2006**, *6*, 662–668.
26. Seddon, J. M.; Squires, A. M.; Conn, C. E.; Ces, O.; Heron, A. J.; Mulet, X.; Shearman, G. C.; Templer, R. H. Pressure-Jump X-Ray Studies of Liquid Crystal Transitions in Lipids. *Philos. Trans. R. Soc., A* **2006**, *364*, 2635–2655.

Self-Assembly and Applications of Ultra-Concentrated Nanoparticle Solutions

Vladimir A. Turek, Laura N. Elliott, Arwen I. I. Tyler, Angela Demetriadou, Jack Paget, Michael P. Cecchini, Anthony R. Kucernak, Alexei A. Kornyshev, Joshua B. Edel*

Department of Chemistry, Imperial College London, South Kensington Campus, London, SW7 2AZ

Corresponding author: joshua.edel@imperial.ac.uk

Size Separation

A

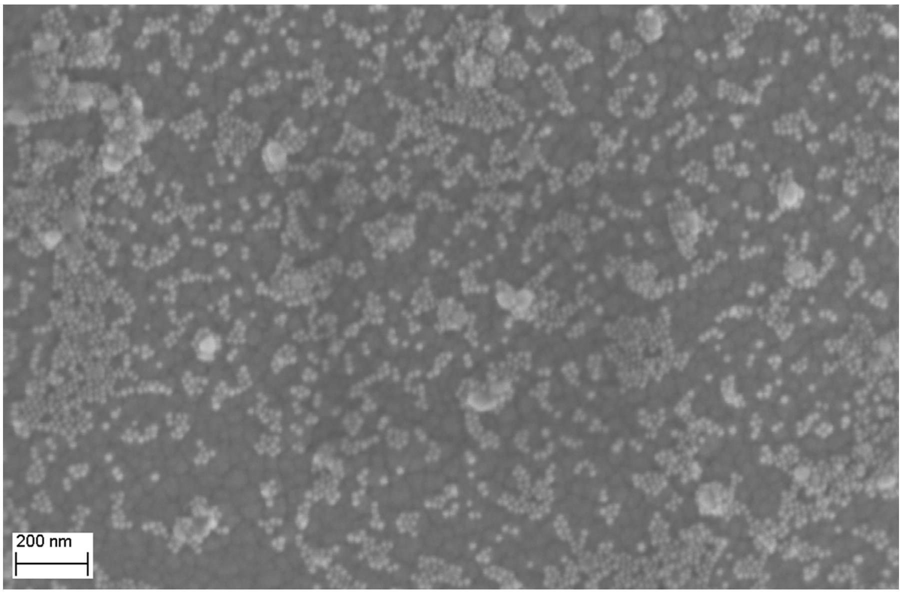

B

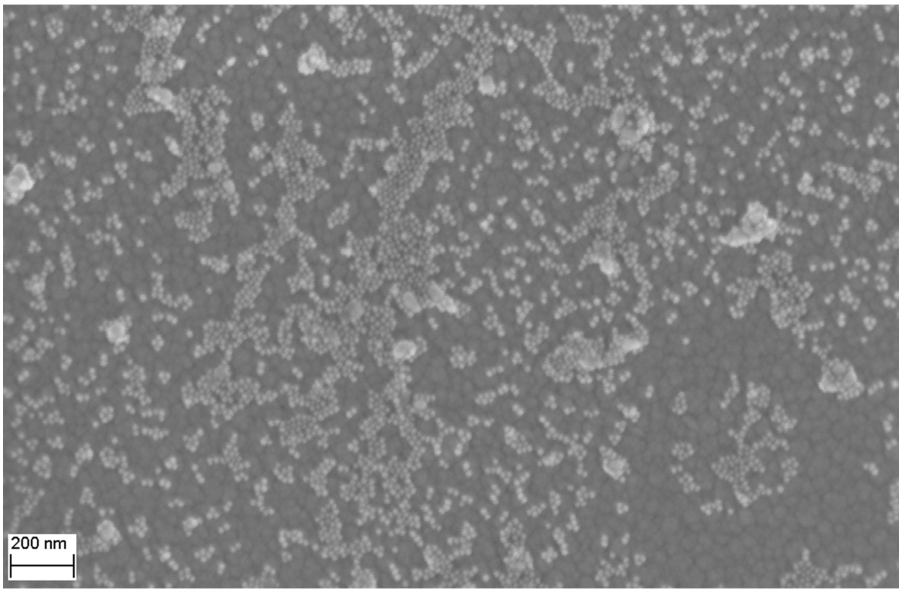

C

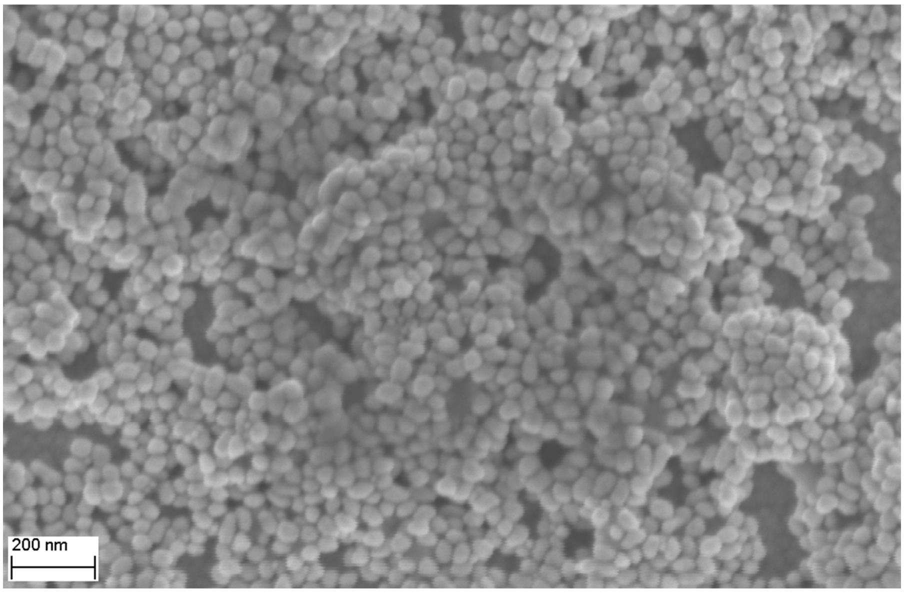

D

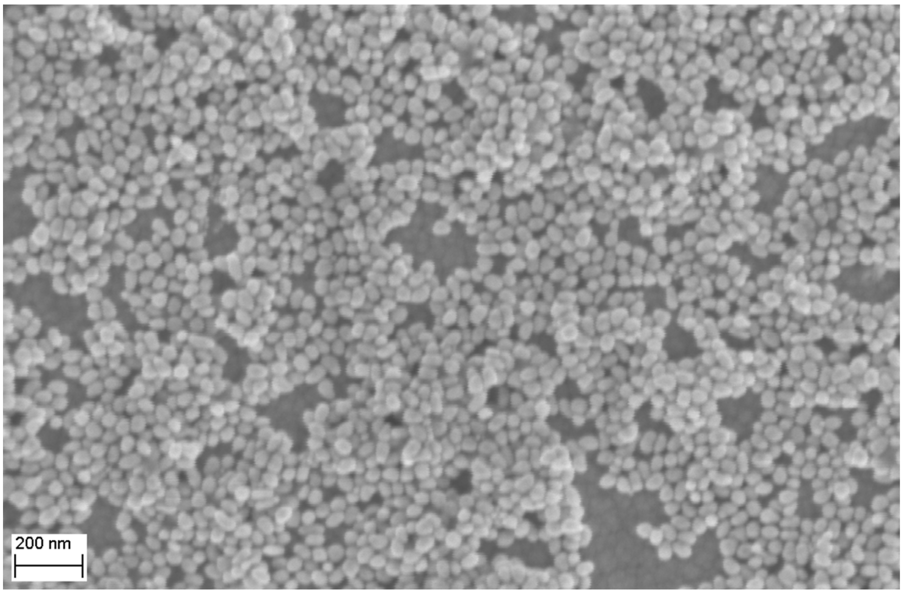

Figure S1. SEM images demonstrating size separation. (A) and (B) Mixed sample of 16 and 43 nm NPs in a 1:1 (vol/vol) ratio at as-made concentrations. (C) and (D) NPs extracted from the NP-rich droplet after a 15 minute centrifugation at 1,503 g.

NP-rich droplet Density Measurements

The mass of the NP-rich droplet was determined by extracting it from the DCE, followed by weighing it on a pre-weighed coverslip. The droplet was then sandwiched by another coverslip, with two more coverslips of a constant thickness (140 µm) either side acting as the height markers, Figure S2. The area of the droplet was then calculated through ImageJ, followed by multiplication by the known height to determine the volume.

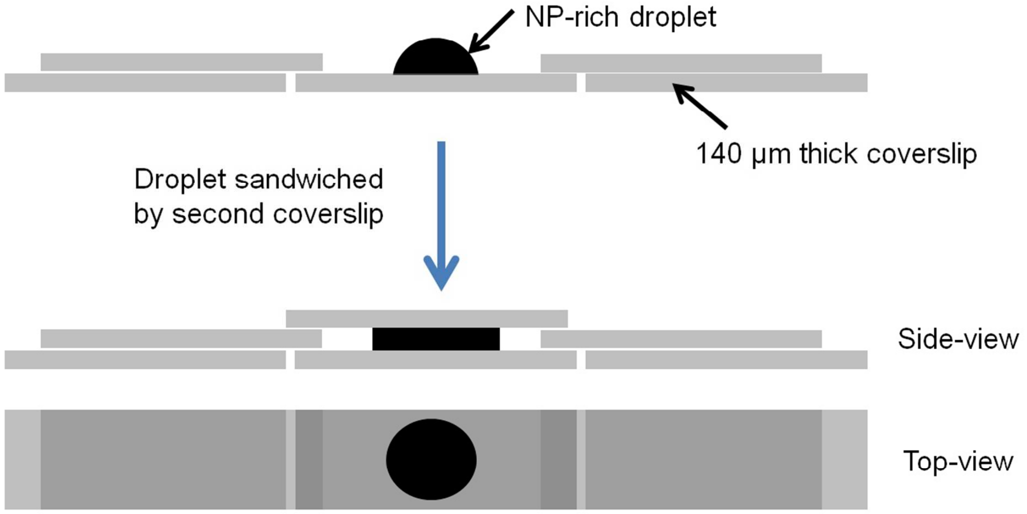

Figure S2. Schematic of volume measurements of the NP-rich droplets. The droplets were sandwiched and photographed between two coverslips with a known height. From the known dimensions of the coverslips, ImageJ was used to determine the area of the circle from the top-view, followed by multiplication by the height to determine the volume.

Localized Surface Plasmon Resonance Measurements

Due to the ultra-high absorbance of the NP-rich phase, transmission measurements were performed by first sandwiching the droplet between two coverslips followed spreading and compressing the solution to yield a larger area (and thereby thinner) film. The transmitted spectrum from a halogen light source was then measured by an Ocean Optics S2000 fibre coupled spectrophotometer. The resultant spectra were then fitted to a 6th order polynomial before being normalized.

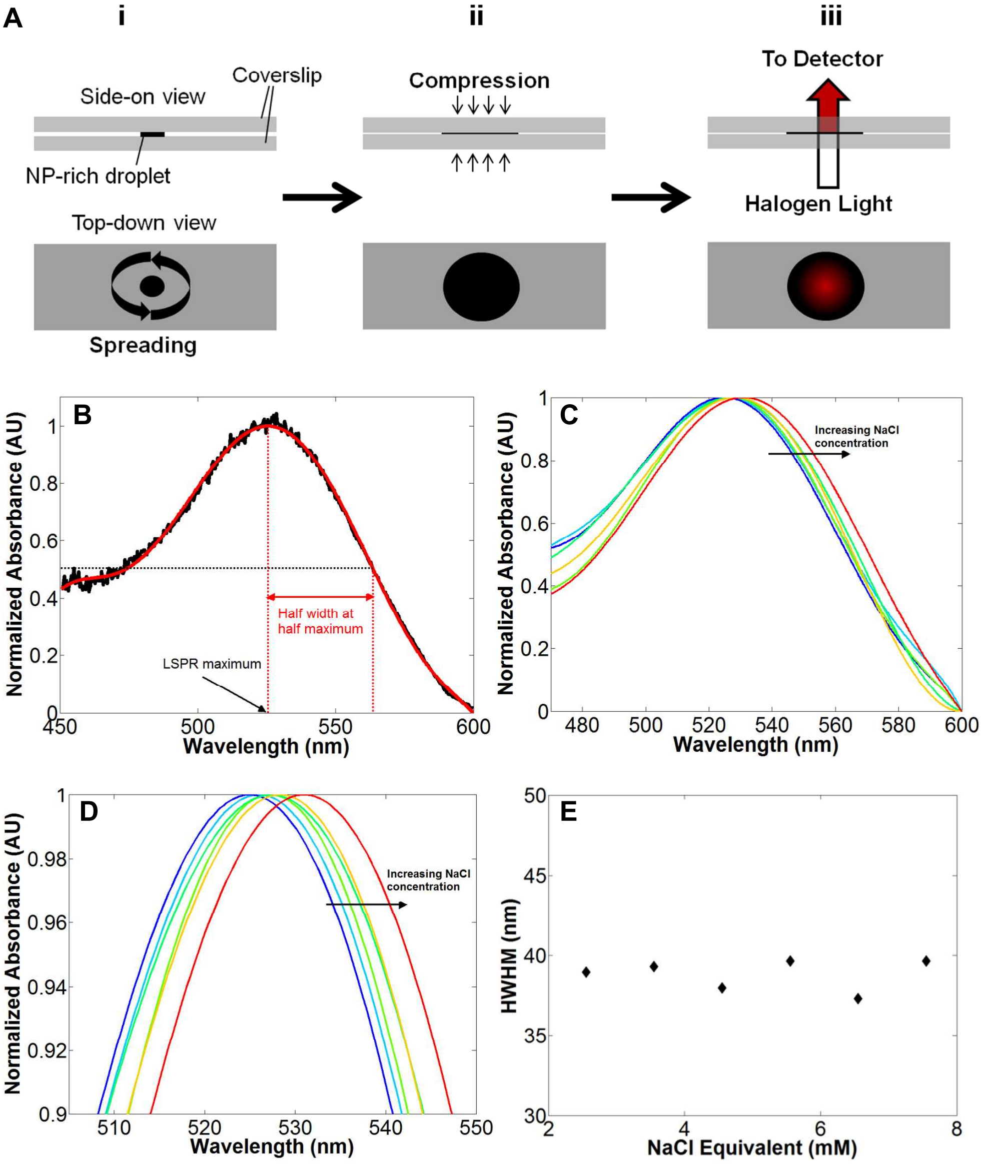

Figure S3. LSPR measurements, analysis and peak broadness. (A) Schematic of the transmission measurements – the NP-rich droplet is first sandwiched between two coverslips, then spread to reduce the height (i), followed by compression (ii) towards the centre of the droplet. Once the droplet is sufficiently thin that a red coloration is seen, transmission measurements are then performed (iii). (B) The obtained absorbance spectra (black) are fitted

to a 6th order polynomial (red) and then normalized. The maximum of the polynomial is taken to be the LSPR maximum and the wavelength shift between the maximum and the red-shifted half maximum is defined as the half-width at half maximum. (C) and (D) The resultant full spectra and close up of the peaks, respectively, show a clear red shift as the NaCl concentration is increased, indicating control over the separation of the NPs. (E) The HWHM remains approximately uniform at these ionic strengths, suggesting the shift in the LSPR maximum is not due to aggregation.

Electromagnetic calculations for the nanoparticle plasmonic resonance

Finite-integration techniques[1] were used to solve Maxwell's equations in the frequency domain and calculate the optical spectra of gold NPs in a water solution arranged in an hcp lattice. Palik's experimental data[2] was used to model the permittivity of gold at optical frequencies. The normalized absorbance calculated is plotted in figure S4a for 11-layers of gold nanoparticles with various surface-to-surface separations. We observe that the resonance red-shifts as the separation between the nanoparticles is reduced (Figure 3B). The spectra calculations show remarkable agreement with the experimentally obtained data plotted in figure S3 (C) and (D).

We also calculate the electric field distribution at the plasmonic resonance, shown in figure S4(B) for various nanoparticle separations. As expected, there is stronger coupling between neighbouring nanoparticles for the more dense nanoparticle solutions.

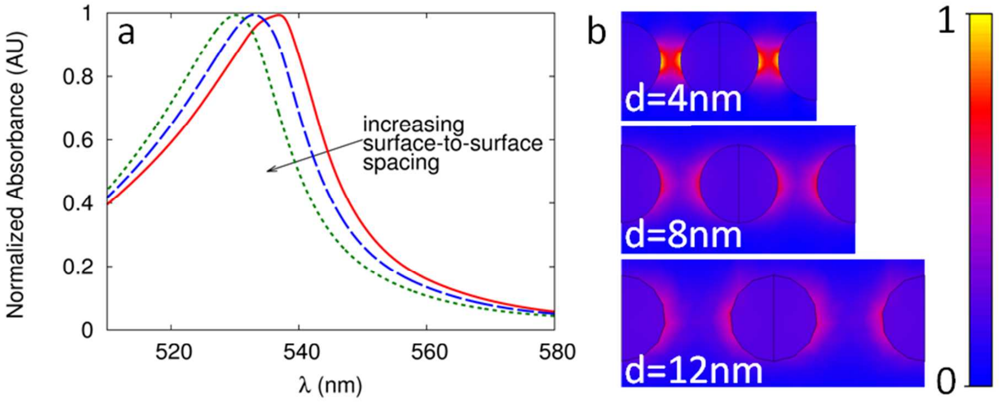

Figure S4. FIT Computer Simulations. (A) Normalized absorbance for gold nanoparticles with various surface-to-surface separations. (B) The electric fields at the wavelength of the plasmonic resonance for various nanoparticle separations.

References

1 CST GmbH, Darmstadt, Germany

2 Palik, E. D.; Handbook of Optical Constants of Solids, Academic Press, Boston, 1985

nature materials

ARTICLES

| DOI: 10.1038/NMAT3488

Self-assembled nanoparticle arrays for multiphase trace analyte detection

Michael P. Cecchini†, Vladimir A. Turek†, Jack Paget, Alexei A. Kornyshev* and Joshua B. Edel*

Nanoplasmonic structures designed for trace analyte detection using surface-enhanced Raman spectroscopy typically require sophisticated nanofabrication techniques. An alternative to fabricating such substrates is to rely on self-assembly of nanoparticles into close-packed arrays at liquid/liquid or liquid/air interfaces. The density of the arrays can be controlled by modifying the nanoparticle functionality, pH of the solution and salt concentration. Importantly, these arrays are robust, self-healing, reproducible and extremely easy to handle. Here, we report on the use of such platforms formed by Au nanoparticles for the detection of multi-analytes from the aqueous, organic or air phases. The interfacial area of the Au array in our system is ≈25 mm^2 and can be made smaller, making this platform ideal for small-volume samples, low concentrations and trace analytes. Importantly, the ease of assembly and rapid detection make this platform ideal for in-the-field sample testing of toxins, explosives, narcotics or other hazardous chemicals.

Various analytical techniques exist that can be used for molecular detection of pollutants[1,2], explosives[3–5], narcotics[6,7] and pesticides[8]. Often, real samples contain a complex mixture of compounds that need to be quantified. Furthermore, they frequently also contain analytes dispersed in various phases (for example, air, organic and aqueous), thus making identification of chemical species a real challenge. This problem is amplified when trace analyte detection is required, as signals from background molecules can swamp the signal of the analyte.

One technique that holds great promise in this regard is surface-enhance Raman spectroscopy (SERS). It is an extremely sensitive technique that can be tailored to provide the detection of specific analytes through their unique vibrational fingerprints. The narrow linewidth of SERS spectra allows for multiple-analyte detection within complex mixtures, including detection down to the single-molecule level[9–11]. It is already an established technique to detect explosives[4,12,13], narcotics[14,15] and pesticides[16].

The enhancement of the Raman signal comes as a result of exciting localized surface plasmons within metallic nanostructures[17]. Increasing the signal strength further can be achieved by tailoring the metallic substrate, thereby lowering the limits of detection (LOD). Of particular note are two-dimensional arrays of closely packed metallic nanoparticles on a substrate[18] or metallic nanocavities[19–21]. These benefit from multiple hotspots being generated in a uniform fashion over a larger substrate area, generating high signal enhancement[22] across the substrate. Various methods exist to fabricate such structures including lithographic[18,23,24] and chemical approaches[19]. Metallic structures can also be fabricated from self-assembled non-metallic scaffolds[25]. However, minimizing the gap between particles or cavities and the complexity of substrate preparation, while maximizing uniformity, is crucial to optimizing the electromagnetic field enhancement[26,27]. Precise nanofabrication techniques capable of achieving these goals can be costly, time-consuming and non-scalable. Furthermore, most SERS substrates are difficult to clean after use, which is impractical for in-the-field applications. In this context, a disposable, self-assembled platform is highly advantageous for practical applications.

Among the self-assembly techniques that are available, templated assembly is one of the most convenient methods to generate a two-dimensional nanoparticle array[28]. To avoid assembly at the solid interface, which generally requires chemical treatment before assembly[29], nanoparticle films formed at the interface between two immiscible phases, such as a liquid/liquid interface (LLI) or liquid/air interface (LAI), can be used[30,31]. The interfacial tension between phases is reduced by the adsorption of nanoparticles[32] that stabilizes the assembly[33,34].

Herein, we show a SERS sensor assembled at the LLI capable of trace dual-phase–dual-analyte detection. We demonstrate the benefits of liquid/liquid systems to allow for either hydrophilic, hydrophobic and/or amphiphilic molecules to be captured and detected individually or simultaneously. The LLI self-assembles the nanoparticles into an array of closely packed spheres creating a multitude of hotspots uniformly distributed within the detection volume and ensuring all captured analyte molecules are at the point of detection[35]. Finally, a method for the detection of airborne analytes is also presented, which is based on the conversion of a LLI to a LAI.

Self-assembly of the nanoparticles at the LLI

The method used throughout this work is aimed towards a practical and in-the-field device. With this in mind, the SERS sensor was made using cost-effective and simple methods that require no specialized equipment or qualified personnel. Self-assembly of a thin film of nanoparticles at the LLI was achieved by vigorously shaking a 2 ml polypropylene tube containing 0.5 ml of 1,2-dichloroethane (DCE) and a 0.5 ml aqueous solution for approximately 10 s. The aqueous solution consisted of 20 mM NaCl and Au nanoparticles with a diameter of 43 ± 4 nm. The aspect ratio of the nanoparticles was 1.35 ± 0.22 at a concentration of $4.35 \pm 0.02 \times 10^{10}$ particles per millilitre . Initially, 16 nm particles were used; however the larger particles provided greater SERS intensities for the same number of analytes dissolved in either the aqueous or organic phase (Supplementary Fig. S3). The physical steps towards generating a nanoparticle film at the LLI are shown

---

Department of Chemistry, Imperial College London, South Kensington Campus, London SW7 2AZ, UK. †These authors contributed equally to this work. *e-mail: a.kornyshev@imperial.ac.uk; joshua.edel@imperial.ac.uk.

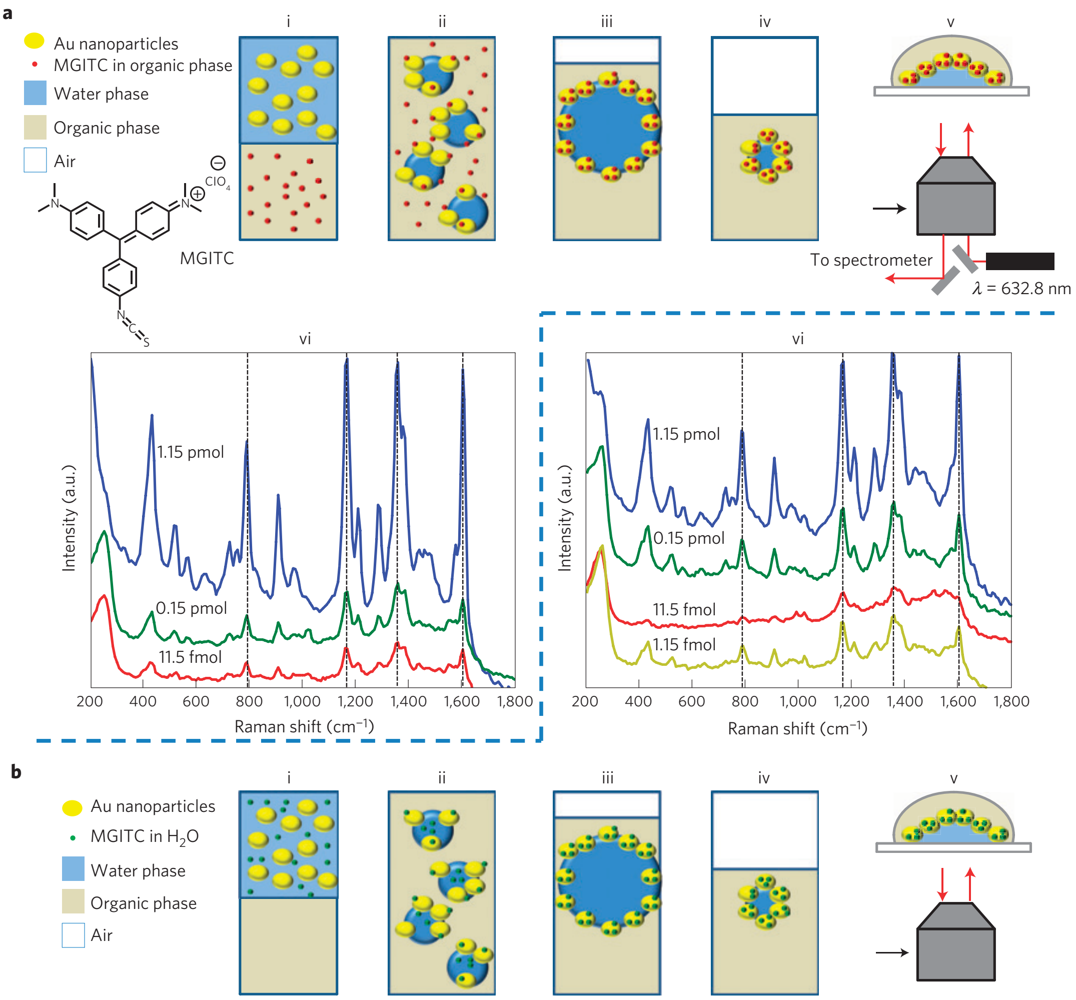

Figure 1 | Schematic of nanoparticle assembly at the LLI and MGITC detection. a, (i–v) Schematic of LLI formation incorporating nanoparticles and MGITC. (i) The analyte is loaded into the organic phase and nanoparticles in the aqueous phase. (ii) Gentle agitation causes the formation of an emulsion. (iii) The small emulsion droplets rearrange to form a LLI consisting of nanoparticles and MGITC. (iv) Water is removed from the droplet bringing the nanoparticles close together. (v) The droplet is transferred onto a coverslip. (vi) Surface enhanced Raman spectra showing a dilution series of MGITC adsorbed to the nanoparticles at the LLI. **b**, (i–vi) The same as in **a**, with the exception of MGITC initially being dissolved in the aqueous phase.

in Figs 1a(i–v) and 1b(i–v). After shaking, the resulting emulsion quickly separated into two distinct phases with the formation of a thin layer of self-assembled nanoparticles between them. A golden reflection was observed at the DCE/water interface, suggesting nanoparticle localization. Although there are a number of alternative methods for nanoparticle assembly at the LLI, such as (m)ethanol addition[36,37] and electrochemistry[38,39], emulsification was used throughout this work owing to its simplicity and cost effectiveness. Assembly of the nanoparticles relies on the spontaneous diffusion-limited nanoparticle localization to the LLI as well as an increased efficiency of assembly with increasing ionic strength of the aqueous phase. The emulsification process played two key roles, the first being a reduction in the average distance between the nanoparticles and the LLI, thereby speeding up the diffusion-limited localization to the interface; and the second was a reduction of the average analyte distance to the LLI and hence the nanoparticles, allowing efficient analyte capture.

The exact structure of the layers of nanoparticles at the LLI is extremely difficult to assess; however, the two-dimensional nature of the dried assembly is evident from scanning electron micrographs (Supplementary Fig. S1). After thin-film formation, all but 50 μl of the aqueous phase was removed (Fig. 1a(iv)). This step increases the particle density at the LLI, resulting in an aqueous droplet being formed that consists of nanoparticles at the interface. The total number of nanoparticles in the sample was determined to be $1.74\pm0.05\times10^{10}$. The actual number of nanoparticles assembled at the LLI was confirmed to be in the range of 1.39×10^{10} to 1.71×10^{10}, calculated by ultraviolet–visible spectroscopy using the Beer–Lambert law. To perform SERS measurements, the sample was transferred onto a 130–160-μm-thick coverslip (Fig. 1a(v)), which resulted in the nanoparticles forming a thin film (in this case, the aqueous phase was below the nanoparticles and the organic phase above). The diameter of the LLI interface once placed on the coverslip was approximately 5 mm. Importantly, all measurements were recorded as full spectra with an acquisition time of 100 ms per spectrum.

Analyte loading on the nanoparticles

As a feasibility study, the reporter fluorophore malachite green isothiocyanate (MGITC) was used as the target analyte. This dye was initially chosen because of the resonance enhancement that can be achieved. Indeed, MGITC absorbs light near the 632.8 nm wavelength of the excitation source used in the experiments that increases the intensity of the Raman signal. Furthermore, at low concentrations, MGITC is soluble in both the aqueous and organic phases and was used to test the performance and assess whether the platform was capable of detecting analytes in either phase. The method of LLI formation in this case is identical to what is described above, with the exception of analyte incorporation. This was simply performed by initially dissolving MGITC in the organic phase (before shaking) at varying initial concentrations ranging from 115 ± 14 pmol to 1.15 ± 0.37 fmol in tenfold increments (Fig. 1a(i–v)). At the highest MGITC concentration, there were approximately $4.03 \pm 0.48 \times 10^3$ dye molecules bound to one nanoparticle, assuming that all MGITC dissolved in solution was homogeneously distributed across all nanoparticles in solution. At the lowest concentration, there were on average 25 ± 12 nanoparticles containing one MGITC molecule.

Examples of the SERS spectra for these samples at the LLI are shown in Fig. 1a(vi). As expected, a decrease in analyte concentration resulted in a decrease in the total count intensity rate. For example, comparing the intensities of the 1,170 cm^{-1} vibrational band for the 1.15±0.23 pmol and 11.5±3.2 fmol samples, the peak intensity decreased by 99%. Although even lower LODs were achieved, the spectra there were not reproducible, the variance in the detected signals affected, presumably, by random fluctuations in the morphology of the nanoparticle arrays and/or by defects in the nanoparticle–analyte conjugation. For practical purposes, a ≈10 fmol LOD was reached for reproducible SERS signals of MGITC dissolved in DCE. Similarly, a further experiment was performed with MGITC dissolved in the aqueous phase (Fig. 1b(i–vi)). This showed a tenfold improvement, with a LOD of 1.15±0.30 fmol, when compared with the previous case. This is probably due to MGITC in the aqueous phase having a direct route for binding to the nanoparticles.

To test the versatility and the sensitivity of the system, non-resonant analytes were also used. The first example was a water-soluble analyte, mercapto-5-nitrobenzimidazole (MNBI; Fig. 2a). Concentrations down to 8.20±1.81 pmol could be detected, which equates to approximately 347 ± 63 MNBI molecules bound per nanoparticle. Compared with MGITC, the LOD using MNBI was higher as a result of the non-resonant nature of the enhancement. We expect the binding efficiency to be similar between MGITC and MNBI, as both form strong bonds with the gold nanoparticles. Finally, a DCE-soluble analyte, 4-methoxy-α-toluenethiol (MATT), was used to quantify the detection limits of a non-resonant analyte dissolved in the organic phase (Fig. 2b). The LOD for this analyte was 323±91 pmol, which is much higher than for analytes dissolved in the aqueous phase. This is probably due to the different binding chemistry taking place across the phase boundary. For example, MNBI is able to bind to the nanoparticle's surface before the nanoparticle adsorbs to the LLI, whereas most of the MATT will bind only once the nanoparticles are assembled at the LLI, because MATT does not like to cross the interface into the water. Interestingly, as seen in Fig. 2b, the SERS intensity remains similar for the dilutions shown. This is due to complete MATT monolayer surface coverage of the nanoparticle even at the lowest dilution. Below 323±91 pmol, a submonolayer coverage was obtained and resulted in the SERS signal being irreproducible (see Supplementary Fig. S4).

In addition to MATT and MNBI, other analytes that did not contain either a thiol group or a phenyl group were detected, as shown in Fig. 3 for 2,4-dinitrotoluene (DNT) and aniline dissolved in the organic phase, as well as cysteine and adenosine-5′-triphosphate (ATP) dissolved in the aqueous phase. The presence of an amine, phosphate, nitro or thiol moiety on the analyte leads to an affinity with the gold's surface. Furthermore, the high Raman cross-section of phenyl groups gives a more resolvable signal. For example, despite the very high gold affinity of the thiol on cysteine, the absence of a phenyl results in lower signal-to-noise when compared with the unthiolated ATP, DNT and aniline. This clearly demonstrates the versatility of the sensor with respect to detecting either weaker binding or analytes with lower Raman cross-sections. Furthermore, these spectra show that the LLI does not adversely affect the sensor[40–43]. For all of these analytes, the signal-to-noise ratio and sensitivity are as good (if not better) at the LLI. A multitude of other analytes with differing functionalities were also detected, further highlighting the versatility of the sensor; the SERS spectra of these are shown in the Supplementary Information and Fig. S5.

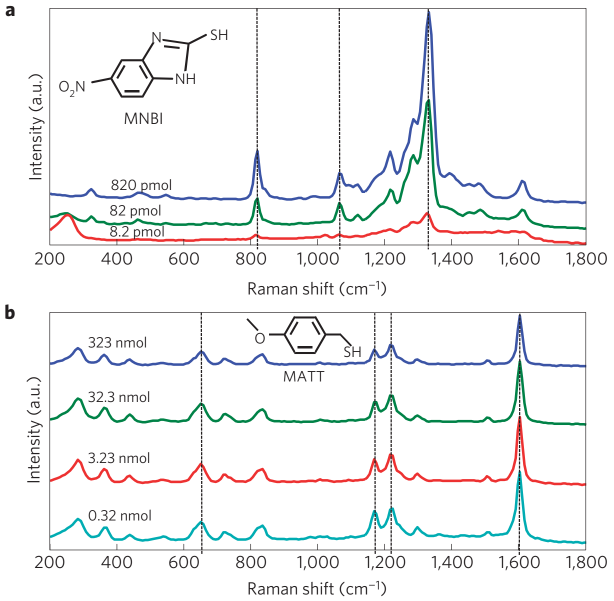

Figure 2 | Detection of analytes dissolved in the aqueous and organic interface. a, Surface enhanced Raman spectra showing a dilution series of MNBI adsorbed to the nanoparticles at the LLI. Initially MNBI was dissolved in the aqueous phase. **b**, Surface enhanced Raman spectra showing a dilution series of MATT adsorbed to the nanoparticles at the LLI. MATT was initially dissolved in the organic phase.

Simultaneous multiphase analyte detection at the LLI

Successful detection of individual analytes dissolved in either the aqueous or organic phase using the same sensor design opened the door for simultaneous dual-phase-dual-analyte detection. From a sensor perspective, the unique ability to simultaneously dress the nanoparticles with analytes with different solubilities across multiple phases is a step towards building a universal sensor. Furthermore, from more of a chemical perspective, this multiphase system can also be used to decorate a nanoparticle surface with both aqueous- and organic-phase-soluble analytes simultaneously. This allows for direct control of not only the analyte type but the relative concentrations of different analytes on the nanoparticle surface. This is a significant advantage when compared with a solid-state substrate. Although solid-state substrates can potentially conjugate analytes from either phase, to detect both analytes, the conjugation processes would have to be separated. As such, there is little control over the relative analyte concentration on the nanoparticles. Furthermore, the nanoparticles on a solid-state surface are irreversibly bound, unlike in a solution-based system.

To characterize the LOD of simultaneous binding of analytes from both the organic and aqueous phases, the mole ratio of MNBI and MATT dissolved in each phase was precisely defined. MATT/MNBI was varied between 8.20 nmol:82 pmol (100:1) to

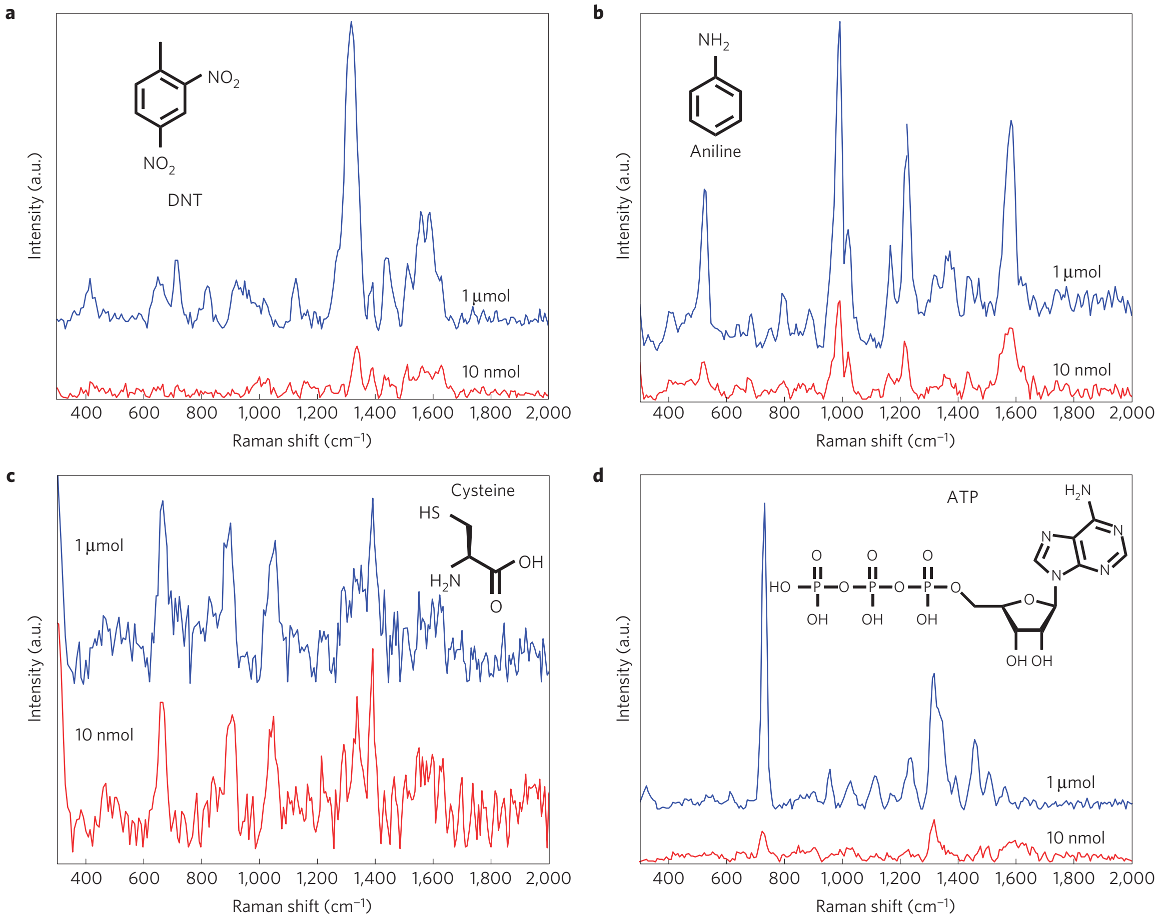

Figure 3 | Detection of analytes with either a weaker binding affinity to Au or a lower Raman cross-section. Thiolated analytes with a phenyl ring have a high affinity and Raman cross-section and are therefore ideal test analytes. **a**–**d**, To demonstrate the versatility of the sensor, analytes containing amine, nitro and phosphate groups can also be used to promote adsorption to Au. This is demonstrated for aniline (**b**), DNT (**a**) and ATP (**d**) for a total of 1 µmol (blue) and 10 nmol (red) analyte molecules. Furthermore, cysteine—a non-phenylated analyte—which has a low Raman cross-section, is also shown (**c**). Further examples are shown in the Supplementary Information and Fig. S5.

82.0 pmol:410 pmol (1:5). As an example, the effect of the mole ratio on the SERS intensity of the two analytes can be seen in Fig. 4a–c, for mole ratios of 20:1, 2:1 and 1:5. In all spectra, it is clear that the vibrational bands of both analytes could be seen and detected. For example, the 651, 1,169, 1,224 and 1,604 cm^{-1} bands of MATT could easily be distinguished from the 1,064, 1,285 and 1,333 cm^{-1} bands of MNBI. Furthermore, the relative intensities correlated well with the analyte concentration. Although fluctuations in intensity did occur during the acquisition, the vibrational bands from both analytes resulted in equal enhancement, which suggests their equal distribution across all nanoparticles. The intensities of the MATT and MNBI vibrational bands were proportional to the concentration of each analyte dissolved in each phase. This was verified by comparing the average intensity ratio between the 1,604 cm^{-1} vibrational band of MATT and the 1,333 cm^{-1} vibrational band of MNBI (Fig. 4d). Notably, the mole ratio has been varied by over three orders of magnitude. Tri-analyte detection was also achieved as described in the Supplementary Information and Fig. S6.

Analyte detection at the LAI

A significant advantage of the system described here relates to the possibility of converting the nanoparticles embedded at a LLI to a LAI. This exciting prospect opens the door to using such a platform to detect volatile or gaseous compounds. The LAI is simply produced by allowing the DCE phase at the LLI to evaporate. This process effectively removes the organic phase from the system while keeping the nanoparticles at the aqueous/air interface. To test the capabilities of this platform, and a 5 µl drop of pure aniline were placed inside an enclosed container together with the self-assembled nanoparticle film at the LAI. The separation between the LAI and analyte was 15 mm. A continuous, single-spot acquisition was performed on the interface, while adjusting the focal point to account for evaporation of the aqueous phase, using a 100 ms exposure time. The spectra of both analytes at 10, 25, 35, 83 and 180 s are shown in Fig. 5. It is clear from the spectra that analyte capture can be achieved even for unthiolated analytes at the LAI. A time trace monitoring the intensity of the 1,175 cm^{-1} peak for MATT is shown in the Supplementary Information and Fig. S7. The intensity shows a sharp increase within the first 60 s, followed by a plateau indicating saturation of the analyte on the nanoparticle.

Towards a universal sensor

We have shown an alternative, highly sensitive analytical system based on a thin-film nanoparticle array self-assembled at the LLI and LAI for trace analyte detection in various phases. There are numerous advantages of the sensor. An efficient capture mechanism is established by conjugating the nanoparticles while they are still

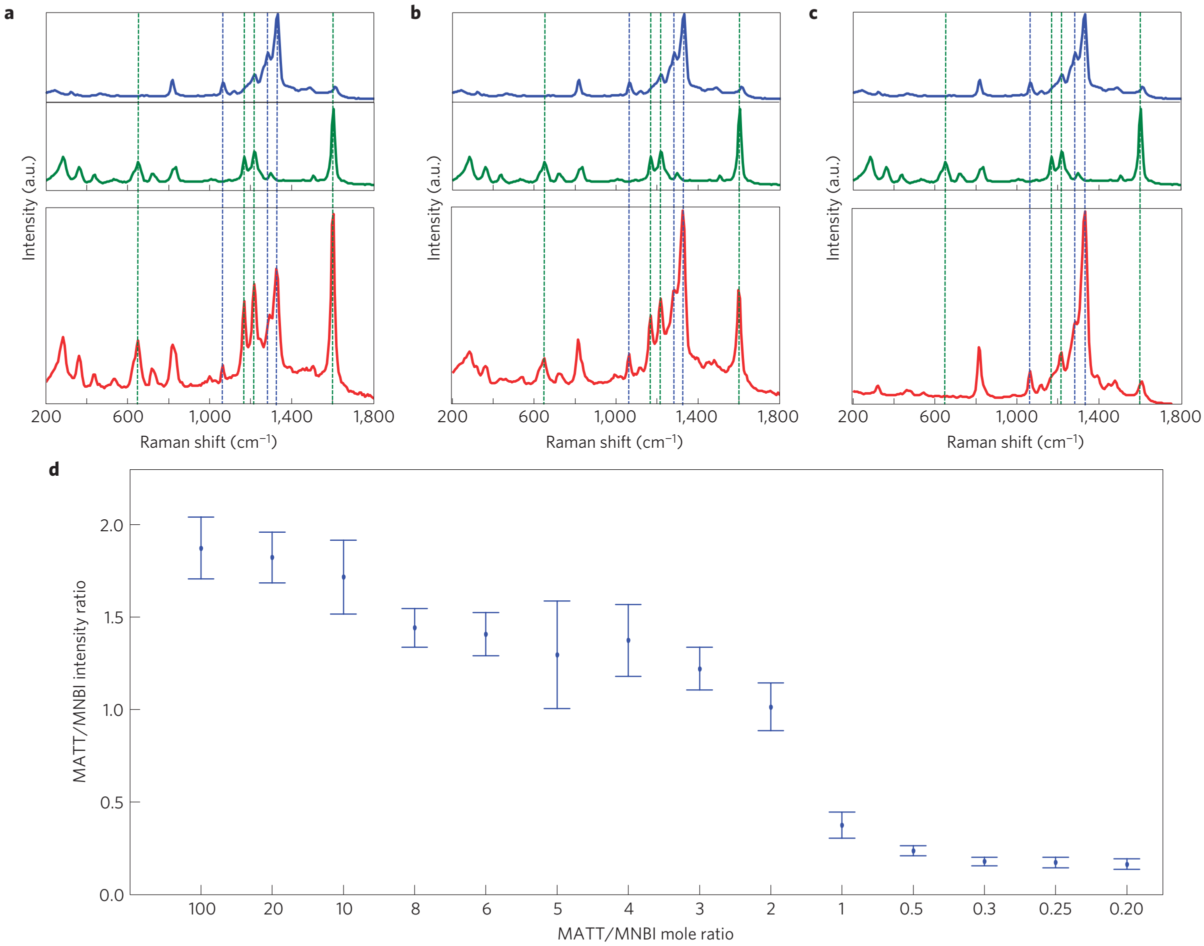

Figure 4 | Dual-analyte detection. a–c, SERS spectra showing dual-analyte detection (bottom) at the LLI for a mole ratio (MNBI/MATT) of 20:1 (**a**), 2:1 (**b**) and 1:5 (**c**). As a reference, SERS spectra of pure MNBI (top) and MATT (middle) are also shown. **d**, The ratio of the MATT 1,604 cm^{-1} vibrational band versus the MNBI 1,333 cm^{-1} vibrational band is compared for mole ratios spanning between 100:1 to 1:5, showing the dependence of mole ratio on the SERS intensity. All error bars denote 1 standard deviation.

in the bulk. The conjugated nanoparticles are quickly and easily brought to the point of detection where they form into a thin film of closely packed nanospheres. Such a film is ideal for SERS-based detection because the space between closely packed spheres is where the electromagnetic field is markedly enhanced, which increases the SERS intensity and lowers the LOD.

A remarkable feature of this liquid sensor is the ability to detect multiple analytes dissolved in dual phases, which we have successfully demonstrated by detecting water-soluble and organic-phase-soluble molecules. Other thiolated and unthiolated molecules dissolved in either the water or organic phase were also detected with similar success. This versatility in analyte detection eliminates the need for multiple devices, reducing analysis time and offering multiplexing capabilities. In addition to single-phase analyte detection, the sensor has also shown the ability to detect analytes that can be dissolved both in the organic and aqueous phase simultaneously. The technique directly compares the SERS intensity of multiple analytes. For dual-analyte detection, we have shown that the mole ratios of both analytes play an important role in the SERS intensity of individual vibrational bands. Such a dependency allows direct comparison of mole ratios, using known and unknown analyte quantities. Another advantage of the sensor is the ability to use it at the LAI to detect both thiolated and unthiolated airborne analytes.

We expect that it will be possible to further reduce the LODs by adjusting the nanoparticle size, nanoparticle shape, tuning the interparticle spacing[44] or changing the organic phase. We believe that this system opens vast possibilities for the in-the-field applications in various environmental, crime-prevention, anti-terror and defence activities.

Methods

Chemicals. All analytes were purchased from Sigma-Aldrich and used without further purification. The chemicals used were: 1,2-DCE (≥99.0%, ACS reagent); MATT (90%, technical grade); MNBI (97.0%); sodium chloride (≥99.5%, puriss. p.a.); $HAuCl_4 \approx 3H_2O$ (f.w. 339.79 (anhydrous), 99.999% trace metal basis); trisodium citrate dihydrate (≥99%); 2,4-DNT (97%); L-cysteine (97%); aniline (≥99.5%*F*, ACS reagent); ATP disodium salt hydrate (≥99%, Grade I). Ultrapure water with a resistivity of 18.2 MΩ cm was used in all cases.

Nanoparticle synthesis. Citrate-stabilized Au nanoparticles were synthesized using the Turkevich–Frens method[45,46]. The particles used in this work had an average hydrodynamic diameter of 64.7 ± 30.5 nm with a polydispersity index of 0.268 measured using dynamic light scattering. An extinction coefficient, $\varepsilon_{\max}$, at 532 nm of 1.31×10^{10} M^{-1} cm^{-1} (ref. 47) was used for 43-nm-diameter nanoparticles (from scanning electron microscopy). This value was used for all nanoparticle concentration evaluations using ultraviolet–visible spectroscopy Supplementary Fig. S2. The concentration of the nanoparticles was adjusted using deionized water for dilutions and centrifugation for concentration to a final working concentration of approximately 31.9 pM or 4.35×10^{10} nanoparticles per millilitre. After the nanoparticles were assembled at the interface, the concentration of

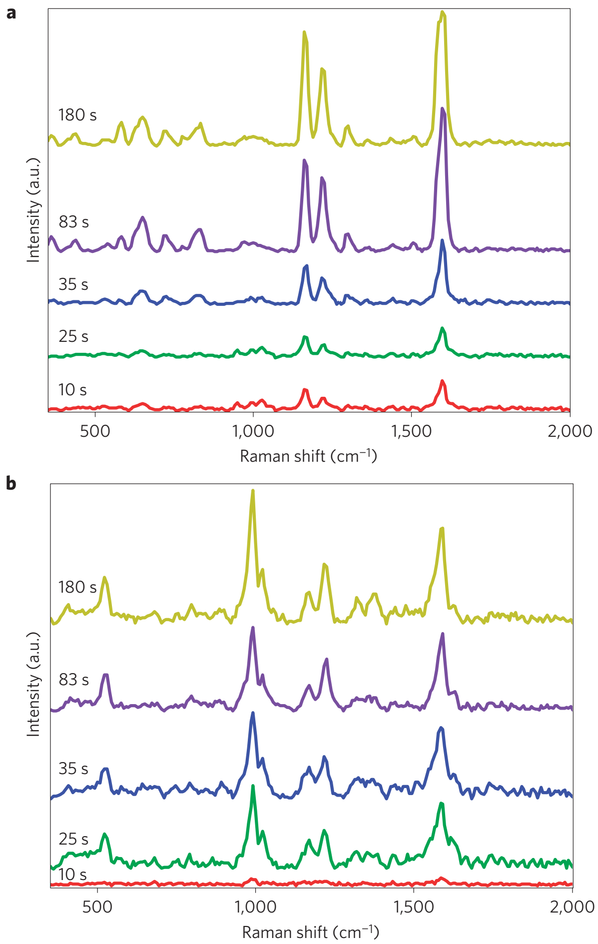

Figure 5 | Airborne detection of MATT and aniline at a LAI. The same sensor capable of detecting analytes dissolved in the aqueous or organic phase can be used for airborne detection. After the sensor is assembled using the same method shown in Fig. 1a(i–v), the DCE evaporates exposing the nanoparticles to the air. **a**,**b**, Thiolated MATT (**a**) and unthiolated aniline (**b**) were placed 15 mm away from the interface. Full spectra snapshots at 10 s (red), 25 s (green), 35 s (blue), 83 s (purple) and 180 s (gold) over a single point on the interface show the increasing SERS intensity over time as a result of loading more analyte onto the nanoparticles.

the aqueous bulk was measured. The difference between the initial nanoparticle concentration and the aqueous bulk was used to determine the number of particles located at the interface. Further details are included in the Supplementary Information and Fig. S2.

Optical configuration. SERS measurements were performed on a home-built Raman microscope[48,49]. Briefly, a 632.8 nm HeNe laser (HRP170, Thorlabs, 17 mW) excitation source was guided through two clean-up filters (LL01-633-12.5, Semrock) into an optical inverted microscope (IX71, Olympus). A linear polarizer (PRM1/M, Thorlabs) controlled the light polarization direction on the sample. The laser light was reflected into a ×40 air objective (LUCPLANFLN, Olympus, numerical aperture 0.6, 4 mm working distance) using a dichroic mirror (D1, LPD01-633RU-25x36x2.0, Semrock) mounted at a 45° angle of incidence. A long-working-distance objective was required to reach the nanoparticle assembly. The laser intensity at the sample was measured to be 8.5 mW using a digital power meter (PM100, Thorlabs). Backscattered light was collected through the same objective and transmitted through the same dichroic mirror. A long-pass filter (LP1, LP02-633RU-25, Semrock) was used to reject the anti-Stokes scattered light and Rayleigh laser line. A Ø1’ lens (LA1805-B, $f = 30$ mm, Thorlabs) focused the transmitted light onto the 50 µm entrance slit of the spectrograph (303 mm focal length, Shamrock SR-303i, Andor). The polychromatic light was then dispersed by a 600 l mm^{-1} grating (SR3-GRT-0600-0500, Andor), where it was imaged using an electron-multiplying CCD (charge-coupled device; Newton DU970BV, Andor). All spectra were acquired using a 100 ms exposure time. The measurement was performed on the droplet and evaporation altered the optical path length; over the course of the acquisition, the stage position and focus were manually adjusted to probe different areas of the substrate. At higher concentrations, signal was emitted from all areas within the substrate. At lower dilutions, the uniformity in the signal intensity diminished as the coverage of analyte within the probe volume was not uniform.

Analyte preparation For MGITC, 3 µl of 0.388 mM MGITC was dissolved in 1,000 µl of either fresh DCE or water. Then, 100 µl of this solution was added to 400 µl of the solvent (either water of DCE), providing 0.116 (±11.1–11.6%) nmol for detection (at the highest concentration). This was followed by tenfold serial dilutions using 100 µl of the previous solution and diluting with 900 µl of the solvent. Again 100 µl was added to 400 µl of either the organic or aqueous phase for the subsequent sample. This dilution methodology was performed for all samples.

For MATT, 5 µl of MATT was initially diluted with 995 µl of DCE. Then, 100 µl of this solution was added to 400 µl of fresh DCE providing 3.23 µmol for detection. Tenfold serial dilutions followed using 100 µl of the previous dilutions sample and diluting with 900 µl of fresh DCE. The solubility of MATT in water is calculated to be 0.74 g l^{-1}. The solubility of MATT in DCE or log $P_{\mathrm{DCE/wat}}$ is not available; however, the log $P_{\mathrm{oct/wat}}$ is calculated to be 2.474 ± 0.238 (at 25 °C) and the polar surface area is 48.0 Å. This means that most of the MATT will be dissolved in the organic (DCE) phase (see the note below).

For MNBI, 0.16 mg 2-MNBI was initially diluted with 10 ml of water. Subsequently, 100 µl of this was mixed with 400 µl of nanoparticles. Tenfold serial dilutions followed using 100 µl of the previous sample and diluting with 900 µl of water. Then, 100 µl of that was added to 400 µl of nanoparticles. The solubility of MNBI in water is calculated to be 0.43 g l^{-1}. The solubility of MNBI in DCE or log $P_{\mathrm{DCE/wat}}$ is not available; however, the log $P_{\mathrm{oct/wat}}$ is calculated to be 1.404 ± 0.738 (at 25 °C) and the polar surface area is 102 Å^2. This means that MNBI is likely to have a greater mole fraction in water than MATT (see the note below).

Note, solubility, log P and polar surface area values for MATT and MNBI were obtained through SciFinder—calculated by Advanced Chemical Development (ACD/Labs) Software V11.02 (© 1994–2012 ACD/Labs)).

Received 11 June 2012; accepted 9 October 2012; published online 18 November 2012; corrected online 27 November 2012 and 19 December 2012

References

1. Lefevre, F. *et al.* Algal fluorescence sensor integrated into a microfluidic chip for water pollutant detection. *Lab Chip* **12,** 787–793 (2012).
2. Byer, R. L. & Garbuny, M. Pollutant detection by absorption using mie scattering and topographic targets as retroreflectors. *Appl. Opt.* **12,** 1496–1505 (1973).
3. Pushkarsky, M. B. *et al.* High-sensitivity detection of TNT. *Proc. Natl Acad. Sci. USA* **103,** 19630–19634 (2006).
4. Sylvia, J. M., Janni, J. A., Klein, J. D. & Spencer, K. M. Surface-enhanced Raman detection of 2,4-dinitrotoluene impurity vapor as a marker to locate landmines. *Anal. Chem.* **72,** 5834–5840 (2000).
5. Anderson, G. P. *et al.* TNT detection using multiplexed liquid array displacement immunoassays. *Anal. Chem.* **78,** 2279–2285 (2006).
6. Kawano, R. *et al.* Rapid detection of a cocaine-binding aptamer using biological nanopores on a chip. *J. Am. Chem. Soc.* **133,** 8474–8477 (2011).
7. Zhang, J. *et al.* Visual cocaine detection with gold nanoparticles and rationally engineered aptamer structures. *Small* **4,** 1196–1200 (2008).
8. Liu, C. *et al.* Lateral flow immunochromatographic assay for sensitive pesticide detection by using Fe_3O_4 nanoparticle aggregates as color reagents. *Anal. Chem.* **83,** 6778–6784 (2011).
9. Kneipp, K. *et al.* Single molecule detection using surface-enhanced Raman scattering (SERS). *Phys. Rev. Lett.* **78,** 1667–1670 (1997).
10. Nie, S. & Emory, S. R. Probing single molecules and single nanoparticles by surface-enhanced raman scattering. *Science* **275,** 1102–1106 (1997).
11. Liu, H. *et al.* Single molecule detection from a large-scale SERS-active $\text{Au}_{79}\text{Ag}_{21}$ substrate. *Sci. Rep.* **1,** 112 (2011).
12. Xu, J. Y. *et al.* SERS detection of explosive agent by macrocyclic compound functionalized triangular gold nanoprisms. *J. Raman Spectrosc.* **42,** 1728–1735 (2011).
13. Yang, L., Ma, L., Chen, G., Liu, J. & Tian, Z-Q. Ultrasensitive SERS detection of TNT by imprinting molecular recognition using a new type of stable substrate. *Chemistry* **16,** 12683–12693 (2010).
14. Carter, J. C., Brewer, W. E. & Angel, S. M. Raman spectroscopy for the *in situ* identification of cocaine and selected adulterants. *Appl. Spectrosc.* **54,** 1876–1881 (2000).
15. Bell, S. E. & Sirimuthu, N. M. Rapid, quantitative analysis of ppm/ppb nicotine using surface-enhanced Raman scattering from polymer-encapsulated Ag nanoparticles (gel-colls). *Analyst* **129,** 1032–1036 (2004).

16. Shende, C., Gift, A., Inscore, F., Maksymiuk, P., Farquharson, S., 1st edn, (eds Bennedsen, B. S. *et al.*) *SPIE* Vol. 5271, 28–34 (2004).
17. Kelly, K. L., Coronado, E., Zhao, L. L. & Schatz, G. C. The optical properties of metal nanoparticles: The influence of size, shape, and dielectric environment. *J. Phys. Chem. B* **107,** 668–677 (2002).
18. Yan, B. *et al.* Engineered SERS substrates with multiscale signal enhancement: Nanoparticle cluster arrays. *ACS Nano* **3,** 1190–1202 (2009).
19. Chen, A. *et al.* Self-assembled large Au nanoparticle arrays with regular hot spots for SERS. *Small* **7,** 2365–2371 (2011).
20. Cintra, S. *et al.* Sculpted substrates for SERS. *Faraday Discuss.* **132,** 191–199 (2006).
21. Mahajan, S., Baumberg, J. J., Russell, A. E. & Bartlett, P. N. Reproducible SERRS from structured gold surfaces. *Phys. Chem. Chem. Phys.* **9,** 6016–6020 (2007).
22. Dadosh, T. *et al.* Plasmonic control of the shape of the Raman spectrum of a single molecule in a silver nanoparticle dimer. *ACS Nano* **3,** 1988–1994 (2009).
23. Kahl, M., Voges, E., Kostrewa, S., Viets, C. & Hill, W. Periodically structured metallic substrates for SERS. *Sens. Actuat. B* **51,** 285–291 (1998).
24. Das, G. *et al.* Nano-patterned SERS substrate: Application for protein analysis versus temperature. *Biosens. Bioelectron.* **24,** 1693–1699 (2009).
25. Vignolini, S. *et al.* A 3D optical metamaterial made by self-assembly. *Adv. Mater.* **24,** OP23–OP27 (2012).
26. Hao, E. & Schatz, G. C. Electromagnetic fields around silver nanoparticles and dimers. *J. Chem. Phys.* **120,** 357–366 (2004).
27. Yang, Z-L., Li, Q-H., Ren, B. & Tian, Z-Q. Tunable SERS from aluminium nanohole arrays in the ultraviolet region. *Chem. Commun.* **47,** 3909–3911 (2011).
28. Grzelczak, M., Vermant, J., Furst, E. M. & Liz-Marza'n, L. M. Directed self-assembly of nanoparticles. *ACS Nano* **4,** 3591–3605 (2010).
29. Liu, S., Zhu, T., Hu, R. & Liu, Z. Evaporation-induced self-assembly of gold nanoparticles into a highly organized two-dimensional array. *Phys. Chem. Chem. Phys.* **4,** 6059–6062 (2002).
30. Boker, A., He, J., Emrick, T. & Russell, T. P. Self-assembly of nanoparticles at interfaces. *Soft Matter* **3,** 1231–1248 (2007).
31. Santos, H. A. *et al.* Electrochemical study of interfacial composite nanostructures: Polyelectrolyte/gold nanoparticle multilayers assembled on phospholipid/dextran sulfate monolayers at a liquid–liquid interface. *J. Phys. Chem. B* **109,** 20105–20114 (2005).
32. Du, K., Glogowski, E., Emrick, T., Russell, T. P. & Dinsmore, A. D. Adsorption energy of nano- and microparticles at liquid–liquid interfaces. *Langmuir* **26,** 12518–12522 (2010).
33. Pickering, S. U. Emulsions. *J. Chem. Soc. D* **91,** 2021 (1907).
34. Gordon, K. C., McGarvey, J. J. & Taylor, K. P. Enhanced Raman scattering from liquid metal films formed from silver sols. *J. Phys. Chem.* **93,** 6814–6817 (1989).
35. Oh, M. K., Yun, S., Kim, S. K. & Park, S. Effect of layer structures of gold nanoparticle films on surface enhanced Raman scattering. *Anal. Chim. Acta* **649,** 111–116 (2009).
36. Li, Y-J., Huang, W-J. & Sun, S-G. A Universal approach for the self-assembly of hydrophilic nanoparticles into ordered monolayer films at a toluene/water interface. *Angew. Chem. Int. Ed.* **45,** 2537–2539 (2006).
37. Luo, M. X., Song, Y. M. & Dai, L. L. Effects of methanol on nanoparticle self-assembly at liquid–liquid interfaces: A molecular dynamics approach. *J. Chem. Phys.* **131,** 194703 (2009).
38. Su, B. *et al.* reversible voltage-induced assembly of Au nanoparticles at liquid–liquid interfaces. *J. Am. Chem. Soc.* **126,** 915–919 (2003).
39. Flatté, M. E., Kornyshev, A. A. & Urbakh, M. Electrovariable nanoplasmonics and self-assembling smart mirrors. *J. Phys. Chem. C* **114,** 1735–1747 (2010).
40. Sauer, G., Brehm, G. & Schneider, S. Preparation of SERS-active gold film electrodes via electrocrystallization: Their characterization and application with NIR excitation. *J. Raman Spectrosc.* **35,** 568–576 (2004).
41. Kumar, G. V. P. *et al.* Hot spots in Ag core-Au shell nanoparticles potent for surface-enhanced raman scattering studies of biomolecules. *J. Phys. Chem. C* **111,** 4388–4392 (2007).
42. Jing, C. & Fang, Y. Experimental (SERS) and theoretical (DFT) studies on the adsorption behaviors of l-cysteine on gold/silver nanoparticles. *Chem. Phys.* **332,** 27–32 (2007).
43. Khaing Oo, M. K., Chang, C-F., Sun, Y. & Fan, X. Rapid, sensitive DNT vapor detection with UV-assisted photo-chemically synthesized gold nanoparticle SERS substrates. *Analyst* **136,** 2811–2817 (2011).
44. Turek, V. A. *et al.* Plasmonic ruler at the liquid–liquid interface. *ACS Nano* **6,** 7789–7799 (2012).
45. Turkevich, J. A study of the nucleation and growth processes in the synthesis of colloidal gold. *Discuss. Faraday Soc.* **11,** 55–75 (1951).
46. Frens, G. Controlled nucleation for the regulation of the particle size in monodisperse gold suspensions. *Nature* **241,** 20–22 (1973).
47. Liu, X., Atwater, M., Wang, J. & Huo, Q. Extinction coefficient of gold nanoparticles with different sizes and different capping ligands. *Colloids Surf. B* **58,** 3–7 (2007).
48. Cecchini, M. P., Stapountzi, M. A., McComb, D. W., Albrecht, T. & Edel, J. B. Flow-based autocorrelation studies for the detection and investigation of single-particle surface-enhanced resonance Raman spectroscopic events. *Anal. Chem.* **83,** 1418–1424 (2011).
49. Cecchini, M. P. *et al.* Ultrafast surface enhanced resonance Raman scattering detection in droplet-based microfluidic system. *Anal. Chem.* **83,** 3076–3081 (2011).

Acknowledgements

We are grateful to A. Kucernak (Imperial College), M. Urbakh (University of Tel Aviv) and S. Goodchild (DSTL) for illuminating discussions and inspiration. A.A.K. and J.B.E. thank the DSTL for financial support of this project. This work was also financially supported in part by an ERC starting investigator grant to J.B.E. and an EU FP7 'Nanodetector' grant (NMP4-SE-2012-280478) to A.A.K.

Author contributions

M.P.C., V.A.T., J.P., A.A.K. and J.B.E. designed the experiments, wrote the paper and analysed the results. M.P.C., V.A.T. and J.B.E. performed the experiments.

Additional information

Supplementary information is available in the online version of the paper. Reprints and permissions information is available online at www.nature.com/reprints. Correspondence and requests for materials should be addressed to A.A.K. or J.B.E.

Competing financial interests

The authors declare no competing financial interests.

ERRATUM

Self-assembled nanoparticle arrays for multiphase trace analyte detection

Michael P. Cecchini, Vladimir A. Turek, Jack Paget, Alexei A. Kornyshev and Joshua B. Edel

Nature Materials http://dx.doi.org/10.1038/nmat3488 (2012); published online 18 November 2012; corrected online 27 November 2012.

In the version of this Article originally published online, in Fig. 1a, the second item in the legend should have read 'MGITC in organic phase'. In Fig. 1b, the fourth item in the legend should have read 'Organic phase'. These errors have been corrected in all versions of the Article.

ERRATUM

Self-assembled nanoparticle arrays for multiphase trace analyte detection

Michael P. Cecchini, Vladimir A. Turek, Jack Paget, Alexei A. Kornyshev and Joshua B. Edel

Nature Materials http://dx.doi.org/10.1038/nmat3488 (2012); published online 18 November 2012; corrected online 27 November 2012 and 19 December 2012.

In the version of this Article originally published online, in Fig. 1b panel vi, the units on the bottom two curves (red and yellow) should have read 'fmol'. These errors have been corrected in all versions of the Article.

nature materials

SUPPLEMENTARY INFORMATION

DOI: 10.1038/NMAT3488

Self-assembled nanoparticle arrays for multiphase trace analyte detection

Michael P. Cecchini, [‡&] Vladimir Turek, [‡&] Jack Paget, [‡] Alexei A. Kornyshev,*[‡] and Joshua B. Edel*[‡]

[‡]Department of Chemistry, Imperial College London, South Kensington Campus, London, SW7 2AZ

[&] These authors contributed equally to this publication

[*] Corresponding author: joshua.edel@imperial.ac.uk ; a.kornyshev@imperial.ac.uk

Figure 1 | SEM image of the 43 ± 4 nm Au NPs used for the experiments.

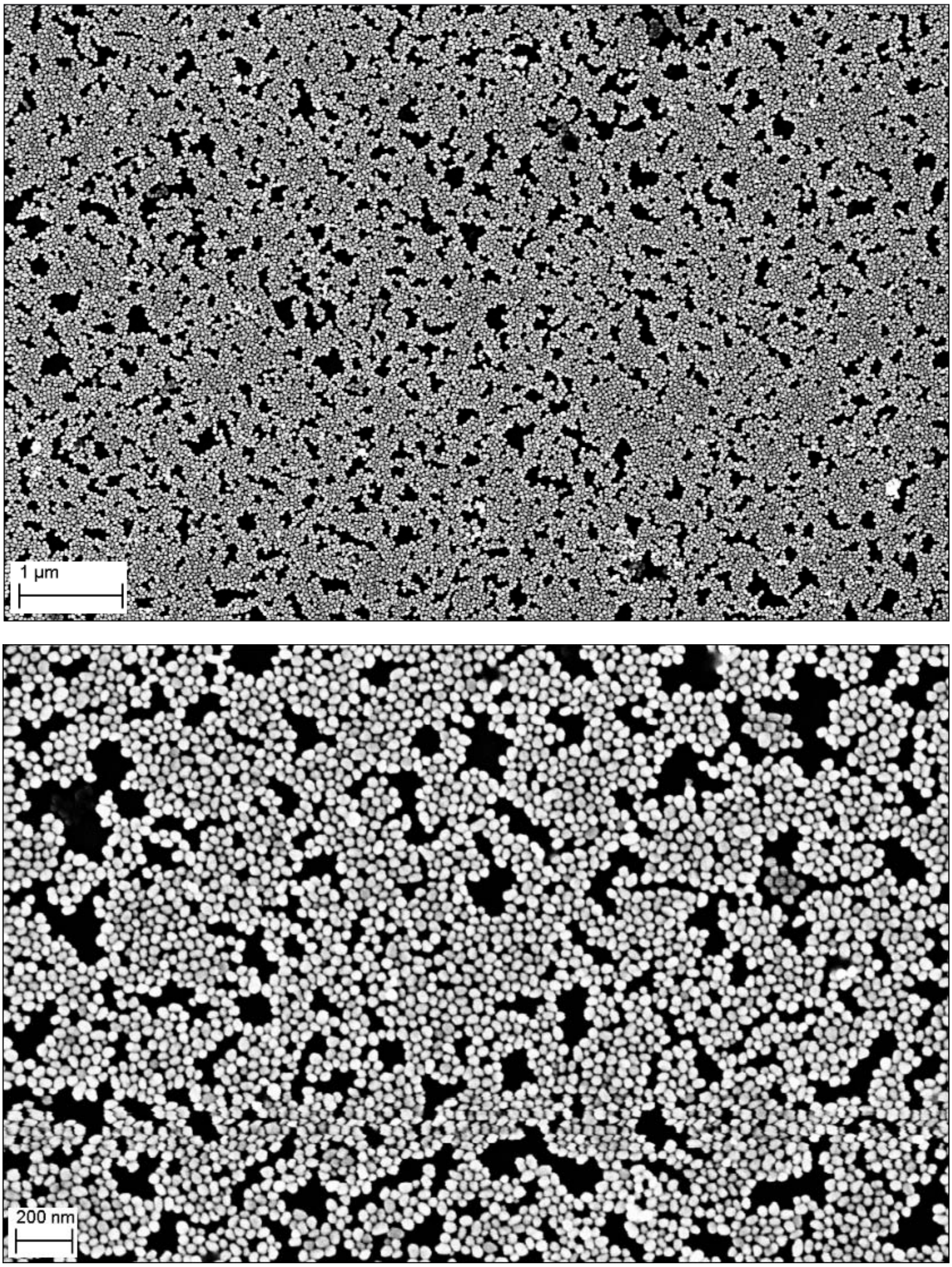

A monolayer was deposited on a glass cover slip by vigorously shaking a 0.51 mL aq. NP solution containing 2.18 × 10^{10} NPs at a NaCl concentration of 20 mM with 0.5 mL DCE, followed by a reduction in the aqueous volume to 50 µL and dilution of the aqueous salt concentration by 2 consecutive 1 mL ultrapure water additions/1 mL aqueous phase extractions (this step prevents the formation of salt crystals during the drying process). The resulting 50 µL droplet was then transferred to a glass coverslip and as much of the water was removed as possible by pipetting (the water's contact area with the glass remained roughly constant during this volume reduction) and finally allowing the water to dry at ambient conditions for about 5 minutes. The glass coverslip was then secured to an SEM stub with carbon tape and silver paint was applied between the edge of the monolayer and the aluminium stub to provide an electrical path of conductivity. No further treatment (such as sputtering a thin layer of conductive metal on the coverslip) was required to obtain the SEM, suggesting that there is a good lateral conductivity throughout the film (although certain regions where an insufficient contact was made between the NPs displayed charging – an example of this is the isolated cluster in the top left hand corner of the 200 nm scale-bar-image). Though the morphology of the NP packing at the liquid/liquid or liquid/air interface will likely be substantially different to that which is observed on the dry monolayer, it is evident that there is a 2 dimensional NP array with a multitude of NPs in close enough proximity to each other to be able to plasmonically couple and provide a roughly uniform distribution of SERS hot-spots.

Gold nanoparticles prepared by the Turkevich-Frens method of this size show some shape polydispersity. In order to calculate the average core diameter, ImageJ was used to calculate the average area per NP. This area was then used to calculate the average diameter of the NPs if they were perfectly spherical. This is the reason for the large discrepancy between the DLS hydrodynamic diameter reading of 64.7 ± 30.5 nm and the 43 ± 4 nm quoted from SEM.

Figure 2 | Calculating the number of nanoparticles assembled at the interface.

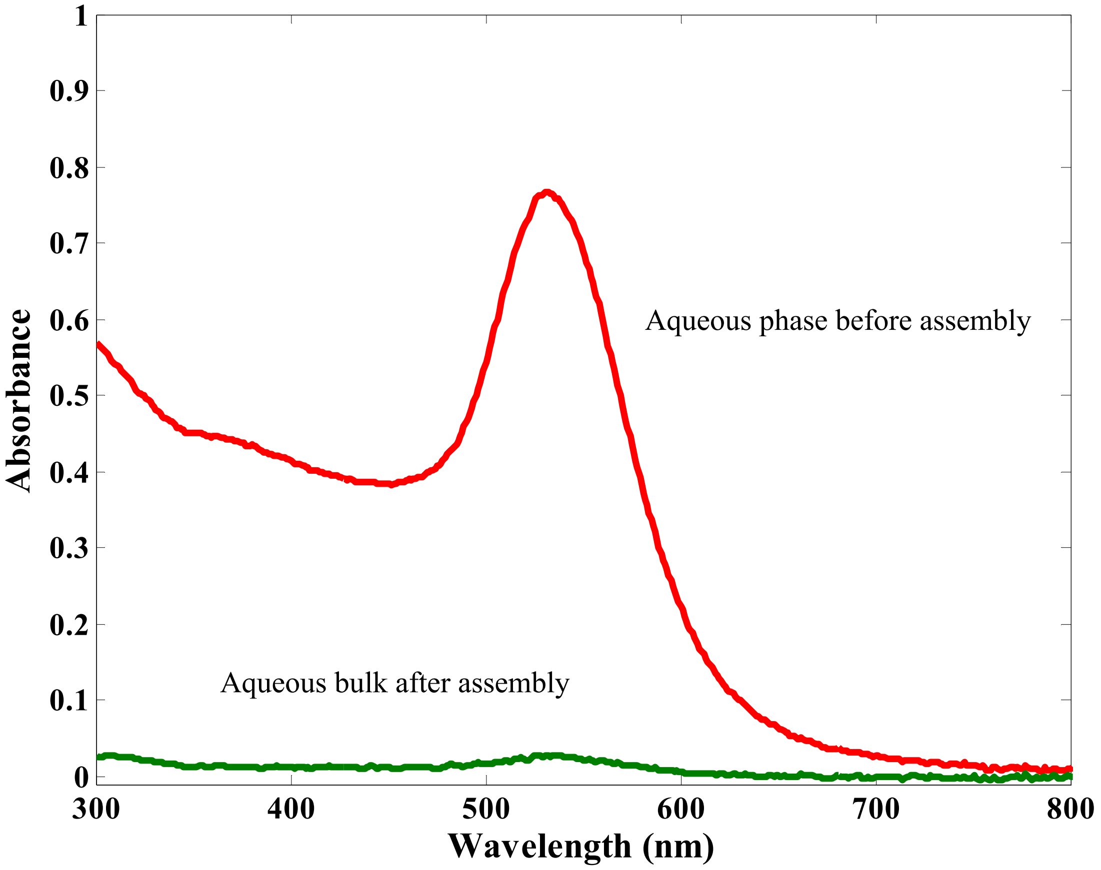

The number of particles attached to the LLI was determined by measuring the concentration of particles within the 510 µL aqueous phase prior to bringing them to the interface. After assembly, the concentration of the aqueous phase was again measured. The difference between the two concentrations allowed us to figure out how many particles were assembled at the interface. These concentration measurements were done using UV-Vis using an extinction coefficient of 1.31×10^{10} $M^{-1}cm^{-1}$ obtained from reference 38 for a 43 nm Au nanoparticle.

Figure 3 | Comparison between the SERS intensity using different particle sizes.

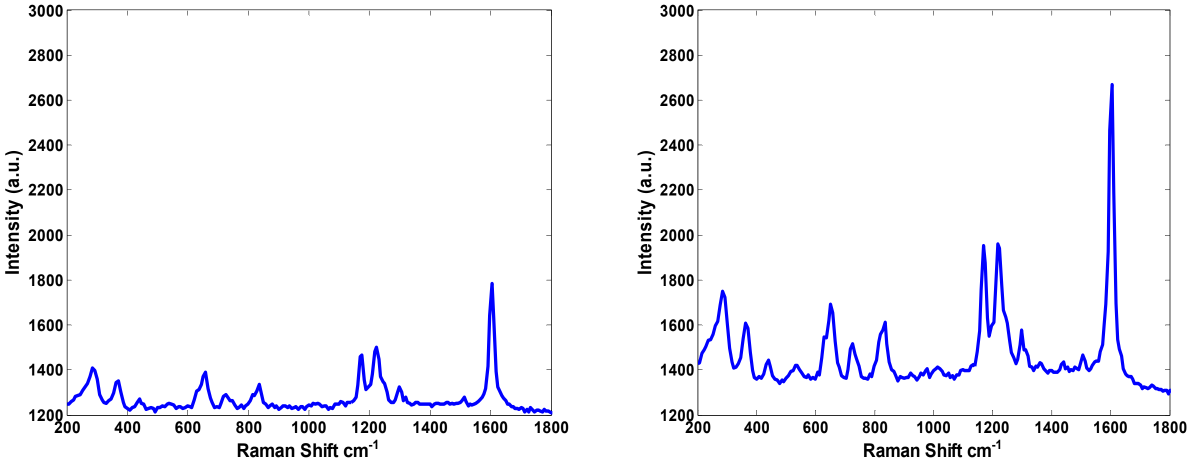

A comparison between using 16 nm Au particles (left) and 43 nm Au particles (right) for 0.32 nmoles MATT. The SERS intensity is greater for the larger particles. 43 nm particles have a greater surface area compared to 16 nm particles which increases the analyte capture in the bulk affecting the SERS intensity.

Figure 4 | Occasional lower limits of detection

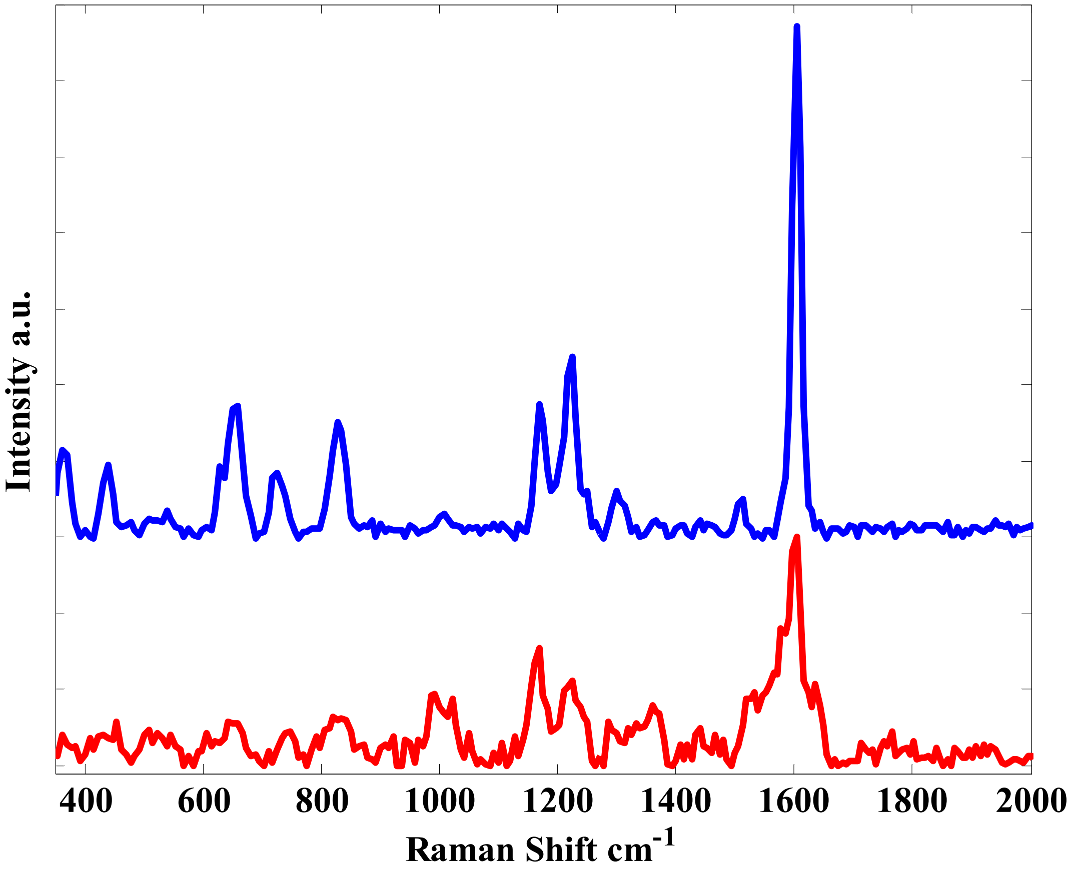

Although not consistently reproducible at times, a LOD lower than 0.32 nmoles could be achieved: the red (lower) curve shows a spectrum obtained for 32.3 pmoles of MATT, dissolved in the organic phase. The vibrational bands of MATT are present and distinguishable (1169, 1224, and 1604 cm^{-1}) even at these low dilutions.

Figure 5 | Demonstration of the versatility of the sensor

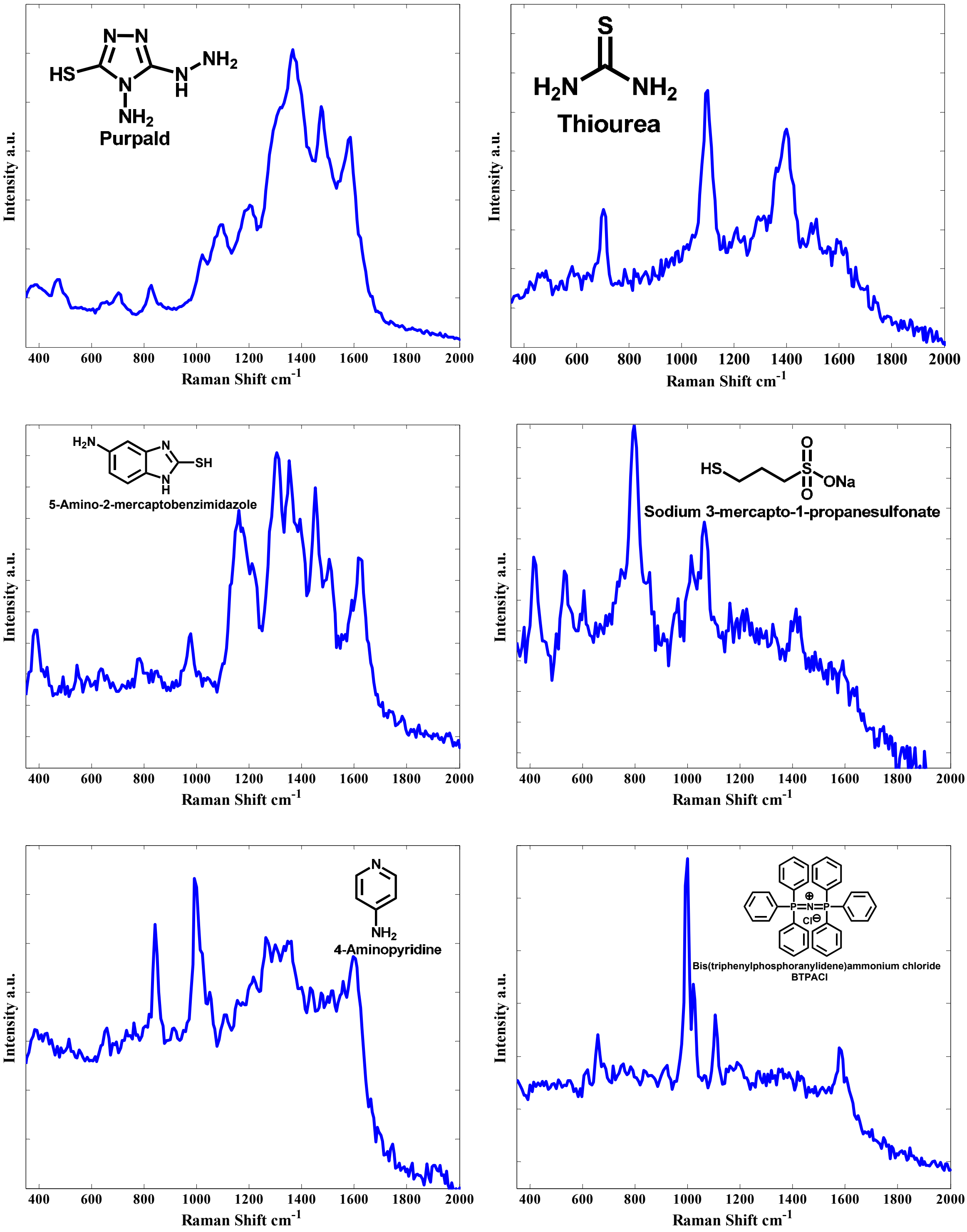

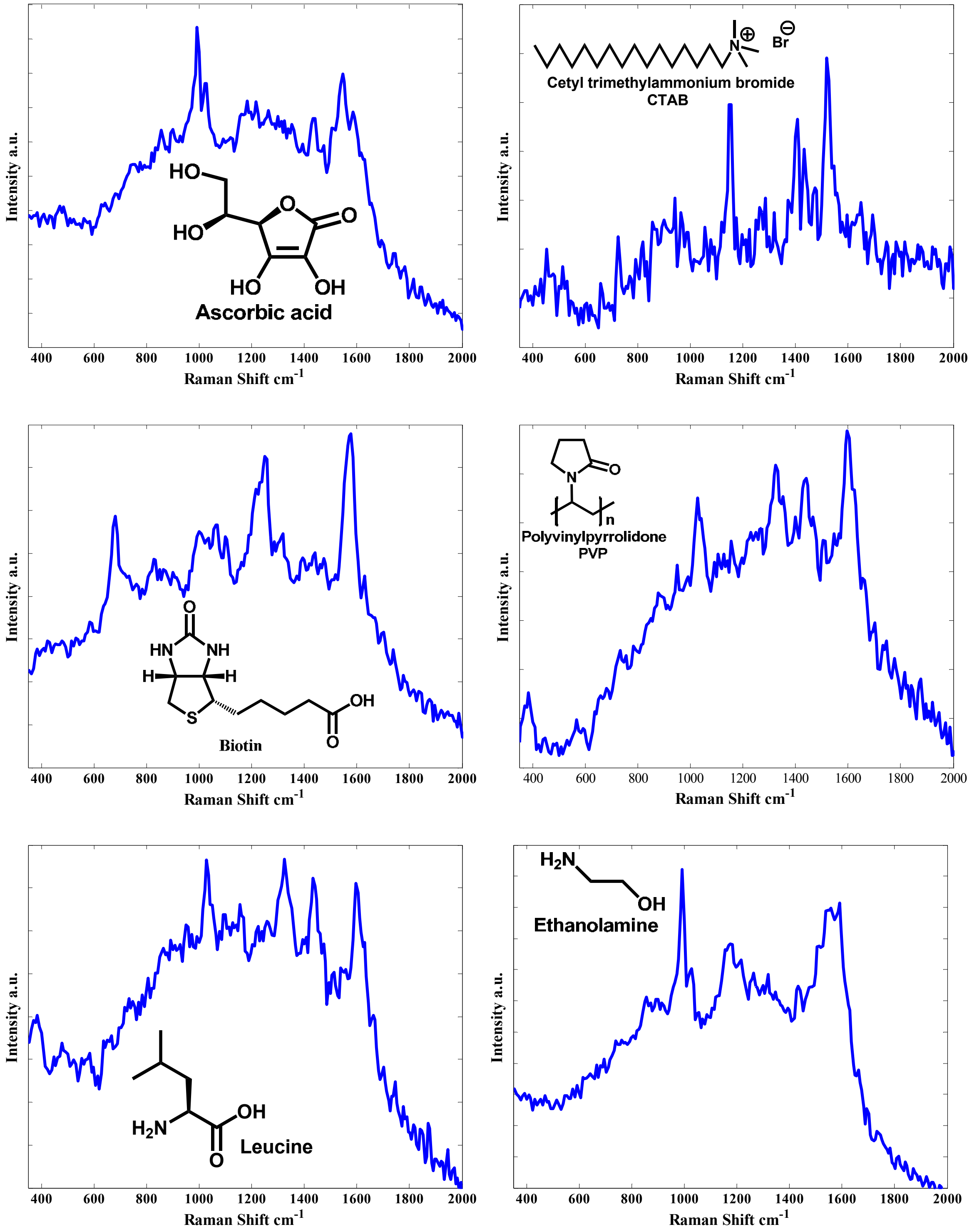

This set of spectra show that various analytes with different functionalities can be successfully detected at the LLI. Spectra were obtained from the analytes dissolved in the aqueous phase and [in each case a 1 μmole was dissolved in solution].

Figure 6 | Tri-analyte detection.

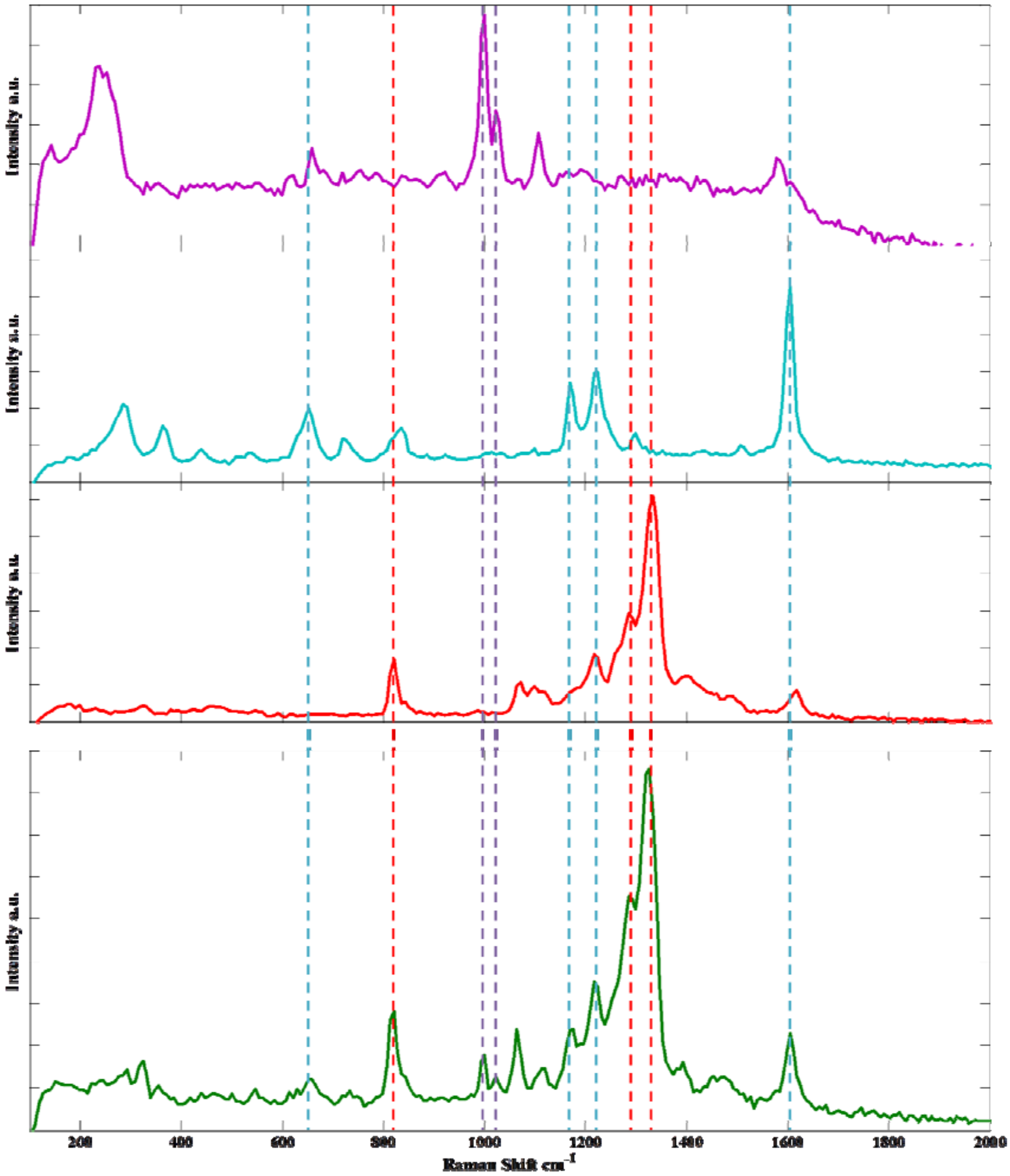

In addition to dual analyte detection using MNBI and MATT, tri-analyte detection was also achieved by dissolving Bis(triphenylphosporanylidene)ammonium chloride (BTPACl) in the water phase along with MNBI. MATT was dissolved in the organic phase. The resulting SERS spectrum (green) is composed of vibrational bands of all three analytes. Reference spectra for BTPACl (purple), MATT (turquoise), and MBNI (red) are shown for reference.

Figure 7 | Airborne detection of MATT at the LAI.

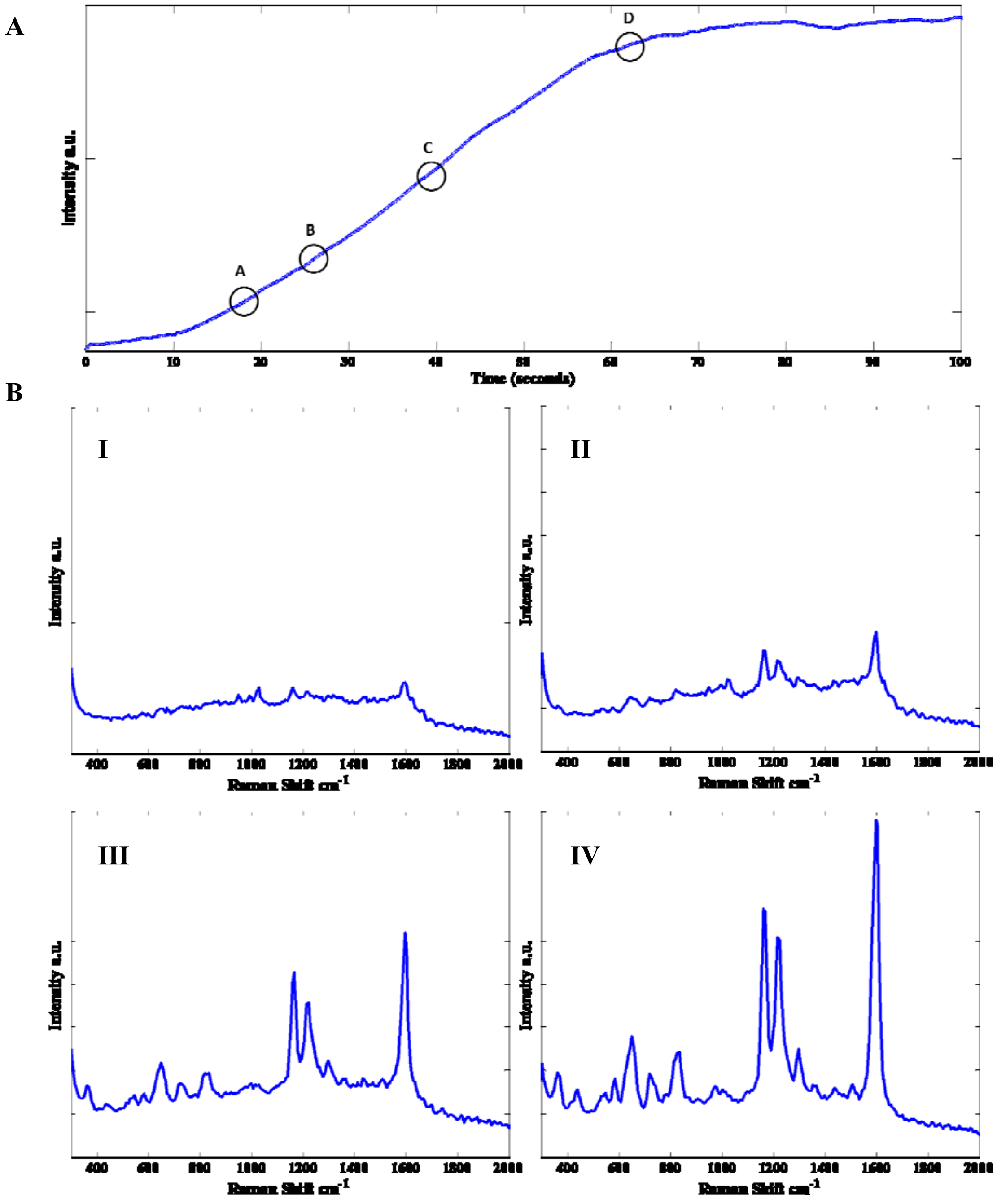

(A) The 1175 cm^{-1} vibrational band of MATT was used to construct a time series of the airborne detection of MATT. A plateau is observed which is a result of the NPs being saturated with MATT. (B) Examples of the full spectra SERS acquisitions for 4 different times are shown in for times of 18 (I), 26 (II), 40 (III), and 61 (IV) seconds.